A Study of Sound Generated by a Turbulent Wall Jet Flow Over Rough Surfaces

Dustin Leonard Grissom

Dissertation submitted to the faculty of the Virginia Polytechnic Institute and State University in partial fulfillment of the requirements for the degree of

Doctor of Philosophy
In
Aerospace Engineering

William J. Devenport
Roger L. Simpson
Ricardo A. Burdisso
Martin E. Johnson
Stewart A.L. Glegg

July 10, 2007
Blacksburg, Virginia

Keywords: rough wall boundary layer noise, wall jet, turbulent flow noise, acoustic scattering

A Study of Sound Generated by a Turbulent Wall Jet Flow Over Rough Surfaces

Dustin Leonard Grissom

A Study of Sound Generated by a Turbulent Wall Jet Flow Over Rough Surfaces

Dustin Leonard Grissom

ABSTRACT

The far field acoustics generated by turbulent flow over rough surfaces has been experimentally investigated in an acoustically treated wall jet facility. The facility allows direct measurement of the far field sound from small patches of surface roughness, without contamination from edge or other aerodynamic noise sources. The facility is capable of generating turbulent boundary layer flows with momentum thickness Reynolds numbers, ($\theta U_e/\nu$), between 450 and 1160. The variation of surface conditions tested cover the range from hydrodynamically smooth surfaces through most of the transitional range, with h^+ variations from 3 to 85. Single microphone narrow band acoustic spectra, measured in the far field, show sound levels as much as 15 dB above the background from 0.186 m^2 roughness patches. The measurements revealed the spectral shape and level variations with flow velocity, boundary layer thickness, and roughness size; providing the first data set large enough to assess the affects of many aerodynamic properties on the acoustic spectra. Increases in the size of grit type roughness produced significant increases in acoustic levels. Patches of hydrodynamically smooth roughness generated measurable acoustic levels, confirming that acoustic scattering is at least one of the physical mechanisms responsible for roughness noise. The shapes of the measured spectra show a strong dependence on the form of the surface roughness. The acoustic spectra generated by periodic two-dimensional surfaces have a much narrower louder peak than that generated by three-dimensional grit type roughness. Measurements also show the orientation of the two-dimensional surface significantly affects the acoustic levels and directivity.

The variation of sound levels with flow velocity and roughness size suggests the acoustic field is significantly affected by changes in the near wall flow due to the presence of the roughness. Previously proposed scaling models showed the general trends seen in measurements for flows over grit and two-dimensional roughness in the range of $20<h^+<50$. However, in cases with a low Reynolds number or large grit size, where the roughness is likely to significantly affect the hydrodynamic pressure field, the scaling models did not perform as well.

Acknowledgement

I would like to take this opportunity to thank all of those who have helped to make this dissertation possible. The support of my family has been instrumental throughout my life. My parents Jeri and Larry Grissom have always encouraged me to follow my ambitions and to not settle for the easy path. They have also lovingly taught me the lessons of dedication, persistence, and work that are needed to achieve ones goals. I also appreciate the support and example of my brother, Drew Grissom. His friendship has been invaluable, and his passion and dedication to those around him is a constant example to me.

I would also like to thank Dr. James Marchman for introducing me to experimental research during my sophomore year. His excitement and curiosity towards research have been an example of the attitude needed for research. I would also like to thank Dr. Wayne Neu and the Virginia Tech Human Powered Submarine Team for developing my skills and knowledge of applied aerodynamics and problem solving. The satisfaction of solving a "real" problem has always provided motivation to continue through challenges.

For this project I would like to thank the Office of Naval Research, and especially Dr. Ki-Han Kim, for sponsoring this work through grant N00014-05-1-051. I would also like to thank the National Science Foundation for providing me with a fellowship that allowed me to continue my education through this process. I also wish to thank my advisory committee; Dr. Roger Simpson, Dr. Stewart Glegg, Dr. Ricardo Burdisso, Dr. Martin Johnson, and Dr. Joseph Schetz. Their support and guidance throughout this process have been indispensable.

A special thanks is needed for my advisor Dr. William Devenport. His abilities as an instructor and mentor are matched only by his excitement for knowledge. My skills as a researcher and problem solver have grown more as a result of our discussions and dialogues, which I will miss greatly, than through anything else. His actions and example have also taught me to always remember your family and loved ones. These personal relationships are more important than any discovery, honor, or award that can be achieved in the lab.

The staff of the Aerospace and Ocean Engineering department has also been of tremendous help throughout this process. The help of Bruce Stanger, James Lambert, Mark Montgomery, Bill Oetjens, and Steve Edwards in designing, constructing, and trouble shooting the various facilities and instruments needed for this project was tremendous. I would also have never made it this far without the help of the AOE office staff of Wanda Foushee, Hannah Swiger, Janet Murphy, Nancy Moorman, Gail Coe, Bettie Williams, and Sue Teel.

The support of all my colleagues and friends has also been tremendous, especially everyone who is part of Lab 7. Thanks to Josh Staubs, Aurelian Boroltz, Nanyaporn Intaratep, Nicolas Spitz, and J.V. Larssen for their assistance and support throughout my graduate experience. A special thanks to Elizabeth Craig for her assistance, and the many hours spent in the wind tunnel helping me complete measurements. Also, this work would not have been possible without the work of Ben Smith. His assistance, work, and parallel research have been indispensable. The many long nights together in the wind tunnel have produced not just mounds of data, but a wonderful friendship.

Finally, I would like to thank my wonderful wife Kathy. Her understanding, support, and dedication throughout this process have allowed me to meet the challenges research often presents. Without her advice, assistance, and many days and nights given up to helping this project, it would have never reached completion. She is a constant source of love and encouragement, and for this I will always love her.

Table of Contents

Chapter 1 Introduction 1
1.1 Motivation 1
1.2 Problem Definition 1
1.3 Review of Previous Work 3
1.3.1 Topics of Further Discussion 10
1.3.2 The Source Mechanism, Scattering or Vortex Shedding 13
1.3.3 Modeling of Wall Pressure Spectrum 15
1.4 Parallel Theoretical Work 23
1.4.1 Scaling Parameters 25
1.5 Alternative Derivation methods 27
1.5.1 Dimensional Analysis 27
1.5.2 Specific Models 28
1.6 Quadrupole Scaling 31
1.6.1 Dimensional Analysis 31
1.6.2 Specific Models 31
1.7 Shortcomings of Previous Work 32
1.8 Objectives and Approach 33
1.9 Experimental Approach 36
Chapter 2 Facility Design and Preliminary Tests 37
2.1 Wall Jet Facility 37
2.2 Early Designs 37
2.3 Preliminary Wall Jet Facility 39
2.3.1 Nozzle Design 39
2.3.2 Blower Selection 43
2.3.3 Settling Chamber Design 44
2.3.4 Acoustic Enclosure 48
2.3.5 Facility Construction 49
2.3.6 Preliminary Instrumentation 50
2.3.7 Preliminary Configuration Calibration 51
2.3.8 Flow Quality and Acoustics at Different Speeds and Conditions 56
2.3.9 Detection of Roughness noise 60
2.3.10 Phased Array Measurements 62
Chapter 3 Facility and Instrumentation 65
3.1 Final Facility 65
3.1.1 Settling Chamber Modifications 65
3.1.2 Final Wall Jet Configuration Calibration 72
3.1.3 Acoustic Enclosure Modifications 76
3.2 Instrumentation 81
3.2.1 Acoustic Instrumentation 81
3.2.2 Aerodynamic Instrumentation 82
3.2.3 Surface Roughness Instrumentation 83
Chapter 4 Experimental Setup 84
4.1 Coordinate System 84
4.2 Surface Roughness 85

4.3 Sampling Schemes 87
4.4 Uncertainty 87
4.4.1 Acoustic Measurements 87
4.4.2 Aerodynamic Measurements 88
4.4.3 Other Measurements 88
4.5 Aerodynamic Test Matrix 89
4.6 Acoustic Test Matrix 94
4.7 Scalloping Correction 99
4.8 Spectral Subtraction Method 100
Chapter 5 Wall Jet Aerodynamics 102
5.1 Smooth Plate Measurements 102
5.2 Two-Dimensional Wall Jet Flow Model 105
5.3 Rough Wall Aerodynamic Measurements 107
Chapter 6 Acoustic Measurements from Stochastic Roughness 113
6.1 Effects of Velocity 113
6.1.1 Acoustic Measurements 113
6.1.2 Spectral Scaling 115
6.2 Effects of Roughness Size Variation 124
6.2.1 Acoustic Measurements 124
6.2.2 Spectral Scaling 126
6.3 Vertical Directivity 135
6.4 Buildup Test 136
6.5 Summary 142
Chapter 7 Two-Dimensional Roughness 144
7.1 Surface Characteristics and Edge Effects 144
7.2 Influence of Flow Velocity 145
7.3 Vertical Directivity 152
7.4 Effects of Roughness Orientation 154
7.4.1 Orientation Effects at a Fixed Observer Position 155
7.4.2 Orientation Effects on Horizontal Directivity 156
Chapter 8 Discussion 161
8.1 Reynolds Number Effects 161
8.2 Simple Scaling Models 162
Chapter 9 Conclusions 166
References 168

Nomenclature

Capital Roman Letters

A_h	Characteristic correlation area of scattered portion of the hydrodynamic pressure field
A_m	Amplitude
A_u, A_δ	Coefficent values for the wall jet model of Wygnanski *et al.* (Wygnanski, *et al.,* 1992)
L	Characteristic length
L_a, L_b	Semi-major and minor axis lengths of nozzle
L_h	Length scale characteristic of the height of the source region
M	Mach number
$P(k,\omega)$	Pressure wavenumber frequency spectrum
P_{ref}	Acoustic reference pressure, $20x10^{-6}$ Pa
S	Surface area
T	Lighthill's stress tensor
T_h	Characteristic time scale of the scattered field
U_e	Edge Velocity
U	Characteristic velocity
U_c	Convection velocity
U_∞	Freestream velocity
U_0	Velocity at the nozzle exit
V	Volume

Lower Case Roman Letters

a	Cylinder radius
b	Nozzle height
c	Speed of sound
f	Frequency, Hz
h	Roughness height
h_g	Geometric roughness height
h_s	Equivalent sand grain roughness height
h_1, h_2	Chamber and nozzle height parameters used for nozzle design
k, k_i	Wavenumber vector, or wavenumber component in the i direction
k_r	Wavnumber vector of the surface roughness
l_e	Roughness streamwise correlation length
n_u, n_δ	Exponent values for the wall jet model of Wygnanski *et al.* (Wygnanski, *et al.,* 1992)
p	Pressure
p'	Unsteady pressure fluctuations
u	streamwise instantaneous velocity
u'_{max}	Maximum rms streamwise turbulent velocity fluctuation
u'_{maxbl}	Maximum rms streamwise turbulent velocity fluctuation measured in the boundary layer

$u_{'min}$	Minimum rms streamwise turbulent velocity fluctuation
u_τ	Skin friction velocity
v	Spanwise instantaneous velocity
w	Wall normal instantaneous velocity
x	Streamwise dimension
y	Spanwise dimension
$y_{1/2}$	Height to the point of half velocity in the free shear layer of a wall jet
$y_{u'max}$	Distance from the wall to $u_{'max}$ in a vertical wall jet profile
$y_{u'maxbl}$	Distance from the wall to $u_{'maxbl}$ in a vertical wall jet profile measured in the boundary layer
$y_{u'min}$	Distance from the wall to $u_{'min}$ in a vertical wall jet profile
z	wall normal dimension

Greek Letters

α_y, α_z	Scaling parameters from the Corcos surface pressure model (Corcos, 1963)
δ	Boundary layer thickness
δ^*	Boundary layer displacement thickness
θ	Boundary layer momentum thickness
θ	Angle in the x-y plane away from the x-axis
Λ_y, Λ_z	Scaling parameters from the Efimtsov surface pressure model (Efimtsov, 1982)
ρ	Fluid density
ρ'	Density fluctuation
σ_h	Characteristic hydrodynamic stress or pressure
τ, τ_w	Shear, wall shear
τ^*	Retarded time
φ	Angle in the x-z plane away from the x-axis
$\Phi(\omega)$	Pressure frequency spectrum
$\Phi_{pp}(\omega,k)$	Surface pressure frequency wavenumber spectrum
ω	frequency, rad/s

List of Figures

Figure 1-1 Schematic of the rough-wall boundary layer noise problem..... 3
Figure 1-2 Polar plots of source directivity from Chanaud (1969) for (a) a smooth disk and (b) a ring roughened disk. Sound levels were measured 5.65 disk radii away from the disk center with a disk edge speed of 80 m/s..... 11
Figure 1-3 Polar plot of sound levels reported by Chanaud (1969) for a ring roughened spinning disk with the smooth disk sound level removed. The directivity patterns by circumferentially aligned dipoles have been added for reference with the two higher frequency measurements..... 12
Figure 1-4 The three graphs show qualitatively the behavior of the wall pressure wave number spectrum. Contour levels in (a) show the convective ridge and super sonic region. (b) Shows contour levels in the wave number plane at a typical frequency. The levels in both figures are representative, and not to scale. 16
Figure 1-5 Wavenumber frequency spectrum predicted by Corcos (1963) model for a typical boundary layer flow, U_c = 30 m/s. 17
Figure 1-6 Wavenumber frequency spectrum predicted by Efimtsov (1982) model for a typical boundary layer flow, U_c = 30 m/s. 18
Figure 1-7 Wavenumber frequency spectrum predicted by Smol'yakov and Tkachenko (1991) model for a typical boundary layer flow, U_c = 30 m/s..... 19
Figure 1-8 Wavenumber frequency spectrum predicted by Chase II (1987) model for a typical boundary layer flow, U_c = 30 m/s. 21
Figure 1-9 Wall pressure spectrum models for a turbulent boundary layer flow with U_c = 30 m/s at 5000 rad/s..... 21
Figure 1-10 Schematic defining the orientation of two-dimensional roughness relative to the mean flow. The figure is looking down on the roughness from above..... 25
Figure 1-11 Sound pressure spectrum measured by Cole (1980) at four different speeds (24 m/s diamonds, 31.4m/s triangles, 38.3m/s squares, and 46.5m/s circles) over 40 grit (blue) and 80 grit (green) roughened surfaces. Results are scaled on the dipole scaling law proposed by Cole..... 26
Figure 1-12 Schematic layout of a 2D wall jet flow..... 34
Figure 2-1 Early channel design. Settling chamber shown on right with one wall removed. The channel top and nozzle would be adjustable to allow control of the channel height. A blower not shown in the figure drives the system. 39
Figure 2-2 Color contour plot of showing velocity magnitude inside a 2:1 aspect ratio nozzle predicted by ideal source panels. 40
Figure 2-3 Pressure coefficient predicted by panel method along the nozzle surface for flow through a 2:1 aspect ratio nozzle using ideal source panels. 41
Figure 2-4 Pressure coefficient along nozzle wall for various nozzle shapes as predicted by ideal source panels..... 42
Figure 2-5 Boundary layer growth along the nozzle surface, s, for a 3:6 aspect ratio nozzle. Results shown are from implicit laminar and turbulent boundary layer methods for their respective regions. The nozzle begins at s = 450 mm and ends at s = 700mm..... 43

Figure 2-6 Layout of the Anechoic Flow Facility at the David Taylor Model Basin, figure taken from NAVSEA website (Anechoic Flow Facility, 2004). The figure shows two sets of curved vanes, circled in red, used to reduce fan noise contamination in the test section. 45
Figure 2-7 Contour plot of the relative sound level inside the settling chamber final configuration predicted by a ray tracing model. The chamber is 3300 mm long and 1244 mm wide. The black circle on the left shows the source region, and the channel entrance is in the middle of the right side wall. 46
Figure 2-8 Picture of acoustic egg crate foam used to line the interior of the settling chamber. Also shown are the absorption coefficient values for the 95.25 mm thick foam. 47
Figure 2-9 Top and Side view drawings of the preliminary settling chamber configuration. All white components are built of 19 mm thick MDF. Flow enters the chamber through the green collar on the left, and exits through the pink nozzle on the right. All dimensions are in mm. 47
Figure 2-10 Photograph showing the acoustic enclosure around the smooth plate wall jet. 48
Figure 2-11 Photographs of the settling chamber showing: (a) preliminary settling chamber and blower enclosure during assembly and (b) internal acoustic treatment in spacer and inlet sections. 49
Figure 2-12 Front of preliminary settling chamber showing bolts for nozzle adjustment. 50
Figure 2-13 Total SPL measured 1.3m from blower nozzle at different speeds with and without exit silencer..... 51
Figure 2-14 Narrow band spectra of sound measured 1.3 m from blower exit with and without exhaust silencer installed. Spectra were taken at two exit speeds 18 m/s (solid lines) and 42 m/s (dotted lines). 52
Figure 2-15 Photo of the initial wall jet configuration used to test the settling chamber and nozzle performance. 53
Figure 2-16 Vertical and horizontal profiles measured at the settling chamber nozzle. (a) shows profiles measured along a horizontal line at x = 38.1mm, y = b/2, (b) shows vertical profiles measured at x = 38.1mm, z = 0. Results are shown for 3 different nozzle heights. 54
Figure 2-17 Sound spectra measured at different locations along the settling chamber. The nozzle exit speed during these runs was 54 m/s, with a motor speed of 35 Hz. 55
Figure 2-18 Acoustic spectra measured in the acoustic enclosure with flow of various speeds over a smooth plate. 57
Figure 2-19 Acoustic spectra measured for flow over a smooth plate. Spectral levels are normalized on the jet exit velocity to the eighth and the nozzle height. 58
Figure 2-20 Vertical velocity profiles measured along the plate. Profiles have been normalized on the local maximum velocity, and height to half decay. The solid curve is the profile shape predicted by Narasimha (1973) for a self similar wall jet flow. 59
Figure 2-21 Horizontal velocity profiles measured at three streamwise locations for a wall jet with an exit velocity of 50 m/s and a nozzle height of 25.4 mm. The

profiles were measured at a height above the plate corresponding to the height for maximum velocity for each streamwise location. 60
Figure 2-22 Photograph showing the edge of a patch of 36 grit roughness attached to the plate surface with aluminum foil tape. The tape has been smoothed on the surface, and pressed into the sandpaper surface to prevent the tape or paper from peeling off and flapping..... 61
Figure 2-23 Acoustic spectra measured from the wall jet flow for 4 different surface conditions. Smooth is the smooth plate, 80 grit is with an 80 grit sanding belt attached, inverted is with the sanding belt attached with the sand down, and Mylar is with a sheet of Mylar covering the fabric backing of the inverted sanding belt. Levels are single Hz bandwidth shown in ⅛ octave band averages..... 62
Figure 2-24 Beam formed maps of sound pressure levels measured by the 63 microphone array at 2000 Hz. The contour plot on the left was taken over the clean plate; the plot on the right was with a patch of Lego roughness on the plate in the rectangle shown. The contour levels range from -5 to 40 dB, axis are distances in mm. Both measurements were taken for a nozzle exit flow speed of 60 m/s, with flow from top to bottom of the contour plots. The upper plot shows single microphone sound levels measured for various flows, with the two corresponding conditions circled..... 63
Figure 3-1 Schematic of generic contraction profile based on method of Fang *et al.* (2001)..... 66
Figure 3-2 Comparison of three possible contraction profiles for modified nozzle chamber section. The blue dotted line is the nozzle shape used in the original configuration. The red dashed curved is the design selected for the final nozzle section..... 67
Figure 3-3 Side view drawing of the final nozzle section design. The nozzle itself is shown in pink, along with the beginning of the extended contraction that ends at the bottom floor of the settling chamber. The upper nozzle is adjustable through a screw system shown in blue, and the purple is the round side piece to reduce edge noise..... 68
Figure 3-4 Side and Top view drawings of the final configuration of the inlet section of the settling chamber. Piece made of 19 mm thick MDF panels are shown in white, acoustic foam is shown in gray, steel reinforcement bars are shown blue, the flow inlet is shown in green, and the fiber glass pillow is shown in yellow. 69
Figure 3-5 Side and Top view drawings of the final configuration of the spacer section of the settling chamber. Piece made of 19 mm thick MDF panels are shown in white, acoustic foam is shown in gray, and steel reinforcement bars are shown blue..... 70
Figure 3-6 Side and Top view drawings of the final configuration of the spacer section of the settling chamber. Piece made of 19 mm thick MDF panels are shown in white, acoustic foam is shown in gray, nozzle components are shown in pink, and steel reinforcement bars are shown blue..... 71
Figure 3-7 Top and side view drawings of the final settling chamber configuration. Drawings show the internal layout of the settling chamber including the placement of acoustic foam, shown in gray. 72

Figure 3-8 (a) Vertical velocity profiles measured 38.1 mm downstream of the nozzle exit at three spanwise locations, on center, and ±305 mm. (b) Photo of oil flow visualization on the center of the nozzle. This shows a separation bubble as a result of the joint between the two nozzle halves. 73
Figure 3-9 Horizontal velocity profiles measured at three streamwise locations for a nozzle height of 12.7 mm, and a jet exit velocity of 30 m/s. All profiles have been normalized on the jet exit velocity. 74
Figure 3-10 Vertical velocity profiles measured at on the plate centerline and at the edge of the two-dimensional jet region. The green and blue profiles were measured 952.5mm downstream of the nozzle exit, the red and black profiles were measured 1905mm downstream. 75
Figure 3-11 Maximum sustainable jet exit velocity, U_0, for a range of nozzle openings, b, measured in the final facility configuration. 76
Figure 3-12 Side view drawings of the preliminary and final configurations for the acoustic enclosure around the plate, all dimensions in mm. The walls in both configuration are covered with 457 mm acoustic wedges, and the ceiling and shelf are covered in 95 mm egg crate acoustic foam. 77
Figure 3-13 Background noise levels measured using a single microphone in the original and final configurations of the acoustic enclosure. Sound levels are shown integrated over 25 Hz bands. Plot (a) shows the sound levels measured in both configurations, plot (b) these levels are scaled on jet velocity to the 8^{th} power. 79
Figure 3-14 Integrated sound levels measured in the Final and Preliminary wall jet configuration over a smooth plate. Also shown are lines corresponding to scaling laws for dipole, U^6, and quadrupole, U^8, acoustic sources. 80
Figure 3-15 Acoustic spectra measured under the flow conditions of cases 37-45 for two different surface conditions. The spectrum labeled smooth have no surface treatment. The curve labeled Mylar has a 305 mm by 610 mm patch of smooth Mylar film attached to the plate. 81
Figure 3-16 Typical sensitivity variation for B&K 4190 and 4191 microphones used in study. Variation is shown for a free field acoustic source with protection grid on the microphone. 82
Figure 4-1 Schematic of the wall jet flow and reference system. The nozzle height, b, and the nozzle exit speed, U_0, can be adjusted by the facility setup. 84
Figure 4-2 Example images of rough surfaces. (a) – 60 grit sandpaper roughness. (b) – 60 grit floor sanding sheet. 86
Figure 4-3 Illustration of the two-dimensional roughness pattern used in Chapter 7. (a) shows a magnified photograph of the edge of the lens sheet, (b) shows the lens schematically, with the roughness height, h, and length scale, l_e, labeled, and (c) shows the measured lens profile in black with the absolute value of a sine function overlaying it in blue. 86
Figure 4-4 Acoustic response functions measured inside the acoustic enclosure. The black curve shows the original response measured above the shelf, the red curve shows the response measured after the shelf was modified to reduce scalloping. 100

Figure 4-5 Acoustic spectra shown for the same flow conditions. One with roughness on the plate (Case 149), and one with a smooth plate (Case 140). The blue curve shows the spectrum due only to the roughness, which is found by subtracting the two spectra. 101
Figure 5-1 Schematic of the wall jet flow and reference system. The nozzle height, b, and the nozzle exit speed, U_0, can be adjusted by the facility setup. At each streamwise location the flow profiles can be described by a number of different scales shown in the figure as δ, $y_{1/2}$, and U_e. 102
Figure 5-2 Vertical velocity profiles measured on the center line of the smooth plate at several downstream locations. The legend lists the distance from the nozzle to the measurement location in millimeter. (a) Measured levels plotted as measured. (b) Velocity profiles normalized on the local maximum velocity and half velocity height. 103
Figure 5-3 Normalized mean velocity profiles for all the smooth wall cases compared with Wygnanski *et al.* (1992). 104
Figure 5-4 Spanwise velocity profiles measured at x=38 mm (blue symbols), 952 mm (green symbols) and 1867 mm (red symbols) at a distance y of 6.4 mm above the test plate for a nozzle height of 12.7 mm and nominal exit velocity U_0 of 30 m/s. 105
Figure 5-5 Plot of measured boundary layer length scales compared with measured boundary layer thickness for smooth wall jet flow cases measured in table 3-2. 106
Figure 5-6 Comparison of velocity and length scales modeled by Equation 5.1 and measured in the wall jet facility. 106
Figure 5-7 Mean velocity profiles measured after different lengths of 40 grit sandpaper. The sandpaper fetch begins at x = 1245 mm for all cases. The curve marked by squares was measured under the same conditions as the curve marked by * but with no roughness on the plate. 107
Figure 5-8 Mean velocity profiles measured after different lengths of 40 grit roughness. (a) Shows these profiles normalized on $y_{1/2}$ and edge velocity. (b) Shows the same measurements in the inner region. The blue curve was measured at the same location as the downstream most roughness case but with no roughness present. 108
Figure 5-9 Maximum velocity values predicted by Equation 5.1 for conditions of Table 4-3 plotted against the measured maximum velocity values. 109
Figure 5-10 Turbulence intensity profiles measured downstream of patches of different lengths of 40-grit sandpaper roughness (cases 32 to 35 from Table 4-3) compared with a profile measured above the smooth wall (case 10 from Table 4-2). The nozzle height is 12.7mm and jet exit velocity 30 m/s for all cases. (a) Normalized on the fixed scales U_o and b, (b) normalized on mixing layer mean flow scales U_e and $y_{1/2}$, (c) Normalized on boundary layer scales U_e and δ. 110
Figure 5-11 Length scales measured downstream of a 305 mm long roughness patches of different sandpaper roughness sizes. Measurements are taken from cases 37-45, group J, of Table 4-3 with a nozzle height of 12.7 mm and a jet exit velocity of 60 m/s. 111

Figure 5-12 Mean velocity profiles measured downstream of a 310 mm long roughness fetch of different roughness heights. The roughness patch began at x = 1245 mm with a wall jet flow from a nozzle height of 12.7 mm and U_0 = 30 m/s..... 112
Figure 6-1 Raw acoustic spectra measured by a single microphone at different speeds in m/s over a clean surface (solid) and a 305x610 mm patch of 40 grit sandpaper (dotted)..... 114
Figure 6-2 Linear difference in rough wall and smooth wall spectra plot on a decibel scale referenced to 20×10^{-6}Pa. The legend lists the mean edge velocity over the patch, averaged between the leading and trailing edge measured values, and h^+, based on the mean skin friction velocity..... 115
Figure 6-3 Acoustic spectra measured from a wall jet flow over a patch of 40 grit sandpaper at different speeds normalized based on the dipole velocity scaling proposed by Cole (1980), (a), and the quadrupole velocity scaling of Cole, (b). 117
Figure 6-4 Acoustic spectra measured from a wall jet flow over a patch of 40 grit sandpaper at different speeds with amplitude normalized on the maximum turbulent velocity fluctuations and frequency normalized on the maximum mean velocity. The scaling in figure (a) uses $U_e u'^4$ for amplitude scaling; in figure (b) $U_e u'^4$ is used..... 119
Figure 6-5 Acoustic spectra measured from a wall jet flow over a patch of 40 grit sandpaper at different speeds with amplitude and frequency normalized on the skin friction velocity and roughness height. The scaling in (a) uses u_τ^5 as suggested by Howe (1988) for amplitude scaling, (b) is u_τ^7..... 121
Figure 6-6 Acoustic spectra measured from a wall jet flow over a patch of 40 grit sandpaper at different speeds normalized on two mixed dipole scales. (a) is the scaling presented by Glegg (2007), (b) is the scaling presented by Farabee and Geib (1991)..... 123
Figure 6-7 Acoustic spectra radiated by different roughness patches under a wall jet flow with U_o = 60 m/s, b = 12.7 mm. Raw spectra are shown on plot (a). Spectral levels on the right, (b) are the levels above those of the smooth wall flow..... 125
Figure 6-8 Acoustic spectra measured for flow past patches of different surface roughnesse normalized on the outer flow scaling of Cole (1980)..... 128
Figure 6-9 Acoustic spectra measured for flow past different surface roughnesses normalized on the inner flow scaling of Howe (1988)..... 129
Figure 6-10 Acoustic spectra measured for flow past patches of different surface roughness normalized on the mixed flow scaling of Farabee and Geib (1991). 130
Figure 6-11 Acoustic spectra measured for flow past patches of different surface roughness normalized on the mixed flow scaling of Glegg (2007)..... 131
Figure 6-12 Acoustic spectra measured for flow past patches of different surface roughness normalized on the quadrupole scaling model of Cole (1980) (a), and an inner variable scaling model (b)..... 132
Figure 6-13 Acoustic spectra measured for the same flow conditions over patches of different surface roughness. Spectra are normalized using the maximum

turbulence level to scale the hydrodynamic shear, and the roughness height and edge velocity for time and area scales. 134
Figure 6-14 Acoustic spectra measured for the same flow conditions over patches of different surface roughness. Spectra are normalized using the skin friction to scale the hydrodynamic shear, and the displacement thickness and skin friction velocity for time and area scales. 134
Figure 6-15 Acoustic spectra measured for the same flow conditions over patches of different surface roughness. The scaling shown modifies the Cole (1980) scaling to include the effects of *h* in the spectral level normalization. 135
Figure 6-16 Directivity measured in a vertical arc over a patch of 40 grit sand paper. Flow is from right to left, with the roughness patch centered at the origin. The black curve shows the directivity of a flow aligned dipole centered on the roughness patch, the level has been set for comparison with the measurement. 136
Figure 6-17 Acoustic effectiveness as a function of streamwise distance from the nozzle. 138
Figure 6-18 Sound levels measured at a fixed observer location for three different roughness patch lengths under the same flow conditions. 139
Figure 6-19 Sound levels measured at a fixed observer location for three different roughness patch lengths under the flow generated for a 25.4 mm nozzle exit with a nozzle exit velocity of 20 m/s. 140
Figure 6-20 Sound levels measured at a fixed observer location for three different roughness patch lengths under the flow generated for a 12.7 mm nozzle exit with a nozzle exit velocity of 30 m/s. 141
Figure 6-21 Sound levels measured at a fixed observer location for three different roughness patch lengths under the flow generated for a 12.7 mm nozzle exit with a nozzle exit velocity of 40 m/s. 142
Figure 7-1 Acoustic spectra measured for the wall jet flow generated by a 25.4 mm nozzle with 45 m/s exit speed over a smooth plate, 2d roughness patch, and the 2d roughness patch covered with mylar. 145
Figure 7-2 Acoustic spectra measured at different flow speeds for flow over a patch of two-dimensional roughness. 147
Figure 7-3 Far field acoustic pressure spectra from a two-dimensional roughness patch normalized on a dipole scaling using the local edge velocity, U_e, and displacement thickness, δ*. 148
Figure 7-4 Far field acoustic pressure spectra from a two-dimensional roughness patch normalized on a quadrupole scaling using the local edge velocity, U_e, and displacement thickness, δ*. 149
Figure 7-5 Far field acoustic pressure spectra from a two-dimensional roughness patch normalized on the dipole scaling model proposed by Glegg (2007). 150
Figure 7-6 Far field acoustic pressure spectra from a two-dimensional roughness patch normalized on: (a) the model of Farabee and Geib (1991), and (b) the model of Howe (1988). 151
Figure 7-7 Far field acoustic pressure spectra for two-dimensional roughness, shown as solid and dashed lines, and sand grit roughness, shown as lines with triangles, shown for variations in flow speed. 152

Figure 7-8 Schematic of the microphone arrangement used for the vertical directivity test. 153
Figure 7-9 Acoustic spectra measured in a vertical arc centered over the two-dimensional roughness patch. The legend values are the vertical angles, θ, between the microphone position and the center of the roughness patch. 153
Figure 7-10 Ratio in acoustic spectra levels relative to spectra measured at 37° above the plate for flow over a two-dimensional roughness patch at different speeds. The legend values are the vertical angles, θ, between the microphone position and the center of the roughness patch. 154
Figure 7-11 Acoustic spectra measured for flow over a lens patch at different orientations to the flow. Legend titles give the angle between the flow and the roughness ridges in degrees..... 155
Figure 7-12 Microphone locations shown for the horizontal directivity test over the two-dimensional surface roughness patch. 157
Figure 7-13 Spectra measured by four microphones at different angles along a horizontal arc around a patch of two-dimensional roughness. The roughness ridges were aligned perpendicular with the flow. The legend values are the horizontal angles, ϕ, between the microphone position and the center of the roughness patch..... 158
Figure 7-14 Spectra measured by four microphones at different angles along a horizontal arc around a patch of two-dimensional roughness. The roughness ridges form a 60° angle with the flow direction. The legend values are the horizontal angles, ϕ, between the microphone position and the center of the roughness patch..... 159
Figure 7-15 Spectra measured by four microphones at different angles along a horizontal arc around a patch of two-dimensional roughness. The roughness ridges form a 30° angle with the flow direction. The legend values are the horizontal angles, ϕ, between the microphone position and the center of the roughness patch..... 160
Figure 8-1 Measurements taken over 40 grit sandpaper roughness marked by triangles, compared with measurements over the two dimensional roughness shown with lines. 162
Figure 8-2 Acoustic spectra measured for flow past 40 grit sand paper at different speeds. The frequency has been non-dimensionalized using outer flow variables, and the amplitudes are shown as 1/8th octave band levels. On the right, the spectral level is plotted against the edge velocity for three non-dimensional frequencies. 164
Figure 8-3 Acoustic spectra measured for flow past different sand grits under the same flow conditions (a). The frequency has been non-dimensionalized using outer flow variables, and the amplitudes are shown as 1/8th octave band levels. In (b), the spectral level is plotted against the roughness height for three non-dimensional frequencies. 165

List of Tables

Table 1-1 Possible dipole scaling models 30
Table 1-2 Possible quadrupole scaling methods..... 32
Table 4-1 Rough surface detail summary..... 85
Table 4-2 Smooth wall aerodynamic conditions summary 90
Table 4-3 Aerodynamic measurements for flow over rough surfaces 92
Table 4-4 Acoustic measurement conditions summary..... 95

Chapter 1 Introduction

1.1 Motivation

In many practical engineering flows sound radiation is an important consideration. Noise generated by the interaction of a turbulent boundary layer with a rough surface is commonly found in high Reynolds number flows. This is especially common in naval applications. For example, low Mach numbers and high Reynolds numbers in the boundary layer characterize the flow past a submarine. The lifting surfaces, which generate edge noise, are also much smaller in naval applications than on aircraft when compared to the area covered by a turbulent boundary layer. Under these conditions, boundary layer noise is likely a dominant acoustic source. The high Reynolds number flows associated with naval applications cause relatively smooth surfaces to appear hydrodynamically rough, increasing the importance of rough wall boundary layer noise.

Despite the prevalence of rough wall boundary layer flows in engineering applications, little conclusive information about the topic is found in published literature. This is primarily due to the low acoustic levels of roughness noise that can be generated in a laboratory setting. However, as other acoustic source mechanisms are reduced, as is currently occurring with commercial aircraft, rough wall boundary layer noise will become more important. Few analytical models exist to describe roughness noise and they do not agree on the physical process that generates the far field noise. This lack of agreement is largely due to the limited experimental database that is available for model validation. Experimental studies have shown that roughness noise measurements are often contaminated by other noise sources. In addition measurements often require unusual flow configurations, which make application of the results to conventional flows difficult.

The report presents an overview of the current understanding of sound generated by turbulent boundary layer flow past a rough surface and discusses previously published experimental and analytical studies on this topic. This review shows that a more diverse experimental data set is needed to verify and develop models of roughness noise. This report then discusses a new wall jet facility developed at Virginia Tech to test roughness noise. Finally, measurements from this facility are presented and discussed which reveal the shape of the far field roughness noise spectrum and the effects of surface conditions, flow speed, and boundary layer thickness on roughness noise. This data is also compared with the analytical models of roughness noise that are currently available.

1.2 Problem Definition

The physical problem being investigated is shown schematically in Figure 1-1. A turbulent boundary layer flow is shown moving past a rough surface, which results in the propagation of acoustic waves into the far field. The boundary layer flow is defined by the edge velocity U_e, and a boundary layer thickness δ. The shape of the boundary layer

can be described by other typical boundary layer thickness variables such as the displacement thickness, δ^*, and the momentum thickness, θ. The presence of the wall induces a shear on the fluid shown by τ. The wall shear is often used to define a skin friction velocity using the fluid density, ρ, as shown in Equation 1.1.

$$u_\tau = \sqrt{\frac{\tau}{\rho}} \tag{1.1}$$

The wall shear force can be enhanced by the surface roughness when this roughness is large enough to reach out of the laminar sublayer at the bottom of the turbulent boundary layer flow. When the roughness is smaller than this, the flow around the roughness elements is slow enough that the presence of the roughness has no measurable effect on the flow. Roughness which exhibits this behavior is termed hydrodynamically smooth, because the flow over the surfaces is the same as the flow over a smooth surface.

The turbulent boundary layer also convects unsteady pressure fluctuations along the wall. The unsteady pressure fluctuations are defined on the wall in terms of a wavenumber frequency spectrum $P(k,\omega)$. Here wavenumbers, and directions, are defined on a Cartesian coordinate system with the 1 or x direction along the surface in the direction of the mean flow, the 3 or z direction along the surface normal to the flow, and the 2 or y direction normal to the surface. Beyond the local flow fluctuations there are also propagating pressure fluctuations within the boundary layer that radiated way from the surface as sound waves. Some of these fluctuations are generated by the turbulent flow itself, and some by the flow interaction with the wall surface and roughness. These fluctuations are defined in the far field by the acoustic sound spectrum $\Phi(\omega)$.

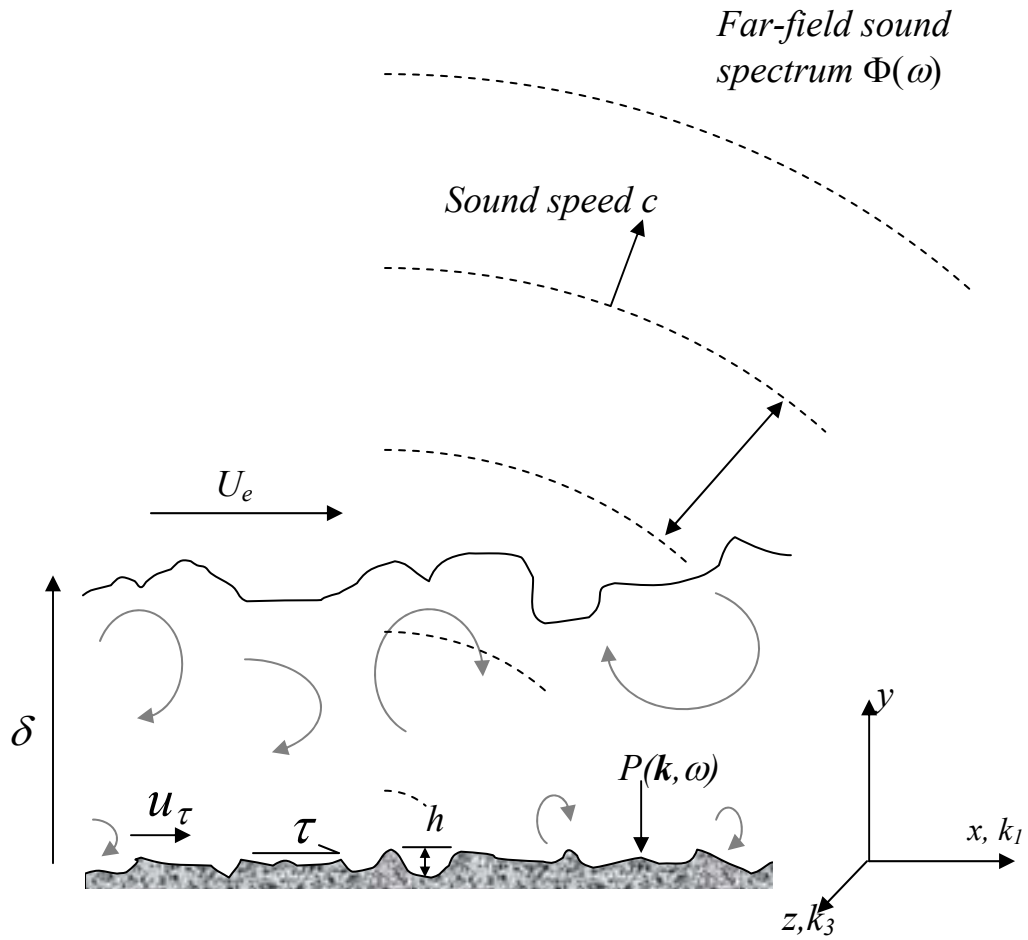

Figure 1-1 Schematic of the rough-wall boundary layer noise problem.

1.3 Review of Previous Work

Since the 1950's, researchers have tried to determine the physical mechanism responsible for roughness noise through experimental and theoretical study. The beginning of aeroacoustics can be traced back to a pair of papers presented by Lighthill in 1952 and 1954. In these papers, Lighthill presents an exact rearrangement of the Navier-Stokes equations into an inhomogeneous wave equation form, shown in Equation 1.2.

$$\frac{\partial^2 \rho}{\partial t^2} - c^2 \nabla^2 \rho = \frac{\partial T_{ij}}{\partial x_i \partial x_j} \qquad (1.2)$$

$$T_{ij} = \rho v_i v_j + p_{ij} - c^2 \rho \delta_{ij}$$

In this equation ρ is the fluid density, c is the speed of sound in the undisturbed medium, p is the fluctuating component of pressure, t is time, v and x are the velocity and directional components of the flow, and T is the Lighthill stress tensor as defined. The subscripts i and j describe the direction associated with v, T, p, and x. This equation

describes the way that a local turbulent region can radiate sound into an otherwise stationary and undisturbed medium. Lighthill (1952) showed that an isolated turbulent region, such as a cold jet, acted like a quadrupole acoustic source due to the fluctuating shear stresses within the turbulence. Dimensional analysis of this result leads to a scaling law for the behavior of the sound spectrum levels shown in Equation 1.3, where *L*, *U*, and *M* are characteristic length, velocity and Mach numbers for the flow.

$$\Phi_Q(\omega) \propto \left(\frac{\rho}{c}\right)^2 \frac{L^3 U^8}{|x|^2 c^2} \tag{1.3}$$

Equation 1.3 shows that the acoustic power spectrum, $\Phi(\omega)$, is proportional to the eighth power of the characteristic flow velocity, and decays with the distance away from the source squared.

In 1955, Curle extended this analysis to include the effects of a solid boundary in the environment. His results found that a solid boundary can produce a more efficient source at low speeds, which behaves like a dipole. A similar process can reveal the typical scaling behavior for a dipole source, which is shown in Equation 1.4. The key distinction between the dipole and quadrupole scaling is the dependence on the velocity power.

$$\Phi_D(\omega) \propto \left(\frac{\rho}{c}\right)^2 \frac{L^3 U^6}{|x|^2} \tag{1.4}$$

The dipole sources predicted by this solution are proportional to the sixth power of the characteristic velocity. This means that as the characteristic Mach number of a flow decreases the strength of quadrupole sources decreases faster than dipole sources. The relative strength of dipole sources to quadrupole sources increases as the square of the change in speed.

Within this theoretical framework early experimental researchers begin to investigate on the acoustics from rough wall boundary layer flows. In 1960, Skudrzyk and Haddle presented results from sound radiated by a spinning cylinder mounted in a water tunnel with smooth and rough surfaces. Far field sound levels were measured using 63.5 mm diameter hydrophones mounted on the tunnel walls. When the radiated sound levels were plotted against velocity it was found that the pressure rise corresponded to the cylinder surface velocity raised to the 6, 10.3, and 12 power for smooth, 80 grit, and 60 grit roughened surfaces respectively. Only the smooth wall case corresponds with the two source mechanisms identified in the theoretical setting. In 1969, Chanaud presented results for the sound radiated from a spinning disk mounted inside an anechoic chamber with various surface and edge treatments. Similar to the Skudrzyk and Haddle tests a moving surface is used to reduce flow noise other than boundary layer noise. Chanaud found that disks with a ring of roughness on the upper surface and a disk with a rough edge produced more noise above 3 kHz. Chanaud found that for the smooth disk the total sound level measured perpendicular to the plane of the disk increased with the velocity to the 5.3 power while the ring roughened disk scaled with the 6^{th} power of velocity. Based on the 6^{th} power scaling and the measured directivity of the smooth and rough disks, Chanaud suggests the acoustic source is a dipole aligned perpendicular to the surface, although he presented no physical mechanism for the process. Further analysis of his directivity patterns, shown in Section 1.3.1.1, show that a surface aligned dipole matches the data just as well.

Cole (1980) conducted one of the first studies of turbulent boundary layer noise using a fully developed turbulent boundary layer growing on a wall. In this experiment he used microphone measurements of noise in the far field. By using a microphone mounted in a parabolic reflector outside the flow in the Anechoic Flow Facility (AFF) at the David Taylor Research Center (DTRC), he was able to measure sound from localized sources. He used short strips (15 cm long) of 40 and 80 grit sand paper to determine the directivity of the acoustic source. He also used large blankets of 40 and 80 grit sand paper to obtain fully developed flow while measuring the sound from a localized portion of the blanket using the directional microphone. At points where acoustic measurements were taken, aerodynamic measurements were also made. Boundary layer thicknesses varied from 4 to 11 mm depending on the surface and flow speed, which ranged from 24 to 47 m/s. His measurements of the sound spectrum made over the roughness blankets (perpendicular to the plate surface) did show a 2-3 dB increase compared with the smooth wall for both roughness levels at all speeds. Cole presents his data scaled on dipole and quadrupole scaling laws derived from Lighthill's (1952) non-dimensional analysis. Both of these models, based on the characteristic flow dimensions U_e and δ^*, showed a good collapse of the experimental data.

Hersh (1983) presents results for sound radiated from the smooth and rough pipes which exit into anechoic chambers. The results are presented from two studies, the first using a 38.1 mm pipe flow with a thin turbulent boundary layer growing on the walls surrounding a potential core. The jet noise of the pipe exhaust is shown to scale well with the 8^{th} power of the exit velocity, which is varied from 51.8 to 122 m/s, consistent with cold jet flows predicted by Lighthill. (1952) When the interior of the pipe was roughened with 40 grit sandpaper the resulting sound measurements scaled with the 6^{th} power of the exit velocity, suggesting a dipole source. Hersh (1983) suggests that the dipole is the result of the fluctuating shear stress at the wall due to the presence of the roughness elements. Results are also presented for pipes roughened with 120, 150, and 180 grit sandpaper, which show ⅓ octave band sound levels increase 3-5 dB above the smooth pipe levels at frequencies above 20 kHz. The 40 grit roughness shows increases of greater than 10 dB over the range of 10 to 40 kHz measured in the test. Test results are also presented to demonstrate that pipe vibration and lip noise were not responsible for the sound levels measured.

Results from a second study are also presented by Hersh (1983) in which he studied the sound from a larger, 127 mm diameter, pipe exhausting a fully developed turbulent flow. Mean velocity profiles were taken to determine the effective sand grain roughness size, and the pressure drop along the pipe was measured to determine the wall shear stress. Measurements were made at a single velocity, 26.2 m/s, over several transitionally and fully rough surfaces. Results showed that the fully rough surfaces produced on the order of 15 dB more noise then the clean pipe exhaust in the frequency range from 3 to 40 kHz. The transitional cases showed slightly higher sound levels at frequencies above 10 kHz. Hersh (1983) presents his results scaled using a dipole scaling law, but uses skin friction velocity, u_τ, and equivalent sand grain roughness height, h_s, instead of the edge velocity and boundary layer thickness as used in earlier studies. He finds this scaling, shown in Equation 1.5, gives a fair collapse of his data except for one case of mesh type roughness.

$$\frac{\Phi(\omega)}{(\rho/c)^2 u_\tau^5 h_s} \quad vs \quad \frac{\omega h_s}{u_\tau} \tag{1.5}$$

Howe produced a series of papers on rough wall boundary layer noise from 1984-1991 based on the experimental results presented by Hersh and earlier theoretical work he had done on turbulent boundary layer noise. Hersh (1983) suggested that the acoustic source responsible for the rough wall turbulent boundary layer noise was a dipole driven by the fluctuating drag force on the roughness elements. Howe (1984) recognized that this process could be modeled with equal validity as scattering of the surface pressure field by the roughness elements. However, the model of surface pressure must account for all flow features that act on the roughness elements, including any flow around the elements and wakes formed on the elements themselves. Howe's 1984 paper modeled the wall surface as a series of regularly spaced hemispherical bosses. In order to solve the scattering problem Howe had to add one additional restriction to the relation between the wall surface and the wall pressure spectrum model. Howe (1984) assumes the elements do not penetrate into the flow sufficiently to alter the wall pressure spectrum, especially around the convective ridge. He suggests that this restriction is likely only valid for boundary layer flows were the roughness elements do not penetrate beyond the buffer zone (transitionally rough surfaces). Howe (1984) acknowledges that there is insufficient information to determine the wall pressure spectrum at the bottom of a turbulent rough wall boundary layer. He uses models from Chase (1987) and Corcos (1963) to approximate the wall pressure spectrum and then uses a Green's function solution to model the far field pressure spectrum. Howe compares the predicted shape of the far field sound spectrum with that measured by Hersh (1983) earlier. He cannot compare the absolute levels directly because of the refractive properties of the pipe exit and jet flow that influences the directivity of the radiated sound from the boundary layer. The comparison shows good agreement with Hersh's data from three different rough surfaces both in the transitional and fully rough range. The functional form of the spectrum determined by Howe is also the same as that proposed by Hersh with the exception of changing h_s, equivalent sand grain roughness height, to h, geometric roughness height, as shown in Equation 1.6.

$$\frac{\Phi(\omega)}{(\rho/c)^2 u_\tau^5 h} \quad vs \quad \frac{\omega h}{u_\tau} \tag{1.6}$$

In Howe's 1986 paper he addresses the influence of viscous surface shear as it affects the diffraction mechanism. This does not address how the viscous process affects the wall pressure spectrum by the creation of vortex shedding and wakes from roughness elements. It addresses how the viscous process affects the ability of the surface to scatter a given pressure field. The scattered field is derived in terms of a first order perturbation model of the surface. This approach allows him to incorporate viscosity directly into the scattered potential field and determine its affect on the magnitude of the scattered field. The perturbation approach also results in a form of the scattered field that depends on both the wall pressure wavenumber frequency spectrum and also the wall roughness wavenumber spectrum. To illustrate the influence of viscosity, Howe models the wall roughness spectrum as a delta function, which he suggests is a reasonable model for sparsely roughened surface. His results show that over the range of frequencies of

interest to roughness noise predictions, the viscous model only predicts increases of 2 to 3 dB. Howe suggests that this illustrates that the use of an invisid diffraction model is still valid in the viscous sublayer of a turbulent boundary layer.

Based on the confirmation from his 1986 paper that the invisid scattering model could accurately predict roughness noise scattering even for viscous flows, Howe extended his 1984 paper approach to formally include fully rough surfaces and the influence of interstitial flows and wakes in 1988 and 1991. His overall approach is largely the same as in 1984; however, he separated the wall pressure field into two parts. The first part is taken from the experimentally derived model of Chase (1987) for the wall pressure spectrum over a rough surface. The second is an additional term that accounts for the small-scale flow around the roughness elements that is not accounted for in the Chase model. This term is typically much smaller than the scattering of the main flow pressure spectrum, often around 20 dB, except for surfaces with large densely packed roughness elements. Howe uses the data from Hersh again for comparison of shape and to set the two free constants in his model for the interstitial flows. This correction allows Howe's model to match the data from Hersh (1983) throughout the frequency range within 6dB.

Howe's (1988) use of the scattering model for roughness noise made the accurate modeling of wall pressure spectrum a major factor in the prediction of rough wall boundary layer noise. Graham (1997) presented a review of many of smooth wall pressure spectrum models and assessed their validity in predicting turbulent boundary layer noise in aircraft cabins. Much of the discussion on surface pressure follows this review. The earliest model comes from Corcos (1963), who presented an analysis of a series of his own on others measurements of wall pressure measurements made under a turbulent boundary layer flow. This model is based on a series of spatial correlation measurements made under a boundary layer flow and depends on the flow convection speed and two tunable parameters, α_y, and α_z. The model has the form given in Equation 1.7 with the values of α_y and α_z suggested as 0.77 and 0.1 or 0.7 and 0.32 for smooth and rough plates respectively.

$$\Phi_w(k,\omega) = \frac{4\alpha_y\alpha_z}{\left[\alpha_y^2 + U_c^2 k_y^2/\omega^2\right]\left[\alpha_z^2 + \left(U_c k_z/\omega - 1\right)^2\right]} \tag{1.7}$$

Experimental data has shown that this spectral shape tends to over-predict the spectral levels below the convective ridge. In 1982, Efimtsov presented a modified version of the Corcos (1963) model that accounts for the influence of boundary layer thickness δ on the correlation lengths. This model replaces the tuning constants α_y and α_z with empirically derived length scales Λ_y and Λ_z. A large amount of flight data was used to determine the empirical form for the models of these length scales, which are given for low Mach numbers and supersonic flows. At high frequencies this model reduces to that of Corcos (1963) using the smooth wall constants. Since this model is for the same spectral form of the Corcos model it also tends to over-predict the spectral levels below the convective peak.

In 1980 and 1987, Chase presented a series of papers that proposed a different model for the wall pressure spectrum. According to Graham (1997), this model begins by assuming the boundary layer velocity spectra are of the general form presented by Corcos (1963) and then uses Lighthill's acoustic analogy to develop the functional form of the wall pressure spectrum. Chase also incorporates a number a theoretical limits

derived for turbulent flows to restrict the asymptotic limits of the wall pressure spectrum at high frequency and wavenumbers. These asymptotic limits resulted in some problems with the model presented in 1980. The model did not properly account for the low wavenumber behavior of the wall pressure spectrum, either in the subconvective region or in the supersonic region. Chase reevaluated some of these assumptions and presented a new model in 1987. The new model incorporated behavior in the acoustic region, which improved results in the subconvective region, but resulted in a non-analytic result in the supersonic region.

In 1991, Smol'yakov and Tkachenko presented a new model using a different spectral form from Corcos (1963). Instead of basing the spectral behavior on the correlation lengths, they used the square of the correlation distances to determine the decay behavior. This improved the prediction of the low wavenumber region compared with the Corcos model, but still over-predicted the spectral levels, so a correcting function was added to reduce the low wavenumber levels while maintaining the level of the convective peak. The total form of the spectrum including the correction function results in a good match with experimental data throughout the convective wavenumber range.

Farabee and Geib (1991) presented the results of an experimental study that examines the sound radiated from a turbulent boundary layer flow in a wind tunnel passing over large patches of roughness. The study used a series of microphones mounted flush in the wall downstream of the roughness patches to measure the wall pressure spectrum at the bottom of the boundary layer, where the source terms should be most easily detectable. By using the microphone set as a wavenumber filter, estimates of the farfield acoustics could be made by looking only at the propagating wave speeds. Measurements were made just downstream of a roughness patch roughly 2 m long and 1 m wide using an array of 6 1-inch diameter condenser microphones. Three levels of roughness (40 grit sandpaper, 5.08 mm gravel, and 6.35 mm simulated barnacles) and one smooth surface were used with flow speeds varied from 12 to 48.5 m/s. The wavenumber filter was able to detect pressure fluctuation increases near the acoustic wavenumber despite the levels being on the order of 60 dB less than the pressure spectrum levels in the convective ridge. By varying the flow speed and measuring at a constant wavenumber, Farabee and Geib were able to measure the change in the acoustic pressure fluctuations at different non-dimensional frequencies. Farabee and Geib's results indicate a dipole scaling accurately scales the measured acoustic pressure levels when using outer flow variables (δ^* for length scaling and U_e for a velocity scale) to scale the frequency, and a mixed variable set, u_τ, δ^*, and U_e, to scale the pressure spectrum. This results in a far field dipole scaling given by Equation 1.8.

$$\frac{\Phi(\omega)}{(\rho/c)^2 u_\tau^4 \delta^* U_e} = f_f\left(\frac{\omega\delta^*}{U_e}\right) \tag{1.8}$$

Arguillat *et al.* (2005) presented experimental measurements of the wavenumber pressure spectrum for a turbulent boundary layer flow on the wall of a small wind tunnel in 2005. An array of pinholes were made on a plate in the wall of the wind tunnel which were then connected to remotely located ¼" acoustic microphones. This approach allowed very tight spacing of the pinholes for better resolution of the low wavenumber spectrum levels. The array consisted of 17 microphones, which could be rotated around a

central point to determine both the streamwise and spanwise wavenumber behavior of the pressure spectrum. The results show a well-defined convective ridge as well as a relatively large rise (5% of the convective ridge value) in the acoustic cone. The large pressure fluctuations could be the result of acoustic contamination within the wind tunnel. The wind tunnel was not treated and peaks in the pressure spectrum of the acoustic region matched the expected resonance frequencies of the square tunnel cross section.

In 2001, Smol'yakov presented another prediction method for the sound generated by turbulent boundary layer flow over a rough surface. Smol'yakov argues for fully rough surfaces with roughness elements extending beyond the buffer layer, that each roughness element will act like a small bluff body and radiate dipole noise as a result of vortex shedding. By combining the velocity probability function in the boundary layer with the probability function of roughness height, Smol'yakov determines the shape of the radiated sound spectrum. He notes that there is little data on the probability functions of various rough surfaces but uses a χ^2 distribution which he suggests would be a reasonable model since it only allows positive roughness heights and severely restricts the odds of encountering very large elements. This method depends on two constants; the first constant determines the location of the spectral peak on the frequency axis and the second constant determines the absolute magnitude of the spectral peak. Smol'yakov determines these values by fitting his results with data he presented earlier in his study of the wall pressure spectrum discussed earlier.

Liu, Dowling, and Shin (2006) presented experimental results attempting to verify the scattering model presented by Howe (1988). Results were shown for flow over a flat plate that had been a 0.64 by 0.64 m roughened by large (3 and 4 mm radius) regularly spaced hemispherical bosses. A turbulent boundary layer was then allowed to grow over this surface in an open jet wind tunnel and far field sound measurements were made using a set of condenser microphones (which acted as a single microphone) and a microphone phased array. Their results match well with Howe's predictions from 1-2 kHz where the sound level is predicted to peak, but the experimental data falls off much faster then Howe's predictions. Measurements made with the phased array are hard to interpret as the nature of a dipole source signal in a phased array image is poorly defined and easily contaminated in an open tunnel. Liu (2006) also determined a new method for evaluating the scattering model proposed by Howe. Howe uses an approximate solution to the integral of the wall pressure spectrum with the Green's function, Liu presents a way to evaluate this integral numerically which allows various models for the wall pressure spectrum to be easily compared. Six different wall pressure models were compared, along with the approximate solution originally given by Howe (1988). The numerical approach showed a slightly sharper peak shape compared with the approximate solution of Howe, it also showed that the wall pressure model made very little change in the predicted peak shape or level (variations were less then 3dB). In 2007, phased array measurements were presented for sound generated by shorter, 0.32 m long, patches of the same surface roughness. These measurements showed the largest increase in sound level occurred in the first ⅓ of the roughened area. The phased array algorithm used to reprocess the measurements assumed a monopole source distribution on the plate surface. To determine the extent to which this was a valid analysis a numerically generated dipole sound field was processed through the same algorithm. This showed the beam formed

plots measured from the roughness patch were consistent with the simulated dipole distribution.

1.3.1 Topics of Further Discussion

1.3.1.1 Dipole Orientation

Since Chanaud's measurements in 1969 confirmed the dipole velocity scaling predicted as early as 1955 by Curle for a surface source, researchers have suspected that rough wall boundary layer noise behaves as a dipole. However, there has been very little data on the orientation of this dipole by direct measurement. This fact can be attributed to the experimental difficulty of conducting a directivity study above a boundary layer. This typically requires microphone placement within the flow which makes separation of boundary layer noise from microphone self noise problematic. The two studies that were not hampered by this constraint were the early studies of Skudrzyk and Haddle (1960) and the study of Chanaud (1969). In these studies, the boundary layer flow was generated by spinning either a cylinder or a disk in an otherwise stationary medium. This allowed the placement of microphones outside the flow during all measurements. Skudrzyk and Haddle (1960) did not attempt directivity measurements, as their setup could not discriminate between flow aligned and wall normal dipoles. Chanaud (1969) did make directivity measurements above the plane of a spinning disk and based on his measurements concluded that sound was generated by a wall normal dipole. The polar plots in Figure 1-2 show directivity measurements at three frequencies for a smooth and ring roughened disk spinning with an edge speed of 263 ft/s. The directivity pattern of a surface normal point dipole is also shown for reference. While this curve provides a reasonable fit for the lowest frequency, results at higher frequencies, where roughness noise is most significant, there are large errors with this pattern.

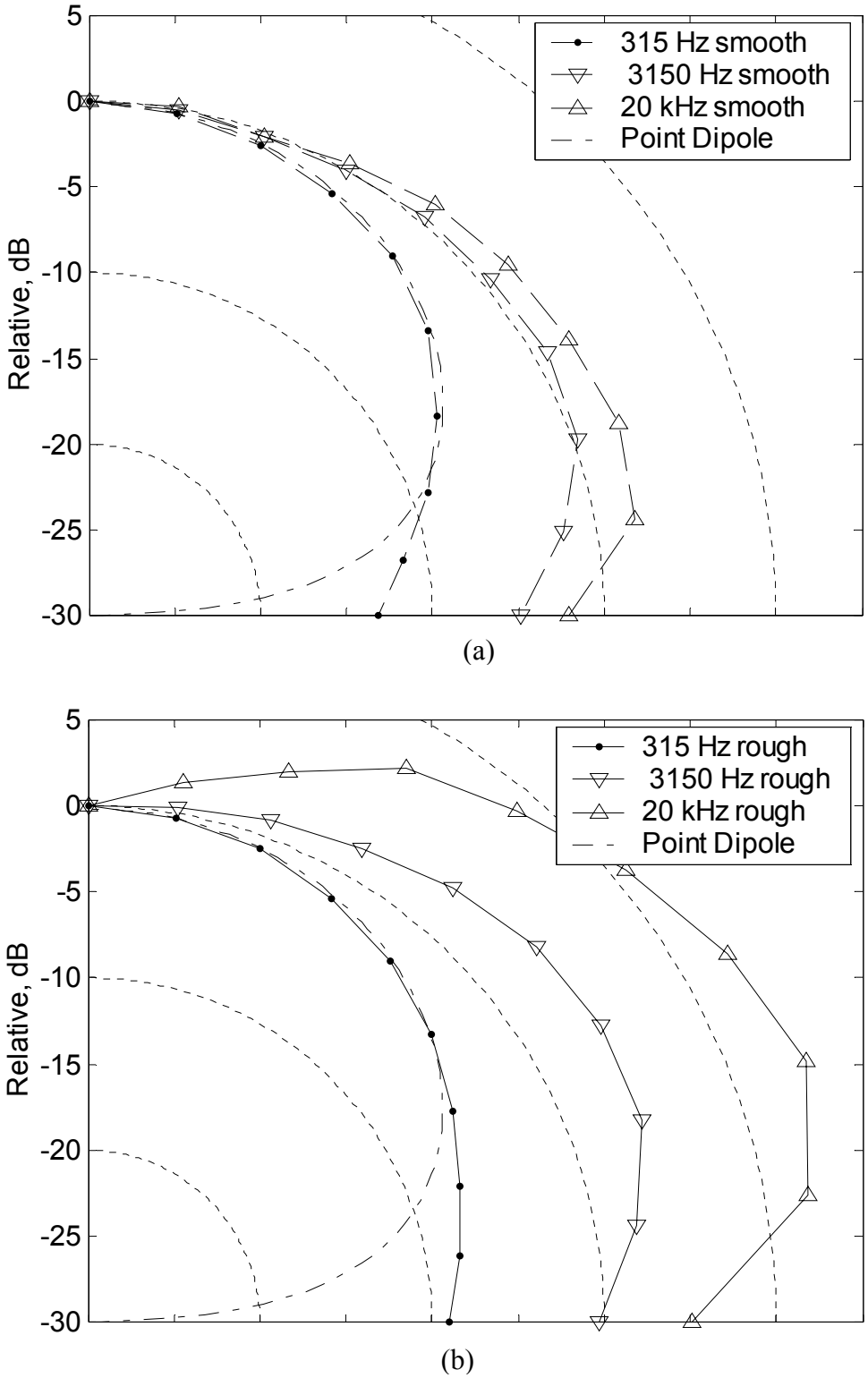

Figure 1-2 Polar plots of source directivity from Chanaud (1969) for (a) a smooth disk and (b) a ring roughened disk. Sound levels were measured 5.65 disk radii away from the disk center with a disk edge speed of 80 m/s.

The scattering model presented by Howe (1991) suggests that the dipole should be aligned with the flow direction. This is the result of the non-penetration condition be imposed on the surface of the roughness elements, which causes the most response in the mean flow directions. In Chanaud's (1969) case, this would result in an acoustic dipole aligned with the plate surface, perpendicular to his result. Further analysis of Chanaud's data reveals that a flow aligned dipole models his data as well as a surface normal dipole would. To see this, first the clean plate noise levels are removed from the roughness noise levels, to leave only noise due to the roughness. This can be done if the source models are assumed to be incoherent, and if the patch of roughness is reasonably small compared to the total surface size. For Chanaud's tests both of these conditions are met. The subtraction allows the influence of any edge noise from the disk, motor noise, and plate vibrations to be removed from the measured results. Edge noise is the most likely of these to vary between the smooth and rough disks since the roughness is likely to increase the boundary layer turbulence which is scattered by the disk edge. Figure 1-3 shows polar plots of the resulting directivity for the roughness noise minus the smooth disk directivity pattern. Again the directivity is plotted at three frequencies for a disk speed of 263 ft/s.

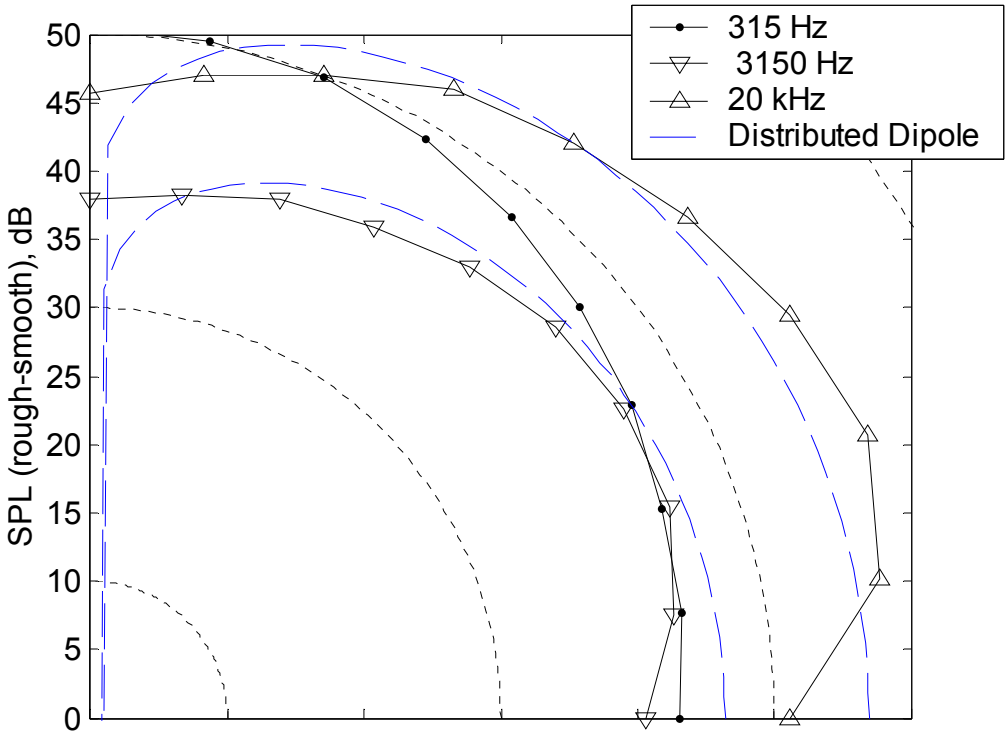

Figure 1-3 Polar plot of sound levels reported by Chanaud (1969) for a ring roughened spinning disk with the smooth disk sound level removed. The directivity patterns by circumferentially aligned dipoles have been added for reference with the two higher frequency measurements.

There are two things to note in Figure 1-3, the first is the difference in the shape of the directivity pattern between the 315 Hz and the two high frequency curves for 3150 Hz and 20 kHz. The low frequency curve has its peak level directly over the disk and then monotonically decreases as the observer position is moved to lower angles with a minimum 7 dB below its maximum value when measured in the plane of the disk. The

two high frequency curves have their minimum values when measured vertically above the disk and the levels increase as the disk plane is approached, with the exception of the last two points. The fact that the two high frequency curves have a similar shape that is noticeably different from the low frequency curve is significant because Chanaud (1969) reports that the increase in measured noise levels becomes more significant at frequencies above 2000 Hz. This shows that the change in directivity is likely associated with a change in source mechanism caused by the presence of the roughness. The second thing to note in the figure is the level to which the high frequency curves match the blue dashed curves that represent the directivity of a distribution of dipoles acting along the roughness ring on the disk. The axis of the dipole distribution is assumed to be locally circumferential at all locations. This shape models the directivity pattern well from 20° to 60° above the plane for both frequencies. At angles nearly perpendicular to the plane the ideal dipole sound is greatly diminished, while the measured data in only slightly reduced. This is often seen in experimental results, as the background levels often make it difficult to measure the quiet regions of a dipole. In the plane of the disk the discrepancy could be the result of diffraction of the sound field by the wake on the edge of the disk. This analysis suggests that either a flow aligned or wall normal dipole could generate the directivity seen by Chanaud (1969).

1.3.2 The Source Mechanism, Scattering or Vortex Shedding

Two physical processes are suggested in published literature which could be responsible for a dipole type noise source due to roughness. The first of these sources is acoustic scattering of the wall pressure spectrum. This is the mechanism proposed by Curle, (1955) Howe, (1984) and Glegg (2007). In this process, the surface roughness can be thought of as a diffracting surface that converts energy from the evanescent portions of the wall pressure spectrum, those portions associated with the hydrodynamic flow, to the propagating portion of the pressure spectrum, acoustic waves. The second mechanism, which was presented by Smol'yakov (2001), is sound from vortex shedding. In this mechanism the sound is thought to be generated by vortices shed by a region of separated flow on the downstream side of the roughness elements. These processes are often difficult to distinguish. This section will present a frame work for consideration of both processes, and discuss possible physical differences that could be used to identify the sources.

As mentioned, roughness noise due to scattering results because the roughness acts as a diffracting surface for the wall pressure spectrum. This implies a direct dependence of the far field sound on the wall pressure spectrum that is not seen in the vortex shedding mechanism. For scattering to occur there must be an unsteady pressure field imposed on the diffracting surface. To determine the relation of the far field sound to the wall pressure spectrum the spatial correlation of the surface roughness must be known. The surface correlation determines which portions of the wall pressure spectrum are diffracted or scattered into the acoustic domain. This type of analysis often leads to an artificial separation of the imposed pressure spectrum and the scattering surface. Lui *et al*. (2006) for example, modified Howe's scattering model (1991) to allow different models of the wall pressure spectrum to be used as the imposed flow. Many of the models presented in Section 1.3.3 were analyzed to determine the affect of changing the wall pressure spectrum. However, as presented in Section 1.3.3 few of these models

account for the presence of surface roughness, or do so only indirectly. In a turbulent boundary layer flow, the separation of the imposed pressure field and diffracting surface cannot strictly be made. As Blake (1986) has shown, surface roughness decreases the correlation lengths of the wall pressure spectrum as compared to those measured over smooth wall boundary layers. In general, a scattering model must therefore know the wall pressure spectrum in the presence of the roughness to predict the far field acoustic levels. However, because the roughness is the scattering surface its spatial correlation must also be known. Often the roughness is modeled only by a roughness height, or grain size. This is often sufficient in aerodynamic analysis to account for roughness effects on the flow properties, but this is insufficient to define its diffracting properties. So a scattering model must account for the affect of the roughness on the wall pressure spectrum and model the roughness distribution sufficiently to determine its diffraction properties.

The vortex shedding model proposed by Smol'yakov (2001) suggests the roughness elements act like bluff bodies in a flow. On the down stream side the flow experiences separation which results in the periodic shedding of vortex structures. This Strouhol type vortex shedding induces an unsteady pressure distribution around the roughness element, which radiates as a dipole source. This mechanism is responsible for the tonal noise generated by flow past bluff bodies and airfoils with blunt trailing edges. Smol'yakov (2001) argues that roughness noise is not tonal because grit roughness consists of elements of different sizes which are exposed to a number of different flow speeds due to the velocity fluctuations in a turbulent boundary layer. The frequency content of the far field sound will be the combined distributions of the roughness sizes and velocity fluctuations they experience. In this framework the distribution of the roughness heights are needed but information about the special distribution of the roughness is less important, as it does not directly affect the shedding frequencies of the elements. Instead of modeling the wall pressure distribution as with the scattering model, the velocity distribution near the wall needs to be modeled to determine the frequencies associated with vortex shedding.

In addition to the differences required in modeling the surface distribution and aerodynamics for each of these mechanisms, there is a more fundamental difference between the two models. The first distinction between them is related to the pressure field. Vortex shedding noise does not require a fluctuating pressure be imposed on the roughness, but is dependent on pressure fluctuations that result from the flow separation on the roughness elements. The scattering model differs from the vortex shedding model because an externally applied pressure field must be present for the surface to scatter sound.

To illustrate this difference, consider a turbulent boundary layer flow over a rough surface which is hydrodynamically smooth. A hydrodynamically smooth surface is one in which the roughness elements are small enough to be contained fully within the laminar sub-layer of the flow. In this region the flow velocities are low enough that flow separation does not occur on the roughness elements and the flow behavior is indistinguishable from the flow over a smooth surface. In this situation the surface roughness could still act like a diffracting surface and scatter portions of the wall pressure spectrum, but there would be no vortex shedding mechanism because the flow around the roughness elements remains attached.

If the roughness element size were increased, so that the surface became transitionally or fully rough, the distinction between the two mechanisms becomes blurred. In fully rough flows the roughness elements reach above the sub-layer and interact with the flow, changing the wall pressure spectrum and generating wakes and regions of separation. In this case, the wall pressure spectrum which is imposed on the surface is the result of the large scale turbulent flow and the wakes of upstream roughness elements, making the separation of scattering and vortex shedding noise difficult.

One final example to consider is a laminar boundary layer flow past a surface which has been sparsely covered with roughness elements which penetrate above the flow sub-layer, but are contained fully within the boundary layer. Under these conditions the roughness elements will form wakes and generate noise due to vortex shedding. If the distance between roughness elements is sufficiently large the flow will return to a steady state before reaching the next element. In this situation only the vortex shedding mechanism could be responsible for roughness noise.

Typical engineering flows occur in the region where both mechanisms could be present. Currently, experimental methods have not been developed to determine the relative strength of these two mechanisms in fully or transitionally rough flow. Glegg (2007) presents an analytical model of both mechanisms and suggests that vortex shedding noise is typically 40 dB below noise generated by scattering in engineering type flows. However, the strength of the vortex shedding source was based on measurements of vortex noise from large bluff bodies, so its applicability to model bodies contained fully within a boundary layer is uncertain.

1.3.3 Modeling of Wall Pressure Spectrum

To use the scattering model as derived by Howe (1991), an accurate model of the wall pressure spectrum is required. As discussed earlier there have been several models of the wall pressure spectrum proposed since the 1950's, in this section the analytic form of these models will be presented and the resulting spectrums will be compared. Figure 1-4 illustrates qualitative behavior of the wall pressure spectrum. The wall pressure spectrum is traditionally divided into three regions. The convective ridge is the highly energetic region that results from the convection of turbulent eddies downstream by the mean flow. The convection speed, U_c, in a turbulent boundary layer is generally 60% of the freestream speed. This is shown in Figure 1-4 (a) by the region around the line, which represents an eddy moving at U_c, in (b) it is shown by the oval centered on the k_1 axis. The convective ridge only appears on the positive k_1 axis because this represents eddies moving downstream. The limited extent in the k_3 direction shown in (b) occurs because there a few eddies which move across the flow in a typical boundary layer. The other region shown in Figure 1-4 is the supersonic region, which represents pressure fluctuations moving at or above the speed of sound. The supersonic region is shown by the steep triangle in (a) and the circular region around the origin in (b). The spectrum levels in this region are typically 1000 times smaller than in the convective ridge, and peak sharply at the sonic wavenumber. This region tends to be poorly modeled by analytic models because the convective ridge dominates the total energy levels. The region in-between the convective ridge and sonic cone is called the subconvective region.

This region has very little energy with spectral levels 4 to 6 orders of magnitude below the convective ridge levels.

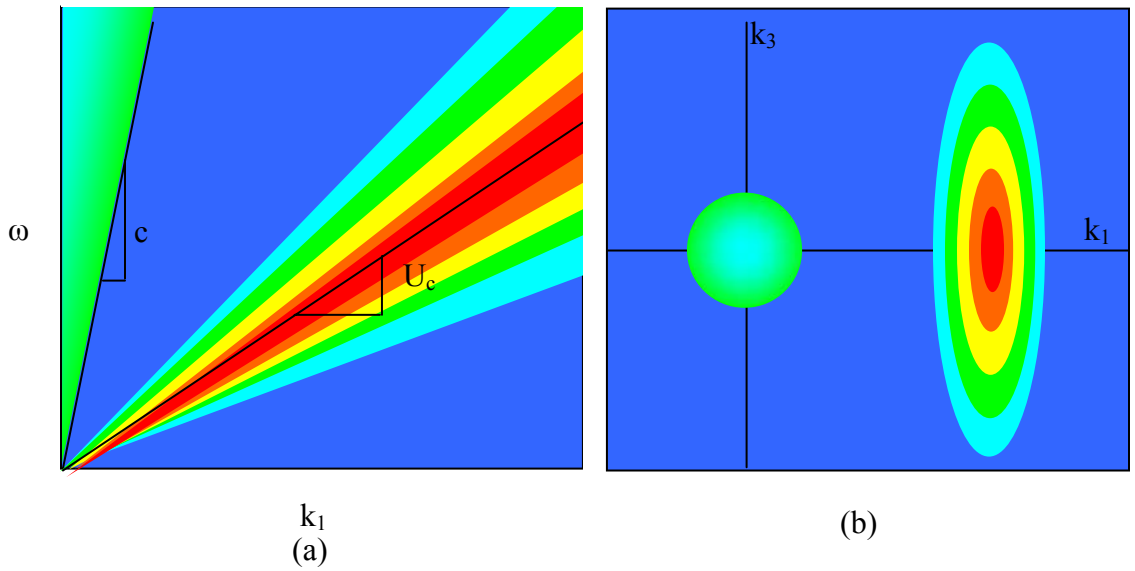

Figure 1-4 The three graphs show qualitatively the behavior of the wall pressure wave number spectrum. Contour levels in (a) show the convective ridge and super sonic region. (b) Shows contour levels in the wave number plane at a typical frequency. The levels in both figures are representative, and not to scale.

Corcos (1963) presented the earliest model of the complete spectrum; this model is based on various measurements made beneath a turbulent boundary layer. Only the convective region is modeled by Corcos. The model is presented below in Equation 1.9, with the values of α_y and α_z suggested as 0.77 and 0.1 or 0.7 and 0.32 for smooth and rough plates respectively.

$$\Phi_w(k,\omega) = \frac{4\alpha_y\alpha_z}{\left[\alpha_y^2 + U_c^2 k_y^2/\omega^2\right]\left[\alpha_z^2 + \left(U_c k_z/\omega - 1\right)^2\right]} \tag{1.9}$$

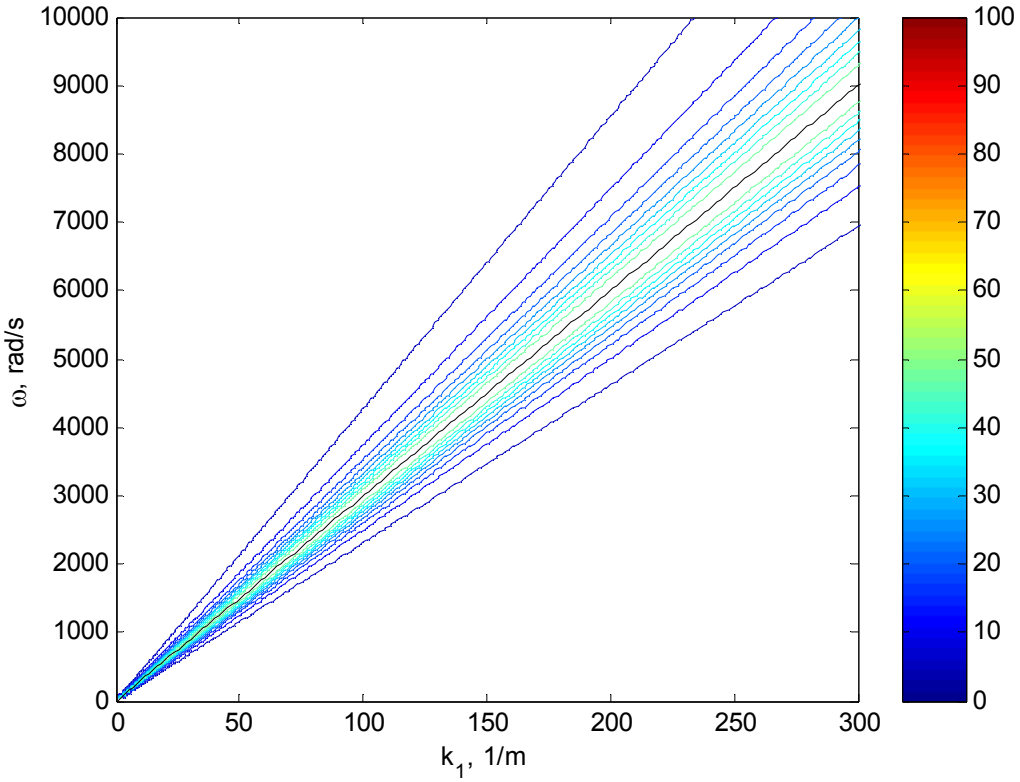

Figure 1-5 Wavenumber frequency spectrum predicted by Corcos (1963) model for a typical boundary layer flow, U_c = 30 m/s.

Figure 1-5 shows the spectral levels predicted by the Corcos (1963) model for a smooth plate. The convective ridge is clearly defined around the convective speed, as shown in Figure 1-4 (a). The Corcos model tends to over-predict the low wavenumber region of the convective ridge, where very large eddies would be responsible for the transport of energy.

Efimtsov (1982) attempted to address the low wavenumber problem of the Corcos (1963) model by incorporating the boundary layer thickness into the spatial correlation length scaling. To do this he derives a new set of correlation lengths Λ_y and Λ_z based on a large experimental data set. He defines the length scales according to Equation 1.10.

$$\frac{\Lambda_z}{\delta} = \left[\left(\frac{a_1 Sh}{U_c/u_\tau} \right)^2 + \frac{a_2^2}{Sh^2 + (a_2/a_3)^2} \right]^{-1/2}$$

$$\frac{\Lambda_y}{\delta} = \left[\left(\frac{a_4 Sh}{U_c/u_\tau} \right)^2 + \frac{a_5^2}{Sh^2 + (a_5/a_6)^2} \right]^{-1/2} \qquad M < 0.75 \qquad (1.10)$$

$$\frac{\Lambda_y}{\delta} = \left[\left(\frac{a_4 Sh}{U_c/u_\tau} \right)^2 + a_7^2 \right]^{-1/2} \qquad M > 0.9$$

The values of Λ defined in Equation 1.10 are then used to define new values for α in Equation 1.9. These values are defined for y and z according to $\alpha = |\omega|/U_c\Lambda$. The

spectrum predicted by combining Equation 1.9 and Equation 1.10 is shown in Figure 1-6 where a_1 through a_7 are given the values suggested by Efimtsov; 0.1, 72.8, 1.54, 0.77, 548, 13.5, and 5.66 respectively. When compared with Figure 1-5 the reduction in levels at low wavenumbers is apparent. At high wavenumbers this model reduces to that of Corcos (1963).

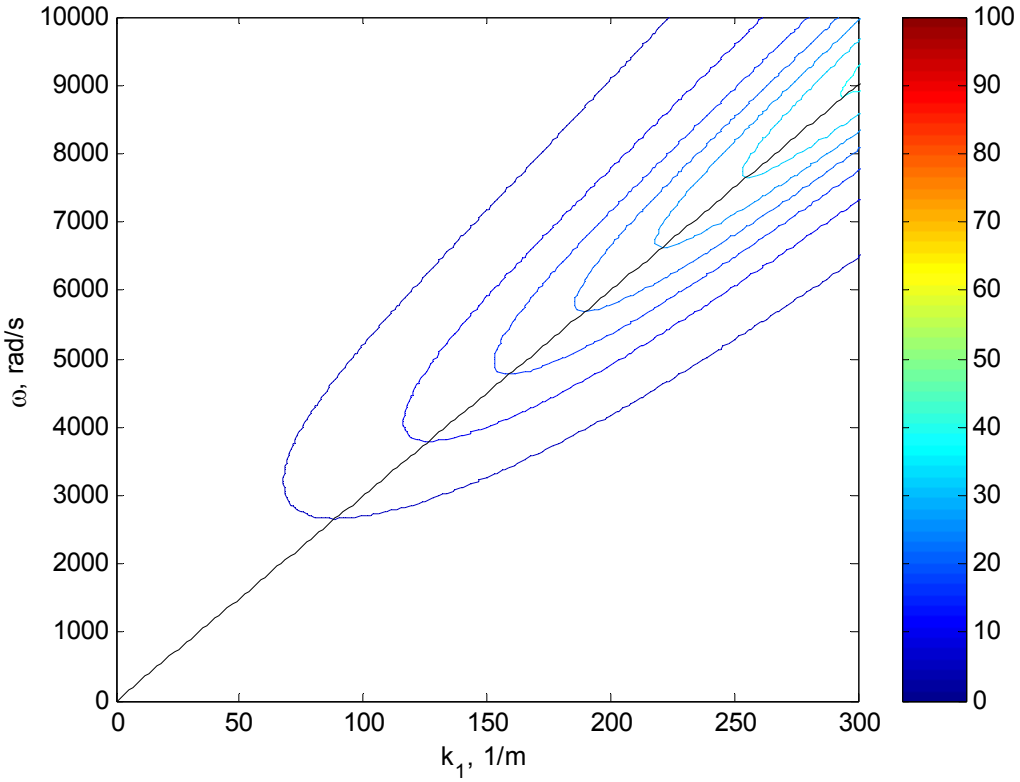

Figure 1-6 Wavenumber frequency spectrum predicted by Efimtsov (1982) model for a typical boundary layer flow, U_c = 30 m/s.

Smol'yakov and Tkachenko (1991) followed a similar approach to Efimtsov (1982) by using the boundary layer thickness to normalize the spatial correlation. However they looked at the combined correlation function of the spatial separation instead of a direct decomposition. They then applied a correction function to the resulting levels to decrease the low wavenumber spectral levels to better-fit experimental data. The resulting spectral form is given by Equation 1.11, and shown in Figure 1-7.

$$\Phi_w(k,\omega) = 0.974 A(\omega) h(\omega) \left[F(k,\omega) - \Delta F(k,\omega) \right]$$

$$A(\omega) = 0.124 \left[1 - \frac{U_c}{4\omega\delta^*} + \left(\frac{U_c}{4\omega\delta^*} \right)^2 \right]^{1/2}$$

$$h(\omega) = \left[1 - \frac{m_1 A}{6.515\sqrt{G}} \right]^{-1}$$

$$m_1 = \frac{1 + A^2}{1.025 + A^2} \quad , \quad G = 1 + A^2 - 1.005 m_1 \tag{1.11}$$

$$F(k,\omega) = \left[A^2 + \left(1 - \frac{k_z U_c}{\omega} \right)^2 + \left(\frac{k_y U_c}{6.45\omega} \right)^2 \right]^{-3/2}$$

$$\Delta F(k,\omega) = 0.995 \left[1 + A^2 + \left\{ \left(m_1 - \frac{k_z U_c}{\omega} \right)^2 + \left(\frac{k_y U_c}{\omega} \right)^2 - m_1^2 \right\} \right]^{-3/2}$$

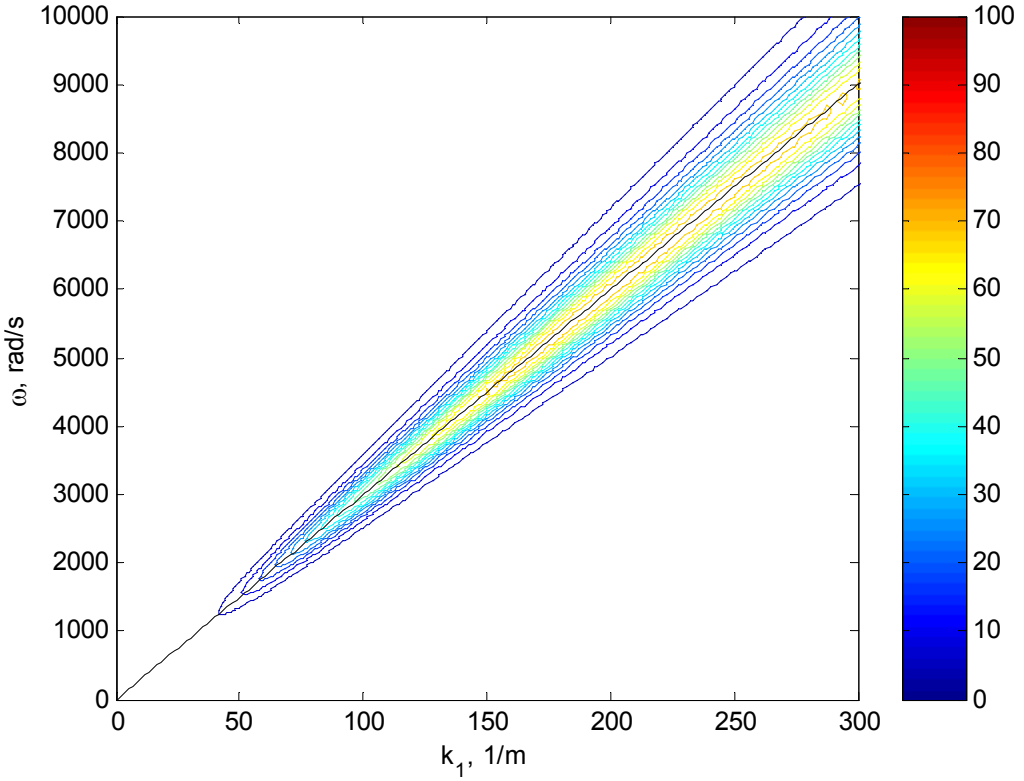

Figure 1-7 Wavenumber frequency spectrum predicted by Smol'yakov and Tkachenko (1991) model for a typical boundary layer flow, U_c = 30 m/s.

Ffowcs Williams (1982) has also proposed a model for the wall pressure spectrum. His model is derived from Lighthill's (1952, 1954) equations using a form similar to Corcos (1963) for the velocity fluctuations at the surface. Hwang and Geib (1984) determined a simplified version of this model that removes the compressibility

effects and results in a form similar to the Corcos (1963) model. The analytic form is shown in Equation 1.12, where the constants have the same values as for Equation 1.9.

$$\Phi_w(k,\omega)=\left(\frac{U_c|k|}{\omega}\right)^2 \frac{4\alpha_y\alpha_z}{\left[\alpha_y^2+U_c^2k_y^2/\omega^2\right]\left[\alpha_z^2+(U_ck_z/\omega-1)^2\right]} \tag{1.12}$$

Chase (1980, 1987) produced two models of similar form to the Ffowcs Williams (1982) models for the wall pressure spectrum. The first model begins with Lighthill's (1952, 1954) equations and using the asymptotic behavior of the wall pressure spectrum he derives a simplified expression for the wall pressure spectrum. The first Chase model does not account for the supersonic region, like the other models, but also does not accurately model the subconvective region, where the spectrum has a nearly uniform magnitude. Chase (1987) reassessed some of his assertions and produced a second model. This model like the Ffowcs Williams (1982) model accounts for the compressible region, but no measurements are available to determine the constants for this region. Equation 1.13 shows the incompressible form of this model.

$$\Phi_w(k,\omega)=\frac{(2\pi)^3\rho^2\omega^2u_\tau^3}{U_c^2\Phi(\omega)\left[K_+^2+(b\delta)^{-2}\right]^{5/2}}\left(C_Mk_z^2+C_T|k|^2\frac{K_+^2+(b\delta)^{-2}}{|k|^2+(b\delta)^{-2}}\right) \tag{1.13}$$

In Equation 1.14, $\Phi_w(\omega)$ is the wall pressure frequency spectrum taken at a single point. The form of this and the remaining functions for Equation 1.13 are given in Equation 1.14.

$$\begin{aligned}\Phi_w(\omega)&=\frac{4\pi^2h\rho^2u_\tau^4}{3\omega(1+\mu^2)}(C_MF_M+C_TF_T)\\ F_M&=\frac{1+\mu^2\alpha^2+\mu^4(\alpha^2-1)}{\left[\alpha^2+\mu^2(\alpha^2-1)\right]^{3/2}}\\ F_T&=\frac{3(1+\mu^2)(1+\alpha^2)}{2\alpha^3}\end{aligned} \tag{1.14}$$

The remaining constants are given values of h=3, hC_M = 0.466, hC_T = 0.014, and b = 0.75. Figure 1-8 shows the spectral shape from this model. This model shows similar shape and levels to the previously presented models, but decays away from the convective peak faster than the Corcos (1963) model. Figure 1-9 shows a slice of the wall pressure spectrum for a single frequency as a function of wavenumber, k_1, for all the models discussed in this section. From Figure 1-9 the difference in the steepness of the convective peak can be seen. The Corcos (1963) and Efimtsov (1982) models have the most broad peaks and highest subconvective spectral levels, while the Chase (1980, 1987) and Smol'yakov and Tkachenko (1991) models are the most sharply peaked. The Ffowcs Williams (1982) model has significant subconvective region decay similar to the Chase models, but has the highest spectral levels at high frequencies.

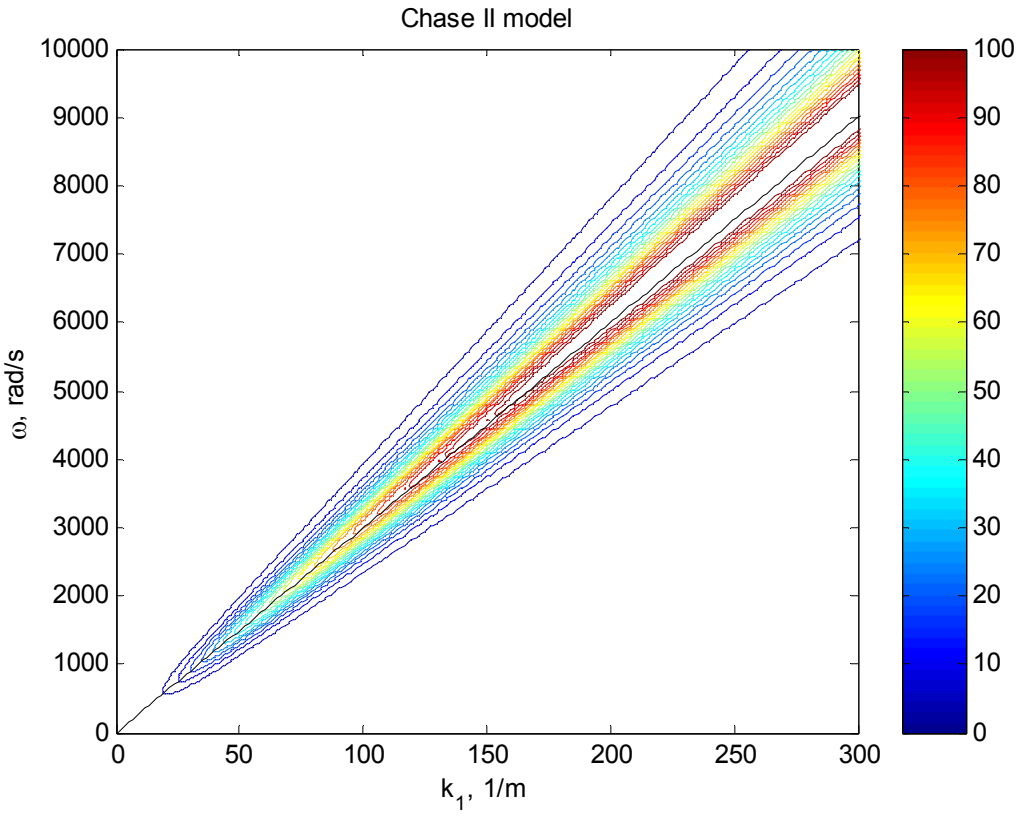

Figure 1-8 Wavenumber frequency spectrum predicted by Chase II (1987) model for a typical boundary layer flow, U_c = 30 m/s.

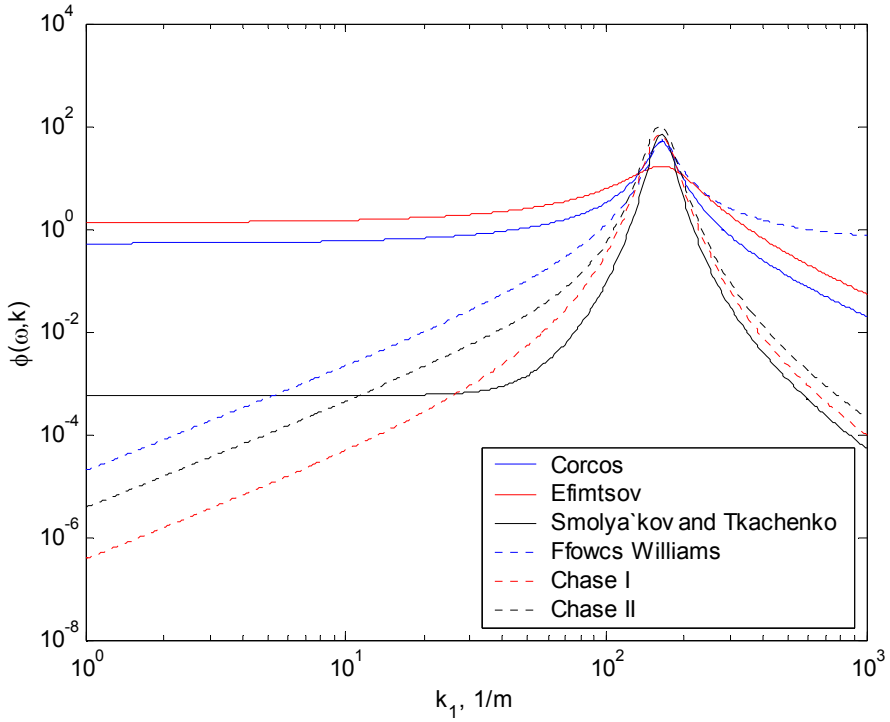

Figure 1-9 Wall pressure spectrum models for a turbulent boundary layer flow with U_c = 30 m/s at 5000 rad/s.

Goody (2004) produced a number of papers investigating the wall pressure spectrum beneath two and three dimensional turbulent boundary layer flows. These focused on the behavior of the wall pressure frequency spectrum measured beneath smooth wall turbulent boundary layers. In 2004, Goody presents a semi-empirical model for the behavior of the frequency pressure spectrum at high Reynolds numbers based on the measurements of seven researchers. Goody (2004) normalized the wall pressure on a pressure scale based on the wall shear, and a time scale based on the boundary layer thickness and edge velocity. Earlier work by Goody showed that these scales collapse the wall pressure frequency spectrum over a large frequency range. The model contained three frequency regions. The low region was characterized by a spectral increase proportional to ω^2, while the high frequency region showed a roll off of ω^{-5}. Both of these limits match theoretical expectations at high Reynolds numbers. The third region is an overlap range were the spectral levels decay as $\omega^{-0.7}$. Goody also accounts for Reynolds number variations using the ratio of relevant flow scales, which he defines as R_T. This ratio is used to set the width of the overlap region. The model shows agreement within ±4dB of the measured spectra when corrected for microphone attenuation at high frequency. This model is shown in Equation 1.15.

$$\frac{\Phi(\omega)U_e}{\tau_w^2\delta} = \frac{3.0\left(\frac{\omega\delta}{U_e}\right)^2}{\left[\left(\frac{\omega\delta}{U_e}\right)^{0.75} + 0.5\right]^{3.7} + \left[1.1R_T^{-0.57}\left(\frac{\omega\delta}{U_e}\right)\right]^7} \qquad (1.15)$$

$$R_T = \left(\frac{u_\tau\delta}{\nu}\right)\sqrt{\frac{C_f}{2}}$$

Another review of wall pressure spectrum was presented by Blake (1986). He presents a number of the models that are already presented in this chapter and reviews measurements used to support these models. He finds that roughness affects the wall pressure spectrum in two ways. The first effect is a reduction in the convection velocity of the boundary layer flow. He finds that for smooth wall flows the convection velocity is typically between $0.7U_e$ and $0.8U_e$, while for rough wall flows the convection velocity is closer to $0.5U_e$. He also finds that the roughness breaks up the eddy structures in the boundary layer and reduces the correlation lengths within the flow. Analysis is also presented on the behavior of the wall pressure frequency spectrum. He suggests a two scale model for the frequency spectrum to account for the high and low frequency scaling. At low frequencies the frequency is scaled on the outer flow variables δ^* and U_e for both smooth and rough walls. At high frequencies the relevant time scale is h/u_τ for rough surfaces and ν/u_τ^2 for smooth surfaces. In all cases the wall shear and time scales are used to normalize the wall pressure spectrum amplitude.

1.4 Parallel Theoretical Work

A theoretical study of roughness noise was conducted concurrently with the experimental work presented in this report. This work, carried out at Florida Atlantic University by Stewart Glegg, aimed to reassess the theoretical framework available for modeling roughness noise. Previous work in this area was primarily limited to the work of Howe (1991) and Smol'yakov (2001) presented in section 1.3. Throughout Chapters 6-9 the models of Howe (1991), Smol'yakov (2001), and Glegg (2007) will be compared with measured spectra. This section outlines the development of this model, and presents an alternative derivation that is used for comparison with the two-dimensional surface roughness presented in Chapter 8.

The Glegg model is based on the acoustic scattering mechanism outlined in Morse and Ingard (1986) for acoustic pressures scattered by a surface irregularities. The scattered field is found using a Green's function solution based on the wall surface pressure and surface distribution, as shown by Equation 1.16.

$$\Phi(\mathbf{x},\omega) = -\int_S \frac{\partial \Phi_w(\mathbf{x}_o,\omega)}{\partial n_o} G(\mathbf{x} \mid \mathbf{x}_o) - \Phi_w(\mathbf{x}_o,\omega)\frac{\partial G(\mathbf{x} \mid \mathbf{x}_o)}{\partial n_o} dS(\mathbf{x}_o) \qquad (1.16)$$

Where Φ is the scattered acoustic pressure frequency spectrum, Φ_w is the wall pressure frequency spectrum, G is the Green's function associated with the surface roughness, and n_0 is the unit vector normal to the surface at x_0. S is the surface area of the roughness, and x, and x_0 are the observer position and surface position respectively. If the surface roughness is assumed to be much smaller than the acoustic wavelengths involved, then the Green's function required for Equation 1.16 can be approximated by the smooth wall Green's function. If the surface is ridge, Equation 1.16 is further simplified because the first term is uniformly zero. Glegg further assumes that the wall pressure spectrum is dominated by the convected hydrodynamic pressure fluctuations associated with the low Mach number turbulent boundary layer. When these approximations are combined Equation 1.16 can be rewritten as Equation 1.17.

$$\Phi(\mathbf{x},\omega) = \int \Phi_w(\mathbf{k}',\omega)\frac{\cos^2\theta}{(2\pi)^2 \mid \mathbf{x} \mid^2}(kh)^2(k''_1 h)^2 Sf(\mathbf{k}'' l_e) d\mathbf{k}'$$

$$f(\mathbf{k}'' l_e) = \frac{1}{Sh^4}\int_{S'}\int_{S''} R_{\xi\xi}(\mathbf{x}',\mathbf{x}'') e^{-i\mathbf{k}''.(\mathbf{x}'-\mathbf{x}'')} dS(\mathbf{x}') dS(\mathbf{x}'') \qquad (1.17)$$

$$\mathbf{k}'' = \mathbf{k}' + \frac{k\mathbf{x}}{|\mathbf{x}|}$$

Where $\Phi(k,\omega)$ is the wavenumber-frequency spectrum of the wall pressure, k is the acoustic wavenumber, $k = \omega/c$, $R_{\zeta\zeta}$ is the surface height correlation function, l_e is the correlation length of the surface, and h is the characteristic roughness height. The angle θ is defined by $cos(\theta) = x_1/|x|$. Glegg uses the Corcos (1963) model for the wavenumber-frequency spectrum of the wall pressure needed in Equation 1.17. The form of this model is given in Equation 1.9. Glegg uses the surface correlation function model presented by Morse and Ingard for a randomly rough surface, shown in Equation 1.18.

$$R_{\xi\xi}(\mathbf{x}',\mathbf{x}'') = h^2 e^{-|\mathbf{x}'-\mathbf{x}''|^2/4l_e^2} \tag{1.18}$$

Where h_{rms} is the root mean square (rms) height of the roughness on S. Equation 1.19 shows the results of combining equations 1.17, 1.18, and the Corcos model for the wall pressure spectrum.

$$\begin{aligned}
\Phi_{pp}(\mathbf{x},\omega) &= \left(\frac{\cos\theta}{\pi\,|\,\mathbf{x}\,|\,c_o}\right)^2 \left(\pi(\rho u_\tau^2)^2 USh\right)\left(\frac{h}{l_e}\right) G(\omega) \\
G(\omega) &= \left\{\frac{\Omega_L \Omega_p^3 \Psi_1(\Omega_L)\Psi_3(\Omega_L)}{\left\{\alpha_p^2 + \Omega_p^2\right\}^{3/2}}\right\} \\
\Psi_1(\omega) &= \left(\frac{\omega l_e}{9U_c}\right)^2 \int \frac{e^{-(\alpha\omega l_e/9U_c)^2}}{\pi\left\{1+(\alpha-9)^2\right\}}\alpha^2 d\alpha \\
\Psi_3(\omega) &= \int \frac{e^{-(\beta\omega l_e/1.4U_c)^2}}{\pi\left\{1+\beta^2\right\}} d\beta
\end{aligned} \tag{1.19}$$

Where α_p is the constant from the Corcos model with a value of 0.12, $\Omega_p = \omega\delta^*/U_e$, $\Omega_L = \omega l_e/U_c$, and the integrals for Ψ_1 and Ψ_3 are carried out from -∞ to ∞. Glegg argues that in a typical flow the terms containing Ω_p in Equation 1.19 nearly cancel and $G(\omega)$ can be written as $G(\Omega_L)$. This reduces Equation 1.19 to a single scale model with a general form given by equation 1.20

$$\frac{\Phi(\omega)}{(\rho/c)^2 u_\tau^4 U_c h^2/l_e} = f\left(\frac{\omega l_e}{U_c}\right) \tag{1.20}$$

The primary difference between this model and the others presented thus far is the incorporation of the roughness length scale. This parameter appears in both the frequency and amplitude scaling of the Glegg model and, to some extent, accounts for differences in the roughness shape and density that is not accounted for in models which only depend on the roughness height.

This model can be derived for any surface shape by changing the surface correlation function and heights accordingly. Results in Chapter 7 of this report are for measurements taken over a rough surface which is periodic and two-dimensional. The surface shape can be approximated, to first order, as a sinusoidal curve with a period equal to the lens spacing and an orientation given by k_r, as shown in Equation 1.21 and Figure 1-10.

$$\begin{aligned}
R_{\xi\xi} &= h^2 \sin\left(\mathbf{k}_\mathbf{r}\left(\mathbf{x}' - \mathbf{x}''\right)\right) \\
\mathbf{k}_\mathbf{r} &= \frac{2\pi}{l_e}\left(\cos(\varphi), 0, \sin(\varphi)\right)
\end{aligned} \tag{1.21}$$

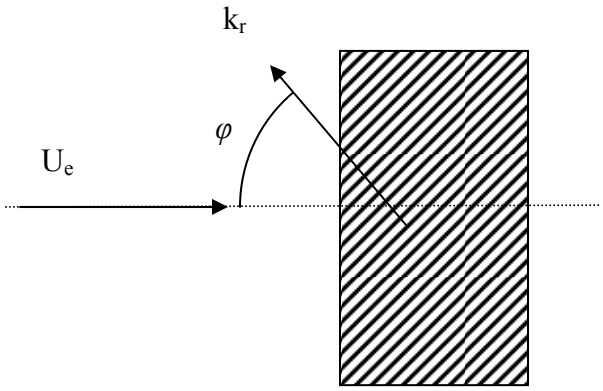

Figure 1-10 Schematic defining the orientation of two-dimensional roughness relative to the mean flow. The figure is looking down on the roughness from above.

Where φ is the angle between a line which runs normal to the surface roughness and the mean flow direction as shown in Figure 1-10. The result of using this model to determine f from Equation 1.17 are shown in Equation 1.22

$$f(k'') = \frac{1}{Sh^4}\iint_{S'S''} h^2 \sin\left(k_r\left(x' - x''\right)\right)e^{-ik}\,dS'dS'' = \frac{S}{h^2}\delta\left(k_r - k''\right) \tag{1.22}$$

Where δ is the Dirac δ-function. Since f is reduced to a δ-function the other integrals in Equation 1.17 are eliminated. The acoustic pressure generated from this surface is shown in Equation 1.23.

$$\Phi(x,\omega) = \frac{\cos^2(\theta)}{4\pi^2|x|^2}(kh)^2\Phi_{pp}\left(\frac{2\pi h}{l_e}\cos(\varphi)\right)\frac{l_1}{\pi\left(1+l_1^2\left(\frac{2\pi}{l_e}\cos(\varphi)-\frac{\omega}{U_c}\right)^2\right)}\frac{l_3}{\pi\left(1+l_3^2\left(\frac{2\pi}{l_e}\sin(\varphi)\right)^2\right)} \tag{1.23}$$

1.4.1 Scaling Parameters

With the exception of Skudrzyk and Haddle (1960) and Cole (1980) all the previous research has suggested that roughness noise behaves according to a dipole scaling law. There has been very little agreement as to what velocity and length scales should be used with this scaling model. When Curle (1955) originally proposed the dipole scaling behavior it was derived for any fluid dynamic process that occurs in the presence of a rigid surface, so the length and velocity scales were considered to be those appropriate for the flow, as shown in Equation 1.24.

$$\Phi_D(\omega) \propto \left(\frac{\rho}{c}\right)^2 L^3U^5 \tag{1.24}$$

Cole (1980) attempted to scale his measurements according to the dipole law in Equation 1.24, using U_e and δ^* as the appropriate velocity and length scales respectively. It should be recalled that Cole's interest was not in understanding the effects of roughness on noise generation, but on the behavior of boundary layer noise in general. The roughness was only used as a method of changing the various boundary layer parameters. From this frame work the edge velocity and boundary layer thickness would seem to be appropriate choices. Cole also uses these parameters to non-dimensionalize the sound spectrum frequency. This results in a functional form shown by Equation 1.25.

$$\frac{\phi(\omega)}{(\rho/c)^2 U_e^5 \delta^{*3}} = f\left(\frac{\omega\delta^*}{U_e}\right) \tag{1.25}$$

Cole (1980) showed that this form produced a reasonable collapse of the sound spectrum, measured at different speeds for the same surface condition. Cole does not report any attempts to scale data from different surfaces using this model. Figure 1-11 shows the results of this scaling for both rough blanket cases.

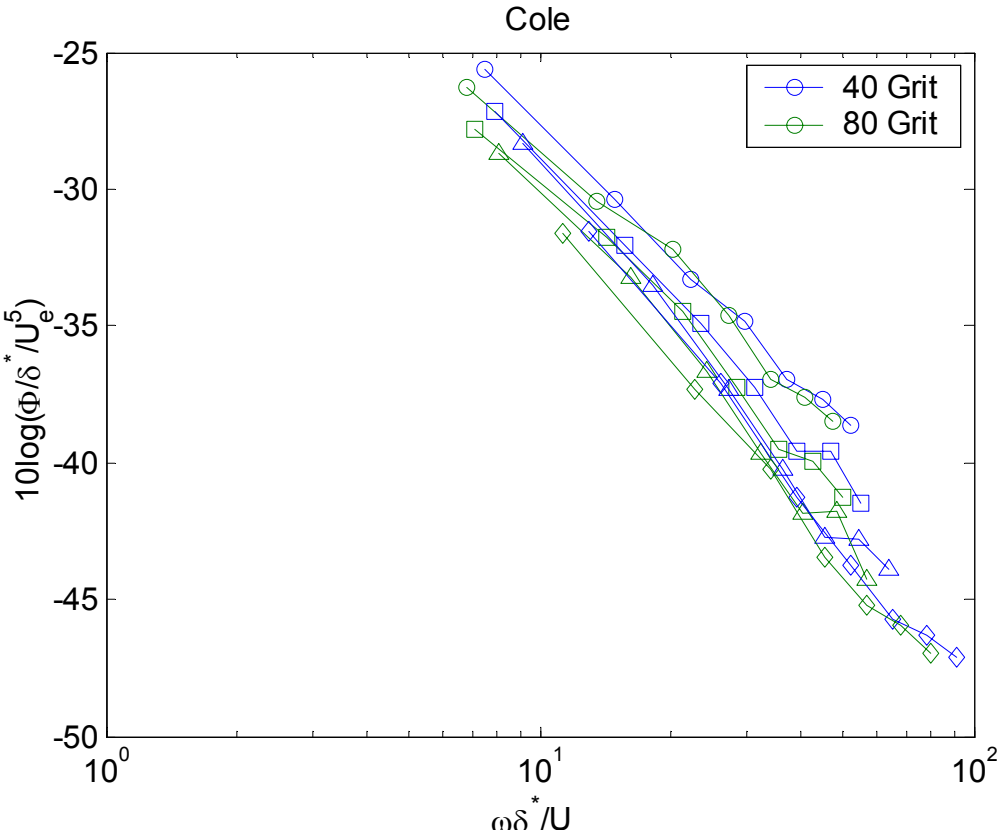

Figure 1-11 Sound pressure spectrum measured by Cole (1980) at four different speeds (24 m/s diamonds, 31.4m/s triangles, 38.3m/s squares, and 46.5m/s circles) over 40 grit (blue) and 80 grit (green) roughened surfaces. Results are scaled on the dipole scaling law proposed by Cole.

Hersh (1983) was the next major experimental researcher to attempt to scale results based on the dipole scaling law. He found that his data collapsed best using two different normalizing scales, u_τ for velocity, and h_s for length. He was able to measured u_τ directly from the pressure drop in his fully developed pipe flow experiments. This leads to a scaling behavior with the same form as Cole's dipole model but based only on inner flow variables for the far field sound level given by Equation 1.26.

$$\frac{\phi(\omega)}{(\rho/c)^2 u_\tau^5 h_s} = f\left(\frac{\omega h_s}{u_\tau}\right) \tag{1.26}$$

Howe's (1988) theoretical model yields a dipole scaling with the normalizing parameters being essentially the ones used by Hersh (1983). This result comes from two sources, first Howe uses Hersh's data to tune his model, so one would expect the

resulting scaling to be similar, and second Howe's model depends on the scaling of turbulent boundary layer wall pressure spectrum. Spectral models for the wall pressure spectrum are typically scaled on the inner flow parameters using a skin friction velocity, not boundary layer thickness. Howe's (1988) scaling is shown in Equation 1.27, note the only difference from Equation 1.18 is the replacement of h_s (sand grain equivalent size) with h_g (actual roughness height).

$$\frac{\Phi(\omega)}{(\rho/c)^2 u_\tau^5 h} = f\left(\frac{\omega h}{u_\tau}\right) \tag{1.27}$$

Farabee and Geib (1991) found another non-dimensional grouping that provided good collapse for their measured wall pressure spectrum. Farabee and Geib used the scaling suggested by Blake (1986) to collapse the low-frequency portion of the convective pressure spectrum, given in Equation 1.28.

$$\frac{\Phi_w(k_0,0,\omega)U_e}{\rho^2 u_\tau^4 \delta^{*3}} = f\left(\frac{\omega\delta^*}{U}\right) \tag{1.28}$$

By multiplying this spectral form by the square of the acoustic wavenumber one would get the expected form of the far field spectrum as reported by other researchers. This format is shown in Equation 1.29.

$$\frac{\Phi(\omega)}{(\rho/c)^2 u_\tau^4 U_e \delta^*} = f\left(\frac{\omega\delta^*}{U_e}\right) \tag{1.29}$$

Equation 1.29 shows that the Farabee and Geib (1991) scaling depends on both inner flow and outer flow variables. This is in contrast to the other scalings presented earlier which used one or the other. The frequency scaling is based only on the outer flow variables, δ^* and U_e, while the spectral level is scaled on both inner and outer variables.

The inconsistency in the scaling laws found by previous researchers is one of the key unresolved issues in roughness noise research. Inner, outer, and mixed scaling models have at times been proposed, but none have been shown to resolve all the measured data. The reasons for this will be discussed in the next section, along with a new approach that will help determine a proper scaling behavior.

1.5 Alternative Derivation methods

This section presents another method to derive the scaling models presented in the pervious section. This section derives these models from Curle's solution (1955) for dipole and quadrupole sources. This analysis presents a mathematically consistent form which can be used to develop scaling models. Several of the models presented in the pervious section are then examined along with the physical significance of these scalings. Several addition models are also presented based on other physical assumptions. First this process is presented for dipole scales, and then quadrupole models are derived.

1.5.1 Dimensional Analysis

Curle's (1955) retarded time solution to the Lighthill (1952) equation provides a concise form to develop scaling laws. This solution is derived in a general manner and can account for both flow noise and the effects of the presence of a surface in the flow. This solution is shown in Equation 1.30 broken into three terms. The first term is the

monopole contribution, the second the dipole contribution, and the last term is the quadrupole contribution to the far field pressure spectrum.

$$\rho'(x,t)c_\infty^2 = \iint_S \left[\frac{\partial(\rho v_j)}{\partial\tau}\right]_{\tau=\tau^*} \frac{n_j dS(y)}{4\pi r} + \frac{1}{c_\infty}\frac{x_i}{r}\iint_S \left[\frac{\partial(p_{ij}+\rho v_i v_j)}{\partial\tau}\right]_{\tau=\tau^*} \frac{n_j dS(y)}{4\pi r} + \frac{1}{c_\infty^2}\frac{x_i x_j}{r^2}\iiint_V \left[\frac{\partial^2 T_{ij}}{\partial\tau^2}\right]_{\tau=\tau^*} \frac{dV(y)}{4\pi r} \tag{1.30}$$

Where ρ' is the far field density fluctuation, which can be related to the pressure field by the speed of sound, c. S is a surface that completely encloses the flow in volume, V. S may be composed of solid, flexible, or open boundaries. The observer position is defined by x and r, while y describes the source position within V, and τ^* is the retarded time for an acoustic wave to travel from y to x. Finally, p, v, and T are the pressure, velocity, and Lighthill (1952) stress tensors respectively. The first term in Curle's (1955) solution cannot contribute to the sound produced in the present study. Both of the remaining terms in Curle's (1955) solution are likely to be involved in sound generated in this study. The dipole term results from the unsteady pressure and velocity field interaction with the surface to generate noise. This term has been rewritten in Equation 1.31 noting the $v_i n_i$ on the surface is 0; the quadrupole term will be left for the next section.

$$\rho'(x,t)c_\infty^2 = p'(x,t) = \frac{1}{c_\infty}\frac{x_i}{4\pi r^2}\iint_S \left[\frac{\partial(p_{ij}n_j)}{\partial\tau}\right]_{\tau=\tau} dS(y) \tag{1.31}$$

Where p' is the far field acoustic pressure. The terms to the left of the integral, control the decay and directivity behavior of the acoustic field. The pressure field, time derivative, and surface area, control the source strength inside the integral. Equation 1.32 represents the solution to this equation in terms of dimensional groups resulting from the integration of Equation1.31.

$$\overline{(p')^2}_{\text{dipole}} \sim \frac{x_i^2 S}{|\mathbf{x}|^4}\frac{\sigma_h^2}{c_\infty^2 T_h^2} A_h \tag{1.32}$$

Where σ_h is the characteristic hydrodynamic stress or pressure that is scattered, T_h is the characteristic time scale of the scattered field, and A_h is the characteristic area of the scattered portion of the hydrodynamic pressure field. The first group of terms is controlled by the observer location and size of the scattering surface. The second grouping defines the relationship between the aerodynamic field and the acoustic field. By selecting different models for σ_h, T_h, and A_h different scaling sets can be generated which are physically and mathematically well defined.

1.5.2 Specific Models

Many of the models discussed in Section 1.4.1 can be generated by the proper selection of velocity and length scales for Equation 1.32. For example, the Howe (1988) and Hersh (1983) models have dimensional forms that depend only on inner flow

variables, u_τ and h. This form is shown in Equation 1.33 along with the assumptions need for σ_h, T_h, and A_h.

$$\frac{\overline{(p')^2_{\text{dipole}}}}{\left(\frac{\rho}{c_\infty}\right)^2 u_\tau^6} \sim f\left(\frac{\omega h}{u_\tau}\right), \frac{\Phi(\omega)}{\left(\frac{\rho}{c_\infty}\right)^2 u_\tau^5 h} \sim f\left(\frac{\omega h}{u_\tau}\right)$$
$$\sigma_h \sim \rho u_\tau^2 \quad , T_h \sim \frac{h}{u_\tau}, \; A_h \sim h^2 \tag{1.33}$$

Where Φ is the acoustic power spectral density and is related to the power spectra scale by multiplying the spectral density scaling by the characteristic time scale. This model assumes that the scattered pressure fluctuations are proportional to the mean skin friction on the surface, that the convection velocity of the scattered eddies is proportional to the skin friction velocity, and that the characteristic area is proportional to the roughness height.

Using a similar approach the model proposed by Cole (1980) based on outer flow variables can be seen in Equation 1.34.

$$\frac{\overline{(p')^2_{\text{dipole}}}}{\left(\frac{\rho}{c_\infty}\right)^2 U_e^6} \sim f\left(\frac{\omega \delta^*}{U_e}\right), \frac{\Phi(\omega)}{\left(\frac{\rho}{c_\infty}\right)^2 U_e^5 \delta^*} \sim f\left(\frac{\omega \delta^*}{U_e}\right)$$
$$\sigma_h \sim \rho U_e^2 \quad , T_h \sim \frac{\delta^*}{U_e}, \; A_h \sim \delta^{*2} \tag{1.34}$$

By looking at the values of σ_h, T_h, and A_h it appears this model is unlikely to model sound produced by a rough surface wall. The influence of the roughness on the sound field is only indirectly incorporated into this model through the roughness's effect on U_e and δ^*. As shown in Chapter 5 for the wall jet flow U_e is unaffected by the presence of roughness, making this model nearly independent of roughness size.

Another model from Chapter 1 that can be generated with this method is the model of Farabee and Geib (1991), which used a mixture of inner and outer flow variables. Their model is shown in Equation 1.35. In this form the same time and correlation scales are used as the Cole (1980) model, but the scattered stress term is assumed to be proportional to the mean surface shear stress. This model physically assumes that the scattering is controlled by eddies on the order of the δ^* moving at a speed U_e generating a shear at the surface proportional to the mean shear stress. The effect of the roughness is incorporated by the change it induces in the drag along the surface.

$$\frac{\overline{(p')^2_{\text{dipole}}}}{\left(\frac{\rho}{c_\infty}\right)^2 U_e^2 u_\tau^4} \sim f\left(\frac{\omega \delta^*}{U_e}\right), \frac{\Phi(\omega)}{\left(\frac{\rho}{c_\infty}\right)^2 U_e u_\tau^4 \delta^*} \sim f\left(\frac{\omega \delta^*}{U_e}\right)$$
$$\sigma_h \sim \rho u_\tau^2 \; , T_h \sim \frac{\delta^*}{U_e}, A_h \sim \delta^{*2} \tag{1.35}$$

Table 1-1 lists a number of additional possible choices for σ_h, T_h, and A_h which are used in Chapters 6 and 7. The first column of Table 1-1 lists the first known author to propose the scaling model and the year it was proposed for previously documented models. Models designated by A-F are newly proposed scaling models in this report. Model A is similar to the Howe scaling but assumes the hydrodynamic pressure field scales with the maximum turbulent variation. Since the wall pressure fluctuations are driven by the turbulent velocity fluctuations one would expect the maximum value of the turbulent fluctuations to be physically related to the wall pressure fluctuations at that location. Model B scales the hydrodynamic pressure fluctuations on $\rho u_\tau U_e$ which has been shown to model the boundary layer turbulence at high Reynolds numbers. (DeGraaff and Eaton, 2000) Models C through E change the correlation area to a mixed scale of $h\delta^*$ for several of the earlier models. This represents an acoustic source which is correlated over the length of the boundary layer, which should give the scale of the largest eddy structures and a height proportional to the roughness element size. Model F modifies the Howe scaling to have a time scale controlled by hydrodynamic features, instead of surface roughness features.

Author, year	σ_h	T_h	A_h	SPD form
Howe, 1988	ρu_τ^2	h/u_τ	h^2	$\frac{\Phi(\omega)}{(\rho/c_\infty)^2 u_\tau^5 h} \sim f\left(\frac{\omega h}{u_\tau}\right)$
Farabee and Geib, 1991	ρu_τ^2	δ^*/U	δ^{*2}	$\frac{\Phi(\omega)}{(\rho/c_\infty)^2 u_\tau^4 U\delta^*} \sim f\left(\frac{\omega\delta^*}{U}\right)$
Cole, 1980	ρU^2	δ^*/U	δ^{*2}	$\frac{\Phi(\omega)}{(\rho/c_\infty)^2 U^5 \delta^*} \sim f\left(\frac{\omega\delta^*}{U}\right)$
Glegg, 2007	ρu_τ^2	l_e/U	h^2	$\frac{\Phi(\omega)}{(\rho/c_\infty)^2 u_\tau^4 U(h^2/l_e)} \sim f\left(\frac{\omega l_e}{U}\right)$
A	$\rho u'^2_{max}$	h/U	h^2	$\frac{\Phi(\omega)}{(\rho/c_\infty)^2 u'^4_{\max} Uh} \sim f\left(\frac{\omega h}{U}\right)$
B	$\rho u_\tau U$	δ^*/U	δ^{*2}	$\frac{\Phi(\omega)}{(\rho/c_\infty)^2 u_\tau^2 U^3 \delta^*} \sim f\left(\frac{\omega\delta^*}{U}\right)$
C	ρU^2	δ^*/U	$h\delta^*$	$\frac{\Phi(\omega)}{(\rho/c_\infty)^2 U^5 h} \sim f\left(\frac{\omega\delta^*}{U}\right)$
D	ρu_τ^2	δ^*/U	$h\delta^*$	$\frac{\Phi(\omega)}{(\rho/c_\infty)^2 u_\tau^4 Uh} \sim f\left(\frac{\omega\delta^*}{U}\right)$
E	ρu_τ^2	δ^*/u_τ	$h\delta^*$	$\frac{\Phi(\omega)}{(\rho/c_\infty)^2 u_\tau^5 h} \sim f\left(\frac{\omega\delta^*}{u_\tau}\right)$
F	ρu_τ^2	δ^*/u_τ	h^2	$\frac{\Phi(\omega)}{(\rho/c_\infty)^2 u_\tau^5 h(h/\delta^*)} \sim f\left(\frac{\omega\delta^*}{u_\tau}\right)$

Table 1-1 Possible dipole scaling models

1.6 Quadrupole Scaling

1.6.1 Dimensional Analysis

Quadrupole noise results from the third term in Curle's (1955) solution to the Lighthill (1952) equations. This noise is generated by the unsteady pressure fluctuations in a turbulent flow and does not depend on the presence of a scattering surface to exist.

$$\rho'(x,t)c_\infty^2 = p'(x,t) = \frac{1}{c_\infty^2}\frac{x_i x_j}{4\pi r^3}\iiint_V \left[\frac{\partial^2 T_{ij}}{\partial \tau^2}\right]_{\tau=\tau} dV(y) \qquad (1.36)$$

Following the same methods of the previous section Equation 1.36 can be rewritten in terms of the characteristic turbulent shear, a time scale, and a correlation volume, as shown in Equation 1.37.

$$\overline{(p')^2}_{Quadrupole} \sim \frac{x_i^2 x_j^2 V_s}{|\mathbf{x}|^6}\frac{\sigma_h^2}{c_\infty^4 T_h^4}V_h = \frac{x_i^2 x_j^2 S}{|\mathbf{x}|^6}\frac{\sigma_h^2}{c_\infty^4 T_h^4}V_h L_h \qquad (1.37)$$

Where V_S is the volume of the turbulent fluid that is producing noise, this volume can be rewritten in terms of the roughness area S, and a length scale characteristic of the height of the source region, L_h. Similar to the dipole scaling the first group of terms controls the propagation effects and roughness patch size. The second group defines the source strength and thus source scaling.

1.6.2 Specific Models

By selection of σ_h, T_h, V_h, and L_h different specific scaling models can be generated. Table 1-2 lists a number of specific models, along with the characteristic shear, time, and length scales. The first model was proposed by Cole (1980) and is based on outer scaling variables U_e and δ^*. This model suffers many of the same shortcomings of the Cole (1980) dipole model, in that it has only a weak dependence of the presence of the roughness. The other models in Table 1-2 have not be proposed for roughness noise before, but are based on may of the same characteristic scales as the dipole models.

Author, year	σ_h	T_h	$V_h L_h$	SPD form
Cole, 1980	ρU^2	δ^*/U	δ^{*4}	$\frac{\Phi(\omega)}{(\rho/c_\infty^2)^2 U^7 \delta^*} \sim f\left(\frac{\omega\delta^*}{U}\right)$
Inner Scaling	ρu_τ^2	h/u_τ	h^4	$\frac{\Phi(\omega)}{(\rho/c_\infty^2)^2 u_\tau^7 h} \sim f\left(\frac{\omega h}{u_\tau}\right)$
Mixed Scaling I	ρu_τ^2	h/u_τ	$(h\delta^*)^2$	$\frac{\Phi(\omega)}{(\rho/c_\infty^2)^2 u_\tau^7 h(\delta^*/h)^2} \sim f\left(\frac{\omega h}{u_\tau}\right)$
Mixed Scaling II	ρu_τ^2	δ^*/u_τ	$(h\delta^*)^2$	$\frac{\Phi(\omega)}{(\rho/c_\infty^2)^2 u_\tau^7 \delta^* (h/\delta^*)^2} \sim f\left(\frac{\omega\delta^*}{u_\tau}\right)$

Table 1-2 Possible quadrupole scaling methods

1.7 Shortcomings of Previous Work

As the previous sections have shown, there is significant interest in a prediction method for boundary layer noise generated by flow over rough surfaces; however, it is equally clear that the current models are insufficient. The primary issue that must first be resolved is the proper scaling behavior of the far field sound level. As discussed in the last section there are several theoretical and experimental results that suggest that roughness noise should scale as an acoustic dipole. However, there is little agreement on which velocity and length scale should be used in this scaling behavior. Without knowing the proper scaling parameters predictions of noise in full scale engineering applications is nearly impossible. The inability to determine the correct scaling parameters can be traced to the limited set of experimental data available for analysis. The data of Hersh (1983), Farabee and Geib (1991), and Cole (1980) represent the three best data sets that provide a systematic variation of velocity and surface roughness. However the use of the parabolic microphone by Cole results in low signal to noise ratio, which makes definitive determination of scaling parameters difficult from his results. The work of Hersh (1983) and Farabee and Geib (1991) each suggest different scaling parameters be used.

Beyond the issues associated with the selection of the proper scaling parameters for roughness noise, there are additional questions that need to be addressed. There is no agreement as to the physical source of roughness noise. Scattered sound and sound due to vortex shedding are likely to scale differently. Previous work has not been able to separate these sources, or definitively show the existence of either. Further, the influence of the form of the surface roughness has not been systematically studied. All of the previous data sets are based on sand grit or other similarly roughened surfaces. However, there are also many situations of engineering interest where a periodic or deterministic rough surface may intentionally be created; as in the rivet placement on an aircraft wing, or a ribbed liner to increase heat transfer. No studies of the effects of roughness pattern

or orientation on sound generation have been documented. This prevents validation of scaling and analytic models of flow over these types of surfaces.

1.8 Objectives and Approach

In order to gain a better understanding of roughness noise, more information is needed about the basic structure and behavior of the acoustic spectrum. The primary goal of this study was to measure and characterize the far field spectrum from a turbulent flow past a rough surface. A new facility was developed which allowed measurement of the far field spectrum without confounding influences from other noise sources. With a facility capable of directly measuring roughness noise, additional objectives could be achieved. The next goal was to generate a data set of acoustic and aerodynamic measurements that would allow the various scaling models discussed earlier to be investigated. Physical understand about the source of roughness noise could be gained by comparing these models against a large data set.

Determination of the proper scaling parameters for roughness noise is not an easy task, as in a typical external boundary layer. The change of one of the possible scaling parameters, i.e. roughness height, will result in a change in at least one of the other possible scaling parameters, i.e. boundary layer thickness and skin friction velocity. One possible solution to this is to study an internal flow, where at least the effective boundary layer thickness is limited in fully developed flows, as was done by Hersh (1983). This approach, however, prevents the direct measurement of far field sound levels. Another solution is to use only short fetches of roughness, over which the flow changes very little, even when the surface treatment is changed. Cole (1980) used 15 cm long fetches of grit roughness for some of his tests. Cole measured the boundary layer behavior 12.5 cm downstream from the leading edge of the roughness fetches and found that the change in boundary layer thickness from smooth to 40 and 80 grit roughness was less than 15%, and the change in skin friction was less than 30%. The difference in boundary layer thickness and skin friction between the 40 and 80 grit surfaces was typically less than 10%, although the change in roughness size is nearly 200%. So by using short fetches of roughness under a turbulent boundary layer in a wind tunnel one should be able to vary the different scaling parameters independently, and determine the proper scaling behavior.

While this approach allows one to physically probe the far field in a standard or acoustic wind tunnel, the background noise levels in the tunnel will likely be dominated by the roughness noise from the walls of the tunnel. (Duell *et al.,* 2004) This problem is further compounded by the fact that roughness noise is expected to behave as a flow aligned dipole, so a microphone placed near a test sample in the wind tunnel test section will be exposed to the loudest part of the directivity from the rest of the tunnel walls. As a quantitative example consider the flow over a rectangular array of cylinders 2mm in diameter, 0.76 mm high, and 5.5 mm apart, as reported by George and Simpson (2000). They found that the surface was transitionally to fully rough with a boundary layer thickness of 57.5 mm and a flow speed of 27 m/s. Howe's (1988) theory can be used to calculate the sound radiated from a 1 m^2 fetch of roughness to an observer 1 m away at a 45° angle to the flow, likely the best practical location of a microphone during a test. This calculation shows the sound spectrum peaks at a level of 6 dB near 2 kHz. In

comparison with the quietest large-scale facilities that could generate the boundary layer needed, the background noise level is still on the order of 15 dB above the expected peak sound level generated by the sample.

This example illustrates the need for a special purpose test facility to measure roughness noise. The facility needs to allow for a microphone to measure the acoustic far field while remaining outside the flow, maintain low flow speeds everywhere except over the test sample, and allow the small fetches of roughness to be used which will not significantly change the flow behavior. One approach that meets these needs with a well-defined aerodynamic flow is a wall jet facility. Wall jet flows have been well studied as will be discussed shortly, and allow a large amount of control of the flow speed, and boundary layer properties with small changes in the facility setup. The wall jet also allows direct measurement of the far field sound generated beneath it without impinging on a microphone. It also has the advantage of having only one surface in the flow, if this surface is used as the test sample there is very little contamination of the background acoustics from other noise sources.

A wall jet flow is created when the exhaust jet from a nozzle, usually rectangular, interacts with a flow-aligned surface. The most commonly studied configuration is to have a rectangular nozzle with a flat plate aligned with on of the sides of the nozzle so that the jet exits directly onto the plate. This configuration has a number of applications, mainly related to the flow from a sluice gate. Recently, applications involving ducted propulsion have also been interested in these and similar flows. The wall-jet flow can be broken down into two regions, an outer mixing-layer flow and an inner boundary layer flow. In the outer region the flow spreads and decays in a manner similar to a conventional jet, with the exception that the decay rate is also influenced by the frictional losses due to the presence of the wall. In the inner region a boundary layer is formed by the interaction of the jet with the wall. The inner region can be turbulent or laminar depending on the Reynolds number, and behaves similar to a standard boundary layer in the inner regions of both flows. This configuration is shown schematically in Figure 1-12.

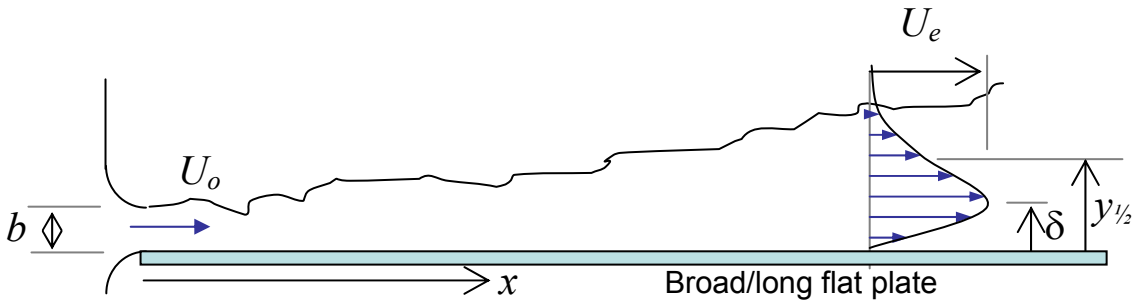

Figure 1-12 Schematic layout of a 2D wall jet flow.

Another key feature to the wall jet flow which makes it well suited for testing roughness noise is that the flow over a smooth plate is nearly self-similar. When the velocity profile at any streamwise location is normalized on its local maximum velocity, U_e, and half height, $y_{1/2}$, the height at which the velocity is half of the maximum, the profile shape is the same. Wygnanski, Katz, and Horev (1992) presented a review and

discussion of wall jet studies and scaling laws. To study the two-dimensional behavior of a wall jet they used a rectangular nozzle with an aspect ratio of 60:1 which exited directly onto a smooth flat plate. They found that the outer region of the wall jet was self-similar over a wide range of Reynolds numbers, and that the inner region was only a weak function of Reynolds numbers. This finding is not unexpected when one considers the boundary layer Reynolds number range that was achieved during their tests; conventional turbulent boundary layers are not fully self-similar at these Reynolds numbers either. Narashima (1973) found that the scaling properties of a wall jet could be well modeled by looking at the jet Reynolds number and the downstream distance of the wall jet by Equations 1.38.

$$\frac{U_e \nu}{J} = A_U \xi^{n_U} \quad \frac{u_\tau \nu}{J} = A_\tau \xi^{n_\tau} \quad \frac{\delta J}{\nu^2} = A_\delta \xi^{n_\delta}$$
$$J = U_0 b \qquad \xi = \frac{xJ}{\nu^2} = \left(\frac{xU_0}{\nu}\right)\left(\frac{bU_0}{\nu}\right) \tag{1.38}$$
$$n_U = -0.472 \qquad n_\tau = -0.535 \qquad n_\delta = 0.409$$

In Equation 1.38, U_e is the maximum velocity measured at a given x location, b is the nozzle exit height, δ is the height of maximum velocity, and U_0 is the jet exit velocity. The values of A for each relation are also suggested although they are highly dependent of the values of n selected, and may depend on the facility setup.

The self similarity of the velocity profile along with the well defined behavior of the scaling parameters of the wall jet, given by Equation 1.38, provide a powerful tool for the investigation of roughness noise scaling parameters. One may note that the three parameters used for scaling U_e, u_τ, and δ, are also three of the possible scaling parameters for roughness noise, and the values of these three parameters in the wall jet are controlled by three facility defined values. By changing the height of the nozzle, the nozzle exit speed, and the streamwise location on the plate, the values of the local flow speed and boundary layer thickness can be manipulated. While all three parameters cannot be controlled independently, the exponential behavior of U_e and u_τ are similar. The boundary layer thickness and velocity relationships can be used to vary these nearly independently. The ability to easily control the boundary layer thickness independently of the velocity is very useful in separating their influence on the scaling of roughness noise.

One issue with this approach is that there is very little published data on the behavior of a wall jet over a rough surface. Some qualitative studies have been done on the influence of surface roughness on erosion levels behind a sluice gate/wall jet type flow, but little is know of how surface roughness effects the self-similarity and decay properties of the wall jet flow. One would expect that for a short enough fetch of roughness the macroscopic flow behavior would remain largely unaffected by the introduction of roughness to the flow. Even if the changes seen in the macroscopic flow parameters is twice what was seen by Cole (1980) for roughness strips under a conventional boundary layer, the wall jet could be used to determine the influence of various flow properties of roughness noise.

1.9 Experimental Approach

An experimental study has been conducted to determine the scaling behavior of roughness noise as presented earlier. The primary focus of the experimental work has been to independently look at the influence of possible scaling parameters including the roughness size, boundary layer thickness, edge velocity, and skin friction velocity. To control all of these properties a special wall jet facility has been constructed at Virginia Tech. The facility generates a largely two-dimensional flow inside an acoustically treated environment, which allows for easy measurement of the far field acoustics generated by the flow. Extensive Pitot static and hot wire anemometry studies were first carried out to quantify the behavior of the wall jet, and the influence of roughness placed beneath the wall jet flow. Pinhole microphone measurements of the surface pressure spectrum were conducted to determine the behavior of the surface pressure beneath this flow, since this should have significant influence on the radiated sound levels. Microphone tests were then conducted in which various scaling parameters were systematically varied to determine their influence on roughness noise levels. Tests have also been conducted which show the nature of the acoustic directivity of the roughness noise source. As a final part of this study, periodic roughness patterns have been examined to provide a data set for future analytical work to incorporate the influence of repeated roughness patterns in the generation of boundary layer noise.

Chapter 2 Facility Design and Preliminary Tests

As discussed earlier, the primary goal of the experimental study for this project was to determine the spectral shape and scaling behavior of roughness noise. This objective requires extensive aerodynamic and aeroacoustic measurements. This chapter will describe the development and testing of a preliminary facility used in this study. This facility was extensively modified after the preliminary tests shown in this chapter to improve both its acoustic and aerodynamic performance. The final facility, which was used for measurements presented from chapter 4 forward, will be described in the next chapter.

2.1 Wall Jet Facility

As discussed earlier, a special facility is needed for the measurement of rough wall boundary layer noise. An acoustically treated wall jet facility was constructed and used for the study presented in this paper. This section will present the analysis and thought process that lead to the wall jet tunnel facility. Design, analysis, sizing, and construction of the facility will be discussed, along with measurements of the acoustic and aerodynamic performance of the wall jet. A second nozzle was also used during testing, and information will be presented on the design and performance of this nozzle as well. Finally, the wall jet flow and acoustics of the facility were calibrated and will be documented at the end of this section.

2.2 Early Designs

The design for the roughness noise facility at Virginia Tech underwent significant changes during the early design process. The initial design concept was for the development of a rectangular channel flow facility. The channel flow would allow for direct control of the effective boundary layer thickness, as well as allow easy determination of the skin friction coefficient by measuring the pressure drop along the length of the channel. By using an array of surface mounted microphones inside the channel the wall surface pressure wavenumber spectrum could be measured, similar to the approach used by Farabee and Geib (1991). By using the wavenumber filtering ability of the microphone array, the acoustic energy content of the spectrum can be separated from the convected turbulence energy. Preliminary analysis showed the resonance modes of the channel would help to amplify the acoustic energy to ease the separation of acoustic from evanescent energy waves. The primary concern with this design was that it provided no means to directly measure the far field sound field. However, working with duct acoustic theories suggested that measurements of the acoustic pressure on the surface of the channel could be related to the far field acoustics over an external flow.

Detailed design and sizing then began for the channel flow facility. One of the primary design constraints for the facility was to minimize noise contamination in the test section from the tunnel driver system. Consideration was given to both closed and open circuit designs, but the open circuit concept seemed to allow for a quieter facility. A closed circuit tunnel required the fan and motor to be a few test section lengths away

from the test section in order to reduce aerodynamic losses along the tunnel. From an acoustic standpoint this design also has problems because the sound from the fan is trapped in the facility and can reach the test section from the upstream and downstream side, requiring more acoustic treatment along the tunnel circuit. Because of these problems with the closed circuit design, the tunnel design focus moved to open circuit designs which allow a number of additional driver systems to be used in addition to a fan or blower. A blow down system was considered which would use a high pressure tank to drive through the test section; this system would not require any motors or fans to be running during testing making it an attractive option. Run times up to thirty minutes could be achieved for typical test cases, if the high pressure storage tank used to operate several supersonic wind tunnels on the campus of Virginia Tech was used to run the wall jet facility. However, concerns about noise generated by the valves required to control the flow speed in such a configuration along with the large amount of piping needed to use the existing tank eliminated this concept.

One design that was further investigated was to use a pressure blower that could be acoustically isolated from the test section to drive the flow through the channel. The blower would be silenced and located away from the test section and deliver air into an acoustically treated settling chamber. The settling chamber would serve the purpose of further reducing the blower noise, and conditioning the flow for the channel. The flow would then pass through a nozzle into the channel region. The channel would end in a flared exit to reduce edge noise from the back of the channel region from traveling upstream to the microphone array. This design is shown in Figure 2-1.

Another design that was further considered is very similar to the channel system shown in Figure 2-1, but provides an external flow as a wall jet facility. This facility would use the same blower and settling chamber system as the channel design in Figure 2-1, but instead of exiting into a channel, the flow would exit parallel to a large flat plate. By placing one side of the nozzle flush with the plate surface the flow would develop into a wall jet, with an external boundary layer flow near the wall. A wall jet flow allows control of the boundary layer thickness and velocity similar to that of a channel flow, but with a constantly decaying mixing layer above it.

After consideration of both designs the wall jet was selected as the design for the facility. The ability to measure the far field radiated noise, without the complications of flow interference and pseudo-noise contamination of surface microphone measurements allows the highest signal to noise ratio for boundary layer noise measurement. However, the preliminary design work was done so that the wall jet facility could easily be converted to a channel facility if the need arose.

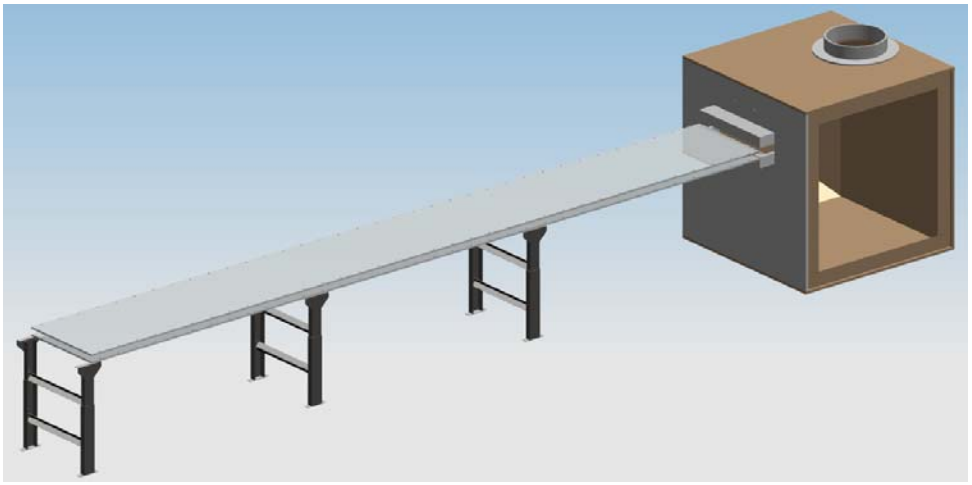

Figure 2-1 Early channel design. Settling chamber shown on right with one wall removed. The channel top and nozzle would be adjustable to allow control of the channel height. A blower not shown in the figure drives the system.

2.3 Preliminary Wall Jet Facility

2.3.1 Nozzle Design

A two dimensional symmetric nozzle was used for the preliminary wall jet facility. The settling chamber contained a two-dimensional contraction upstream of the nozzle. This contraction used a circular radius of 76 mm on each side of the chamber to reduce the chamber width to 560 mm. The nozzle height was variable from 0 to 50 mm, to allow control of the wall jet flow. This maintained a higher aspect ratio than that recommended by Olsson and Sunden (1998) to maintain a two-dimensional rectangular channel flow, which was the original intent of the nozzle design.

A series of elliptical nozzles with different aspect ratios were investigated because they provided a simple shape to create, which matched the position and slope at both ends of the nozzle. These nozzle shapes were defined by the ratio of L_a, the semi-major axis length in the flow direction, to L_b, the semi-minor axis perpendicular to the flow. A constant strength source panel method was developed to model the flow through different nozzle shapes. The source panel method worked by using a set of source panels which each have a constant but unspecified strength. A control point, placed just in front of the center of each of these source panels, specifies the boundary condition that exists at each panel. A matrix equation is then derived which determines the effect of each panel strength on the velocity at each control point. The velocity at each control point is then specified so that there is no flow through solid surfaces, uniform flow into the settling chamber, uniform flow out of the tunnel, and no net flow from the entire system. This matrix problem is then inverted to determine the source panel strengths. Once these are determined, the flow anywhere within the tunnel can be determined. Figure 2-2 below, shows the panels used for this method, along with a typical velocity field for an elliptical nozzle with a 2:1 axis ratio.

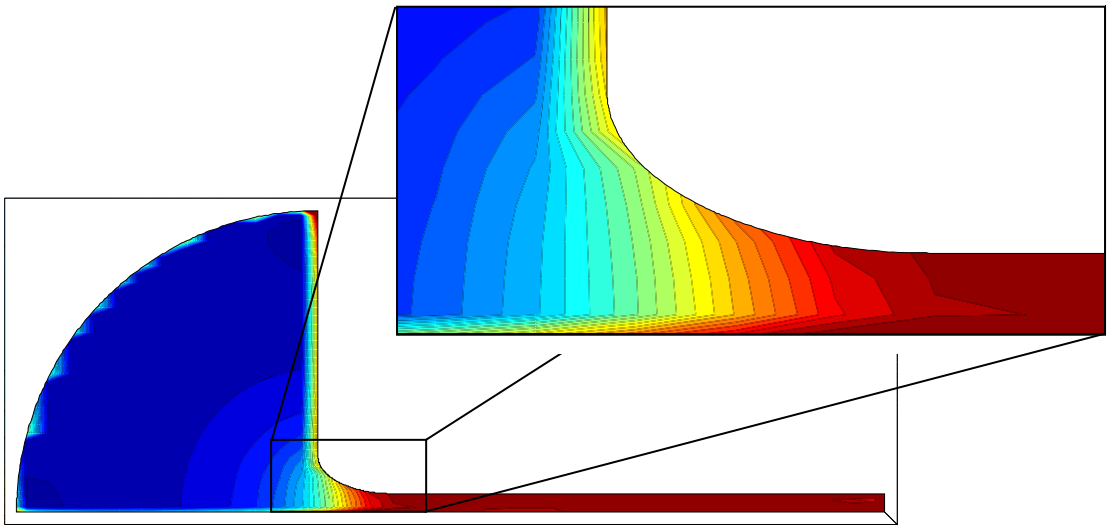

Figure 2-2 Color contour plot of showing velocity magnitude inside a 2:1 aspect ratio nozzle predicted by ideal source panels.

Figure 2-2 also shows how the simulation was set up. All the panels on the quarter circle on the left have control points with boundary conditions set to have equal flow into the computation region. These panels are located five times L_a away from the downstream side of the nozzle. This insures that the inflow boundary condition does not affect the flow through the nozzle. The wind tunnel test section is then shown on the right extending downstream $8L_b$ past the end of the nozzle. The boundary condition on the downstream end of the tunnel is uniform flow leaving the tunnel. All other surfaces have a no penetration condition at the control points. In addition to the boundary conditions set on each panel the source strength for all panels is required to sum to zero. The panel source strengths are then solved to minimize the error from the over-constrained matrix equation numerically in Matlab. In this simulation 1200 control points were used around the perimeter, simulations with 500 to 2500 points yield similar results.

Most importantly the flow along the wall through the nozzle can be determined. In Figure 2-3 below, it shows the wall pressure coefficient plotted along the vertical wall upstream of the nozzle, curving around the nozzle, and along a line parallel with the wall jet exit, representing the dividing streamline of the wall jet.

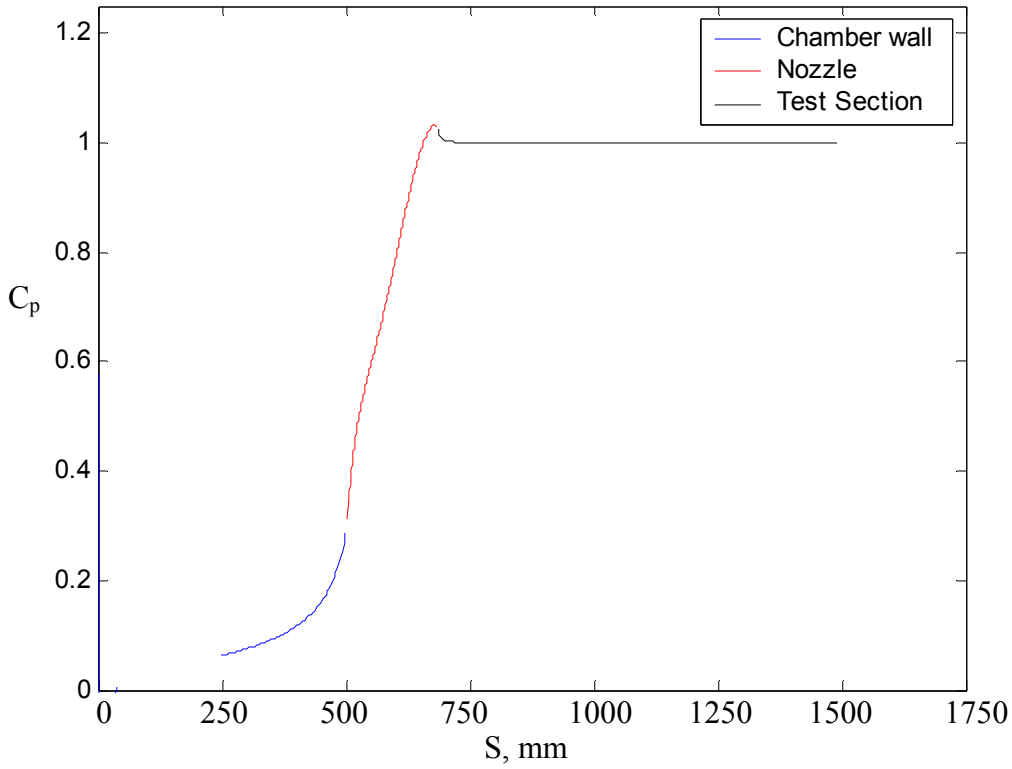

Figure 2-3 Pressure coefficient predicted by panel method along the nozzle surface for flow through a 2:1 aspect ratio nozzle using ideal source panels.

The pressure distribution seen in Figure 2-3 is typical of all nozzles. Along the chamber wall there is a slow increase in the velocity, which begins to rise sharply near the nozzle entrance. In the nozzle, the velocity quickly increases to a maximum just before the end. Then in the transition region from the nozzle to the test section there is a slight recovery region where there is a small adverse pressure gradient where the velocity comes back to the test section speed. This is the region of most concern in nozzle design because it is the only place where separation can occur. The next figure, Figure 2-4, shows how different axis ratios affect this overshoot for elliptical nozzles.

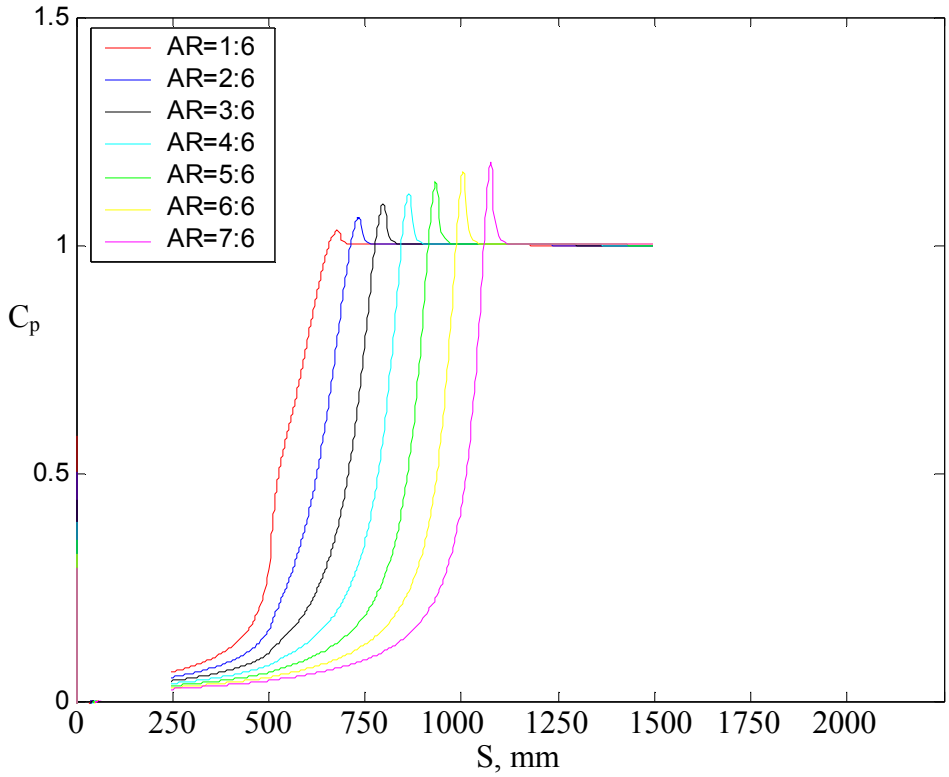

Figure 2-4 Pressure coefficient along nozzle wall for various nozzle shapes as predicted by ideal source panels

Figure 2-4 shows the pressure coefficient along the nozzle wall for a number of different elliptical nozzles. The nozzle aspect ratio is listed in the legend for each curve, and varies for 1:6, a long shallow nozzle, to 7:6, a nozzle with L_b longer than L_a. Figure 2-4 shows the height of the overshoot at the end of the nozzle increases as the vertical nozzle axis, L_b, increases. All of these profiles were run for the same free stream conditions with 1200 grid points around the simulation region. This would lead one to consider a very short nozzle to minimize this region. However, as the nozzle height is reduced the pressure gradient at the nozzle entrance rises very rapidly, as can be seen in the AR = 1:6 curve. This creates an inflection point in the pressure curve; and for very small axis ratio's can cause an adverse pressure gradient. For this reason an axis ratio of 3:6 was chosen for further investigation in the nozzle design. This shape has a smooth transition from chamber wall to tunnel, and a pressure over shoot of 9% at the nozzle exit.

The boundary layer development was analyzed along this surface to determine how likely separation and transition was in the nozzle. To do this, the pressure distribution obtained from the panel method code was used to run an implicit laminar boundary layer code. (Devenport and Schetz, 2002) The initial boundary layer size was set to the size of the smallest y step so the boundary layer effectively grows from zero initial size. Grid for the boundary layer program was more refined than the potential flow grid. There were 4000 x grid points, and 20000 y grid points with spacing of 10^{-5}. This kept the boundary layer thickness well within the computational region, so boundary numeric effects should be minimal. These results were also shown to be consistent with

results for x grids with 500 or more points and y grids with 1000 or more points. The boundary layer profile computed using this method is shown in Figure 2-5.

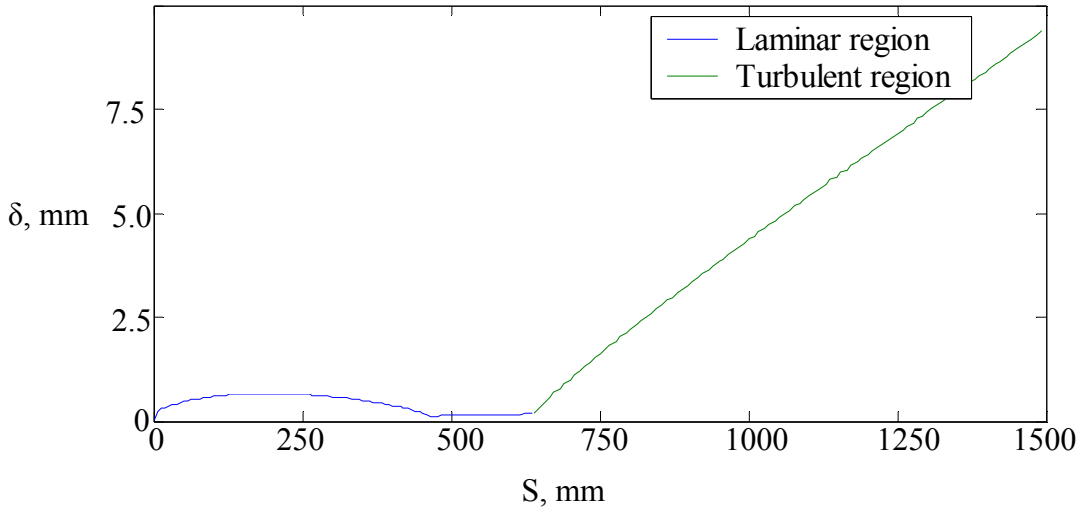

Figure 2-5 Boundary layer growth along the nozzle surface, s, for a 3:6 aspect ratio nozzle. Results shown are from implicit laminar and turbulent boundary layer methods for their respective regions. The nozzle begins at *s* = 450 mm and ends at *s* = 700mm.

The boundary layer method predicts that the boundary layer will transition from laminar to turbulent flow at a length of 680 mm, which corresponds to a location just ahead of the pressure peak at the end of the nozzle. The turbulent flow is then able to handle the adverse pressure gradient associated with the end of the nozzle, and a turbulent boundary layer can then be seen growing along the plate. The blue curve shows the laminar part of the boundary layer, which grows within the settling chamber, and then shrinks in the nozzle as the velocity increases. The green curve shows the turbulent boundary layer and its growth along the plate.

2.3.2 Blower Selection

A Cincinnati Fan model HP-8D20 with a 15 HP electric motor was selected to drive the facility. This is a centrifugal blower with a 508 by 130 mm fan capable of producing a 0.945 m^3/s volume flow rate against 7500 Pa of backpressure. The fan was also outfitted with a SSA-8 steal discharge silencer, which reduced broadband noise in the exhaust flow by 5 to 10 dB. This blower was capable of achieving nozzle exit speeds of 60 m/s for all nozzle heights below 25 mm, and flow speeds of up to 40 m/s at a nozzle height of 50 mm.

The backpressure specification on the blower was influenced by the original channel concept. Using the empirical method presented by Moody (1944), the pressure drop along a rough wall pipe was estimated from the Reynolds number and roughness size. At 60 m/s the channel flow has a Reynolds number based on hydraulic diameter of 370000. The Moody data also requires the ratio of the roughness height to the pipe diameter to determine the pressure loss along the pipe. The largest roughness size expected to be tested at that time in the channel development was a 2 mm

bump. (Details of the various roughness patches to be tested will be discussed later.) Based on these assumptions, the total pressure loss due to friction along the channel was estimated to be 3600 Pa. When this is combined with the 2200 Pa needed to drive the dynamic pressure, the total pressure needed to drive the channel was estimated at 5800 Pa. The remainder of the facility, the ductwork from the blower to the settling chamber and the settling chamber, were designed to keep the flow speed and resistance low. The total estimated pressure loss through this portion of the facility was estimated at 20% of the channel pressure loss. So the total backpressure that the blower needed to overcome was estimated at 7000 Pa.

2.3.3 Settling Chamber Design

In addition to conditioning the flow for the nozzle, the settling chamber also acoustically isolated the wall jet from the blower. To reduce aerodynamic unsteadiness from the blower the internal chamber cross section was 10 times larger than the cross section of the nozzle exit. Because the flow speeds in the settling chamber are so much lower than in the test section any aeroacoustic sources generated by this flow would be easily dwarfed by the sources in the test section. Recall that the dipole sources scale with the velocity to the 6^{th} power so a factor of 10 difference in the flow speed results in a factor of 10^6 difference in source strength.

The most common approach used in acoustic tunnels to isolate fan noise from the test section is to reduce the line of sight from the fan to the test section. In a closed circuit tunnel the fan noise must typically negotiate at least 2 corners before reaching the test section. In anechoic facilities, such as the Anechoic Flow Facility (AFF) at the David Taylor Model Basin (DTMB) shown in Figure 2-6, the fan is further isolated by adding curved vanes in the tunnel circuit to increase the number of reflections needed for sound to reach the measurement area. The AFF is especially quiet in part because these vanes are also acoustically treated to act as passive acoustic mufflers.

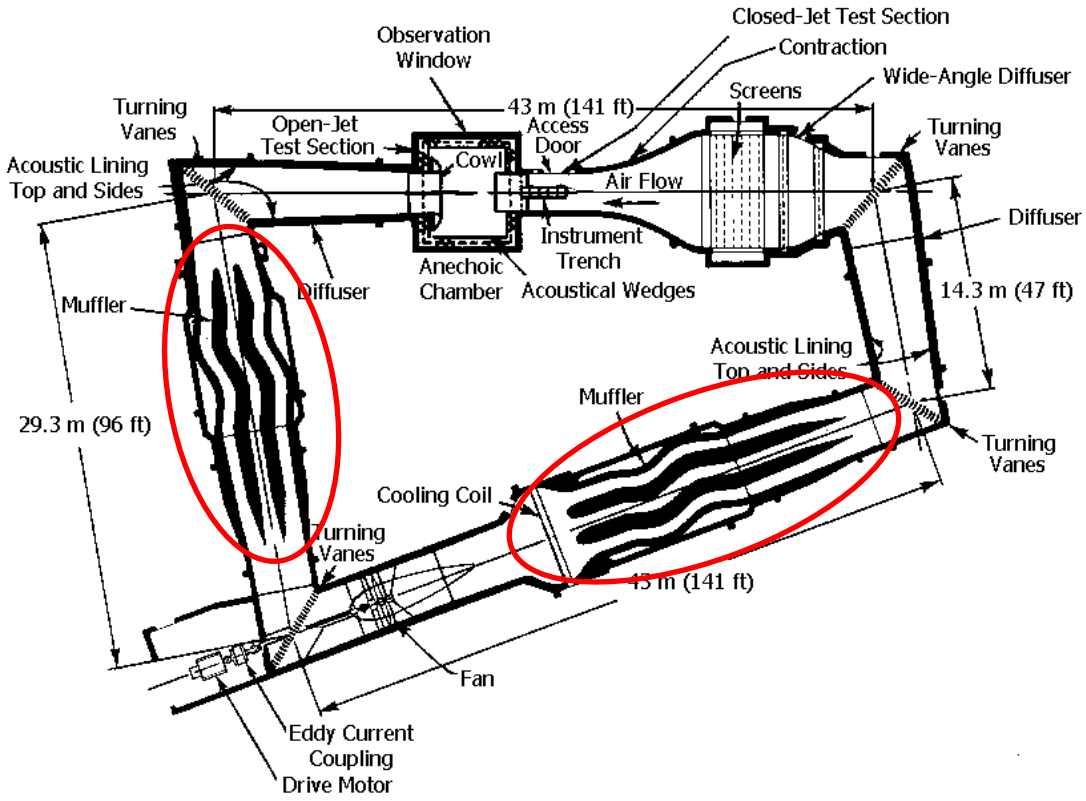

Figure 2-6 Layout of the Anechoic Flow Facility at the David Taylor Model Basin, figure taken from NAVSEA website (Anechoic Flow Facility, 2004). The figure shows two sets of curved vanes, circled in red, used to reduce fan noise contamination in the test section.

In contrast with the AFF where the vanes are located in the regions of the tunnel were the flow speeds are significant, by placing vanes in the settling chamber of the channel flow facility the flow path through the vanes can be more serpentine. To further reduce the transmission of sound through the settling chamber, all the surfaces are treated with absorptive acoustic foam. The foam helps reduce reflection strength from acoustic waves, and scatters the reflected waves due to its egg crate type surface treatment. To determine the amount and configuration of acoustic treatment needed in the settling chamber a ray tracing analysis was used. The analysis was conducted on a two dimensional section of the settling chamber to reduce computational complexity. To further reduce computations the thickness and scattering behavior of the acoustic treatment was neglected. The effect of the surface treatment was modeled conservatively by removing 10% of the wave energy at each reflection. Only 10% of the wave energy was removed to see the effects of different baffle configurations, and not dominate the results with the effects of the acoustic treatment itself. The sound from the blower was modeled using a distribution of uniform strength sources in a circle on one end of the settling chamber. (This distribution was used because the blower was connected to the settling chamber through a large diameter flexible duct to isolate motor vibrations from the settling chamber and channel.) Various baffle and vane options were tested to rank their effectiveness. The configuration selected is shown in Figure 2-7. It consists of three sets of baffles that provide no line of sight from the blower inlet to the nozzle exit.

Each set of baffles consists of a flat baffle located in the middle of the settling chamber and then two baffles located on the outside walls reaching in. Based on the conservative 10% absorption of the acoustic treatment a 10dB decrease in sound levels would be expected from the blower inlet to the nozzle.

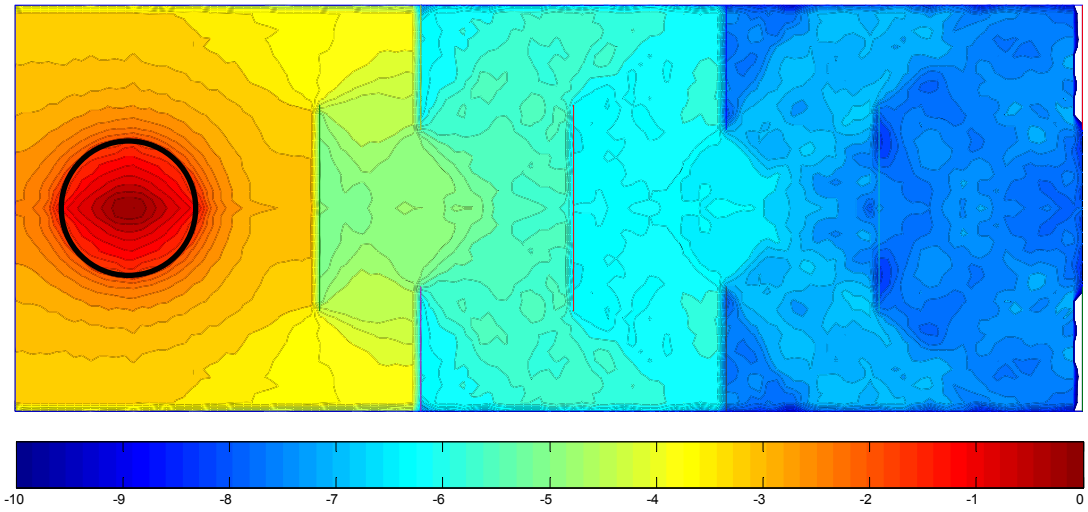

Figure 2-7 Contour plot of the relative sound level inside the settling chamber final configuration predicted by a ray tracing model. The chamber is 3300 mm long and 1244 mm wide. The black circle on the left shows the source region, and the channel entrance is in the middle of the right side wall.

The chamber has a 1246 mm square cross section and a length of 3354 mm. The internal baffles are 610 mm wide and each baffle from the side of the tunnel extended inward 375 mm. The acoustic treatment is 95.25 mm egg crate foam made by Acoustics First. The foam has 44.45 mm of solid foam backing with a surface finish consisting of 50.8 mm tall waves, shown in Figure 2-8. Data on the foam's absorption coefficient for the foam at different frequencies is also shown in Figure 2-8, which shows that above 500 Hz the foam is most effective. The absorption coefficient is formally defined as the fraction of energy absorbed by a material relative to an incident wave assuming the material is only locally reactive. In practice, the absorption coefficient for a material is measured based on the change in reverberation time of a room with and without a sample of that material in it. The projected size of the sample is used to determine the absorption coefficient, which allows material with surface areas larger than their projected area to have absorption coefficients greater than 1.

Frequency	250 Hz	500 Hz	1000 Hz	NRC
Absorption Coefficient	0.93	1.43	1.33	1.25

Figure 2-8 Picture of acoustic egg crate foam used to line the interior of the settling chamber. Also shown are the absorption coefficient values for the 95.25 mm thick foam.

The preliminary settling chamber configuration is shown in Figure 2-9. The figure shows the top and side view drawings of the internal settling chamber configuration. The top view drawing shows the baffle spacing at 457 mm intervals. This creates the serpentine pattern discussed above. The green ring at the left side of the drawings represents the collar that connects to the air supply hose. The pink areas on the right show the elliptical nozzle components discussed in the previous section.

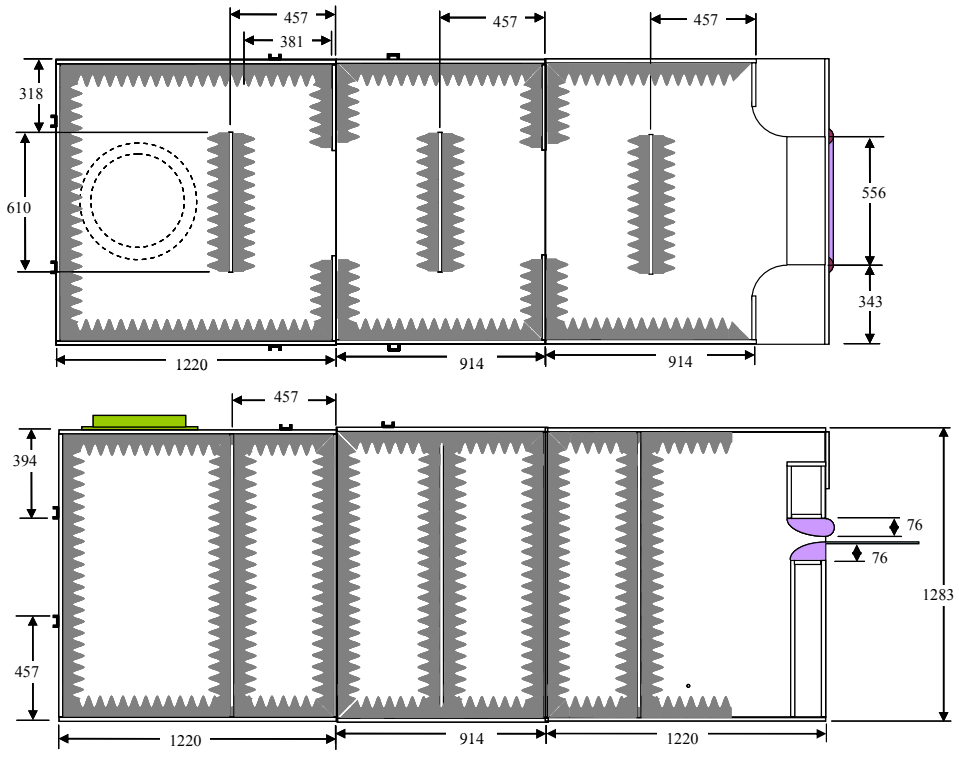

Figure 2-9 Top and Side view drawings of the preliminary settling chamber configuration. All white components are built of 19 mm thick MDF. Flow enters the chamber through the green collar on the left, and exits through the pink nozzle on the right. All dimensions are in mm.

2.3.4 Acoustic Enclosure

During preliminary design an acoustic enclosure was also designed that would cover the channel exit. The enclosure was needed for two reasons, first to reduce the amount of sound that could contaminate measurements by entering through the channel exit. The enclosure would also allow far field acoustic measurements to be taken of the exhaust flow. This would be used to assess the operation of the settling chamber and nozzle during construction. It was also considered that by measuring the sound levels from the exhaust of the channel some information about the radiated sound levels due to the roughness could be determined in a similar manor to that used by Hersh (1983).

Similar to the channel length, the primary design constraint on the acoustic enclosure was the space available in the lab. A large air-handling unit mounted to the ceiling of the lab limited the height of the enclosure. This restricted the enclosure height to 2425 mm. The length and width were limited by the lab space to 2975 mm and 2057 mm respectively. The decision was also made to make the enclosure movable so that the channel could be easily accessed and modified after the enclosure was built by moving it away from the channel. The resulting configuration had a frame made from 50 mm square steel tubing, which supported three walls and a ceiling made of 19 mm thick MDF panels. The MDF panels were lined with 95 mm acoustic egg crate foam, the same as in the settling chamber, on the sides and ceiling, and 610 mm foam wedges on the back wall. The enclosure is shown in Figure 2-10 positioned over the flat plate used for the wall jet flow.

Figure 2-10 Photograph showing the acoustic enclosure around the smooth plate wall jet.

2.3.5 Facility Construction

The facility was constructed as a series of modular components. This would allow simultaneous construction of many of the components, make trouble shooting on the full system faster, and make any future modifications relatively simple. The system was not only broken down as discussed earlier into the blower, settling chamber, and acoustic enclosure, but the settling chamber were further subdivided. The settling chamber was designed and built in three sections, roughly following the lines of the acoustic baffles.

The settling chamber was constructed from MDF panels and steel reinforcing U-channel to support the differential pressure load between the settling chamber and atmospheric pressure. The acoustic foam was then attached to the inside of the settling chamber using a non-reactive construction adhesive. At each junction between settling chamber sections a set of 5 500 pound spring latches were installed to hold the sections together. Foam rubber gaskets were also installed at the junction of each section to prevent leaking. Figure 2-11 (a) shows the settling chamber and blower enclosure during construction. Figure 2-11 (b) shows the acoustic treatment attached to the inside of the settling chamber.

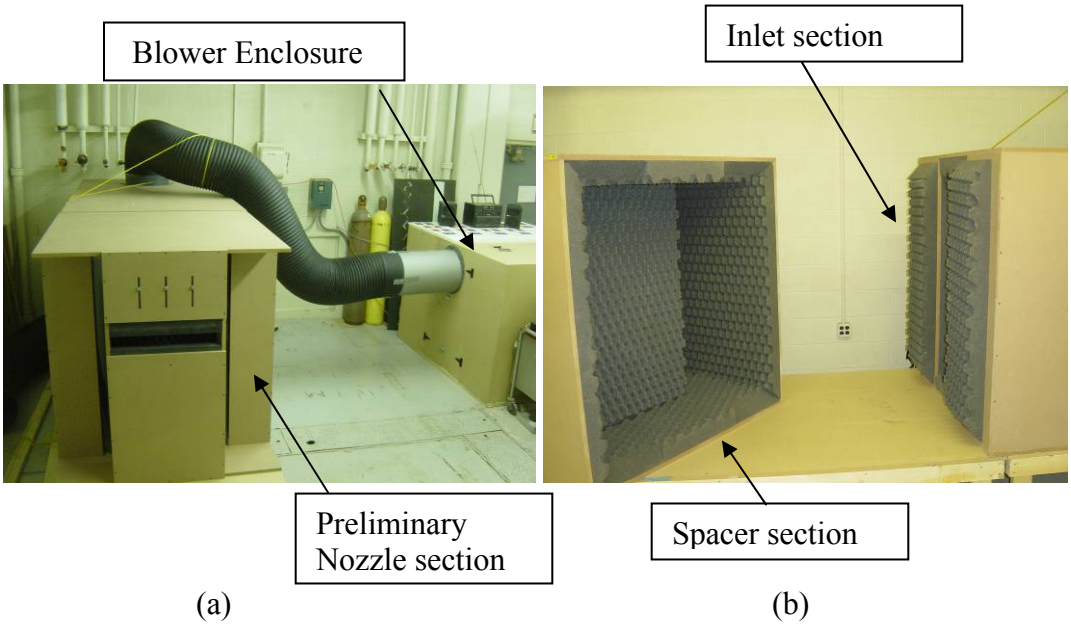

Figure 2-11 Photographs of the settling chamber showing: (a) preliminary settling chamber and blower enclosure during assembly and (b) internal acoustic treatment in spacer and inlet sections.

The nozzle design was discussed in detail earlier. Sections of 310 mm diameter polycarbonate pipe were used to create the first contraction in the horizontal direction, as shown in Figure 2-11. The vertical nozzle was constructed using a 3-axis computer controlled milling machine. The nozzle was milled out of a single piece of PVC plastic. The PVC provides a material that is easy to machine to a smooth finish, while also being inexpensive and durable. To make the nozzle adjustable the upper section of the PVC nozzle is attached to an MDF box, which is held in a channel within the settling chamber. The MDF box has three screws that pass through slots in the front of the settling chamber that can be loosened and tightened to adjust or hold the nozzle in place, shown in Figure

2-12. To reduce edge noise from the nozzle a semicircular piece of wood with a 38.1 mm radius was attached to the upper lip and sides of the nozzle. These pieces were shaped to mate together on the sides. Testing with and without these rounded lips showed a significant reduction in sound levels in the acoustic chamber.

Figure 2-12 Front of preliminary settling chamber showing bolts for nozzle adjustment.

A 3048 mm long, 1524 mm wide, and 9.5 mm thick plate of aluminum was used as the flat plate for the wall jet. A set of three steel frames, each 610 mm long and 1830 mm wide, were used to support the channel. The frames were constructed of 50 mm square steel tubing with a wall thickness of 1.5 mm. The frames were bolted to the floor with adjustable screw feet to allow alignment of the plate with the nozzle exit, nominally 1257 mm above the lab floor.

2.3.6 Preliminary Instrumentation

Single microphone and phased array acoustic measurments were made to characterize the performance of the preliminary wall jet facility. Two microphones were used for preliminary acoustic measurements in the wall jet facility: a ⅛ inch Bruel and Kjaer 4138 (B&K) microphone and a B&K 4010 microphone. The model 4138 microphone has a flat frequency response up to 140 kHz with a sensitivity of 1 mV/Pa, while the 4010 was flat only to 20 kHz, but with a sensitivity of 50 mV/Pa. The microphone was powered and conditioned using a Nexus Conditioning amplifier, and measurements were collected using an Agilent 16 bit A\D converter. A 63 microphone phased array was provided by Dr. Burdisso and the Vibrations and Acoustics Laboratory of Virginia Tech. The array is a single arm spiral configuration optimized for best performance from 5000 to 20000 Hz. More information about the configuration and performance of this array can be found in Smith *et al*, 2005. Aerodynamic measurements were made using a Pitot static probe with a probe diameter of 3 mm. The probe was

connected to a Setra 239 (±2.5 kPa) pressure transducer, which was read using the same A\D converter.

2.3.7 Preliminary Configuration Calibration

As the various components were completed, testing began to assess the performance of each system. The first component to be tested was the blower assembly. The blower was installed in the lab on a set of rubber vibration isolators to reduce vibration transfer from the blower to the channel. To reduce the radiated motor and fan noise an acoustic enclosure was built around the blower as well. The enclosure was made of MDF panels lined with 25.4 mm thick polyurethane foam. To allow air into the enclosure for the blower, a set of 90° bent vanes were installed on the side of the enclosure looking away from the tunnel test section. This enclosure seemed to qualitatively reduce the noise in the lab, but quantitative measurements were never made. To test the acoustic behavior of the blower and the effectiveness of the silencer a series of single microphone measurements were taken of the jet noise from the blower. Measurements were taken using the single ⅛ inch diameter B&K microphone positioned 1.3 m from the blower exit and 45° off the jet axis, in the same horizontal plane as the jet exit. During these tests the blower was in the open lab. This area was not acoustically treated so some reflections and lab background noise may be present in the measured acoustic spectra. Measurements were made at several nozzle exit speeds, as measured by a hand held Pitot-static probe and digital monometer for both the plain blower and the blower with the silencer installed. At each speed the total sound level was calculated from 250 records each containing 8192 points sampled at 51.2 kHz. Figure 2-13 shows that the silencer significantly decreases the jet noise from the blower. At exit speeds above 30 m/s the reduction is better than 15 dB.

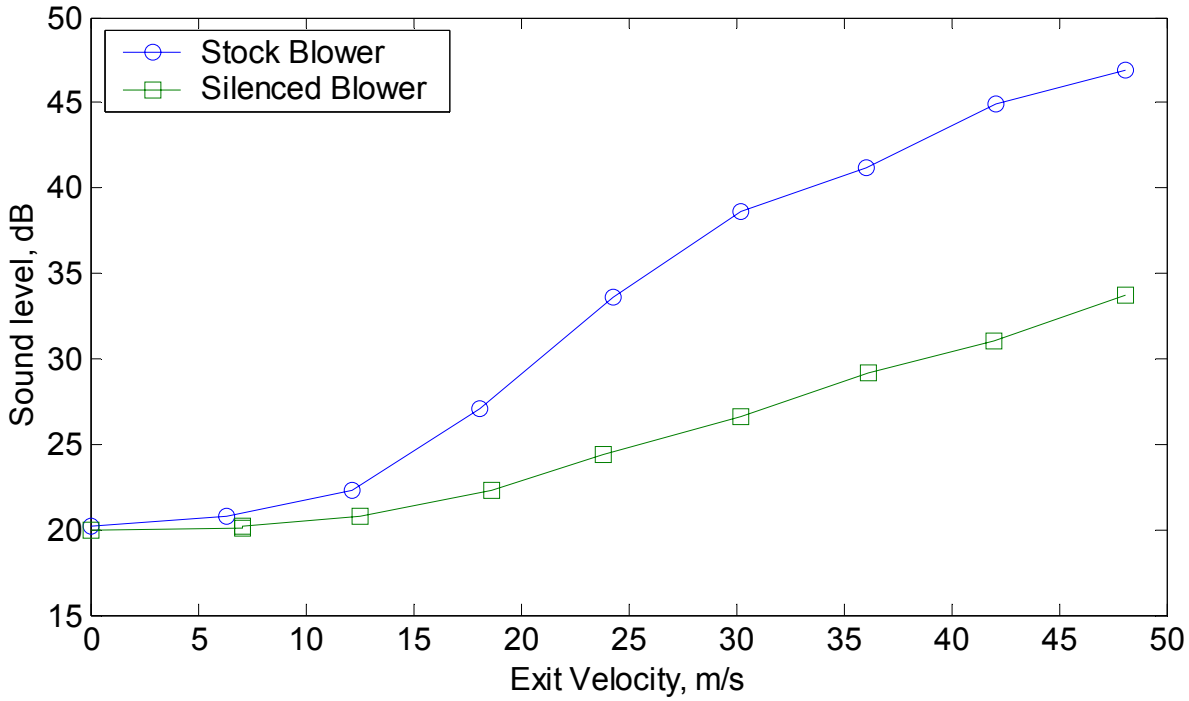

Figure 2-13 Total SPL measured 1.3m from blower nozzle at different speeds with and without exit silencer.

Figure 2-14 shows narrow band spectra measured for the two blower configurations at two different speeds. The spectra show that the silencer is most effective around 1000 Hz where the narrow band reductions are around 5 dB. At higher frequencies the silencer is less effective, providing reductions of only 1 to 2 dB above 10000 Hz.

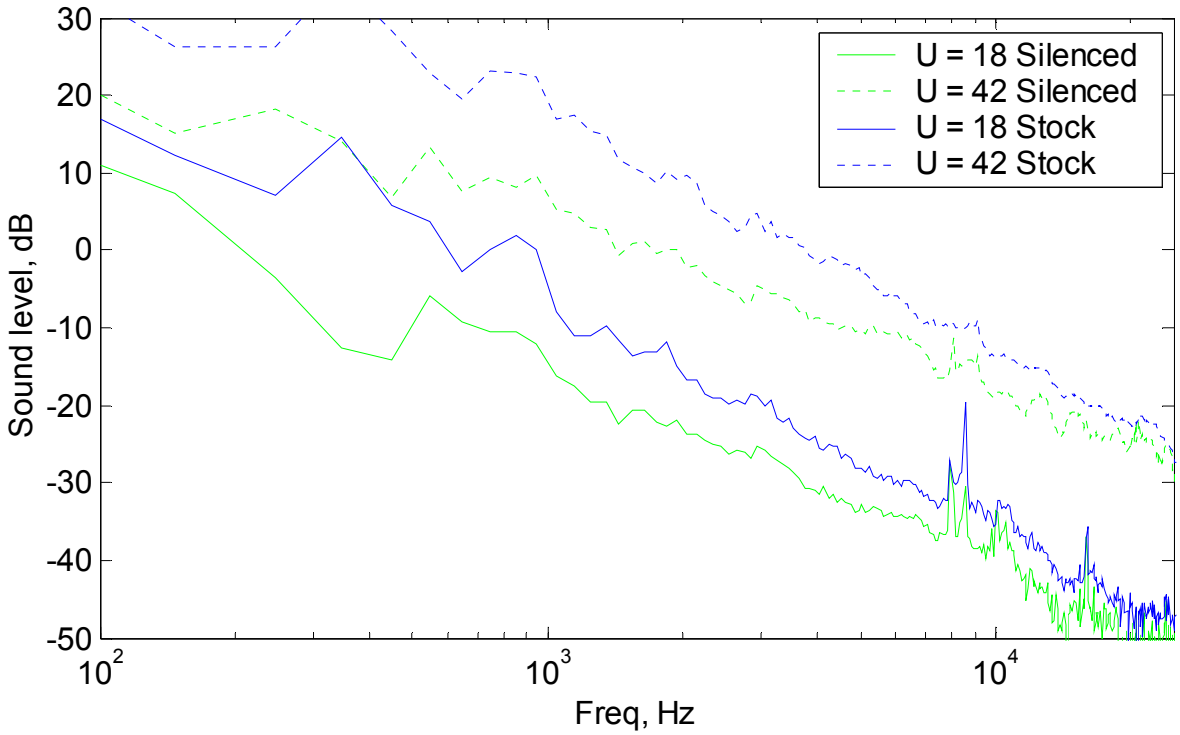

Figure 2-14 Narrow band spectra of sound measured 1.3 m from blower exit with and without exhaust silencer installed. Spectra were taken at two exit speeds 18 m/s (solid lines) and 42 m/s (dotted lines).

Figure 2-15 shows the nozzle, plate, and acoustic enclosure assembled in the preliminary configuration. The photo shows the plate mounted flush with the lower section of the nozzle, and the rounded wooden pieces around the side and upper pieces of the nozzle. Figure 2-15 also shows the section of acoustic treatment which extends over the plate near the nozzle region. This section is 200 mm above the plate, and serves to reduce the amount of noise from the jet flow near the nozzle that radiates into the larger portion of the acoustic enclosure. The acoustic enclosure had an internal width of 2058 mm. This was centered on the plate leaving a 267 mm gap between each side of the acoustic enclosure and the plate. The tips of the acoustic wedges are 381 mm downstream from the end of the plate. The front of the chamber were covered with 645 mm tall polyurethane acoustic wedges, with the sides and ceiling were covered with the same 95 mm thick egg crate style acoustic treatment that was used in the settling chamber.

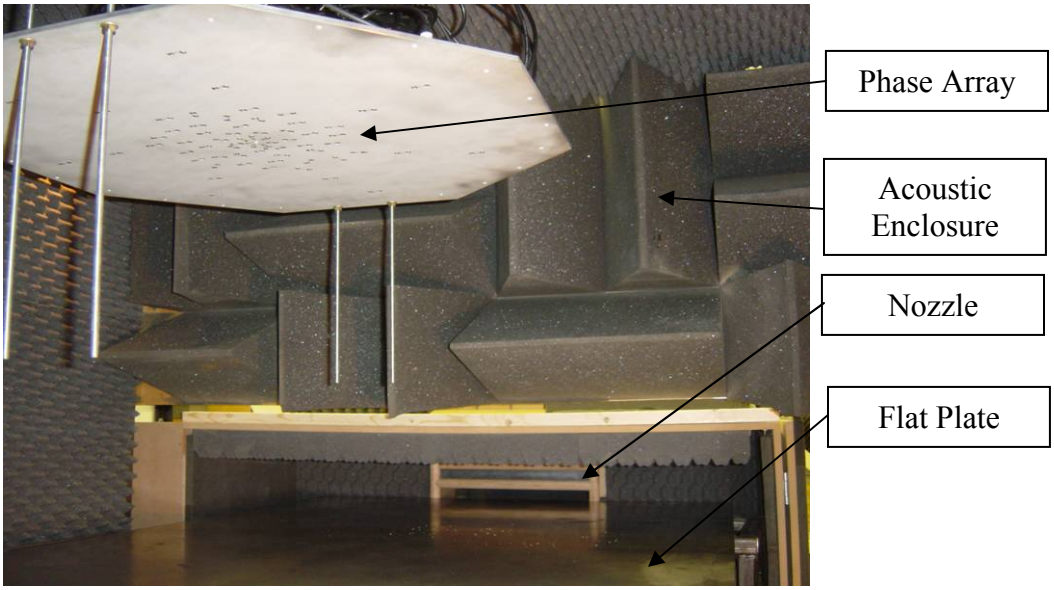

Figure 2-15 Photo of the initial wall jet configuration used to test the settling chamber and nozzle performance.

Figure 2-16 shows the mean velocity profiles measured at the nozzle exit in the preliminary wall jet configuration. The measurements were taken with the miniature Pitot-static probe attached to a computer controlled traverse. The profiles are shown normalized on the mean flow speed at the nozzle, U_0, which was determined by the pressure difference between the settling chamber and room pressure. In the preliminary configuration nozzle exit speeds of up to 60 m/s could be achieved for nozzle heights less than 38.1 mm. In the vertical profiles shown in Figure 2-16 the difference between the three nozzle heights can be seen. These profiles are also normalized on the nozzle exit speed, U_0, of 60 m/s. The boundary layer growth on the lower surface at the plate interface is unchanged with nozzle height, as expected. The upper region of the profile falls off quickly beyond the nozzle height, as the jet has not had room to grow. The horizontal profiles, measured at the nozzle mid height, show that the flow is uniform across the nozzle width to within 2%. The uniformity is also not effected by the nozzle height.

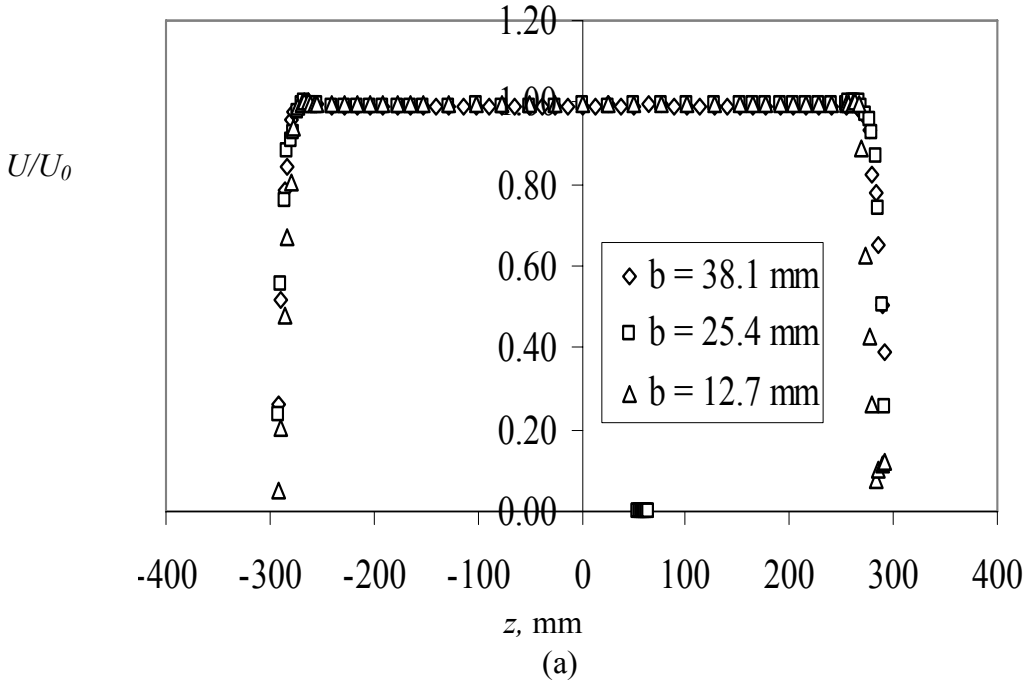

(a)

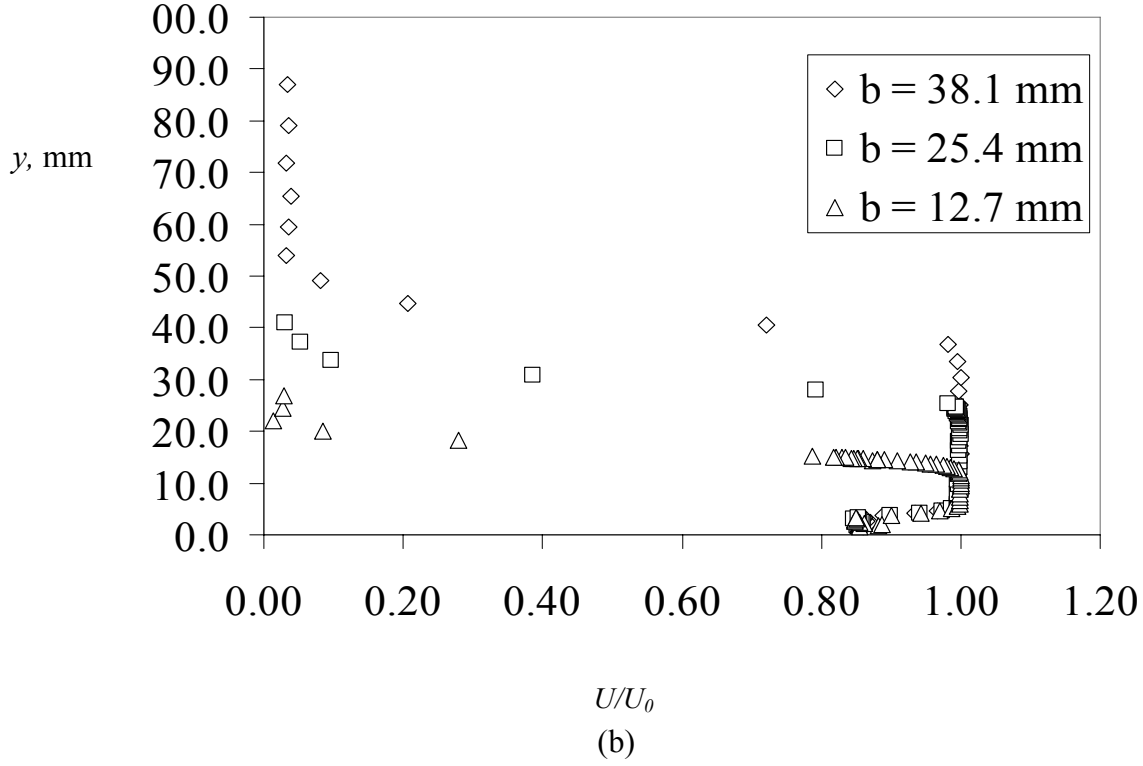

(b)

Figure 2-16 Vertical and horizontal profiles measured at the settling chamber nozzle. (a) shows profiles measured along a horizontal line at x = 38.1mm, $y = b/2$, (b) shows vertical profiles measured at x = 38.1mm, z = 0. Results are shown for 3 different nozzle heights.

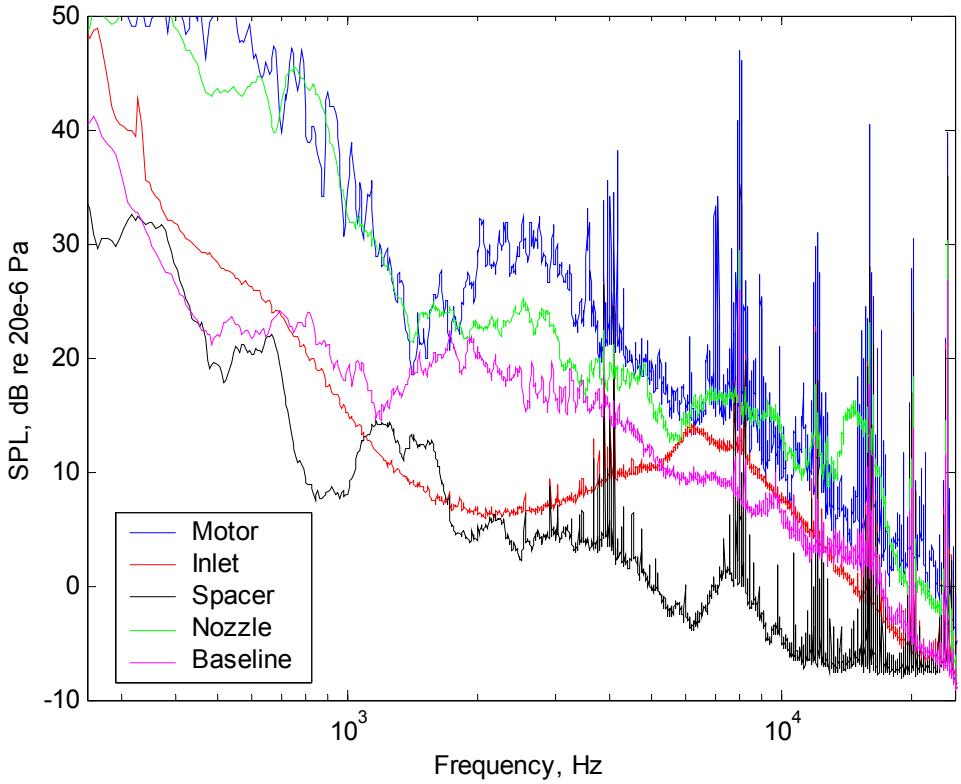

Figure 2-17 Sound spectra measured at different locations along the settling chamber. The nozzle exit speed during these runs was 54 m/s, with a motor speed of 35 Hz.

To examine the acoustic performance of the settling chamber and nozzle, sound levels were measured at 5 different locations along the aerodynamic circuit of the wall jet facility. The single Hertz bandwidth acoustic spectra from these measurements are shown in Figure 2-17. For all of these tests the motor speed was held constant at 35 Hz that generated a nozzle exit speed of 54 m/s. The spectra show that there are two separate acoustic sources in the circuit; the motor and the nozzle. The spectrum labeled motor was measured using the ⅛ inch B&K microphone in the acoustic enclosure surrounding the centrifugal fan. The microphone was located 457 mm from the blower, and 50 mm above the floor, facing the blower. This spectrum contains significant tones generated at 4000 Hz and multiples of this frequency. The red curve was measured in the chamber section connected to the blower, labeled inlet. The microphone was located 50 mm above the acoustic treatment on the floor of the section, and 50 mm downstream of the acoustic treatment on the baffle. The microphone was facing 45° above the floor, towards the upper downstream corner of the inlet section of the settling chamber. In this position flow over the microphone was minimized, so microphone self noise is negligible. In this section there is already a noticeable decrease in the broadband levels, especially below 700 Hz, and the peak tonal levels are reduced by 15 dB. The next section in the chamber is the black curve labeled spacer. Again in this section the microphone is located 50 mm from the floor and downstream side of the central acoustic baffle, facing downstream 45° from the floor. This measurement, shown by the black

spectrum in Figure 2-17, is the quietest measured. The broadband levels are lower here than in the inlet section. The flat portion of the spectrum above 10 kHz is the electrical noise floor, which has overtaken the acoustic signal in this frequency range. However, the tonal noise is not reduced from the inlet to spacer section.

The final two curves in Figure 2-17 show increased acoustic levels compared to the spectrum measured in the spacer section. The green curve, labeled nozzle, was measured in the nozzle section of the tunnel. This curve shows a 15-20 dB broadband level increase compared with the spacer section levels. This is due to the jet noise associated with the accelerated flow exiting through the nozzle onto the plate. In the nozzle section the microphone is positioned 50 mm downstream of the acoustic baffle in a location where microphone self noise will be negligible due to low flow velocities. The final pink curve labeled baseline was measured within the acoustic enclosure, at a position 2.3 m downstream of the nozzle, 940 mm above the plate, and 630 mm from the left wall of the acoustic enclosure. These levels are reduced as they are farther from the jet exit so they only have a line of sight to the lower velocity portions of the wall jet flow.

2.3.8 Flow Quality and Acoustics at Different Speeds and Conditions

Several tests were conducted to assess the range of conditions where the facility could be used for roughness noise investigations. The first test was to investigate the background noise levels in the acoustic enclosure. Figure 2-18 shows single Hertz band width acoustic spectra measure in the acoustic enclosure at several different speeds. These spectra were measured with a B&K 4090 ½ inch microphone, the microphone was located 2.3 m downstream of the nozzle, 0.94 m from the plate centerline, and 0.63 m above the plate surface. In this location the microphone's line of sight to the nozzle exit was blocked by the front wall and shelf of the acoustic enclosure. The microphone signals were also high pass filtered above 250 Hz to reduce interference from low frequency acoustic signals that are not attenuated by the foam acoustic treatment in the enclosure.

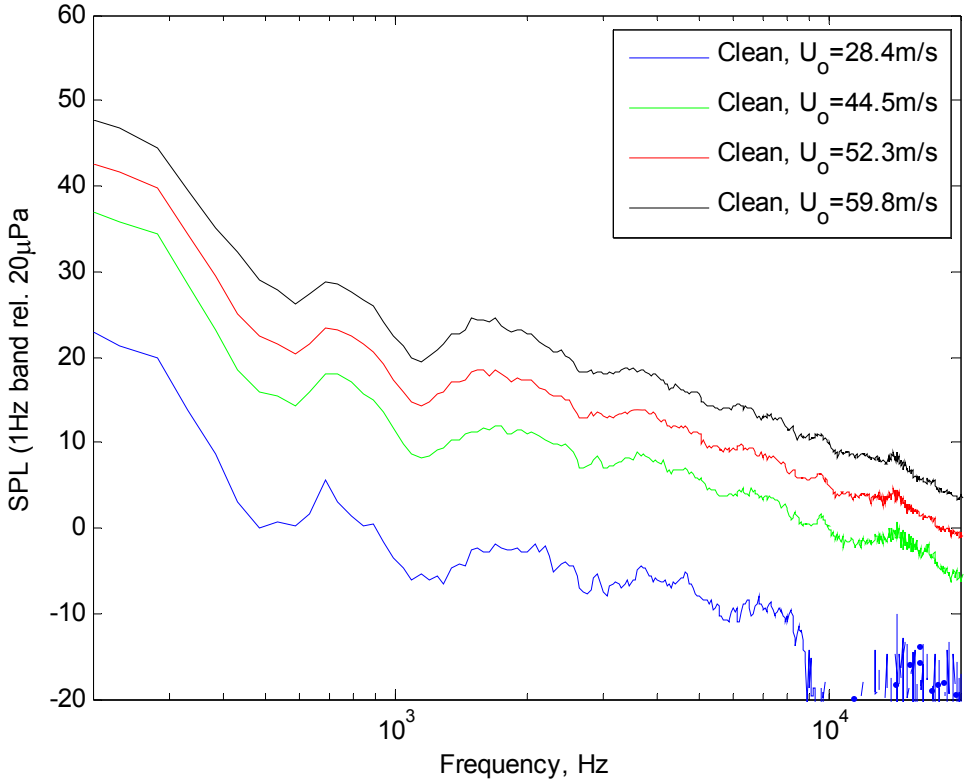

Figure 2-18 Acoustic spectra measured in the acoustic enclosure with flow of various speeds over a smooth plate.

The spectra shown in Figure 2-18 have been corrected for microphone sensitivity variation with frequency, and no flow background noise levels. They show the measured spectral levels decrease with frequency and increase with flow speed. Figure 2-19 shows the spectral levels, integrated into 1 Hz bands, normalized on nozzle height and jet exit velocity to the eighth power. The tight collapse of spectral levels when scaled on the velocity to the eighth power suggests that the background noise level is dominated by jet noise associated with the turbulent fluctuations in the wall jet flow. Because of the decay of the wall jet, the dipole noise generated by the flow over the edges of plate is dominated by the jet noise. It also suggests that the background level can not be further reduced in this facility since the background levels are controlled by the turbulent wall jet flow itself which is the flow of interest.

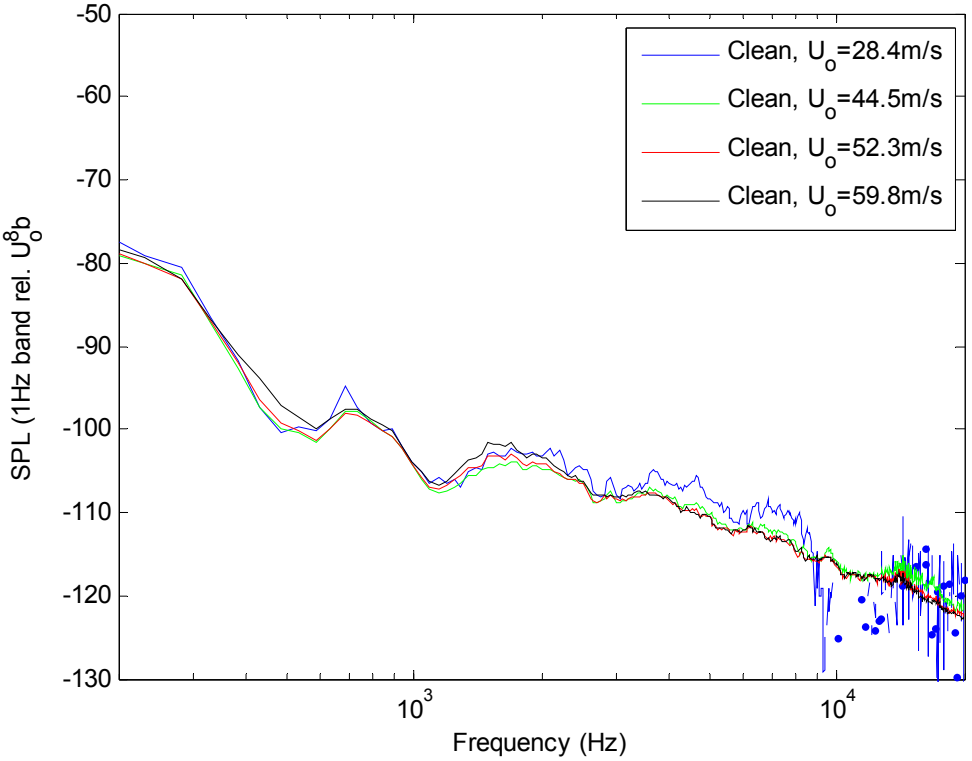

Figure 2-19 Acoustic spectra measured for flow over a smooth plate. Spectral levels are normalized on the jet exit velocity to the eighth and the nozzle height.

The results of Figure 2-18 and Figure 2-19 suggest that the acoustic properties of the facility are suitable for roughness noise research. However, the aerodynamic properties of the facility must also be well defined for measurements to be useful. One of the key features of a wall jet flow is the formation of a self-similar velocity profile. Figure 2-20 shows velocity measurements made at two different locations on the plate for three different nozzle heights, and jet exit velocities. The nozzle height was opened to 12.7, 25.4, and 38.1 mm and nozzle exit velocities were set to 59.5, 49, and 40.1 m/s respectively. This corresponds to jet Reynolds, Re_j, numbers of 47000, 77800, and 95000 respectively. Under each of these conditions vertical velocity profiles were measured using a miniature Pitot probe, with a probe diameter of 3.1 mm, at locations 953 mm and 1875 mm downstream of the nozzle exit. The results of these 6 profiles are shown in Figure 2-20. The profiles have been normalized using local maximum velocity, U_e, measured at each condition and the height above the plate were the velocity falls to half its maximum value in the shear layer, $y_{1/2}$. These two scaling parameters provide an excellent collapse of the profiles as shown in Figure 2-20. The solid line shown in the figure is the normalized profile shape presented by Narasimha (1973) and confirmed by others. (Wygnanski, *et al*., 1992) (Launder and Rodi, 1981)

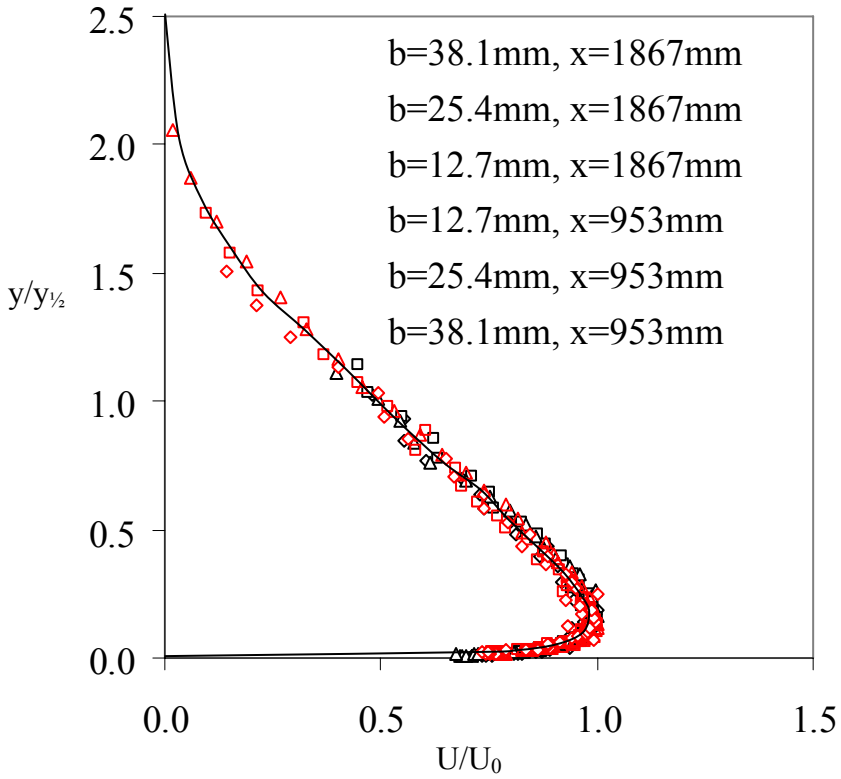

Figure 2-20 Vertical velocity profiles measured along the plate. Profiles have been normalized on the local maximum velocity, and height to half decay. The solid curve is the profile shape predicted by Narasimha (1973) for a self similar wall jet flow.

Another important flow feature is the horizontal uniformity across the plate. Figure 2-21 shows horizontal velocity profiles measured across the flow at three different streamwise locations on the plate. For all three cases the nozzle height was set at 25.4 mm, and the jet exit velocity was 49 m/s. The profiles were measured at a height above the plate corresponding to the height where the vertical velocity profile reached a maximum. These heights were 12.7 mm at x/b = 0, 12.5 mm at x/b = 37.5, and 22.1mm at x/b = 75. The figure shows that at the nozzle exit the flow speed is uniform across the 508 mm width of the nozzle exit. In this region flow uniformity is better than 2% relative to the mean flow speed. When measured 952.2 mm, x/b = 37.5, downstream from the nozzle, the region of uniform flow is significantly reduced. The two-dimensional flow region has reduced in width to 254 mm along the centerline of the flow. The maximum flow velocity has also decayed to about 60% of its initial value. When the downstream distance is doubled, x/b = 75, the flow speed is further reduced to 45% of its value at the nozzle exit. At this location the two-dimensional region of the wall jet is nearly gone. The three-dimensional decay of the wall jet presents a significant limitation on the usefulness of this flow. The scaling model of Narasimha (1973) works for a two-dimensional wall jet, the decay behavior and self similarity do not hold once this two dimensional region is gone. Furthermore, a three-dimensional mean flow field would

further complicate the basic modeling of roughness noise that the facility needed to be used for.

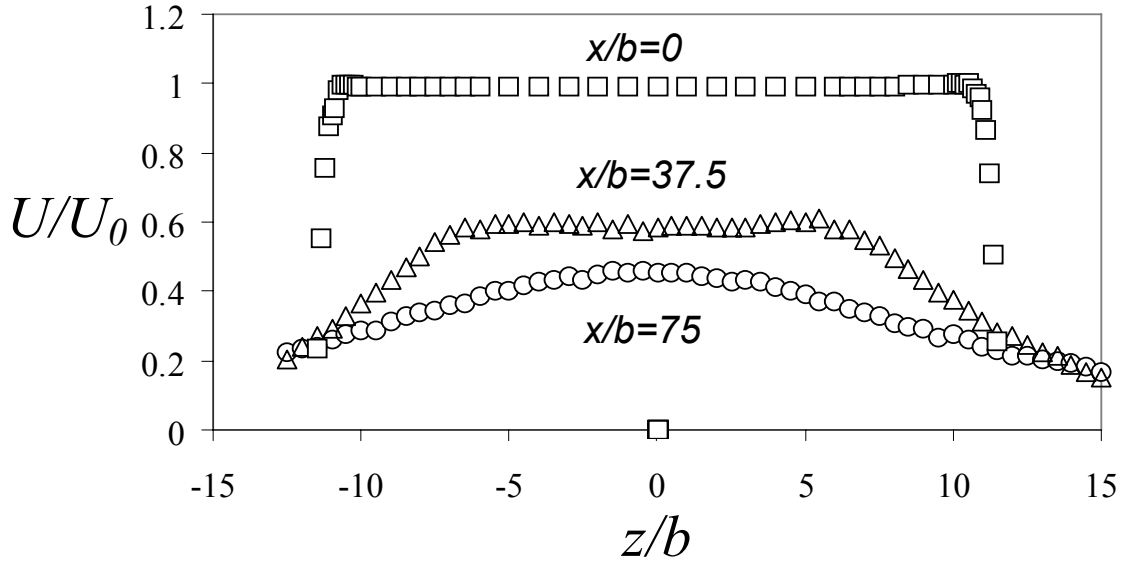

Figure 2-21 Horizontal velocity profiles measured at three streamwise locations for a wall jet with an exit velocity of 50 m/s and a nozzle height of 25.4 mm. The profiles were measured at a height above the plate corresponding to the height for maximum velocity for each streamwise location.

2.3.9 Detection of Roughness noise

Sound generated by the sharp edge around a roughness patch could produce a significant acoustic contamination. To reduce and quantify this effect a repeatable procedure was developed for the installation of roughness patches and the treatment of all edges. The patches were attached using a combination of 50mm wide double-sided tape, and 50mm wide aluminum foil tape, both with a nominal thickness of 0.1mm. Three evenly spaced strips of double sided tape were run along the long direction of each roughness patch. The patch was then attached to the plate surface beginning at the front center of the patch and working to the back corners. As the patch was pressed into position care was taken to insure that no bubbles, folds, or loose sections of sandpaper resulted. After the patch was secured, the foil tape was placed around the perimeter of the patch. This served two purposes, first it helped secure the edges of the roughness patch to the plate to prevent the edges from flapping in the flow, and second it provided a small ramp to decrease the sharpness of the step. The foil tape was placed so that about 25mm of the tape was on the plate, and 25mm was attached to the surface of the roughness. A flat piece of plastic and a dry sponge was used to flatten any air bubbles or folds in the tape along the plate surface. A sponge was then used to press the foil tape onto the border of the roughness patch. This forced the tape to conform to the surface, which secured both the tape and sand paper in place. The resulting edge is shown in Figure 2-22, and was highly repeatable.

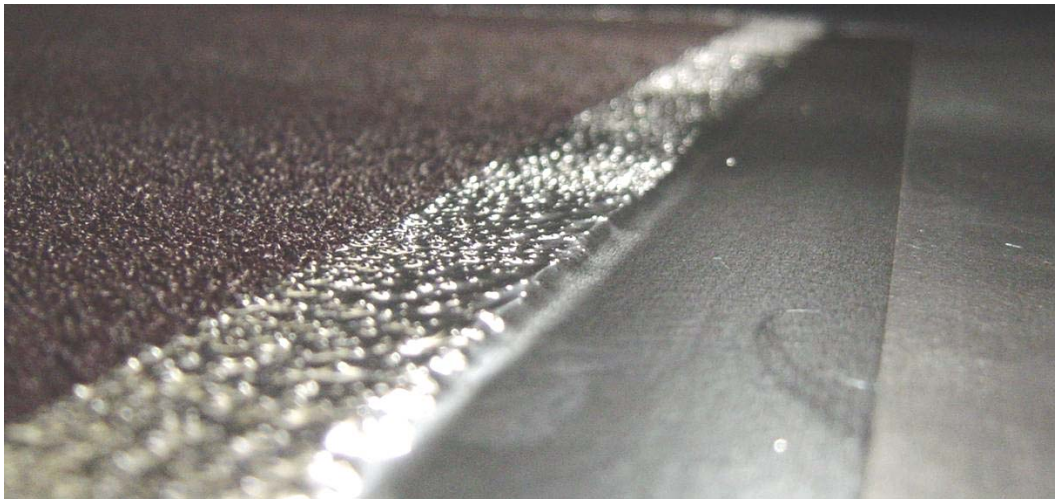

Figure 2-22 Photograph showing the edge of a patch of 36 grit roughness attached to the plate surface with aluminum foil tape. The tape has been smoothed on the surface, and pressed into the sandpaper surface to prevent the tape or paper from peeling off and flapping.

The effects of the step at the edge of the roughness patch on the acoustic field were tested in two configurations. To test the effect of the step at the edge of the patch a patch of sand paper was attached to the plate using the technique described earlier, but the patch was placed with the roughness facing down. This resulted in the same step of tape and sandpaper thicknesses as was present with the patches installed normally, but with a smooth surface over the patch instead of the rough surface. The test was conducted in the preliminary facility configuration using an industrial sanding belt of 80 grit roughness (mean roughness height 0.19mm). The belt had a woven fabric backing so the total thickness of the attached belt and roughness elements was about 1mm. The nozzle height, *b*, was set to 25.4 mm and the nozzle exit speed was held constant at 60 m/s. The roughness patch covered an area 940mm wide and 1520mm long, starting at x = 930mm from the nozzle exit. Far field measurements were taken with nothing on the surface, with the sand paper attached, inverted, and covered in Mylar. Figure 2-23 shows the acoustic spectra measured in these four conditions. The spectral levels shown are single Hertz bandwidth levels that have been averaged over ⅛ octave band intervals. This figure shows the additional noise produced when the roughness is added. From 250Hz (the lowest frequency measured) to 2000 Hz the curves are indistinguishable, but above 3000 Hz the spectral levels measured with the roughness are significantly higher than the smooth wall levels, with the largest difference equivalent to 12dB occurring around 7000 Hz.

In Figure 2-23, the blue curve marked with triangles, labeled inverted, shows the spectrum measured when the roughness patch was installed upside down. (Note that, at frequencies below those shown on the graph, all the measured spectra are equal). The spectrum for the inverted belt shows a much smaller increase, of 1 to 2 dB over the smooth wall levels, above 3kHz. However the sanding belt had a heavy fabric backing, which could be considered a rough surface. To eliminate these effects a smooth sheet of 0.254mm thick Mylar plastic film was taped to the back surface of the roughness patch. The Mylar was attached to the back of the sandpaper sheet using the same methods used to attach the sandpaper to the plate surface. An acoustic spectrum was measured under

the same flow conditions for this surface treatment. The results of this measurement are shown in Figure 2-23 as a green curve marked with circles. This spectrum, which is identical to the smooth wall spectrum, shows that the spectral increase seen with the inverted sand paper sheet is entirely from the fabric pattern on the back of the belt, and not from the edges of the roughness patch.

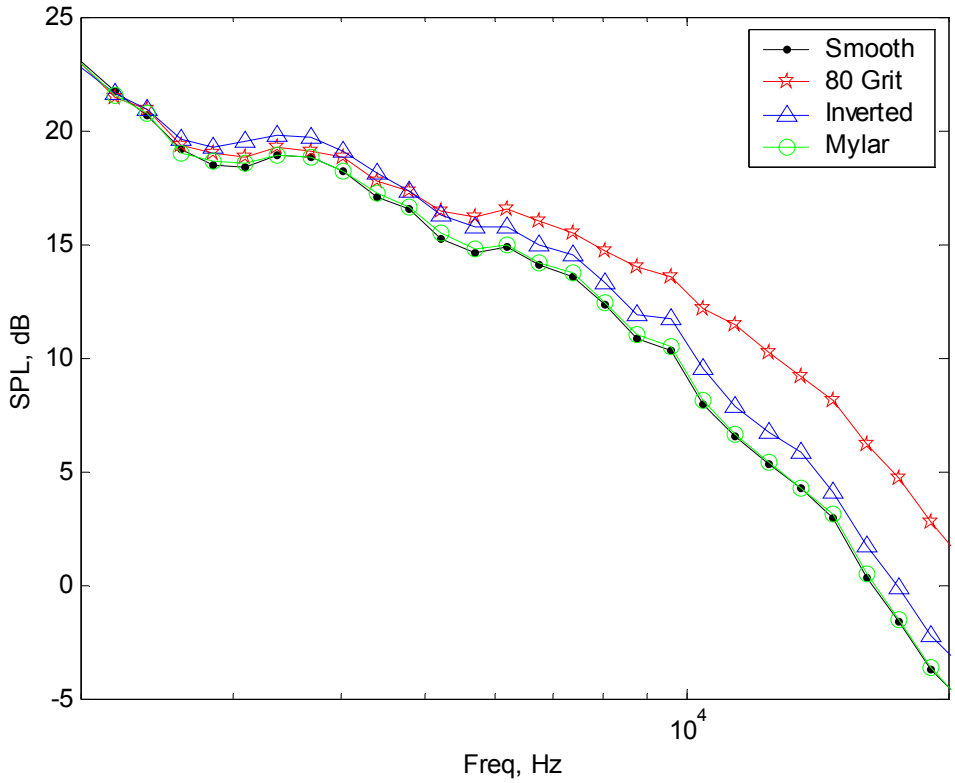

Figure 2-23 Acoustic spectra measured from the wall jet flow for 4 different surface conditions. Smooth is the smooth plate, 80 grit is with an 80 grit sanding belt attached, inverted is with the sanding belt attached with the sand down, and Mylar is with a sheet of Mylar covering the fabric backing of the inverted sanding belt. Levels are single Hz bandwidth shown in ⅛ octave band averages.

2.3.10 Phased Array Measurements

Preliminary tests were conducted using a 63 microphone phased array to measure the sound level generated by flow over a 813 mm wide, 1625.6 mm long patch of Lego blocks. The Lego's surface consists of a rectangular array of cylinders which are 3 mm tall with a 4.8 mm diameter and 7.9 mm spacing. The flow speed at the front of the roughness patch was 45 m/s, with a boundary layer thickness of 25.4 mm. The array used for preliminary testing contains 63 Panasonic Electret microphones arranged in a single spiral arm. A logarithmic spacing pattern is used which gives overall array performance similar to that of a multi-arm spiral array. To analyze the microphone data, a standard beam forming algorithm was used with no deconvolution scheme. This leaves some data relics (See Figure 2-24) in the beam formed maps resulting from spatial aliasing due to the array design, but to evaluate the capability of a phased array to measure roughness noise this configuration will suffice.

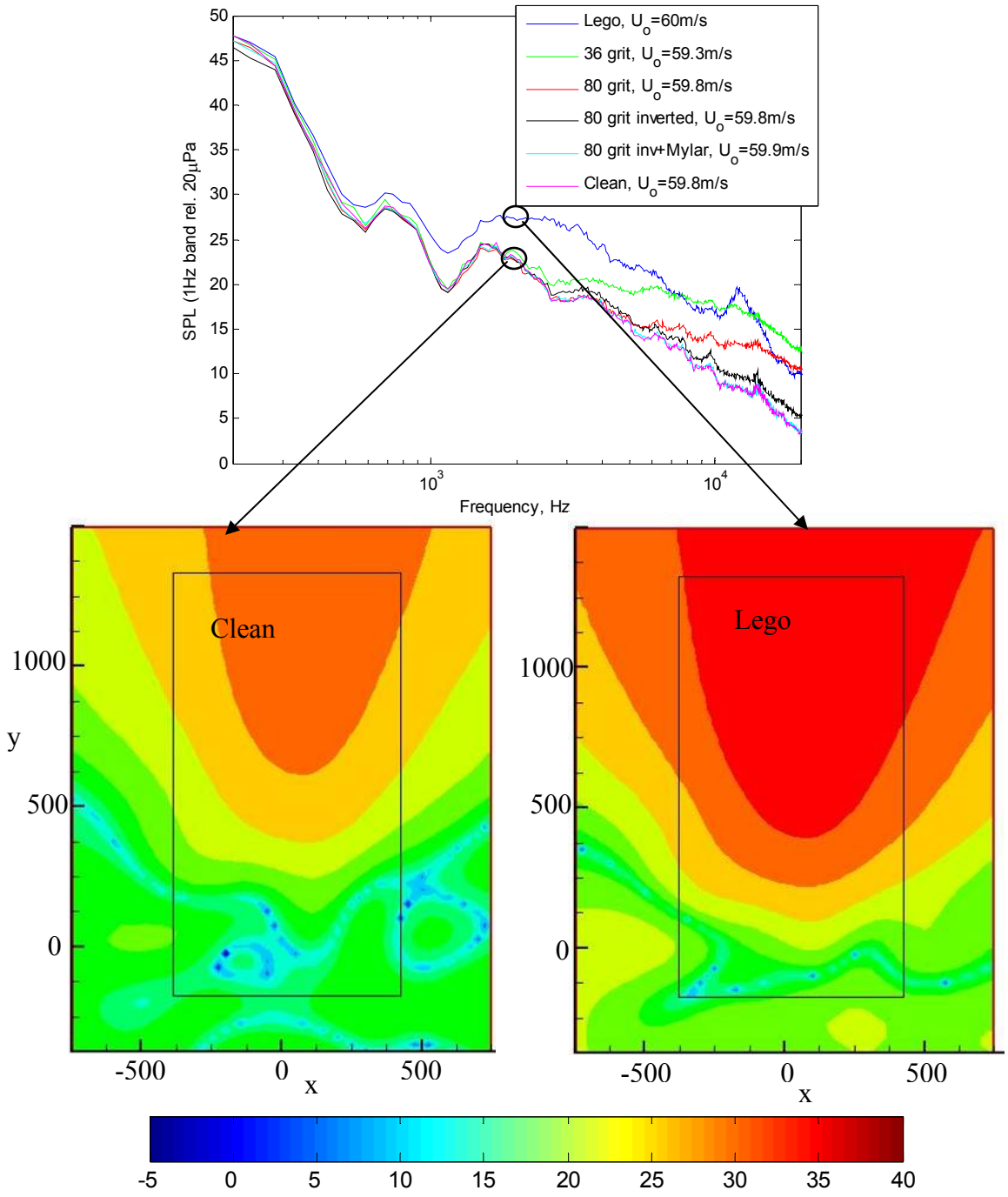

Figure 2-24 Beam formed maps of sound pressure levels measured by the 63 microphone array at 2000 Hz. The contour plot on the left was taken over the clean plate; the plot on the right was with a patch of Lego roughness on the plate in the rectangle shown. The contour levels range from -5 to 40 dB, axis are distances in mm. Both measurements were taken for a nozzle exit flow speed of 60 m/s, with flow from top to bottom of the contour plots. The upper plot shows single microphone sound levels measured for various flows, with the two corresponding conditions circled.

As can be seen by the beam formed maps in Figure 2-24 the array does a poor job of discerning the sound generated from the roughness patch. These measurements were made with the array located 914 mm above the plate centered at the origin of the maps

shown in the figure. The maps are the result of averaging the source distribution from 200 records of data sampled at 52000 Hz for 0.16 seconds. The sound levels detected over the roughness patch are higher; however the array does a poor job of localizing the source to the patch of roughness. The plot above the maps shows single microphone data measured for several surface conditions. The blue curve is for the Lego roughness, while the pink curve is for the smooth plate. This data shows that the Lego roughness was about 5 dB louder than the clean plate at the frequency shown in the maps. The beam formed maps seem to indicate that the nozzle region upstream of the roughness patch is louder in addition to the area over the roughness, but there was no change made to the facility other than the addition of the roughness patch. So while the microphone array can detect a change in the sound level from the roughness patch it does a poor job of localizing the new source.

This can be explained by one of the limitations on the use of phased arrays. At the time of this study all phase array beam-forming techniques are based on a monopole radiation pattern for the source region. This assumption works well in many applications, even when the source is not truly a monopole, because the array can generally be placed to look directly at the primary radiation axis of a multi-pole source such as a dipole. However, with roughness noise, the expected acoustic source is a flow-aligned dipole. In order to see the strongest radiation of dipole noise the array would need to be place either directly upstream or downstream of the roughness fetch, which would require the array to be in the flow region. If the array is placed above the fetch out of the flow it would be looking at the weak side of the dipole and only be able to poorly determine the source strength. From another perspective a dipole can be thought of as a pair of monopoles radiating out of phase. So when viewed from directly overhead the array would see an area filled with monopole sources of equal strength but opposite phases, which would result in a monopole strength of zero.

Chapter 3 Facility and Instrumentation

The tests in the preliminary wall jet showed that this configuration could be a viable test setup for measuring roughness noise, but that the facility as tested would not be suitable. The facility needed a wider nozzle to maintain a large region of two-dimensional flow. The acoustic enclosure also needed further improvement. This chapter presents the facility and instrumentation used throughout the remainder of this report. First, the modifications that were made are described then measurements that compare the two configurations are presented. Finally, the instrumentation used for acoustic and aerodynamic measurements are presented at the end of the chapter.

3.1 Final Facility

3.1.1 Settling Chamber Modifications

The nozzle section underwent several changes to increase the nozzle width, and improve the aerodynamic performance of the nozzle. In the original nozzle section the flow passed from a 1219.2 by 1282.7 mm rectangular cross section through two two-dimensional nozzle sections to reduce to the exit area needed for the wall jet. These contractions were described in Sections 2.3.1 and 2.3.3, and resulted in a well-behaved flow. For the larger jet exit width only one contraction would be needed. The width of the jet exit would be the same as the internal width of the settling chamber, 1219.2 mm, but the height would still be reduced from 1282.7 mm (the height of the settling chamber) to a variable exit height from 12.7 mm to 76.2 mm of the nozzle. The tests run in the preliminary configuration also suggested that acoustic treatment in the nozzle section of the settling chamber were not required, since the noise generated by the blower was nearly eliminated in the inlet and spacer sections and noise from the nozzle itself dominated the sound levels in the nozzle section. This allowed more space in the nozzle section to be used to create a gradual contraction from the settling chamber dimensions down to the nozzle exit size.

The new nozzle and contraction were designed using the method proposed by Fang *et al.* (2001) for a contraction design in a wind tunnel. Fang *et al.* (2001) found the most effective contraction shape was defined by a cubic curve. The general curve he proposes for the contraction shape is given by Equation 3.1.

$$\begin{aligned} y &= (h_1 - h_2)\left[1 - \frac{1}{X_m{}^2}\left(\frac{x}{L}\right)^3\right] + h_2 \qquad for \;\; x < X_m \\ y &= \frac{(h_1 - h_2)}{(1 - X_m)^2}\left(1 - \frac{x}{L}\right)^3 + h_2 \qquad for \;\; x > X_m \end{aligned} \tag{3.1}$$

In this equation, x and y are the coordinates of the final contraction surface with x in the mean flow direction, and y normal to this direction. The chamber half height is given by h_1, the nozzle half height by h_2, and L is the length of the contraction. X_m is an adjustable parameter designating the match point, which sets the inflection point of the contraction curve as shown in Figure 3-1.

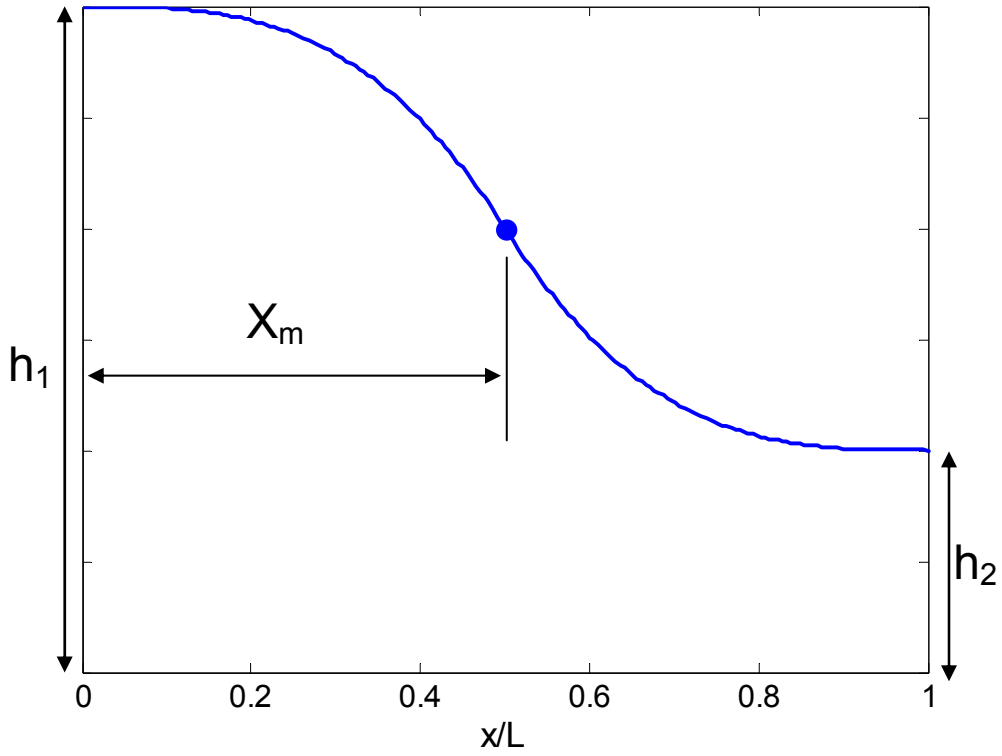

Figure 3-1 Schematic of generic contraction profile based on method of Fang *et al.* (2001)

In the settling chamber the length of the contraction, *L*, was limited to 610 mm to fit in the chamber section, the chamber half height is 752 mm, and nozzle height was set to 76.2 mm, for the largest nozzle height. To select a match point location a number of different locations were considered, and compared with the original nozzle configuration. The original nozzle behaved well, acoustically and aerodynamically, so the new nozzle was selected to nearly match the original nozzle shape in the 152.4 mm closest to the exit. Figure 3-2 shows three contraction shapes that were considered, with the central red curve being the design selected with a match point value of 10. The inset plot shows the three nozzle designs in the region of the original nozzle. The design with a match point of 10 does a good job of following the elliptical nozzle used in the preliminary configuration.

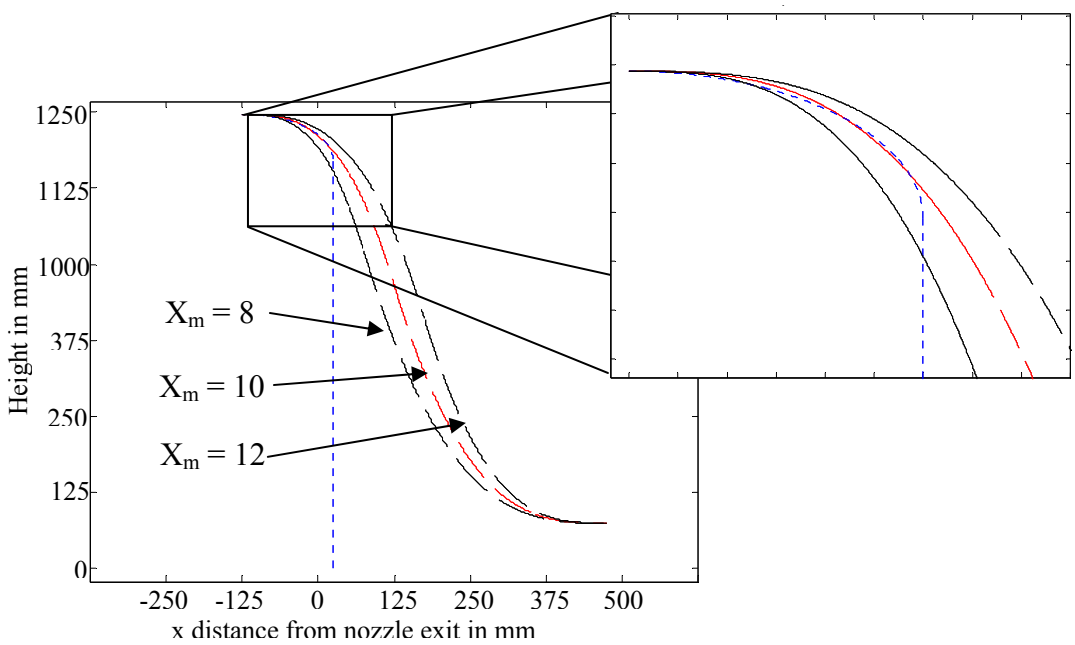

Figure 3-2 Comparison of three possible contraction profiles for modified nozzle chamber section. The blue dotted line is the nozzle shape used in the original configuration. The red dashed curved is the design selected for the final nozzle section.

The upper nozzle half needed to be movable to allow adjustment of the jet exit height, so a continuous contraction from the roof of the settling chamber could not be used. The upper nozzle shape was therefore selected to remain the same as the original design with an elliptical profile with a 3:1 aspect ratio. After passing through the throat of the nozzle the upper section then assumed a circular profile to eliminate the sharp edge that was present on the original nozzle design. Figure 3-3 shows the final combined nozzle shapes for the upper and lower halves of the jet exit. The nozzle itself is shown in pink. Since the lower nozzle shape was selected to match the original elliptical nozzle the mating between the upper and lower nozzle halves results in a nearly symmetric internal nozzle. The upper nozzle has a partial contraction shown in Figure 3-3. This is a circular 154 mm radius fillet used to reduce scattering from the end of the upper nozzle.

The new nozzle was built using the same materials and methods as the original nozzle. The upper and lower nozzle sections (pink in Figure 3-3) were milled from PVC blocks. These had to be made out of two blocks that were joined after machining to accommodate the size of the milling machine. The downstream side of the lower nozzle was machined with a 25.4 mm long 9.6 mm deep step for mounting the flat plate. When the plate was mounted on this step, steel shim stock was used to achieve a flush edge between the step and plate surface. This restricted the misalignment between the plate and nozzle exit to less than 0.125 mm. A drywall filling compound was also used along the junction between the nozzle and plate to smooth any step that remained after shimming, and fill any gaps left between the nozzle and plate. The extended contraction region on the lower half of the nozzle was shaped using 4 MDF panels, which supported a sheet of 6.35 mm thick PVC (pink curve in Figure 3-3). The upper nozzle was mounted to an MDF box that was held in position by two guided wheel tracks. The tracks allowed the upper nozzle to only move vertically. This box was then held in place using two

adjustable screws (shown in blue in Figure 3-3). This method allows the upper nozzle position to be easily changed by turning these screws, which can then be locked into place once the nozzle is in position.

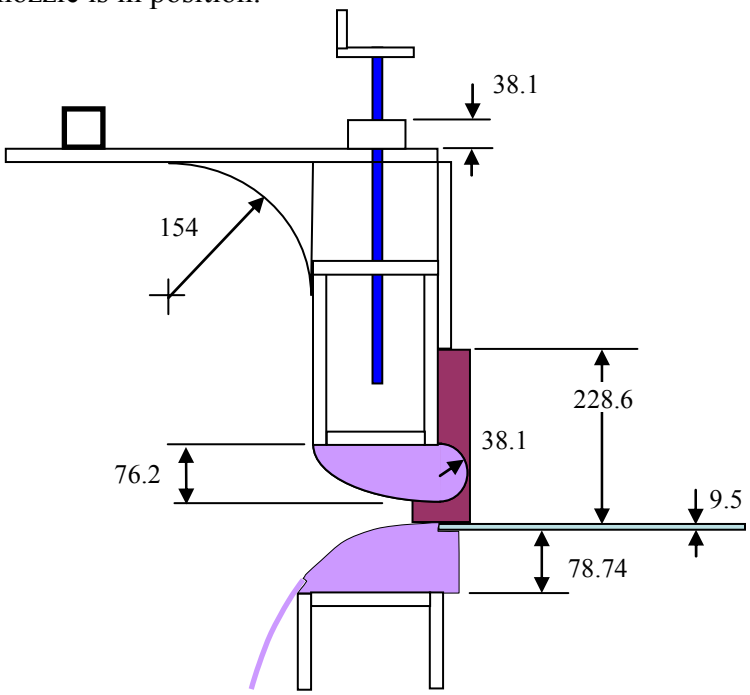

Figure 3-3 Side view drawing of the final nozzle section design. The nozzle itself is shown in pink, along with the beginning of the extended contraction that ends at the bottom floor of the settling chamber. The upper nozzle is adjustable through a screw system shown in blue, and the purple is the round side piece to reduce edge noise.

Figure 3-4 through Figure 3-7 show drawings of the final configuration of each of the settling chamber components. Each component is shown in four views; top external, side external, top internal, and side internal. The external view shows configuration of the MDF sheets, shown in white, and the steel reinforcement, shown in light blue. The internal views show the layout of the acoustic treatment and nozzle components along the settling chamber. Foam was attached to all the internal surfaces of the settling chamber. For clarity only foam which appears in the figures in profile is shown in gray. Foam on surfaces which are parallel to the view is not shown. The nozzle components are shown in pink and the flow inlet is shown in green.

The inlet and spacer sections, shown in Figure 3-4 and Figure 3-5 respectively, received only minor modifications from the preliminary configuration. This included the addition of foam wedges around the baffles connected to the sidewalls to reduce flow separation around the baffles. The wedges were 391 mm long and 279 mm wide and made of smooth acoustic polyurethane foam. These wedges are shown in gray in the top view internal drawings, and shown by a dashed outline in side view drawings for clarity. The other modification was the addition of a fiberglass pillow shown in Figure 3-4 in yellow. This was added after preliminary aerodynamic measurements revealed flow unsteadiness in the nozzle exit. The pillow, made of 100 mm of fiberglass insulation sandwiched between a wire mesh, reduced this problem by acting as a high loss filter.

Figure 3-6 shows the nozzle section in its final configuration. The lower transition from the floor of the settling chamber to the lower nozzle can be seen in its entirety. Another change that can be seen between the final and preliminary configuration of the nozzle section, see Figure 2-9 for comparison of the preliminary configuration, is the removal of an acoustic baffle in the nozzle section. Acoustic measurements taken throughout the settling chamber, shown in Figure 2-17, showed the broadband noise from the blower was low enough in the spacer section that jet noise from the nozzle dominated in the acoustics in the nozzle section. By removing the baffle in the nozzle section, the flow could be better conditioned with a longer ramp with no affect on the acoustics at the nozzle.

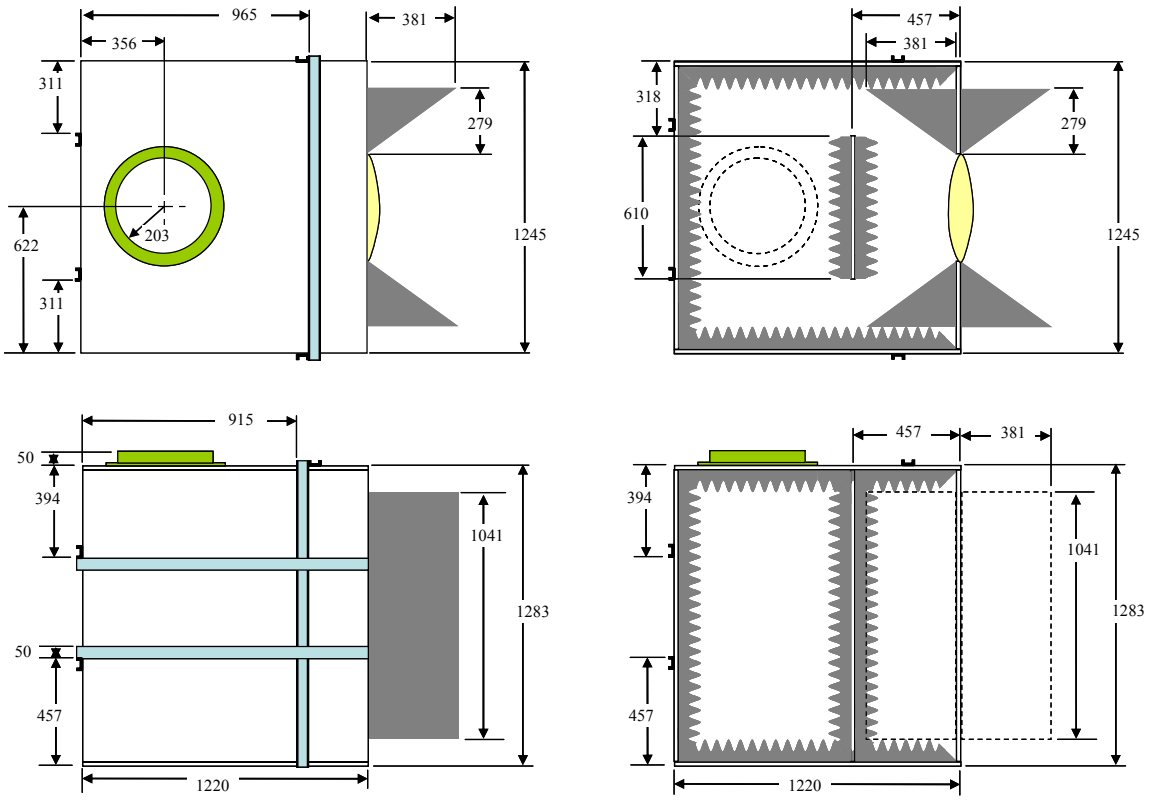

Figure 3-4 Side and Top view drawings of the final configuration of the inlet section of the settling chamber. Piece made of 19 mm thick MDF panels are shown in white, acoustic foam is shown in gray, steel reinforcement bars are shown blue, the flow inlet is shown in green, and the fiber glass pillow is shown in yellow.

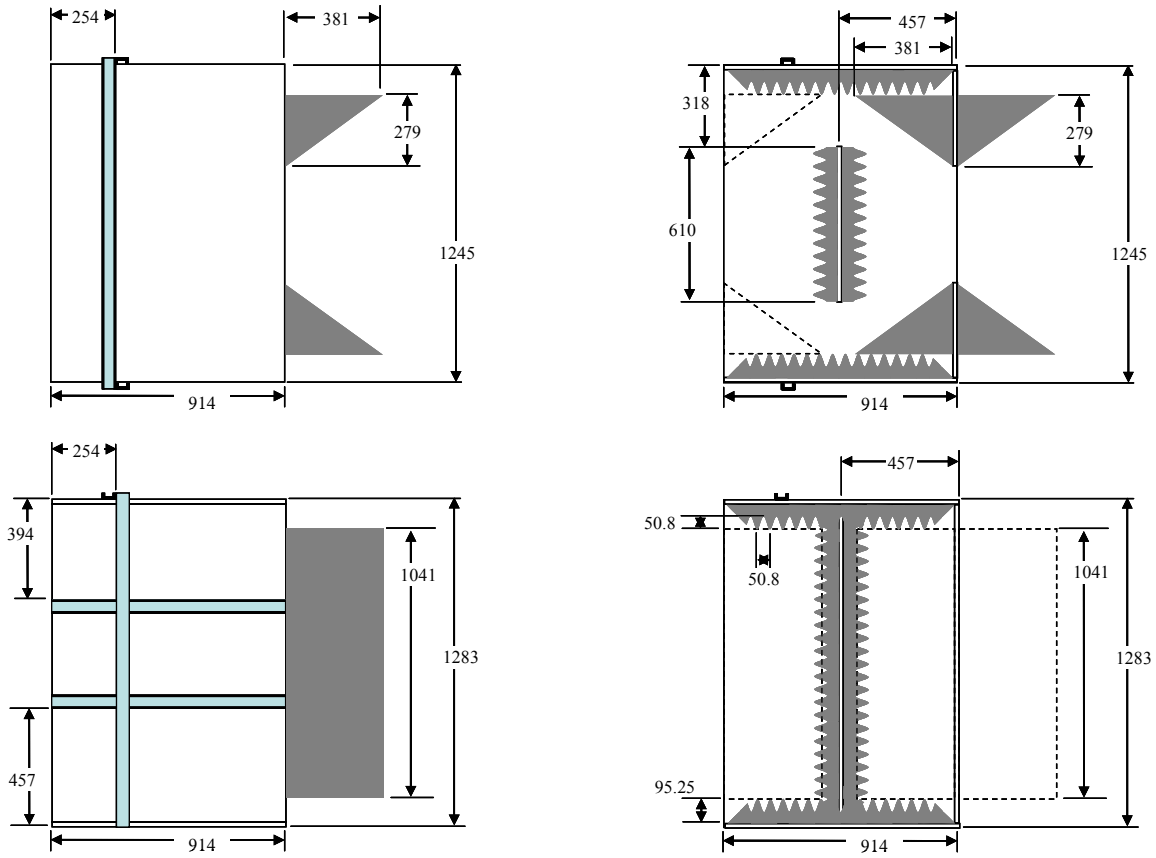

Figure 3-5 Side and Top view drawings of the final configuration of the spacer section of the settling chamber. Piece made of 19 mm thick MDF panels are shown in white, acoustic foam is shown in gray, and steel reinforcement bars are shown blue.

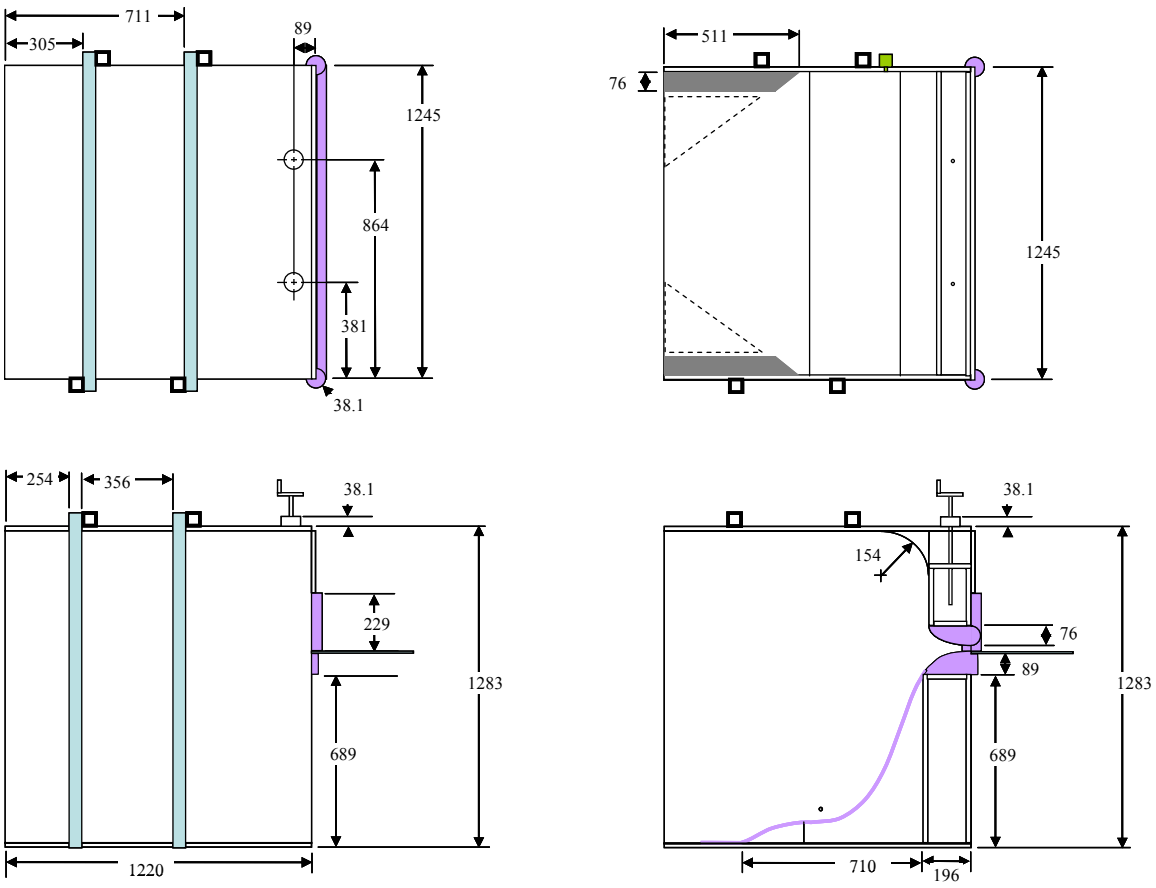

Figure 3-6 Side and Top view drawings of the final configuration of the spacer section of the settling chamber. Piece made of 19 mm thick MDF panels are shown in white, acoustic foam is shown in gray, nozzle components are shown in pink, and steel reinforcement bars are shown blue.

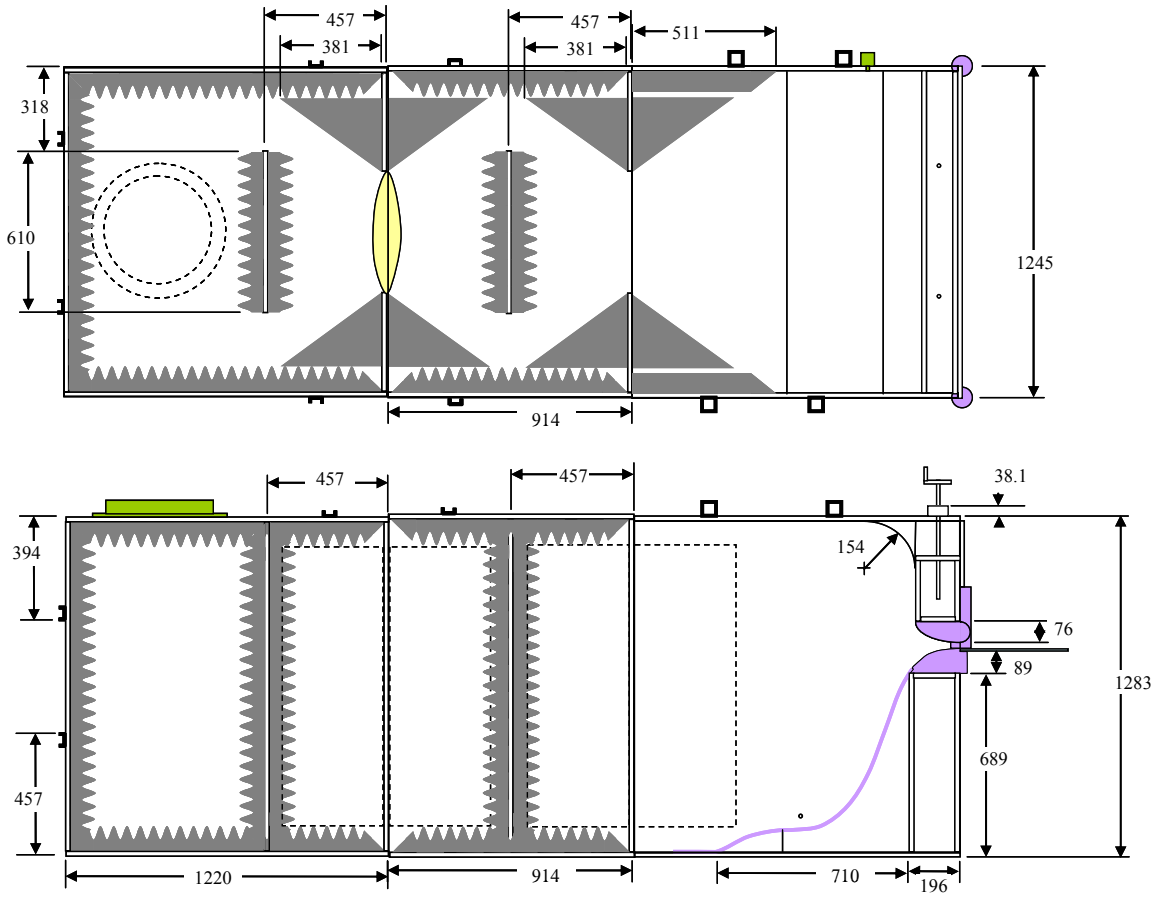

Figure 3-7 Top and side view drawings of the final settling chamber configuration. Drawings show the internal layout of the settling chamber including the placement of acoustic foam, shown in gray.

3.1.2 Final Wall Jet Configuration Calibration

A number of aerodynamic measurements were taken by Smith (2007) to characterize the flow behavior of the final wall jet configuration. Measurements were taken near the nozzle exit and at several locations along the plate. These measurements confirmed the final wall jet configuration maintained a large two-dimensional flow region.

During testing of the new nozzle a problem was uncovered resulting from its manufacture. Figure 3-8 (a) shows three vertical velocity profiles measured 25.4 mm downstream of the nozzle exit. The profile measured at the nozzle centerline shows a velocity deficit at the top of the jet when compared with the profiles measured 305 mm to the side. Oil flow visualization was used to investigate the cause of this non-uniformity. The photo in Figure 3-8 (b) shows that there is a separation bubble, circled in yellow, on the surface of the upper nozzle at the tunnel centerline. The separation bubble is the result of the joint in the two halves of the upper nozzle that had to be joined together to form the upper nozzle. Air leaking through this gap caused the flow to separate earlier here than elsewhere along the nozzle span. To eliminate the separation bubble a piece of 0.1mm thick aluminum tape was placed along the centerline of the nozzle and run back into the settling chamber, fully covering the gap in the nozzle.

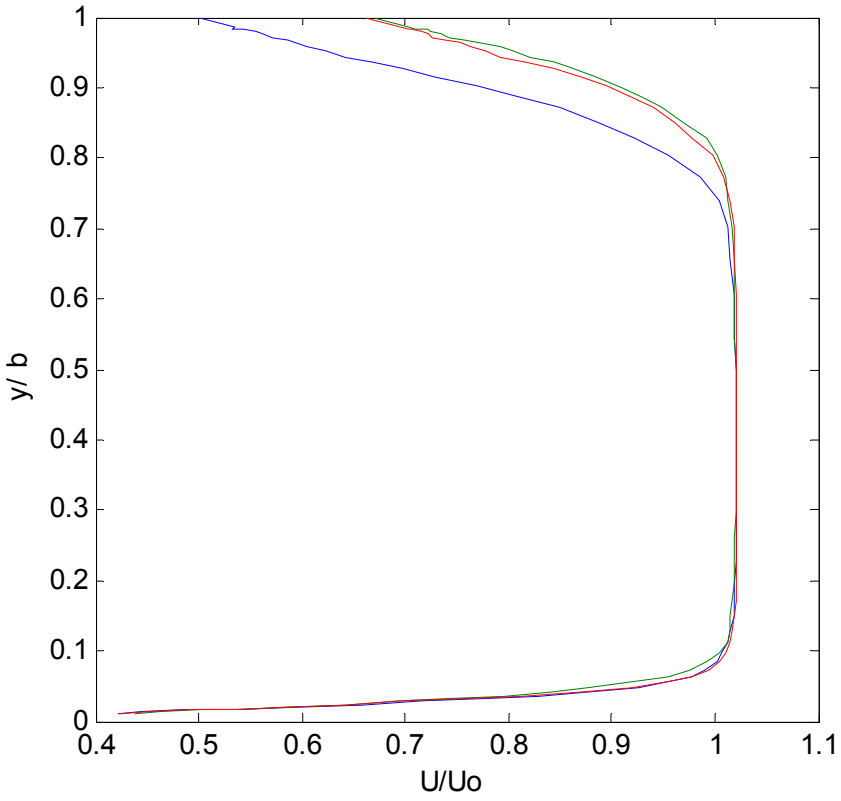

(a)

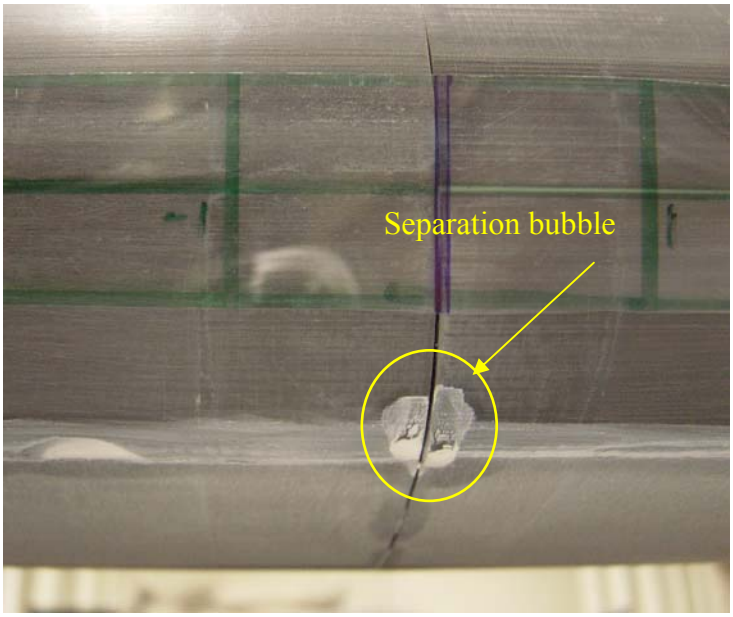

(b)

Figure 3-8 (a) Vertical velocity profiles measured 38.1 mm downstream of the nozzle exit at three spanwise locations, on center, and ±305 mm. (b) Photo of oil flow visualization on the center of the nozzle. This shows a separation bubble as a result of the joint between the two nozzle halves.

Figure 3-9 shows three horizontal velocity profiles measured with the nozzle height set to 12.7 mm and the jet exit speed fixed at 30 m/s. The blue profile, taken 38.1 mm downstream of the nozzle exit, shows the flow uniformity at the nozzle exit is better than 2% over the width of the exit that was measured. This also confirms that the separation problem seen in earlier measurements near the nozzle was fixed by taping over the junction in the nozzle.

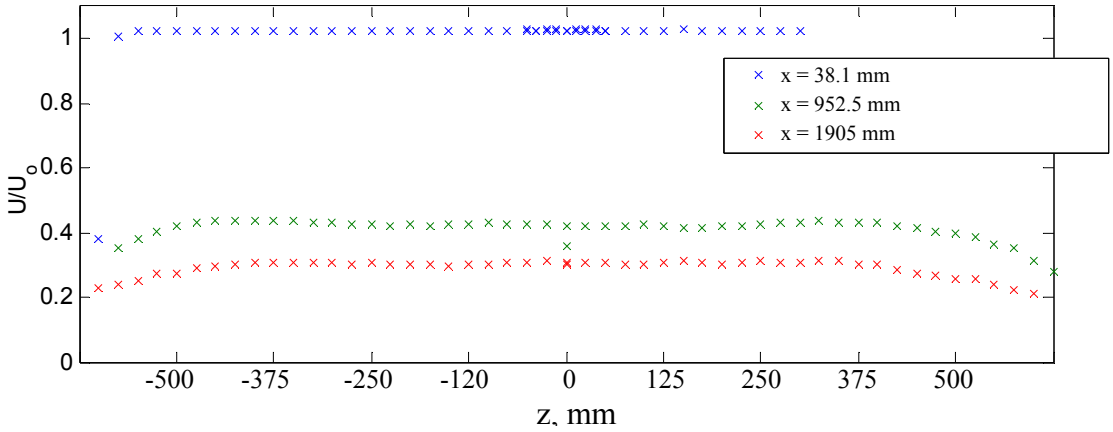

Figure 3-9 Horizontal velocity profiles measured at three streamwise locations for a nozzle height of 12.7 mm, and a jet exit velocity of 30 m/s. All profiles have been normalized on the jet exit velocity.

Figure 3-9 shows profiles measured 952.5 mm, shown in green, and 1905 mm, shown in red, that show a marked improvement in the two dimensional behavior of the flow when compared to similar plots for the preliminary nozzle. The green profile can be compared to the profile in Figure 2-21 measured at the same location for the narrow nozzle. The two-dimensional region in that case was 304.8 mm wide while with the new nozzle the region is 1016 mm wide. Furthermore, since the profiles in Figure 3-9 were taken with a nozzle height of 12.7 mm, while the data in Figure 2-21 was taken for a nozzle height of 25.5 mm. So if we compare profiles measured at the same normalized distance on nozzle height the green profile in Figure 3-9 should compare with the circle profile measured at 1905 mm downstream in Figure 2-21. This profile had almost no two-dimensional region at its core. The red profile shown in Figure 3-9, measured 1905 mm from the nozzle or 150*x/b*, also contains a very large region of two-dimensional flow, extending at least 380 mm on both sides of the center. The extent of the two-dimensional behavior can also bee seen in Figure 3-10. This figure shows vertical profiles measured at the tunnel centerline and 406 mm off the tunnel centerline in the spanwise direction. The green and blue profiles were measured 952.5 mm downstream of the nozzle and are indistinguishable from the wall to a height of 50 mm which is well into the outer mixing layer. The profiles measured 1905 mm downstream of the nozzle, shown in red and black, overlap from the wall to a height of 25 mm which includes most of the boundary layer region.

Figure 3-11 shows the maximum jet velocities that can be sustained in the final facility configuration. The speeds are limited by the volume flow rate that can be produced by the centrifugal fan that is used to run the facility. The facility can still obtain flow speeds above 60 m/s for nozzle heights less than 12.7 mm, but can only sustain a

speed of 44 m/s at 25.4 mm. At 38.1 mm the maximum sustainable speed is reduced to 31 m/s, which limits the usefulness of this and larger nozzle openings.

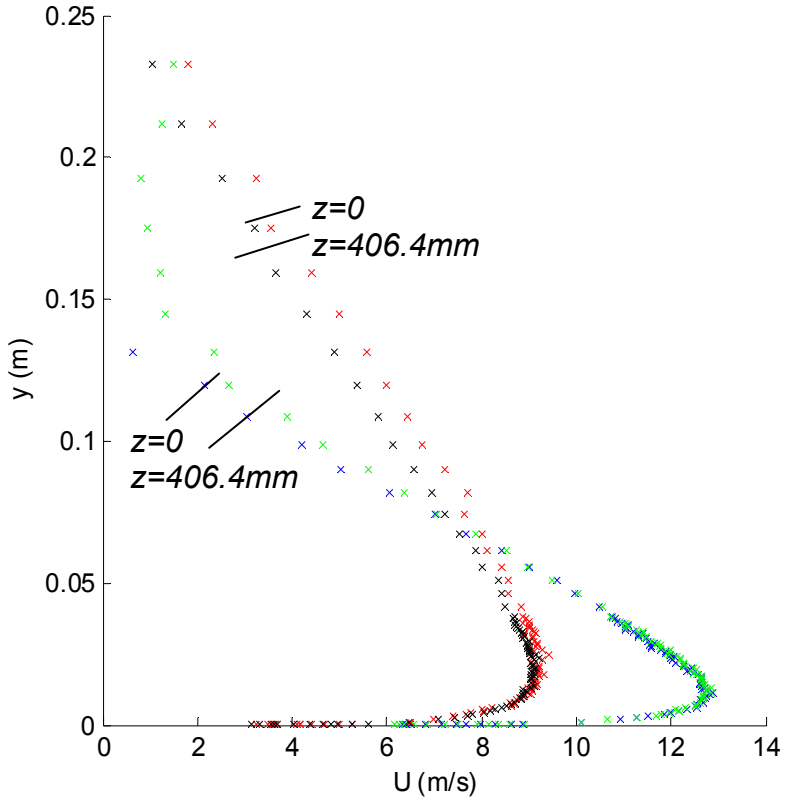

Figure 3-10 Vertical velocity profiles measured at on the plate centerline and at the edge of the two-dimensional jet region. The green and blue profiles were measured 952.5mm downstream of the nozzle exit, the red and black profiles were measured 1905mm downstream.

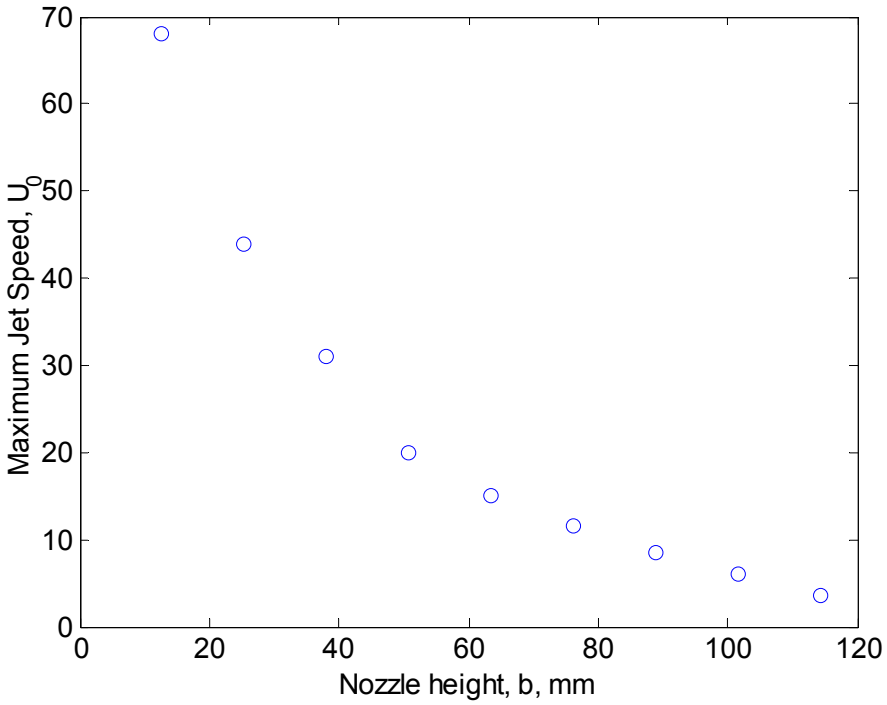

Figure 3-11 Maximum sustainable jet exit velocity, U_0, for a range of nozzle openings, b, measured in the final facility configuration.

3.1.3 Acoustic Enclosure Modifications

While the acoustic enclosure worked well before the modifications, there were several things that could improve its overall performance. The primary modification was to incorporate the shelf that shielded the microphone from the nozzle region into the main body of the acoustic enclosure. The difference in the two designs can be seen in the side view drawings of the acoustic enclosure shown in Figure 3-12. The final configuration has an area 737 mm tall above the shelf, which is within the acoustic enclosure. Placing microphones in this area over the shelf improved measurement quality in two ways. First, the quality is improved because the microphones are better shielded from jet noise coming from the highest speed flow region near the nozzle. Secondly, the quality is improved because the microphones are located in the front of the acoustic enclosure. If roughness noise acts like a flow-aligned dipole, this location will have higher sound levels than locations along the enclosure walls. Further improvements included acoustically sealing all the corners of the enclosure and putting treatment on the floor and underneath the plate.

The final version of the acoustic enclosure is 2057.4 mm wide and 3149.6 mm long on the inside from foam tip to tip. The ceiling of the enclosure is 1168.4 mm above the plate surface, which is mounted 1257.3 mm from above the floor. The original shelf that was mounted near the nozzle was 1143 mm long and built separately from the main body of the acoustic enclosure. A 914 mm long shelf was incorporated into the main acoustic enclosure to replace the original shelf. This shelf was treated with 101.6 mm thick egg crate acoustic foam on both its upper and lower surface. This leaves a 736.6

mm space above the shelf for microphone placement at the front of the chamber. Figure 3-12 shows schematically the original and final configurations of the acoustic enclosure.

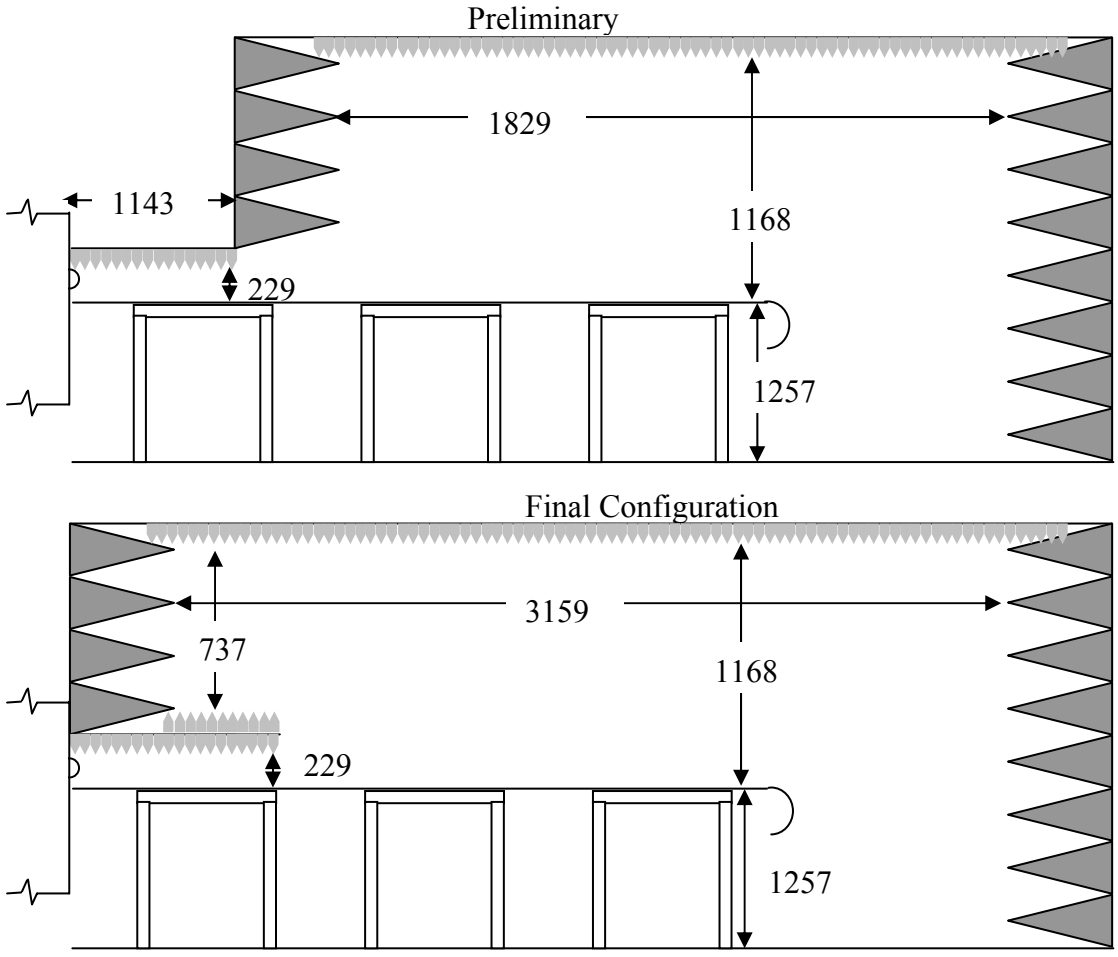

Figure 3-12 Side view drawings of the preliminary and final configurations for the acoustic enclosure around the plate, all dimensions in mm. The walls in both configuration are covered with 457 mm acoustic wedges, and the ceiling and shelf are covered in 95 mm egg crate acoustic foam.

To compare the final and preliminary configurations, a set of measurements were taken under similar conditions to those presented in Figure 2-18 and Figure 2-19. The facility was run with the new nozzle set at a height of 12.7 mm, so that the jet volume was the same as in the runs shown earlier which were done with a 25.4 mm nozzle. The other change in condition was that the microphone was moved from a location along the downstream wall of the acoustic enclosure to a position above the shelf at the front of the acoustic enclosure. The microphone was located on the tunnel centerline 508 mm above the plate, and 1016 mm downstream from the nozzle. In this position it was completely shielded from any line of sight of the first 600 mm of the jet as it exits from the nozzle. Figure 3-13 shows a direct comparison of these two test sets. The spectra presented here have been corrected for the microphone background noise level with no flow for both cases. The solid curves are the levels measured in the original configuration; the dotted lines are the levels for the new configuration. This figure shows that below 1000 Hz the

two chambers act essentially the same, this is to be expected, since the acoustic foam used in the chambers is not very effective at these lower frequencies. Above 2000 Hz the new chamber shows significantly better performance, with noise levels decreased by roughly 10 dB. This large reduction in noise level is primarily due to the change in microphone location. Figure 3-13 also shows the two sets of measurements normalized on the jet exit velocity to the 8^{th} power, consistent with a quadrupole scaling. This confirms that the background level in both configurations is dominated by jet noise from the wall jet. Figure 3-14 shows integrated sound levels flow at different speeds over a smooth plate measured in the preliminary and final chamber configurations. This figure shows that measurements in the final configuration are typically 5 dB below clean plate measurements at the same flow conditions in the preliminary configuration.

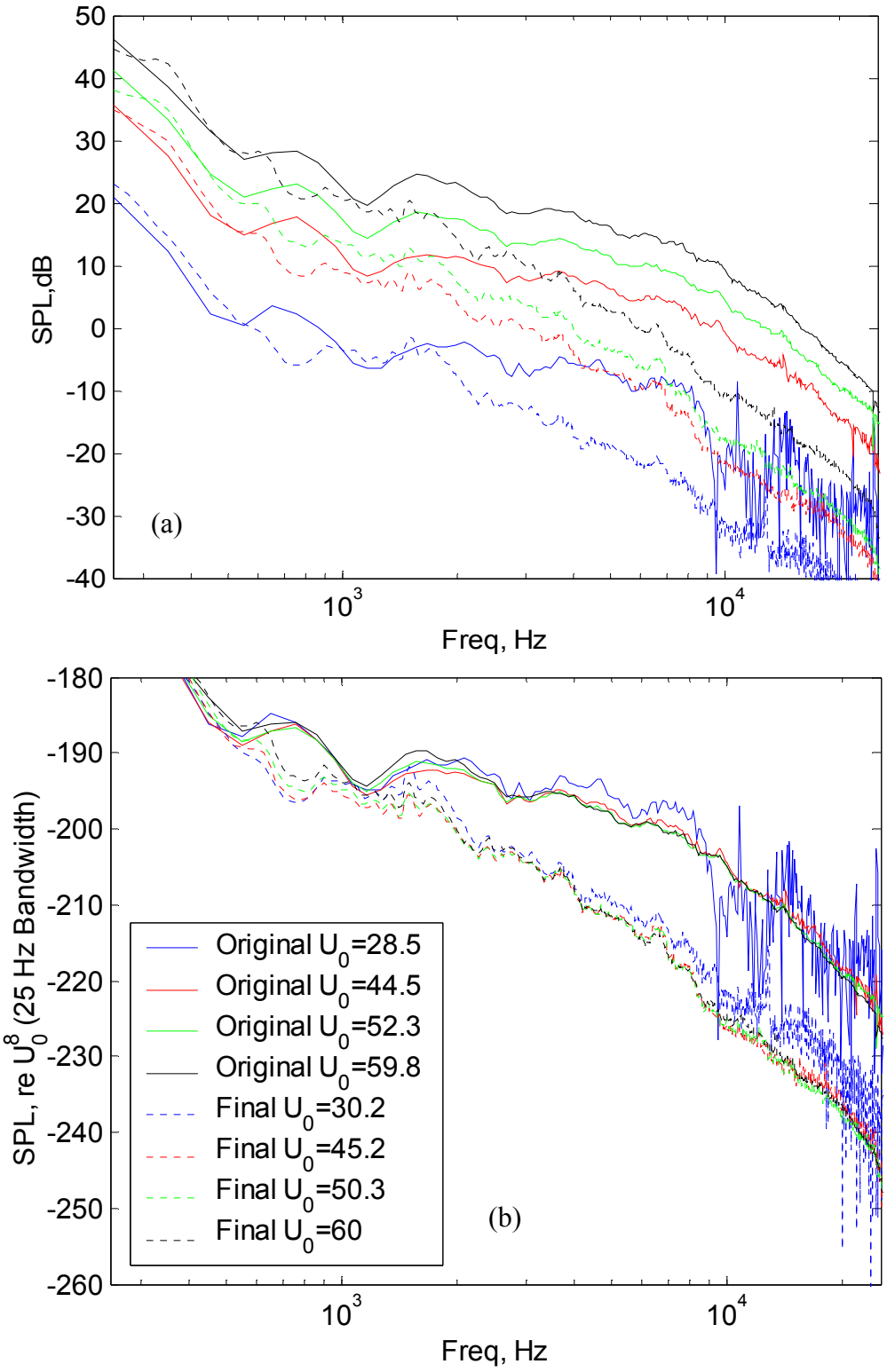

Figure 3-13 Background noise levels measured using a single microphone in the original and final configurations of the acoustic enclosure. Sound levels are shown integrated over 25 Hz bands. Plot (a) shows the sound levels measured in both configurations, plot (b) these levels are scaled on jet velocity to the 8th power.

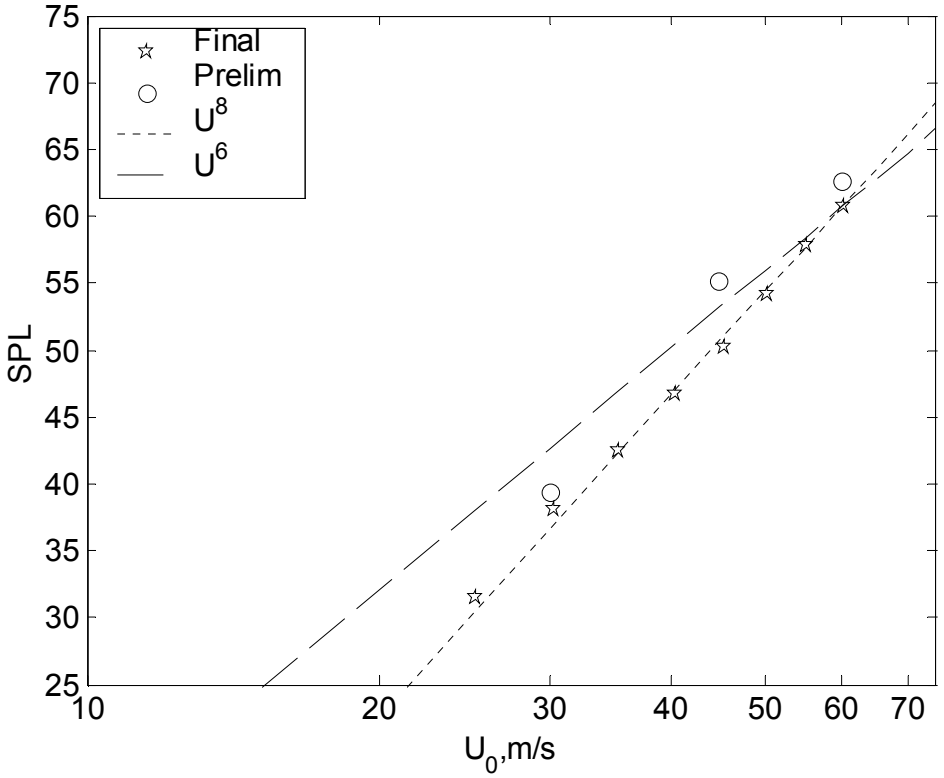

Figure 3-14 Integrated sound levels measured in the Final and Preliminary wall jet configuration over a smooth plate. Also shown are lines corresponding to scaling laws for dipole, U^6, and quadrupole, U^8, acoustic sources.

Smaller patches of roughness were tested in the final configuration because the background noise levels were much lower than in the preliminary configuration. To test that edge noise did not contaminate measurements from these small roughness patches a test similar to the one conducted in the preliminary configuration was conducted in the final facility; see Section 2.3.9. Measurements were taken over the smooth plate and with a patch of Mylar with a thickness of 0.5 mm. The tests were done at a nozzle exit speed of 60 m/s with a nozzle height of 12.7mm. The results of this test are shown in Figure 3-15. This shows that the spectral levels with the Mylar edges are indistinguishable from the smooth plate levels.

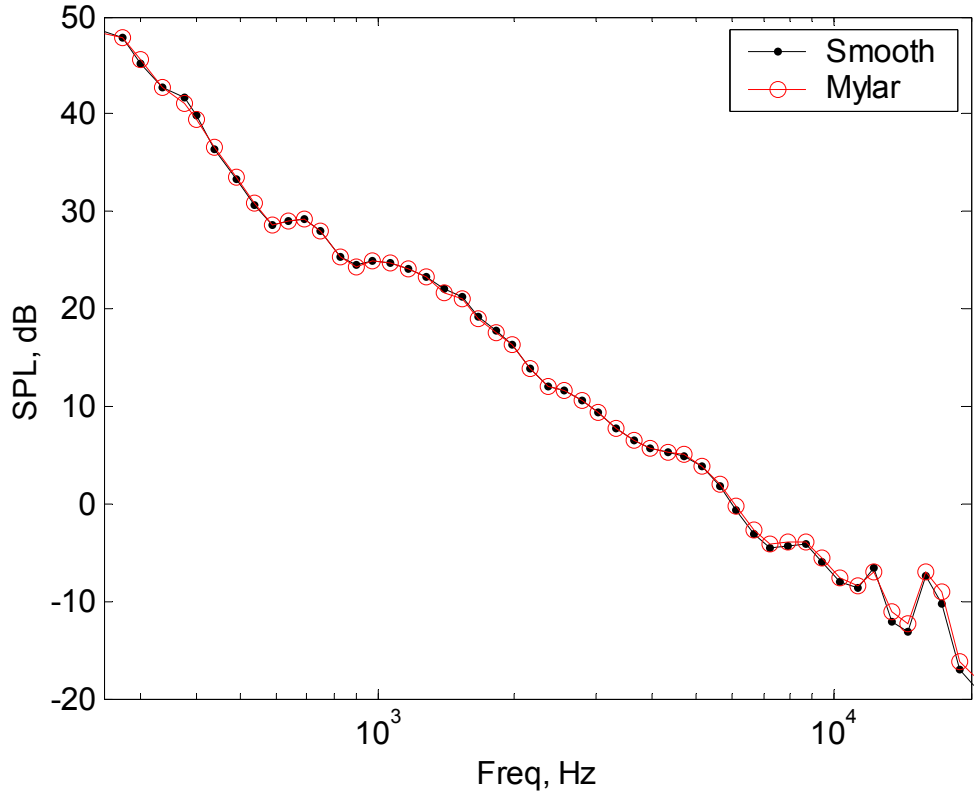

Figure 3-15 Acoustic spectra measured under the flow conditions of cases 37-45 for two different surface conditions. The spectrum labeled smooth have no surface treatment. The curve labeled Mylar has a 305 mm by 610 mm patch of smooth Mylar film attached to the plate.

3.2 Instrumentation

3.2.1 Acoustic Instrumentation

Bruel and Kjaer microphones were used throughout the testing process for far field sound measurements. Bruel and Kjaer (B&K) microphones have become the research standard for sound measurements due to their high sensitivity, low noise contamination, and flat frequency response characteristics. The majority of measurements were made with B&K 4190 microphones. These microphones are ½ inch diameter condenser style free field microphones. They have a nominal sensitivity of 50 mV/Pa and have a flat frequency response up to 20 kHz as shown in Figure 3-16. B&K 4191 microphones were also used for some measurements when high frequency sound needed to be detected. The 4191 microphones have a ½ inch diameter diaphragm with a flat response up to 40 kHz, but a nominal sensitivity of only 12.5 mV/Pa. To improve signal to noise ratio the microphone signal was high pass filtered using a Krohn-Hite Model 3364 4 pole Butterworth filter. To prevent aliasing, the microphone signals were also low pass filtered at 20000 kHz using the Nexus Conditioning amplifier which also powered and amplified the raw microphone signals. All microphone signals were collected using an Agilent E1432 16-bit digitizer, and recorded on a laptop computer.

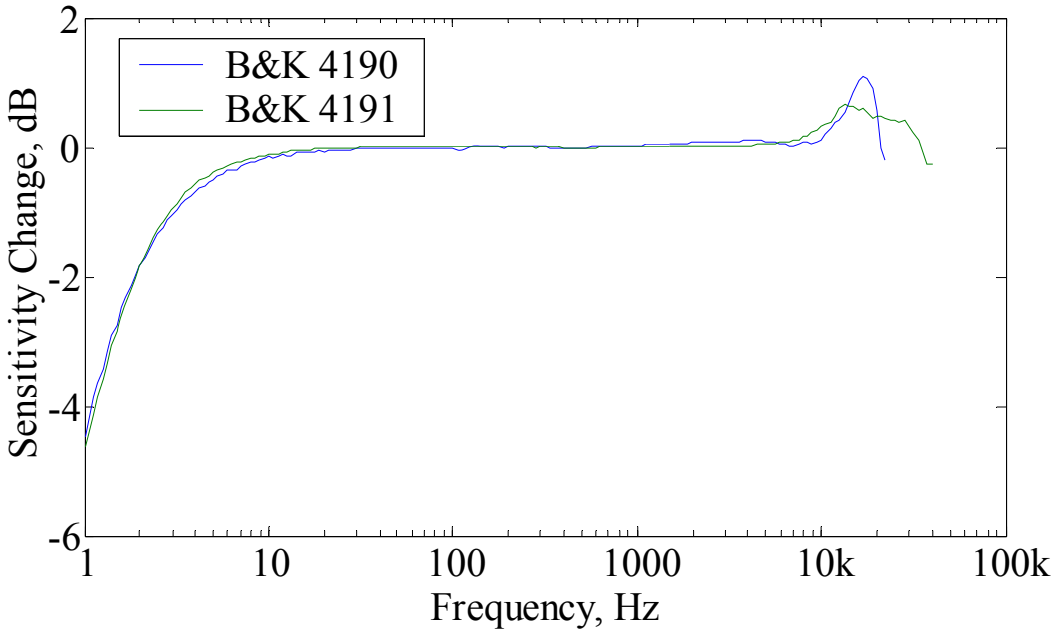

Figure 3-16 Typical sensitivity variation for B&K 4190 and 4191 microphones used in study. Variation is shown for a free field acoustic source with protection grid on the microphone.

3.2.2 Aerodynamic Instrumentation

As discussed, the determination of the various aerodynamic properties is equally important to the measurement of the sound levels to determine the proper scaling behavior. All of the aerodynamic parameters needed for the acoustic scaling models were determined from measurements of the mean flow vertical profile. To measure the mean flow a flattened Pitot probe and a single wire hotwire probe were used. The Pitot-probe was made from a flattened steal tube with a wall thickness of 0.155 mm. To reduce the height of the opening and allow measurements closer to the plate surface the tube was flattened and the thickness of the lower edge of the tube was reduced to 0.09mm. The probe tip had a total height of 0.375 mm, with the center of the probe opening being 0.155 mm from the bottom of the probe. The total probe width was 0.71 mm. The probe could measure at distances as small as 0.155 mm from the plate surface, which was within the laminar sublayer for most smooth plate flows. The pressure measured by the probe was sensed using a Setra 239 (±2.5 kPa) pressure transducer. The pressure in the settling chamber was also monitored with a Setra 239 (±6.89 kPa) pressure transducer to determine the exit flow velocity at the nozzle.

The probes were mounted on a computerized two-axis traverse, which allowed automated data collection for increased testing speed. The traverse used two screw drives to position the probe within the y-z plane. A Compu-motor model S-57-83-MO stepper motor controled each screw drive. The motor and screw system resulted in 117 steps per mm, which allowed repeatable probe location to within 0.0254 mm. This allowed 5 to 10 points to be measured within the laminar sublayer using the flattened Pitot probe.

Additional measurements were taken with a hotwire anemometry probe. A single straight wire Auspex AHWU-100 single-wire probe was used to measure fluctuations in

the mean flow direction. The probe has a 5 micron diameter tungsten wire with a sensing length of 1 mm. A Dantec Model 90C10 Streamline CTA system was used to control the probe during testing. All measurements, both hotwire and pressure, were collected using an Agilent E1432 16-bit digitizer, and recorded and stored on a laptop computer.

3.2.3 Surface Roughness Instrumentation

To determine the size and shape of the various surfaces used during testing, two techniques were used. A white light profilometer was used to determine the detailed structure of the surfaces, and image-processing techniques were used over large area scans of the rough surface. A Wyko NT white light profilometer can measure surfaces with roughness sizes from 0.55 μm up to 1 mm. The system works by measuring the phase shift of light reflected from a surface. The system has a field of view range from a 0.1 mm up to a 4 mm square depending on the lens being used. The largest limitation with this type of system is that highly angled surfaces, common in a grit type surface, scatter the light too much to allow accurate measurement. This limitation significantly hampered the ability of the profilometer to provide reliable data on the macro scale properties of the roughness surface, such as the correlation lengths, and isotropy.

To determine the macro scale properties of the surface, roughness image processing techniques were used. This involved using a flat bed scanner to scan the various surfaces, and then using the image intensity to determine the roughness sizes, density, and correlation functions. The details and results of this technique are discussed in Chapter 4. The scanner used was a Canoscan model 4400F which could scan at resolutions up to 4800 x 9600 dpi.

Chapter 4 Experimental Setup

This chapter will explain general aspects of the experimental setup that apply to all the measurements presented in the remainder of the paper. The reference system used for locating both the surface roughness and the measurement equipment will be defined. Details of the surfaces used in the experiments will be given, along with an explanation of the technique used to calculate the values. The sampling methods and uncertainties associated with the aerodynamic and acoustic measurements will be presented, along with a summary of all the cases measured. These two tables will be referenced throughout the remainder of the paper as different subsets of these measurements are examined in detail. This chapter also describes the data reduction techniques that were used to reduce the effects of scalloping and the methods used to remove background noise from the acoustic measurements. Scalloping is the result of acoustic interference in the acoustic enclosure.

4.1 Coordinate System

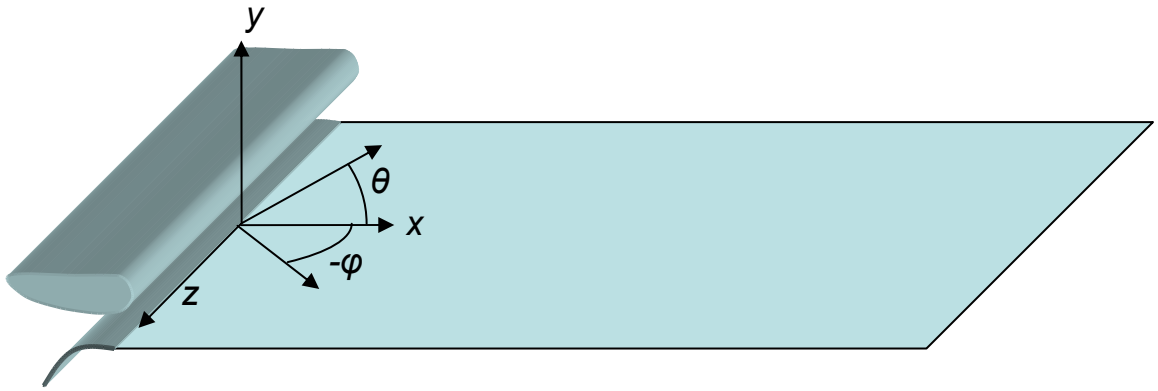

Figure 4-1 Schematic of the wall jet flow and reference system. The nozzle height, *b*, and the nozzle exit speed, U_0, can be adjusted by the facility setup.

Figure 4-1 shows the coordinate system used throughout this paper. The coordinate origin is centered at the spanwise center of the nozzle exit, on the surface of the plate. The x-axis is aligned with the direction of the flow, with the y-axis vertically upward toward to upper side of the nozzle. The z-axis is defined according to the right hand rule, and runs along the junction of the lower nozzle and the plate. Flow velocities are defined in the conventional way with U, V, and W, being the mean flow velocity at a point in the x, y, and z directions respectively. The two other symbols shown in Figure 4-1 define angle measured relative to the coordinate axes. These angles are often used to define the orientation of microphones used for acoustic measurements. The value of θ is the angle measured in the x-y plane away from the positive x-axis. φ is the angle measured in the x-z plane away from the positive x-axis. Signs for both angles are defined positive according to the right hand rule, in Figure 4-1 a positive θ is shown, and a negative φ for clarity.

4.2 Surface Roughness

Standard Aluminum oxide sandpaper (GatorGrit 280mm by 216mm sheets), heavier duty floor sanding sheets (Norton brand with thick paper backing), and a Lenticular Lens sheet were used as rough surfaces. Sheets were attached singly and, to create larger areas, in grids using double sided tape. The result was a continuous roughened area with a shallow step around its periphery equal in height to the thickness of the sheet. Edges of the roughness were taped using 0.1mm thick Aluminum foil tape that covered a 25mm margin of the roughness patch and an equal margin of the surrounding test plate. Care was taken to demonstrate that any sound generated by flow over this step was negligible (see discussion in Section 2.3.9 or 3.1.3). The results of measurement and analysis of the various rough surfaces are given in Table 4-1.

Type	Grit	Sheet thickness (mm)	Nominal mean grain size (mm)	Approx. grain density (per mm^2)	Average spacing / grain size	Estimated RMS surface elevation / grain size	Image correlation length / grain size
Al Oxide	220	0.29	0.068	35	2.5	0.49	1.1
Al Oxide	180	0.29	0.082				1.0
Al Oxide	150	0.33	0.092				1.2
Al Oxide	100	0.38	0.14	10.6	2.2	0.50	0.9
Al Oxide	60	0.58	0.265	2.6	2.4	0.49	1.2
Al Oxide	40	0.76	0.425	1.4	2.0	0.50	1.0
Floor Sanding H425	80	0.66	0.19	6.2	2.1	0.50	0.6
Floor Sanding H425	60	0.81	0.265	4.9	1.7	0.49	0.8
Floor Sanding H425	36	1.13	0.53	1.5	1.5	0.48	0.5
Floor Sanding S413	20	1.27	0.95	0.23	2.2	0.50	0.7
Lenticular Lens	LPI 20	2.17	0.118	0.787	10.77	0.308	10.77

Table 4-1 Rough surface detail summary

The nominal grain sizes are inferred from the grit number using standard tables and were not directly measured. The approximate grain-size density was inferred by counting grains in images of the rough surface taken using a high-resolution scanner. Scans of the surfaces sharp enough to count individual grains have not yet been obtained for the 150 and 180 grit paper. The average spacing per grain size is calculated by dividing the inverse of square root of the grain density by the grain size and, interestingly, varies only by about ±25% for the sandpaper surfaces over a 10 to 1 range of grit sizes. Even more constant is the RMS surface elevation normalized on grain size, estimated here assuming equal size cubic grains, which varies only by about 2%. The correlation length scales in Table 4-1 were calculated based on the gray-scale levels of the scanned images. Figure 4-2 shows enlarged scanned images of the 60-grit sandpaper, and 60 grit floor-sanding sheets. This figure shows, especially for the sanding belts, that while the grayscale levels may not be directly proportional to the surface height, the same behavior is present on each roughness element. So correlation information about the grayscale levels will be proportional to the correlation function of the roughness height.

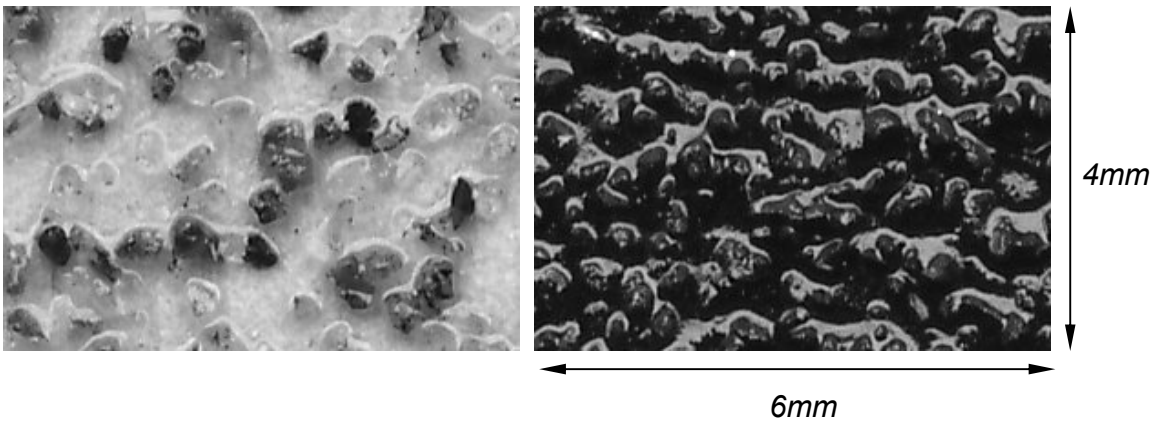

Figure 4-2 Example images of rough surfaces. (a) – 60 grit sandpaper roughness. (b) – 60 grit floor sanding sheet.

The shape of the lenticular lens sheet is shown in Figure 4-3. The drawing in part (b) of this figure shows the rows of the lens attached to a backing 2.17 mm thick. The profile of the lens was measured from a magnified picture shown in part (a) of this figure. This shows that the profile shape is well modeled by the absolute value of the sine function, (c) with a wavelength equal to the manufacturer specified lens spacing.

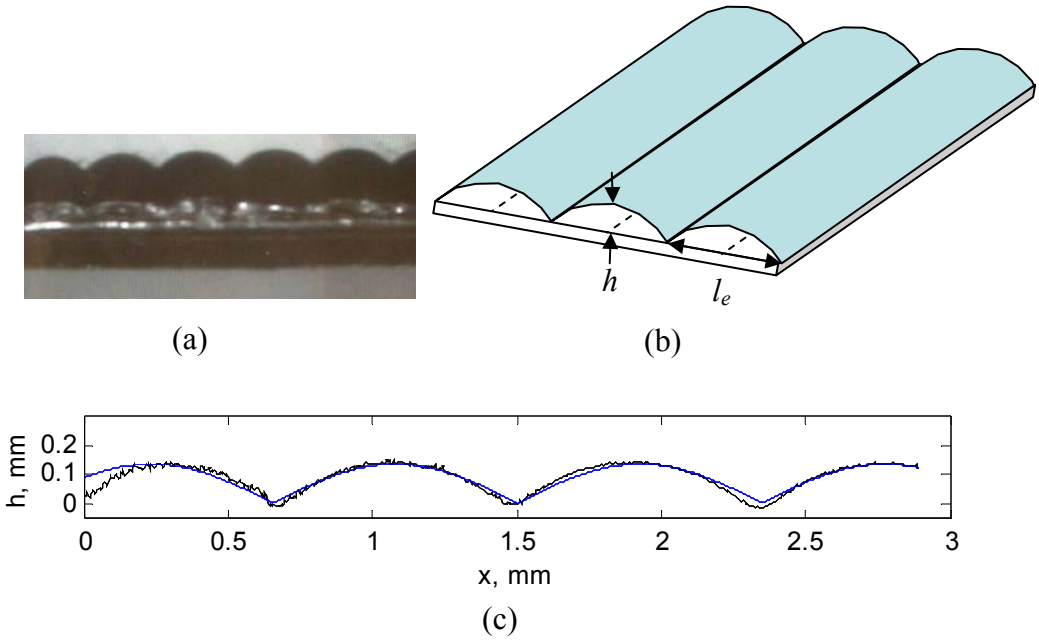

Figure 4-3 Illustration of the two-dimensional roughness pattern used in Chapter 7. (a) shows a magnified photograph of the edge of the lens sheet, (b) shows the lens schematically, with the roughness height, h, and length scale, l_e, labeled, and (c) shows the measured lens profile in black with the absolute value of a sine function overlaying it in blue.

4.3 Sampling Schemes

Acoustic measurements were collected in records of 2048 samples measured at 51200 Hz. Each spectrum presented represents the averaged result of 1000 records, for a total sampling time of 40 seconds. However, data was stored after each sample which required over 1 second. This delay between measurements insures that each sample recorded would be considered statistically independent. The averaging is done on the acoustic power spectrum during post-processing. Acoustic measurements are also band pass filtered between 250 Hz and 20000 Hz using a Krohn-Hite programmable filter. This prevents signal aliasing and reduces noise contamination from low frequency electrical interference. The Agilent E1432 16-bit digitizer also has an adjustable input range which was set to capture the pressure signal from each microphone without clipping the signal. The voltage range was set between ±0.1V and ±0.5V depending on the flow and surface conditions being tested. For the largest voltage range this gives a digital resolution of 20μV.

Aerodynamic measurements, primarily taken by Smith (2007), used two sampling schemes. To measure the mean velocity profile with a Pitot probe 50 records of 1024 samples were collected at each measurement location. Samples were collected at 6400 Hz giving a total sampling time of 8 seconds. Mean velocity values presented are averaged from all data at each measurement location. Vertical velocity profiles contained 60 to 80 measurement points spaced logarithmically away from the wall. Horizontal profiles contain 40 to 60 points, with points distributed evenly across the space of the flow, except in regions near the edge, where the spacing was halved to provide better resolution of the edge gradients. Hot-wire measurements made with a single wire probe used a sampling scheme designed to capture both mean values, and turbulence spectra. Forty records containing 8192 samples were collected at 51200 Hz at each measurement location. This gives a total sampling time of 6 seconds. Velocity power spectra are computed from each record, and then averaged over all the records. Vertical profiles measured using the hotwire contain 40 to 60 points which are evenly distributed near the wall, then logarithmically through the remainder of the flow region. This distribution captures the same features as the Pitot probe distributions, but with less measurement points. Both probes were positioned near the wall using a cathetometer to measure the starting height from the wall. Profiles could start as close as 0.25mm from the wall depending on the roughness and velocity being measured.

4.4 Uncertainty

4.4.1 Acoustic Measurements

The 4190 B&K microphones, described in Chapter 3, were calibrated using a pistophone. The pistophone, B&K 4228, generates a 250 Hz tone with known amplitude. By measuring the microphone signal from this source the microphone sensitivity could be measured. Pistophone calibrations show a drift of 1% in the microphone sensitivity over the course of the experimental work. The microphone specifications show the microphone frequency response to be flat until a frequency of 10 kHz where it diverges by no more than 1dB. The effects of this change have been corrected in the measured

spectra, based on the frequency response for the microphone sensitivity provided by the manufacturer. Another effect which must be accounted for is the variation in sensitivity based on the direction of the acoustic wave relative to the microphone face. If an acoustic wave is not normal to the microphone face the sensitivity with which it is measured is reduced. The B&K 4190 microphones used in this test have a maximum random incident field response correction of 3dB. This correction is needed for frequencies above 10 kHz and is due to the acoustic wavelengths becoming comparable to the microphone diaphragm diameter. The sampling scheme used for acoustic measurements results in a random uncertainty of 3% of the spectral level, 0.25dB, based on the technique outlined in Bendat and Piersol (1986). However, due to scalloping effects and the methods used to correct for them, the uncertainty in narrowband spectra below 3000 Hz is limited to ±2dB. The spectral subtraction and smoothing techniques, described below, used to remove background noise levels are also biased to increasing the uncertainty at low frequencies. The total uncertainty for measured spectra is frequency dependent; below 3000 Hz the spectral uncertainties are on the order of 3 dB while above this they drop to a minimum of 1dB at the highest frequencies.

4.4.2 Aerodynamic Measurements

Based on a jitter analysis the hot wire and Pitot probe measured local mean velocity uncertainties are 3% of the mean value at 20:1 odds. This uncertainty affects the various derived scaling parameters differently. To determine the boundary layer thickness and edge velocity associated with the mean flow profile each profile was compared with the standard wall jet curve. This process uses all the measured data points to compute the scaling parameters. This reduces the uncertainty in the local boundary layer edge velocity to 2%. Since the boundary layer thickness is the measure of a broad maximum, the uncertainty even when using a profile fit is still 5%. The integrated length scales such as δ^* and θ have smaller uncertainties of 2%. The method used to estimate the skin friction velocity required numerical integration of the momentum equation solved for a wall jet flow. This method depends on all of the velocity and length scales discussed previously, and a model of the skin friction in a smooth wall jet flow. Jitter analysis of this method shows the skin friction estimates to have an uncertainty of 7% with 20:1 odds.

4.4.3 Other Measurements

All distance measurements, other than the aerodynamic probes on the automated traverse, were made with a laser range finder or a measuring stick. Each could give measurements within ±1 mm. Microphone angles were measured using a protractor and laser pointer system. A laser pointer with a diameter equal to that of the microphone was placed in the microphone holder. The projected laser line was then measured using the protractor relative to the plate surface. This technique could measure microphone angles with an uncertainty of ±2°. Temperature and atmospheric pressure measurements were taken to complement other aerodynamic data. This data was collected and averaged over the period of each measurement. The atmospheric pressure sensor used had an uncertainty of ±5 mBar and was checked against a departmental standard gauge with uncertainty of ±1 mBar throughout the course of the experimental work. The temperature sensor uncertainty was ±1°C, and was also periodically checked for drift.

4.5 Aerodynamic Test Matrix

Chapter 5 summarizes the results of Smith (2007) which investigated the aerodynamic behavior of the wall jet facility. A number of measurements were made to quantify both the clean plate flow behavior and the flow over roughness patches of various lengths and surfaces. The results of Smith (2007) were used in this study to determine the aerodynamic scaling parameters needed for the acoustic models presented in Chapter 1. Table 4-2 summarizes a series of measurements made in the wall jet facility with no roughness added to the plate surface. These measurements were used to validate the two-dimensional wall jet model for the flow in this facility. The measurements have been grouped according to nozzle conditions, which show the parts of the model being tested. Group B captures the decay behavior of the wall jet along the plate, while Groups A, C, D, E, and F show the effects of changing nozzle height and velocity at fixed locations on the plate. Measurements in Table 4-2 were collected using the flattened Pitot probe, and mean velocity sampling scheme discussed earlier. The nozzle conditions are given in Table 4-2 by the nozzle height, b, and the nozzle exit velocity U_0. These values are also used to calculate the jet Reynolds number Re_j according to Equation 4.1.

$$\mathrm{Re}_j = \frac{U_0 b}{\nu} \tag{4.1}$$

Where ν is the kinematic viscosity. All measurements in Table 4-2 were collected along the tunnel centerline, z = 0 mm, and at the distance downstream from the nozzle, x, shown in the table. Values of momentum thickness, θ, and displacement thickness, δ^*, were computed by numerically integrating the measured flow profiles according to Equation 4.2.

$$\begin{aligned} \delta^* &= \int_{\delta} 1 - \frac{U}{U_e} dy \\ \theta &= \int_{\delta} \frac{U}{U_e}\left(1 - \frac{U}{U_e}\right) dy \end{aligned} \tag{4.2}$$

The values of δ, δ_{90}, $y_{1/2}$, and U_e were determined by matching the measured profiles to the standard wall jet profile shape. The momentum Reynolds number, Re_m, was calculated based on the local momentum thickness and edge velocity, U_e, according the Equation 4.3. Throughout the remainder of this report aerodynamic data will be referenced to the case numbers listed in the following tables.

$$\mathrm{Re}_m = \frac{U_e \theta}{\nu} \tag{4.3}$$

	Case	b (mm)	U_o (m/s)	Re_j	x (mm)	θ (mm)	δ* (mm)	δ_{90} (mm)	δ (mm)	$y_{1/2}$ (mm)	U_e/U_o	Re_m
A	1	12.7	20	15358	953	0.8	1.06	2.87	12.9	83	0.45	450
	2	12.7	19.9	15251	1867	1.08	1.57	6.84	20.4	145	0.33	443
B	3	12.7	29.9	22872	343	0.25	0.37	1.2	4.7	32	0.7	327
	4	12.7	29.9	22871	648	0.46	0.64	2.1	8	57	0.51	438
	5	12.7	29.9	22932	953	0.67	0.92	2.89	12	81	0.43	538
	6	12.7	29.9	22937	1257	0.81	1.1	3.82	14.1	103	0.38	575
	7	12.7	30	22984	1562	0.98	1.32	4.29	17.7	125	0.34	625
	8	12.7	29.9	22917	1867	1.07	1.47	5.6	20	138	0.3	600
	9	12.7	29.9	22910	2172	1.35	1.78	6.18	24.3	172	0.29	732
	10	12.7	29.9	22896	2172	1.43	1.98	6.73	24.6	179	0.29	775
	11	12.7	29.9	22919	2477	1.3	1.79	6.86	26.3	202	0.27	656
C	12	12.7	40.3	30871	953	0.69	0.94	2.94	12.6	80	0.41	713
	13	12.7	39.3	30127	1867	1.19	1.59	5.26	21.6	154	0.3	877
D	14	25.4	19.8	30390	953	0.66	0.9	2.88	12.1	89	0.62	506
	15	25.4	19.7	30170	1867	1.14	1.57	5.9	22	154	0.47	660
E	16	25.4	29.7	45562	953	0.68	0.91	2.87	12.9	93	0.59	745
	17	25.4	29.6	45402	1867	1.22	1.59	4.86	21.2	158	0.44	993
F	18	25.4	39.4	60362	953	0.66	0.87	2.93	12.5	94	0.57	926
	19	25.4	39.5	60494	1867	1.12	1.48	4.91	22.1	167	0.42	1161

Table 4-2 Smooth wall aerodynamic conditions summary

Table 4-3 summarizes the aerodynamic measurements collected over rough surfaces. The aerodynamic data were used to compute scaling parameters which were needed to normalize the far field acoustics using the models presented in Chapter 1. In Table 4-3 values listed at the leading edge of the roughness have been estimated from the nozzle conditions, and the two-dimensional wall jet model discussed in Chapter 5. In addition to listing the aerodynamic properties measured, Table 4-3 also lists the roughness properties for each case, including the roughness height, h, roughness designation, and roughness Reynolds number, h^+, which is defined in Equation 4.4.

$$h^+ = \frac{u_\tau h}{\nu} \tag{4.4}$$

The values of the skin friction coefficient are determined for a smooth wall jet flow according to the model of Bradshaw and Gee (1960), shown in Equation 4.5.

$$C_f = 0.315\,\mathrm{Re}_m^{-0.182} \tag{4.5}$$

Where C_f is the skin friction coefficient and Re_m is the momentum Reynolds number defined in Equation 4.3. The skin friction velocity can be related to the skin friction coefficient by manipulating Equation 1.1. This leads to the relation shown in Equation 4.6.

$$\frac{u_\tau}{U_e} = \sqrt{\frac{C_f}{2}} \tag{4.6}$$

Grit values marked with * correspond the floor sanding belts discussed in section 4.2, while all other grit values are aluminum oxide sheets. Aerodynamic measurements were made using a single wire hot wire probe at location x_2. The hot-wire probe was located 1 to 2 mm downstream of the trailing edge of the roughness patch to allow it to be positioned using a cathetometer. At this location the flow is affected by the step from the roughness patch to the smooth plate. For most roughness cases this effect is small and does not affect the scaling parameters. The exception is case 65, measured downstream of the two-dimensional roughness, where the roughness backing was 2.17 mm. In this case the values listed have been computed by removing all measurements below a height of 1 mm where the flow is likely separated from the wall.

The boundary layer parameters in Table 4-3 were calculated using the same methods used for Table 4-2. The values of u'_{max} and $y_{u'max}$ were determined by matching the measured turbulence profiles to a standard wall jet turbulence profile shape. The values of C_f, and subsequently u_τ and h^+ in Table 4-3, were determined by integrating the momentum equation along the length of the patch. This method is discussed in Grissom *et al*. 2007, and is summarized here. Integration of the momentum equation from the wall to δ yields Equation 4.7.

$$\frac{\tau_w + \tau_\delta}{\rho} = \frac{dU_m^2\theta}{dx} - \left(\delta - \delta^*\right)U_e \frac{dU_e}{dx} \tag{4.7}$$

Where τ_δ is the shear at the top of the boundary layer. Equation 4.7 can be integrated along the length of the roughness patch, and along the same length of smooth plate. The subtraction of these results yields Equation 4.8.

$$\frac{f - f_s}{\rho} = U_e^2\left[\theta_r(x_2) - \theta_s(x_2)\right] - \int_{x_1}^{x_2}\left[(\delta_r - \delta_s) - (\delta_r^* - \delta_s^*)\right]U_e \frac{dU_e}{dx}dx \tag{4.8}$$

Where the subscripts r and s are for values measured in a rough and smooth wall flow respectively and f is the total friction force on the wall from x_1 to x_2. This equation assumes that properties which need to be evaluated at the boundary layer thickness are unaffected by the presence of the roughness. Measurements of mean flow profiles in Chapter 5 show that U_e is unaffected by roughness, and measurements of u' suggest that τ_δ is unlikely to be effected by roughness. This equation was numerically integrated assuming a linear variation in flow properties from x_1 to x_2 to determine the values of C_f, given in Table 4-3. This value was then used to determine the mean skin friction velocity, u_τ, over the patch and the value of h^+ over the patch.

The measurements in Table 4-3 are divided into groups which are analyzed together in Chapter 5. Groups G, H, K, and L measured the growth of the wall jet over roughness patches of different lengths. Group J was measured behind roughness patches of different grit sizes for the same inflow conditions.

							At start of roughness (pos. 1)						At end of roughness (pos. 2)												
	Case	b	U_o	Re_j	Grit	h	x_1	δ^*	U_e/U_o	C_f	u_τ/U_e	h^+	x_2	θ	δ^*	δ_{90}	δ	$y_{u'max}$	$y_{1/2}$	U_e/U_o	$\frac{u'^2_{max}}{U_m^2}$	C_F (x1000)	u_T/U_{m2}	h^+
G	20	12.7	30	23310	180	0.082	1245	1.2	0.39	0.0058	0.054	3	1562	1.16	1.7	5.19	19.1	87	131	0.34	0.043	0.86	0.061	3
	21	12.7	30.1	23451	180	0.082	1245	1.2	0.39	0.0058	0.054	3	1867	1.37	2.05	6.57	23	98	158	0.31	0.045	0.71	0.062	3
	22	12.7	30.2	23513	180	0.082	1245	1.2	0.39	0.0058	0.054	3	2172	1.67	2.39	7.95	28	116	181	0.28	0.043	0.61	0.064	3
	23	12.7	29.8	23187	100	0.14	1245	1.2	0.39	0.0058	0.054	5	1562	1.19	1.68	5.24	21.1	99	128	0.35	0.046	0.78	0.056	5
	24	12.7	30	23308	40	0.425	1245	1.2	0.39	0.0058	0.054	16	1410	1.52	2.31	7.19	19.3	87	116	0.35	0.049	1.76	0.084	23
	25	12.7	29.8	23214	40	0.425	1245	1.2	0.39	0.0058	0.054	16	1562	1.79	2.55	8.87	24.2	90	129	0.34	0.046	1.14	0.069	19
	26	12.7	29.9	23245	40	0.425	1245	1.2	0.39	0.0058	0.054	16	1867	2.12	3.04	10.4	27.9	107	160	0.3	0.053	0.80	0.068	16
	27	12.7	29.9	23233	40	0.425	1245	1.2	0.39	0.0058	0.054	16	2172	2.32	3.38	11.2	31.3	138	188	0.27	0.054	0.66	0.068	14
	28	12.7	30	23369	20*	0.95	1245	1.2	0.39	0.0058	0.054	36	1562	2.06	3.79	9.44	23	93	130	0.35	0.045	1.46	0.077	47
H	29	12.7	39.9	31030	180	0.082	1245	1.14	0.38	0.0055	0.053	4	1562	1.12	1.64	5.37	20.2	88	135	0.33	0.047	0.73	0.057	4
	30	12.7	40	31114	180	0.082	1245	1.14	0.38	0.0055	0.053	4	1867	1.3	1.84	6.31	22.7	108	157	0.3	0.045	0.64	0.059	4
	31	12.7	40.1	31218	180	0.082	1245	1.14	0.38	0.0055	0.053	4	2172	1.44	2.04	6.77	27.2	125	180	0.28	0.045	0.53	0.062	3
	32	12.7	39.9	31033	40	0.425	1245	1.14	0.38	0.0055	0.053	21	1410	1.51	2.3	6.87	19.7	86	119	0.35	0.048	1.68	0.084	30
	33	12.7	40	31116	40	0.425	1245	1.14	0.38	0.0055	0.053	21	1562	1.71	2.46	8.26	24.7	83	137	0.33	0.052	1.00	0.068	23
	34	12.7	39.9	31076	40	0.425	1245	1.14	0.38	0.0055	0.053	21	1867	2.61	3.71	12	32.7	104	164	0.3	0.051	0.75	0.064	20
	35	12.7	40	31159	40	0.425	1245	1.14	0.38	0.0055	0.053	21	2172	2.79	4.05	12.9	35.9	134	191	0.28	0.052	0.57	0.061	18
I	36	12.7	46.1	35902	40	0.425	1854	1.63	0.31	0.0052	0.051	19	2172	2.24	3.22	10.2	30.3	127	182	0.28	0.049	0.84	0.074	25
J	37	12.7	60.1	46787	220	0.068	1245	1.06	0.38	0.0052	0.051	5	1562	1	1.46	4.45	18.4	98	133	0.35	0.047	0.66	0.052	5
	38	12.7	60	46680	150	0.092	1245	1.06	0.38	0.0052	0.051	7	1562	1.14	1.65	5.2	21.7	87	140	0.34	0.051	0.62	0.053	6
	39	12.7	59.8	46531	100	0.14	1245	1.06	0.38	0.0052	0.051	10	1562	1.17	1.69	5.2	20	89	134	0.34	0.05	0.72	0.055	10
	40	12.7	60	46704	80*	0.19	1245	1.06	0.38	0.0052	0.051	13	1562	1.46	2.23	7.03	23	103	135	0.36	0.05	0.82	0.056	14
	41	12.7	60	46706	60	0.265	1245	1.06	0.38	0.0052	0.051	19	1562	1.6	2.41	7.51	22.3	110	134	0.35	0.05	0.97	0.063	21
	42	12.7	60.1	46742	60*	0.265	1245	1.06	0.38	0.0052	0.051	19	1562	1.5	2.39	6.96	21.8	94	132	0.35	0.05	0.92	0.06	21
	43	12.7	59.8	46553	40	0.425	1245	1.06	0.38	0.0052	0.051	30	1562	2.04	2.89	9.75	24.9	109	140	0.34	0.05	1.19	0.071	38
	44	12.7	59.9	46621	36*	0.53	1245	1.06	0.38	0.0052	0.051	38	1562	1.93	3.31	9.14	24.4	99	137	0.34	0.049	1.15	0.07	47
	45	12.7	60	46687	20*	0.95	1245	1.06	0.38	0.0052	0.051	67	1562	2.04	3.67	10.2	25.8	108	136	0.34	0.052	1.19	0.071	85

Table 4-3 Aerodynamic measurements for flow over rough surfaces

							At start of roughness (pos. 1)						At end of roughness (pos. 2)											
	Case	b	U_o	Re_j	Grit	h	x_1	δ^*	U_e/U_o	C_f	u_τ/U_e	h^+	x_2	θ	δ^*	δ_{90}	δ	$y_{u'max}$	$y_{1/2}$	U_e/U_o	$\frac{u'^2_{max}}{U_m^2}$	C_F (x1000)	u_τ/U_{m2}	h^+
K	46	25.4	20.2	31382	180	0.082	1245	1.21	0.55	0.0073	0.06	3	1562	1.21	1.79	6.07	21.6	93	145	0.47	0.046	1.57	0.06	3
	47	25.4	19.9	30964	180	0.082	1245	1.21	0.55	0.0073	0.06	3	1867	1.21	1.81	6.77	22.4	108	163	0.43	0.043	1.37	0.061	3
	48	25.4	19.9	30978	180	0.082	1245	1.21	0.55	0.0073	0.06	3	2172	1.72	2.42	7.58	29.2	130	189	0.39	0.049	1.19	0.064	3
	49	25.4	19.5	30357	100	0.14	1245	1.21	0.55	0.0073	0.06	6	1562	1.15	1.66	5.88	20.4	106	136	0.47	0.05	1.59	0.06	5
	50	25.4	19.7	30625	40	0.425	1245	1.21	0.55	0.0073	0.06	17	1410	1.63	2.44	7.25	23	97	131	0.51	0.047	3.49	0.082	21
	51	25.4	19.5	30403	40	0.425	1245	1.21	0.55	0.0073	0.06	17	1562	1.87	2.68	8.51	22.6	100	139	0.48	0.046	2.58	0.075	18
	52	25.4	19.9	31043	40	0.425	1245	1.21	0.55	0.0073	0.06	17	1867	2.16	3.08	10.2	30.8	118	168	0.42	0.052	1.45	0.064	14
	53	25.4	19.8	30774	40	0.425	1245	1.21	0.55	0.0073	0.06	17	2172	2.49	3.58	12.2	30.7	151	197	0.39	0.05	1.45	0.069	14
	54	25.4	19.8	30835	20*	0.95	1245	1.21	0.55	0.0073	0.06	38	1562	2.19	4	10.2	26.7	103	141	0.48	0.047	2.81	0.077	43
L	55	25.4	30.1	46796	180	0.082	1245	1.13	0.54	0.0068	0.059	5	1562	1.38	1.9	6.71	23.2	93	143	0.47	0.046	1.57	0.06	4
	56	25.4	30.1	46851	180	0.082	1245	1.13	0.54	0.0068	0.059	5	1867	1.56	2.2	8.22	26.2	114	168	0.43	0.046	1.18	0.059	4
	57	25.4	30.3	47142	180	0.082	1245	1.13	0.54	0.0068	0.058	5	2172	1.52	2.08	6.58	26	120	193	0.4	0.044	1.13	0.06	4
	58	25.4	29.7	46152	100	0.14	1245	1.13	0.54	0.0069	0.059	8	1562	1.3	1.83	6.53	23.8	102	145	0.46	0.049	1.40	0.058	7
	59	25.4	29.9	46524	40	0.425	1245	1.13	0.54	0.0069	0.059	25	1410	1.56	2.37	7.98	21.2	94	135	0.48	0.05	3.37	0.085	32
	60	25.4	29.8	46312	40	0.425	1245	1.13	0.54	0.0069	0.059	25	1562	1.89	2.73	9.02	25.6	96	147	0.45	0.052	2.20	0.073	26
	61	25.4	29.9	46547	40	0.425	1245	1.13	0.54	0.0069	0.059	25	1867	2.22	3.18	10.2	30	128	180	0.41	0.054	1.40	0.064	21
	62	25.4	30	46662	40	0.425	1245	1.13	0.54	0.0069	0.059	25	2172	2.86	4.14	12.6	38.6	147	201	0.39	0.055	1.00	0.061	19
	63	25.4	34.6	53922	40	0.425	1854	1.61	0.43	0.0065	0.057	22	2172	2.22	3.19	11.2	29.9	131	193	0.4	0.053	1.67	0.073	26
	64	25.4	30	46619	20*	0.95	1245	1.13	0.54	0.0069	0.059	55	1562	2.29	4.12	11	25.8	89	147	0.48	0.048	2.91	0.08	66

Table 4-3 Aerodynamic measurements for flow over rough surfaces

4.6 Acoustic Test Matrix

The conditions where acoustic measurements were collected are summarized in Table 4-4. This table lists the nozzle flow conditions, roughness type and location, and microphone locations for each measurement. The column labeled "Aero case" lists the case numbers from Table 4-2 and Table 4-3 that are measured for the same flow and surface conditions. The microphones are located using the coordinate system defined in Section 4.1. The microphone orientation is also listed for each microphone, according to the angles defined in Figure 4-1. For groups G1-G14 the microphones are oriented to face directly downstream and not facing the roughness patch. This orientation was found to reduce the effects of scalloping for microphones located in the front of the acoustic enclosure. For most measurements three microphones were located together to measure the far field spectra and the spectra presented later are averaged over these three microphones. This technique was used for all measurements in groups G1-G14. Groups G15, 16, and 21 have the microphones distributed along vertical arcs around a roughness patch. Results from these groups are not averaged over multiple microphones, but are presented for each microphone individually. Results measured from Groups G17-20 are also presented individually. In these groups the microphones are located in a horizontal arc around a roughness patch.

Group	Aero case	Case	b, mm	U_0, m/s	Grit	h, mm	x_1, mm	x_2, mm	microphone 1		microphone 2		microphone 3		microphone 4	
									x, y, z mm	θ, φ	x, y, z mm	θ, φ	x, y, z mm	θ, φ	x, y, z mm	θ, φ
G1	-	101	12.7	60	none	0	1257	1562	1016,533,-25	0,0	1016,476,-38	0,0	1016,476,-13	0,0	1016 ,559 ,152	0,0
	37	102	12.7	60	220	0.068	1257	1562	1016,533,-25	0,0	1016,476,-38	0,0	1016,476,-13	0,0	1016 ,559 ,152	0,0
	-	103	12.7	60	180	0.082	1257	1562	1016,533,-25	0,0	1016,476,-38	0,0	1016,476,-13	0,0	1016 ,559 ,152	0,0
	38	104	12.7	60	150	0.092	1257	1562	1016,533,-25	0,0	1016,476,-38	0,0	1016,476,-13	0,0	1016 ,559 ,152	0,0
	39	105	12.7	60	100	0.14	1257	1562	1016,533,-25	0,0	1016,476,-38	0,0	1016,476,-13	0,0	1016 ,559 ,152	0,0
	40	106	12.7	60	80	0.19	1257	1562	1016,533,-25	0,0	1016,476,-38	0,0	1016,476,-13	0,0	1016 ,559 ,152	0,0
	41	107	12.7	60	60*	0.265	1257	1562	1016,533,-25	0,0	1016,476,-38	0,0	1016,476,-13	0,0	1016 ,559 ,152	0,0
	42	108	12.7	60	60	0.265	1257	1562	1016,533,-25	0,0	1016,476,-38	0,0	1016,476,-13	0,0	1016 ,559 ,152	0,0
	43	109	12.7	60	40	0.425	1257	1562	1016,533,-25	0,0	1016,476,-38	0,0	1016,476,-13	0,0	1016 ,559 ,152	0,0
	44	110	12.7	60	36*	0.53	1257	1562	1016,533,-25	0,0	1016,476,-38	0,0	1016,476,-13	0,0	1016 ,559 ,152	0,0
	45	111	12.7	60	20*	0.95	1257	1562	1016,533,-25	0,0	1016,476,-38	0,0	1016,476,-13	0,0	1016 ,559 ,152	0,0
G2	-	112	12.7	45	none	0	1257	1562	1016,533,-25	0,0	1016,476,-38	0,0	1016,476,-13	0,0	1016 ,559 ,152	0,0
	-	113	12.7	45	220	0.068	1257	1562	1016,533,-25	0,0	1016,476,-38	0,0	1016,476,-13	0,0	1016 ,559 ,152	0,0
	-	114	12.7	45	180	0.082	1257	1562	1016,533,-25	0,0	1016,476,-38	0,0	1016,476,-13	0,0	1016 ,559 ,152	0,0
	-	115	12.7	45	150	0.092	1257	1562	1016,533,-25	0,0	1016,476,-38	0,0	1016,476,-13	0,0	1016 ,559 ,152	0,0
	-	116	12.7	45	100	0.14	1257	1562	1016,533,-25	0,0	1016,476,-38	0,0	1016,476,-13	0,0	1016 ,559 ,152	0,0
	-	117	12.7	45	80	0.19	1257	1562	1016,533,-25	0,0	1016,476,-38	0,0	1016,476,-13	0,0	1016 ,559 ,152	0,0
	-	118	12.7	45	60*	0.265	1257	1562	1016,533,-25	0,0	1016,476,-38	0,0	1016,476,-13	0,0	1016 ,559 ,152	0,0
	-	119	12.7	45	60	0.265	1257	1562	1016,533,-25	0,0	1016,476,-38	0,0	1016,476,-13	0,0	1016 ,559 ,152	0,0
	-	120	12.7	45	40	0.425	1257	1562	1016,533,-25	0,0	1016,476,-38	0,0	1016,476,-13	0,0	1016 ,559 ,152	0,0
	-	121	12.7	45	36*	0.53	1257	1562	1016,533,-25	0,0	1016,476,-38	0,0	1016,476,-13	0,0	1016 ,559 ,152	0,0
	-	122	12.7	45	20*	0.95	1257	1562	1016,533,-25	0,0	1016,476,-38	0,0	1016,476,-13	0,0	1016 ,559 ,152	0,0
G3	6,7	123	12.7	30	none	0	1257	1562	1016,533,-25	0,0	1016,476,-38	0,0	1016,476,-13	0,0	1016 ,559 ,152	0,0
	-	124	12.7	30	220	0.068	1257	1562	1016,533,-25	0,0	1016,476,-38	0,0	1016,476,-13	0,0	1016 ,559 ,152	0,0
	21	125	12.7	30	180	0.082	1257	1562	1016,533,-25	0,0	1016,476,-38	0,0	1016,476,-13	0,0	1016 ,559 ,152	0,0
	-	126	12.7	30	150	0.092	1257	1562	1016,533,-25	0,0	1016,476,-38	0,0	1016,476,-13	0,0	1016 ,559 ,152	0,0
	-	127	12.7	30	100	0.14	1257	1562	1016,533,-25	0,0	1016,476,-38	0,0	1016,476,-13	0,0	1016 ,559 ,152	0,0
	-	128	12.7	30	80	0.19	1257	1562	1016,533,-25	0,0	1016,476,-38	0,0	1016,476,-13	0,0	1016 ,559 ,152	0,0
	-	129	12.7	30	60*	0.265	1257	1562	1016,533,-25	0,0	1016,476,-38	0,0	1016,476,-13	0,0	1016 ,559 ,152	0,0
	-	130	12.7	30	60	0.265	1257	1562	1016,533,-25	0,0	1016,476,-38	0,0	1016,476,-13	0,0	1016 ,559 ,152	0,0
	26	131	12.7	30	40	0.425	1257	1562	1016,533,-25	0,0	1016,476,-38	0,0	1016,476,-13	0,0	1016 ,559 ,152	0,0
	-	132	12.7	30	36*	0.53	1257	1562	1016,533,-25	0,0	1016,476,-38	0,0	1016,476,-13	0,0	1016 ,559 ,152	0,0
	28	133	12.7	30	20*	0.95	1257	1562	1016,533,-25	0,0	1016,476,-38	0,0	1016,476,-13	0,0	1016 ,559 ,152	0,0

Table 4-4 Acoustic measurement conditions summary

Group	Aero case	Case	b, mm	U_0, m/s	Grit	h, mm	x_1, mm	x_2, mm	microphone 1		microphone 2		microphone 3		microphone 4	
									x, y, z mm	θ, φ	x, y, z mm	θ, φ	x, y, z mm	θ, φ	x, y, z mm	θ, φ
G4	1,2	134	12.7	20	none	0	na	na	1016,533,-25	0,0	1016,476,-38	0,0	1016,476,-13	0,0	1016 ,559 ,152	0,0
	-	135	12.7	25	none	0	na	na	1016,533,-25	0,0	1016,476,-38	0,0	1016,476,-13	0,0	1016 ,559 ,152	0,0
	3-11	136	12.7	30	none	0	na	na	1016,533,-25	0,0	1016,476,-38	0,0	1016,476,-13	0,0	1016 ,559 ,152	0,0
	-	137	12.7	35	none	0	na	na	1016,533,-25	0,0	1016,476,-38	0,0	1016,476,-13	0,0	1016 ,559 ,152	0,0
	12,13	138	12.7	40	none	0	na	na	1016,533,-25	0,0	1016,476,-38	0,0	1016,476,-13	0,0	1016 ,559 ,152	0,0
	-	139	12.7	45	none	0	na	na	1016,533,-25	0,0	1016,476,-38	0,0	1016,476,-13	0,0	1016 ,559 ,152	0,0
	-	140	12.7	50	none	0	na	na	1016,533,-25	0,0	1016,476,-38	0,0	1016,476,-13	0,0	1016 ,559 ,152	0,0
	-	141	12.7	55	none	0	na	na	1016,533,-25	0,0	1016,476,-38	0,0	1016,476,-13	0,0	1016 ,559 ,152	0,0
	-	142	12.7	60	none	0	na	na	1016,533,-25	0,0	1016,476,-38	0,0	1016,476,-13	0,0	1016 ,559 ,152	0,0
G5	-	143	12.7	20	40	0.425	1257	1562	1016,533,-25	0,0	1016,476,-38	0,0	1016,476,-13	0,0	1016 ,559 ,152	0,0
	-	144	12.7	25	40	0.425	1257	1562	1016,533,-25	0,0	1016,476,-38	0,0	1016,476,-13	0,0	1016 ,559 ,152	0,0
	25	145	12.7	30	40	0.425	1257	1562	1016,533,-25	0,0	1016,476,-38	0,0	1016,476,-13	0,0	1016 ,559 ,152	0,0
	-	146	12.7	35	40	0.425	1257	1562	1016,533,-25	0,0	1016,476,-38	0,0	1016,476,-13	0,0	1016 ,559 ,152	0,0
	33	147	12.7	40	40	0.425	1257	1562	1016,533,-25	0,0	1016,476,-38	0,0	1016,476,-13	0,0	1016 ,559 ,152	0,0
	-	148	12.7	45	40	0.425	1257	1562	1016,533,-25	0,0	1016,476,-38	0,0	1016,476,-13	0,0	1016 ,559 ,152	0,0
	-	149	12.7	50	40	0.425	1257	1562	1016,533,-25	0,0	1016,476,-38	0,0	1016,476,-13	0,0	1016 ,559 ,152	0,0
	-	150	12.7	55	40	0.425	1257	1562	1016,533,-25	0,0	1016,476,-38	0,0	1016,476,-13	0,0	1016 ,559 ,152	0,0
	43	151	12.7	60	40	0.425	1257	1562	1016,533,-25	0,0	1016,476,-38	0,0	1016,476,-13	0,0	1016 ,559 ,152	0,0
G6	14,15	152	25.4	20	none	0	na	na	1016,533,-25	0,0	1016,476,-38	0,0	1016,476,-13	0,0	1016 ,559 ,152	0,0
	16,17	153	25.4	30	none	0	na	na	1016,533,-25	0,0	1016,476,-38	0,0	1016,476,-13	0,0	1016 ,559 ,152	0,0
G7	25	154	12.7	30	40	0.425	1257	1562	1016,533,-25	0,0	1016,476,-38	0,0	1016,476,-13	0,0	1016 ,559 ,152	0,0
	26	155	12.7	30	40	0.425	1257	1867	1016,533,-25	0,0	1016,476,-38	0,0	1016,476,-13	0,0	1016 ,559 ,152	0,0
	27	156	12.7	30	40	0.425	1257	2172	1016,533,-25	0,0	1016,476,-38	0,0	1016,476,-13	0,0	1016 ,559 ,152	0,0
G8	33	157	12.7	40	40	0.425	1257	1562	1016,533,-25	0,0	1016,476,-38	0,0	1016,476,-13	0,0	1016 ,559 ,152	0,0
	34	158	12.7	40	40	0.425	1257	1867	1016,533,-25	0,0	1016,476,-38	0,0	1016,476,-13	0,0	1016 ,559 ,152	0,0
	35	159	12.7	40	40	0.425	1257	2172	1016,533,-25	0,0	1016,476,-38	0,0	1016,476,-13	0,0	1016 ,559 ,152	0,0
G9	51	160	25.4	20	40	0.425	1257	1562	1016,533,-25	0,0	1016,476,-38	0,0	1016,476,-13	0,0	1016 ,559 ,152	0,0
	52	161	25.4	20	40	0.425	1257	1867	1016,533,-25	0,0	1016,476,-38	0,0	1016,476,-13	0,0	1016 ,559 ,152	0,0
	53	162	25.4	20	40	0.425	1257	2172	1016,533,-25	0,0	1016,476,-38	0,0	1016,476,-13	0,0	1016 ,559 ,152	0,0
G10	60	163	25.4	30	40	0.425	1257	1562	1016,533,-25	0,0	1016,476,-38	0,0	1016,476,-13	0,0	1016 ,559 ,152	0,0
	61	164	25.4	30	40	0.425	1257	1867	1016,533,-25	0,0	1016,476,-38	0,0	1016,476,-13	0,0	1016 ,559 ,152	0,0
	62	165	25.4	30	40	0.425	1257	2172	1016,533,-25	0,0	1016,476,-38	0,0	1016,476,-13	0,0	1016 ,559 ,152	0,0

Table 4-4 Acoustic measurement conditions summary

Group	Aero case	Case	b, mm	U_0, m/s	Grit	h, mm	x_1, mm	x_2, mm	microphone 1		microphone 2		microphone 3		microphone 4	
									x, y, z mm	θ, φ	x, y, z mm	θ, φ	x, y, z mm	θ, φ	x, y, z mm	θ, φ
G11	20	166	12.7	30	180	0.082	1257	1562	1016,533,-25	0,0	1016,476,-38	0,0	1016,476,-13	0,0	1016 ,559 ,152	0,0
	21	167	12.7	30	180	0.082	1257	1867	1016,533,-25	0,0	1016,476,-38	0,0	1016,476,-13	0,0	1016 ,559 ,152	0,0
	22	168	12.7	30	180	0.082	1257	2172	1016,533,-25	0,0	1016,476,-38	0,0	1016,476,-13	0,0	1016 ,559 ,152	0,0
G12	29	169	12.7	40	180	0.082	1257	1562	1016,533,-25	0,0	1016,476,-38	0,0	1016,476,-13	0,0	1016 ,559 ,152	0,0
	30	170	12.7	40	180	0.082	1257	1867	1016,533,-25	0,0	1016,476,-38	0,0	1016,476,-13	0,0	1016 ,559 ,152	0,0
	31	171	12.7	40	180	0.082	1257	2172	1016,533,-25	0,0	1016,476,-38	0,0	1016,476,-13	0,0	1016 ,559 ,152	0,0
G13	46	172	25.4	20	180	0.082	1257	1562	1016,533,-25	0,0	1016,476,-38	0,0	1016,476,-13	0,0	1016 ,559 ,152	0,0
	47	173	25.4	20	180	0.082	1257	1867	1016,533,-25	0,0	1016,476,-38	0,0	1016,476,-13	0,0	1016 ,559 ,152	0,0
	48	174	25.4	20	180	0.082	1257	2172	1016,533,-25	0,0	1016,476,-38	0,0	1016,476,-13	0,0	1016 ,559 ,152	0,0
G14	55	175	25.4	30	180	0.082	1257	1562	1016,533,-25	0,0	1016,476,-38	0,0	1016,476,-13	0,0	1016 ,559 ,152	0,0
	56	176	25.4	30	180	0.082	1257	1867	1016,533,-25	0,0	1016,476,-38	0,0	1016,476,-13	0,0	1016 ,559 ,152	0,0
	57	177	25.4	30	180	0.082	1257	2172	1016,533,-25	0,0	1016,476,-38	0,0	1016,476,-13	0,0	1016 ,559 ,152	0,0
G15	-	178	25.4	18	clean	0	na	na	905, 466,0	-37, 0	996, 567, 0	-47, 0	1184,696,0	-64,0	1551, 774, 0	-92,0
	-	179	25.4	23	clean	0	na	na	905, 466,0	-37, 0	996, 567, 0	-47, 0	1184,696,0	-64,0	1551, 774, 0	-92,0
	-	180	25.4	28	clean	0	na	na	905, 466,0	-37, 0	996, 567, 0	-47, 0	1184,696,0	-64,0	1551, 774, 0	-92,0
	-	181	25.4	32	clean	0	na	na	905, 466,0	-37, 0	996, 567, 0	-47, 0	1184,696,0	-64,0	1551, 774, 0	-92,0
	-	182	25.4	37	clean	0	na	na	905, 466,0	-37, 0	996, 567, 0	-47, 0	1184,696,0	-64,0	1551, 774, 0	-92,0
	-	183	25.4	41	clean	0	na	na	905, 466,0	-37, 0	996, 567, 0	-47, 0	1184,696,0	-64,0	1551, 774, 0	-92,0
	-	184	25.4	45	clean	0	na	na	905, 466,0	-37, 0	996, 567, 0	-47, 0	1184,696,0	-64,0	1551, 774, 0	-92,0
G16	-	185	25.4	18	20 LPI	0.118	1257	1803	905, 466,0	-37, 0	996, 567, 0	-47, 0	1184,696,0	-64,0	1551, 774, 0	-92,0
	-	186	25.4	23	20 LPI	0.118	1257	1803	905, 466,0	-37, 0	996, 567, 0	-47, 0	1184,696,0	-64,0	1551, 774, 0	-92,0
	-	187	25.4	28	20 LPI	0.118	1257	1803	905, 466,0	-37, 0	996, 567, 0	-47, 0	1184,696,0	-64,0	1551, 774, 0	-92,0
	-	188	25.4	32	20 LPI	0.118	1257	1803	905, 466,0	-37, 0	996, 567, 0	-47, 0	1184,696,0	-64,0	1551, 774, 0	-92,0
	-	189	25.4	37	20 LPI	0.118	1257	1803	905, 466,0	-37, 0	996, 567, 0	-47, 0	1184,696,0	-64,0	1551, 774, 0	-92,0
	-	190	25.4	41	20 LPI	0.118	1257	1803	905, 466,0	-37, 0	996, 567, 0	-47, 0	1184,696,0	-64,0	1551, 774, 0	-92,0
	-	191	25.4	45	20 LPI	0.118	1257	1803	905, 466,0	-37, 0	996, 567, 0	-47, 0	1184,696,0	-64,0	1551, 774, 0	-92,0
G17	-	192	25.4	18	20 LPI	0.118	1168	1880	752, 470, 27	31,2	830, 470,-338	31, -26	959,470,-527	31,-43	1059, 470, -617	31,-53
	-	193	25.4	23	20 LPI	0.118	1168	1880	752, 470, 27	31,2	830, 470,-338	31, -26	959,470,-527	31,-43	1059, 470, -617	31,-53
	-	194	25.4	28	20 LPI	0.118	1168	1880	752, 470, 27	31,2	830, 470,-338	31, -26	959,470,-527	31,-43	1059, 470, -617	31,-53
	-	195	25.4	32	20 LPI	0.118	1168	1880	752, 470, 27	31,2	830, 470,-338	31, -26	959,470,-527	31,-43	1059, 470, -617	31,-53
	-	196	25.4	37	20 LPI	0.118	1168	1880	752, 470, 27	31,2	830, 470,-338	31, -26	959,470,-527	31,-43	1059, 470, -617	31,-53
	-	197	25.4	42	20 LPI	0.118	1168	1880	752, 470, 27	31,2	830, 470,-338	31, -26	959,470,-527	31,-43	1059, 470, -617	31,-53
	-	198	25.4	46	20 LPI	0.118	1168	1880	752, 470, 27	31,2	830, 470,-338	31, -26	959,470,-527	31,-43	1059, 470, -617	31,-53

Table 4-4 Acoustic measurement conditions summary

Group	Aero case	Case	b, mm	U_0, m/s	Grit	h, mm	x_1, mm	x_2, mm	microphone 1		microphone 2		microphone 3		microphone 4	
									x, y, z mm	θ, φ	x, y, z mm	θ, φ	x, y, z mm	θ, φ	x, y, z mm	θ, φ
G18	-	199	25.4	18	20 LPI	0.118	1076	1971	752, 470, 27	31,2	830, 470,-338	31, -26	959,470,-527	31,-43	1059, 470, -617	31,-53
	-	200	25.4	23	20 LPI	0.118	1076	1971	752, 470, 27	31,2	830, 470,-338	31, -26	959,470,-527	31,-43	1059, 470, -617	31,-53
	-	201	25.4	27	20 LPI	0.118	1076	1971	752, 470, 27	31,2	830, 470,-338	31, -26	959,470,-527	31,-43	1059, 470, -617	31,-53
	-	202	25.4	32	20 LPI	0.118	1076	1971	752, 470, 27	31,2	830, 470,-338	31, -26	959,470,-527	31,-43	1059, 470, -617	31,-53
	-	203	25.4	37	20 LPI	0.118	1076	1971	752, 470, 27	31,2	830, 470,-338	31, -26	959,470,-527	31,-43	1059, 470, -617	31,-53
	-	204	25.4	41	20 LPI	0.118	1076	1971	752, 470, 27	31,2	830, 470,-338	31, -26	959,470,-527	31,-43	1059, 470, -617	31,-53
	-	205	25.4	46	20 LPI	0.118	1076	1971	752, 470, 27	31,2	830, 470,-338	31, -26	959,470,-527	31,-43	1059, 470, -617	31,-53
G19	-	206	25.4	18	20 LPI	0.118	1104	1943	752, 470, 27	31,2	830, 470,-338	31, -26	959,470,-527	31,-43	1059, 470, -617	31,-53
	-	207	25.4	23	20 LPI	0.118	1104	1943	752, 470, 27	31,2	830, 470,-338	31, -26	959,470,-527	31,-43	1059, 470, -617	31,-53
	-	208	25.4	27	20 LPI	0.118	1104	1943	752, 470, 27	31,2	830, 470,-338	31, -26	959,470,-527	31,-43	1059, 470, -617	31,-53
	-	209	25.4	32	20 LPI	0.118	1104	1943	752, 470, 27	31,2	830, 470,-338	31, -26	959,470,-527	31,-43	1059, 470, -617	31,-53
	-	210	25.4	37	20 LPI	0.118	1104	1943	752, 470, 27	31,2	830, 470,-338	31, -26	959,470,-527	31,-43	1059, 470, -617	31,-53
	-	211	25.4	41	20 LPI	0.118	1104	1943	752, 470, 27	31,2	830, 470,-338	31, -26	959,470,-527	31,-43	1059, 470, -617	31,-53
	-	212	25.4	45	20 LPI	0.118	1104	1943	752, 470, 27	31,2	830, 470,-338	31, -26	959,470,-527	31,-43	1059, 470, -617	31,-53
G20	-	213	25.4	18	20 LPI	0.118	1257	1803	752, 470, 27	31,2	830, 470,-338	31, -26	959,470,-527	31,-43	1059, 470, -617	31,-53
	-	214	25.4	23	20 LPI	0.118	1257	1803	752, 470, 27	31,2	830, 470,-338	31, -26	959,470,-527	31,-43	1059, 470, -617	31,-53
	-	215	25.4	27	20 LPI	0.118	1257	1803	752, 470, 27	31,2	830, 470,-338	31, -26	959,470,-527	31,-43	1059, 470, -617	31,-53
	-	216	25.4	32	20 LPI	0.118	1257	1803	752, 470, 27	31,2	830, 470,-338	31, -26	959,470,-527	31,-43	1059, 470, -617	31,-53
	-	217	25.4	37	20 LPI	0.118	1257	1803	752, 470, 27	31,2	830, 470,-338	31, -26	959,470,-527	31,-43	1059, 470, -617	31,-53
	-	218	25.4	41	20 LPI	0.118	1257	1803	752, 470, 27	31,2	830, 470,-338	31, -26	959,470,-527	31,-43	1059, 470, -617	31,-53
	-	219	25.4	45	20 LPI	0.118	1257	1803	752, 470, 27	31,2	830, 470,-338	31, -26	959,470,-527	31,-43	1059, 470, -617	31,-53
G21	44	220	12.7	60	36*	0.53	1346	1511	956,480,0	-46,0	1009,518,0	-51,0	1055,553,0	-56,0	918,429,0	-40,0
	44	221	12.7	60	36*	0.53	1346	1511	1095,577,0	-60,0	1147,604,0	-65,0	1201,627,0	-70,0	918,429,0	-40,0
	44	222	12.7	60	36*	0.53	1346	1511	1256,644,0	-75,0	1313,657,0	-80,0	1371,664,0	-85,0	918,429,0	-40,0
G22	-	223	25.4	60	Smooth	0	930	2450	2290,630,-940	0,-90	na	na	na	na	na	na
	-	224	25.4	60	80	0.19	930	2450	2290,630,-941	0,-91	na	na	na	na	na	na
	-	225	25.4	60	fabric	~0.08	930	2450	2290,630,-942	0,-92	na	na	na	na	na	na
	-	226	25.4	60	mylar	0	930	2450	2290,630,-943	0,-93	na	na	na	na	na	na

Table 4-4 Acoustic measurement conditions summary

4.7 Scalloping Correction

As discussed in Chapter 3 the acoustic enclosure was not fully anechoic and some resonance modes were noticeable in the acoustic spectra measured. Many of the acoustic spectra discussed in the remainder of this report have been partially corrected for this effect using a measured estimate of the acoustic response function of the chamber. To measure the acoustic response function a speaker was placed beneath the plate and attached to a 600 mm length of rigid 5 mm diameter PVC pipe. The pipe diameter was reduced to 2 mm using a series of adapters. This narrow end of the pipe was placed in a hole in the plate surface so that the pipe end was flush, within 1 mm, with the plate surface. The hole in the plate was located at x = 1256 mm on the tunnel centerline where y and z are zero. This location corresponds with the center point of roughness patches tested and listed in Table 4-4. Three microphones were located at the position of microphones 1, 2, and 3 from groups G1-G14. A fourth microphone was positioned on the plate 50 mm from the speaker exit. This microphone was located at x = 1221 mm, y = 35 mm, z = 0 mm and angled so that θ = -30°, φ = 0°. The fourth microphone was located between with the other three microphones to the speaker exit.

The speaker was driven with a white noise input generated from a function generator. Acoustic spectra were collected with each microphone. The microphone on the plate was removed before the spectra were collected with the other microphones to prevent interference due to blockage and scattering. To estimate the chamber response function the acoustic power spectra measured by microphones one through three was then divided by the acoustic power spectrum measured by the microphone on the plate. The difference in distance from microphone to speaker was accounted for using the spherical spreading law for each microphone. The resulting chamber response function is shown in Figure 4-4.

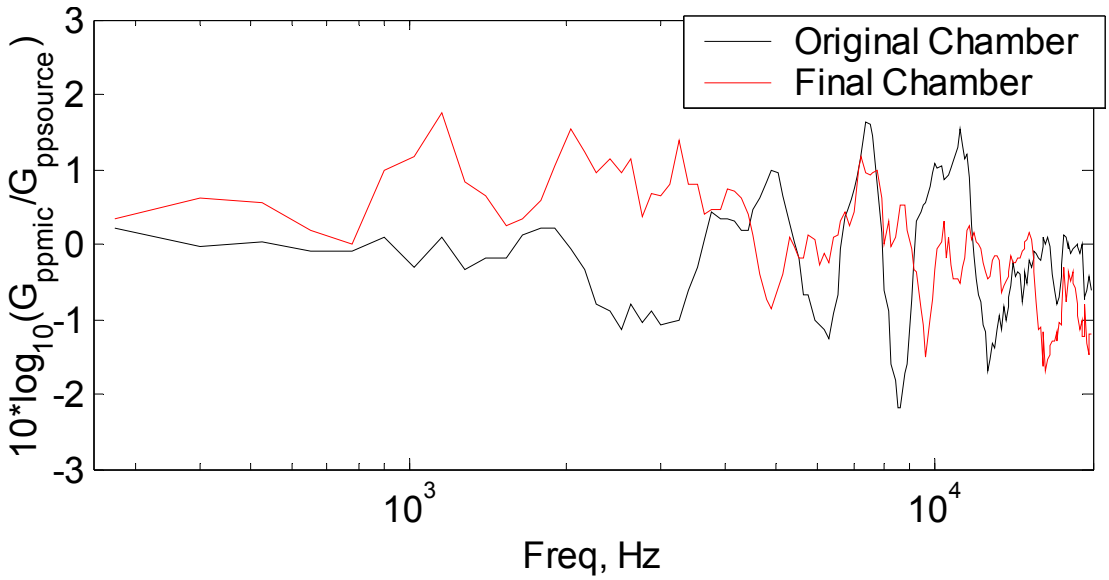

Figure 4-4 Acoustic response functions measured inside the acoustic enclosure. The black curve shows the original response measured above the shelf, the red curve shows the response measured after the shelf was modified to reduce scalloping.

The chamber response function in Figure 4-4 was used in conjunction with multiple microphones averaging to reduce the effects of scalloping on the acoustic spectra. The spectra presented for groups G1-G14 have been averaged over the 4 microphones, and corrected for average chamber effect measured at this location. The spatial averaging that results from averaging the spectra from the four separate microphones significantly reduces the scalloping in the spectra. The wavelength associated with the scalloping is on the order of 55 mm, so each microphone experiences the scalloping at different frequencies, because of the spatial phase variation. The average correction function determined from the three microphones used in the calibration measurement is then applied to the spectra. Above 10000 Hz the correction levels are less than 1 dB, below this frequency they are as high as 2 dB for some of the frequency intervals.

The spectra shown in Chapters 5 and 6 have been corrected using this method, with the exception of spectra showing the vertical directivity of the acoustic field over a 40 grit roughness patch. Spectra presented in Chapter 7 measured over the two-dimensional lens roughness have not been corrected. Based on the differences seen between the uncorrected and corrected spectra it is reasonable to assume the true spectra passes through a curve similar to the general shape of the uncorrected spectra presented.

4.8 Spectral Subtraction Method

To determine the effects of the presence of roughness on the measured acoustic spectra a spectral subtraction method was used. This subtraction is a linear subtraction of the acoustic power spectra measured with the roughness on the plate and with the clean plate under the same flow conditions. This technique is needed because the spectra are

measured using a single microphone, which cannot discriminate against source location as a phased array or similar device could. The purpose of the subtraction is to remove from the spectrum the acoustic levels that are essentially background noise due to the jet noise coming from the boundary layer flowing over a smooth surface. Equation 4.9 shows the process used for this subtraction process.

$$SPL_{roughness\ only} = 10\log_{10}\left(\frac{G_{pproughness} - G_{ppsmooth}}{P_{ref}^2}\right) \tag{4.9}$$

In Equation 4.9 G_{pp} is the acoustic power spectral density measured by the microphones for the cases with and without roughness under the same flow conditions. Figure 4-5 shows the results effect of carrying out this process on a typical acoustic spectrum. The spectra shown in Figure 4-5 have been smoothed by averaging spectral levels across ⅓ octave bands. (These are not ⅓ octave band levels, but per Hertz level averaged into bins with sizes corresponding to ⅓ octave bands.) During the subtraction any points that are less than 7% louder in the rough wall case than the smooth wall case are rejected since they are within the uncertainty of the spectral levels. The process removes the low frequency noise, which is due to background noise outside the acoustic enclosure, and noise due to the jet turbulence.

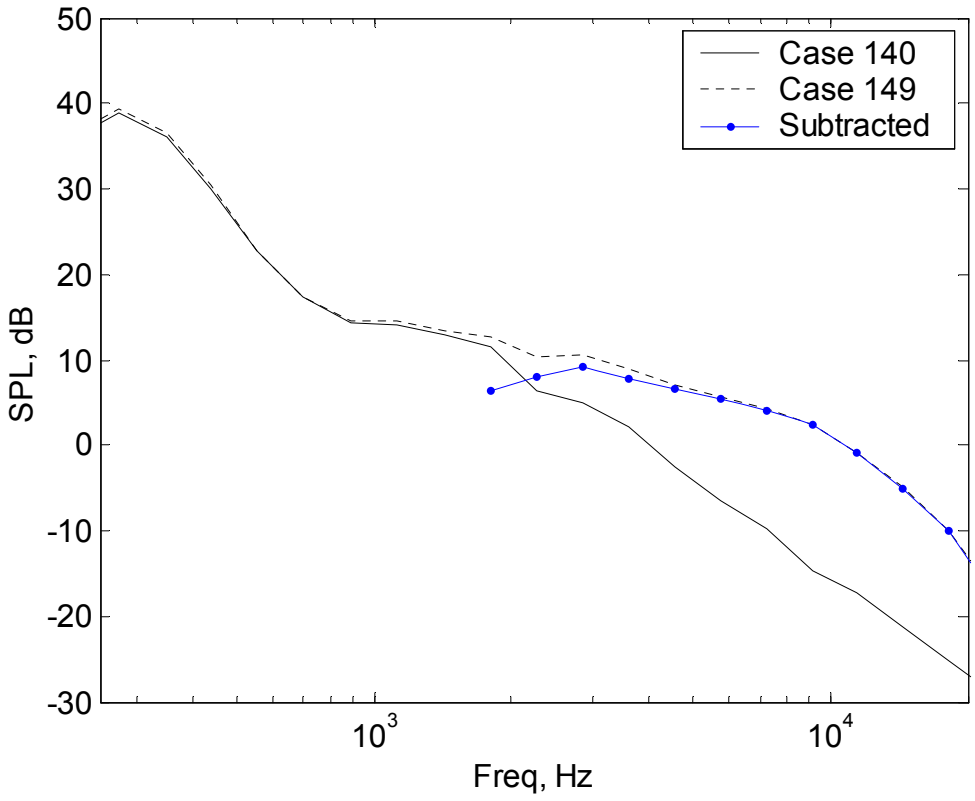

Figure 4-5 Acoustic spectra shown for the same flow conditions. One with roughness on the plate (Case 149), and one with a smooth plate (Case 140). The blue curve shows the spectrum due only to the roughness, which is found by subtracting the two spectra.

Chapter 5 Wall Jet Aerodynamics

The aerodynamic behavior of a wall jet flow is mentioned briefly in pervious sections, but will be discussed in more detail here. This section will summarize the results of Smith (2007), which studied the smooth and rough wall jet flow aerodynamics. The aerodynamic affects of adding roughness to the surface are also summarized, as they pertain to the acoustic field. These affects include the behavior during transition from smooth to rough surface, the affects of the roughness on the wall jet shape, and estimates of skin friction values.

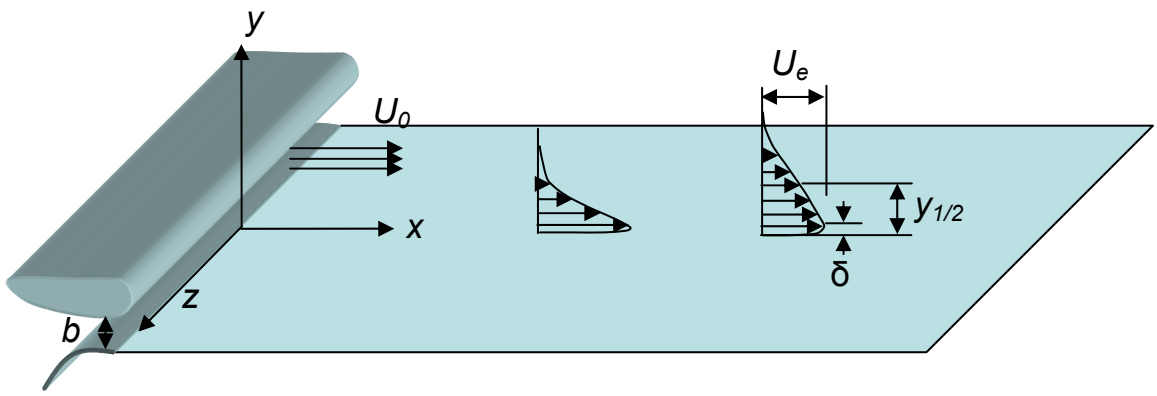

Figure 5-1 Schematic of the wall jet flow and reference system. The nozzle height, *b*, and the nozzle exit speed, U_0, can be adjusted by the facility setup. At each streamwise location the flow profiles can be described by a number of different scales shown in the figure as δ, $y_{1/2}$, and U_e.

Figure 5-1 shows the wall jet flow schematically. The flow is controlled by the conditions at the nozzle, including the nozzle height, b, and the nozzle exit velocity, U_0. As the flow moves along the plate, it develops into two regions, a near wall boundary layer region and an outer shear layer region. The boundary layer region is dominated by the shear along the wall and is similar in many respects to a traditional boundary layer flow. The distance from the wall to the location of the maximum mean velocity, U_e, that defines the end of the boundary layer region, is defined as δ and shown in Figure 5-1. The outer region is controlled by the mixing affects from the flow and the stagnant air above the flow. This region is defined by the same velocity scale, U_e, and a length scale associated with the wake half height, $y_{1/2}$. This length is defined as the height where the velocity is half the maximum velocity in the mixing layer region.

5.1 Smooth Plate Measurements

Table 4-2Table 4-2 lists the smooth plate flow conditions that were measured. The measured conditions identify the affects of variation in nozzle height, jet exit speed, and position along the plate. Figure 5-2 shows the vertical profiles measured as part of group

B from Table 4-2. All of the profiles were measured for jet exit conditions of U_0 = 30 m/s and b = 12.7 mm. The measurement location is shown in the legend in mm. Figure 5-2 (a) clearly shows the general behavior of the wall jet flow. As the distance from the jet exit increases the jet velocity decays and the boundary layer region grows. The peak in the velocity also broadens as the boundary layer and mixing layer grow along the plate.

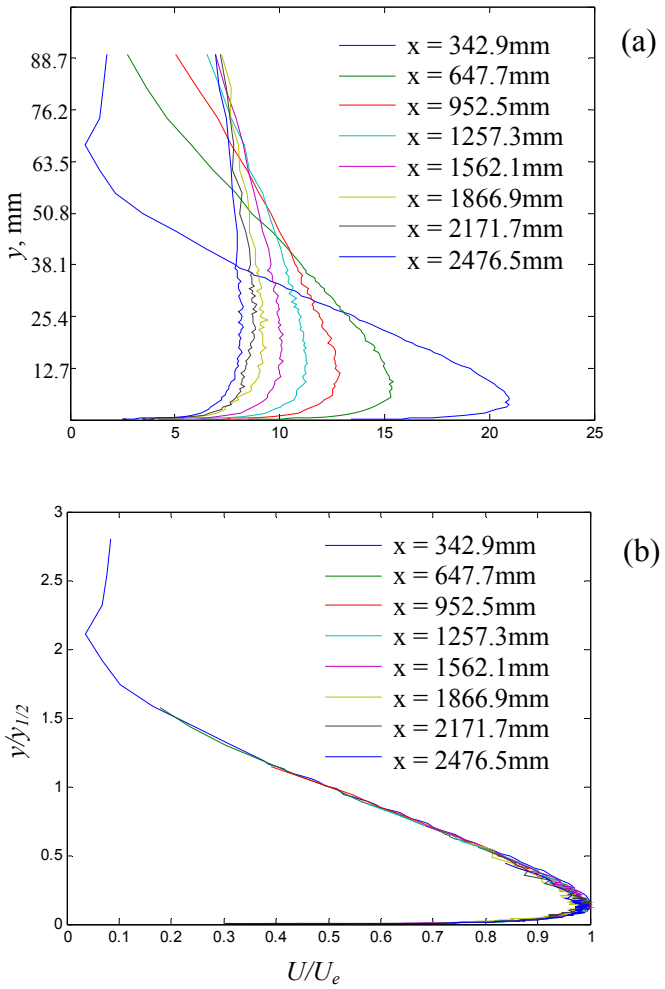

Figure 5-2 Vertical velocity profiles measured on the center line of the smooth plate at several downstream locations. The legend lists the distance from the nozzle to the measurement location in millimeter. (a) Measured levels plotted as measured. (b) Velocity profiles normalized on the local maximum velocity and half velocity height.

Figure 5-3 shows all of the data measured in Table 4-2 normalized on U_e and $y_{1/2}$. This includes not only the effect of streamwise location, but also shows measurements at three different nozzle exit velocities, and two different nozzle heights. Also shown in Figure 5-3 is a curve representative of the collapse reported by Wygnanski *et al.* (1992) for experimental wall jet data measured in another facility. The quality of the data collapse and its agreement with the data set of Wygnanski *et al.* (1992) suggests that the flow would be well modeled by the standard two-dimensional wall jet model. Figure 5-4 shows three measurements that were made to confirm the two-dimensional behavior of the wall jet flow. The green and red profiles were measured for the same conditions as

cases 5 and 8 from Table 4-2, the blue curve was measured for the same flow conditions but along a line of x = 38 mm. The blue profile measured near the nozzle exit showed variations of 0.2% around the mean velocity across the entire span. At the two downstream locations x = 953 mm and x = 1867 mm the two-dimensional region is reduced in space to 800 mm, where velocity variations are 3.4% and 2.4% of the local mean values respectively.

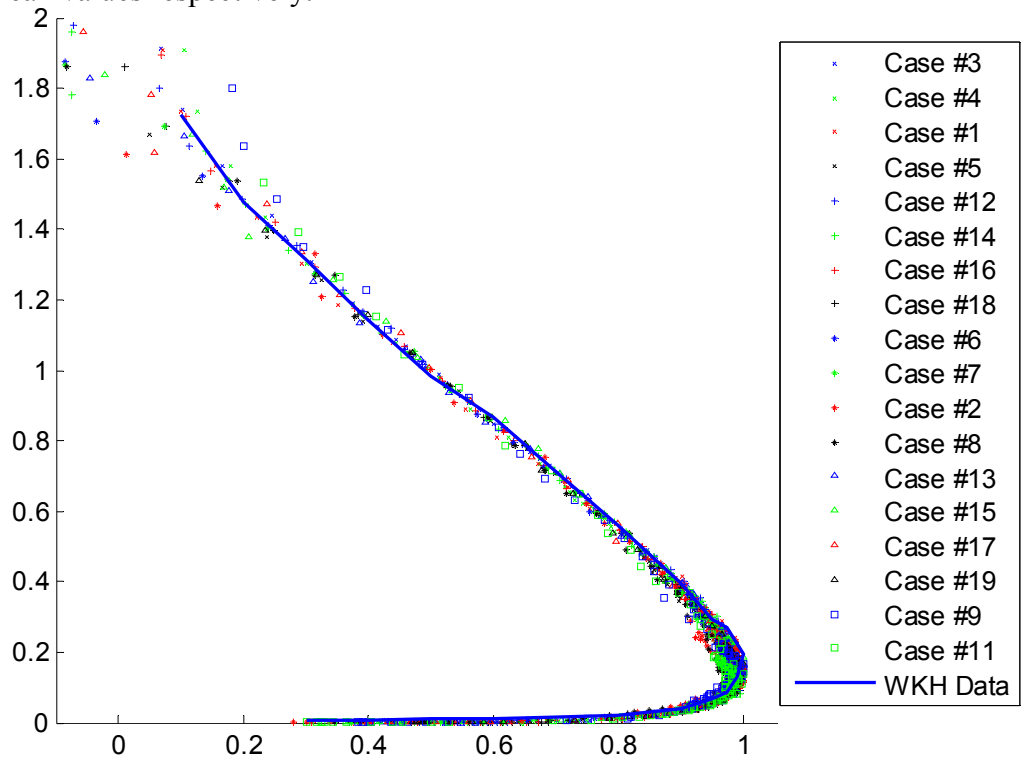

Figure 5-3 Normalized mean velocity profiles for all the smooth wall cases compared with Wygnanski *et al.* (1992).

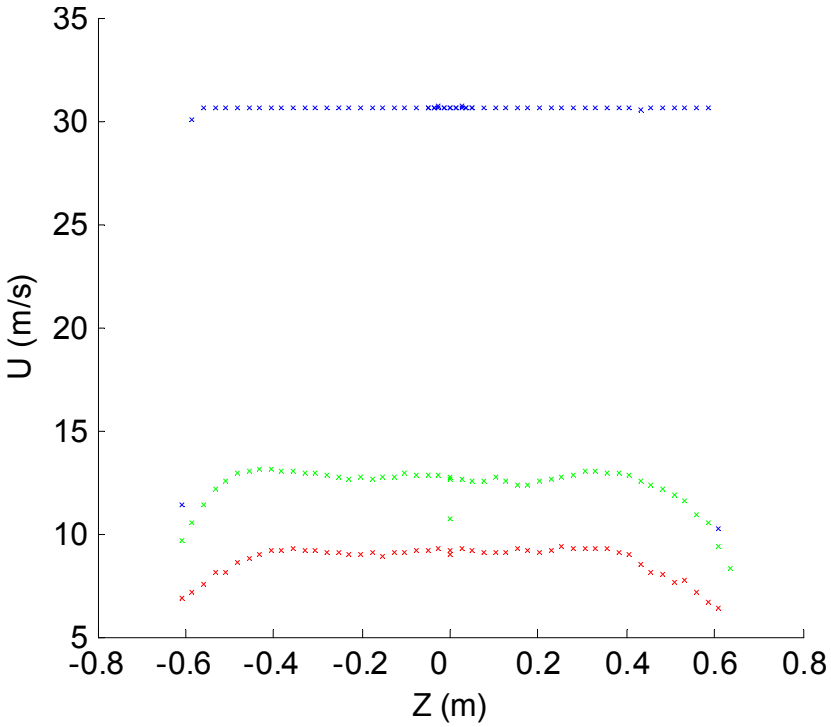

Figure 5-4 Spanwise velocity profiles measured at x=38 mm (blue symbols), 952 mm (green symbols) and 1867 mm (red symbols) at a distance y of 6.4 mm above the test plate for a nozzle height of 12.7 mm and nominal exit velocity U_0 of 30 m/s.

5.2 Two-Dimensional Wall Jet Flow Model

The results of Narasimha *et al.* (1973), and confirmed by Wygnanski *et al*. (1992) show that the scaling parameters U_{vve} and $y_{1/2}$ can be modeled as shown in Equation 5.1. These equations are derived from a momentum flux analysis of the wall jet flow.

$$U_e \sim \frac{J}{\nu}\left[\frac{(x-x_o)J}{\nu^2}\right]^n = U_o Re_j^{n+1} Re_{x-xo}^n$$
$$y_{1/2} \sim \frac{\nu^2}{J}\left[\frac{(x-x_o)J}{\nu^2}\right]^m = bRe_j^{m-2} Re_{x-xo}^m \quad (5.1)$$

Where J is the jet momentum parameter $J = U_o^2 b$, and the virtual origin and exponents are set to best match the measurements. For this facility x_0 = 75 mm, and n and m equal to 0.914 and -0.512, respectively, results in rms errors of 3.2% for U_e and 5.5% for $y_{1/2}$ when compared with all experimental data. These values compare well with the values reported by Wgnanski *et al*. (1992) who reported values of 0.881 and -0.472 for n and m respectively. It should also be noted that since all profiles collapse to the same non-dimensional curve the model for $y_{1/2}$ in Equation 5.1 can be used equally well for any vertical length scale by multiplying it with the appropriate ratio. Based on the measured profile shape the boundary layer thickness, or height to maximum velocity is $y_{1/2}$/7.11. Similarly the displacement and momentum thicknesses can be related to the boundary layer thickness by constants of 0.0746, and 0.0459 respectively. Figure 5-5 shows the

extent to which these length scales are related to one another by these constants. Figure 5-6 shows the extent to which the models expressed by Equation 5.1 match the measured normalizing parameters for the wall jet flow. Each symbol in Figure 5-6 represents either the local maximum velocity or the boundary layer thickness computed for one of the test conditions presented in Table 4-2. For each of the nozzle conditions, Equation 5.1 is used to predict the same quantities. The predicted values are plotted on the vertical axis, and the measured values on the horizontal axis. Excellent agreement can be seen for all cases.

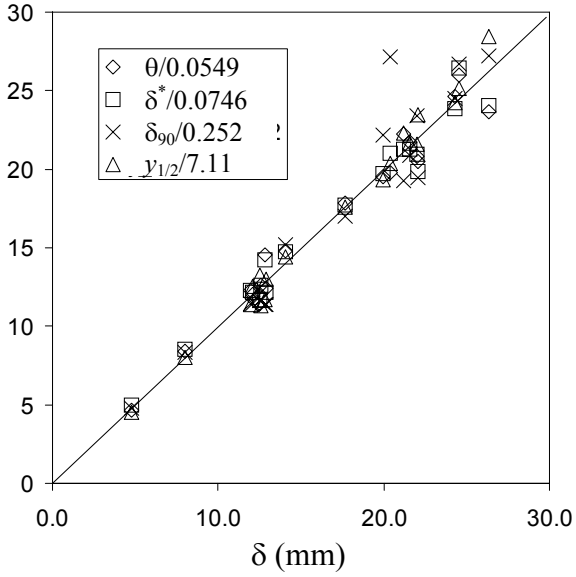

Figure 5-5 Plot of measured boundary layer length scales compared with measured boundary layer thickness for smooth wall jet flow cases measured in table 3-2.

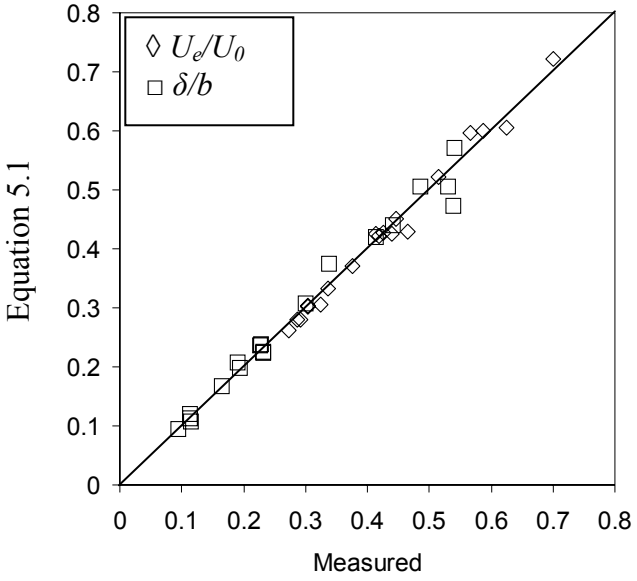

Figure 5-6 Comparison of velocity and length scales modeled by Equation 5.1 and measured in the wall jet facility.

5.3 Rough Wall Aerodynamic Measurements

A series of aerodynamic measurements were made with roughness on the wall to determine the effects of the presence of the roughness. These are listed in Table 4-3. The first group of measurements examined here, look at the effects of transitioning from a smooth to a rough surface by measuring the flow after it had developed over different lengths of a roughness fetch. Shown and discussed here are cases 20-24 from Table 4-3. In these cases the wall jet flow was generated with a nozzle height of 12.7 mm and a nozzle exit speed of 30 m/s and developed over the smooth plate until encountering a 610 mm wide fetch of 40 grit roughness, with a mean roughness height of 0.425 mm. This roughness fetch was attached 1245 mm downstream from the nozzle exit. Measurements at x=1410, 1562, 1867 and 2172 mm, taken 2 mm downstream of the end of the roughness patch, show that the overall wall jet behavior is maintained, shown in Figure 5-7. The velocity decays as the flow moves downstream and the boundary layer thickness tends to increase. One would expect the flow to have reached rough wall equilibrium given that the most downstream location is over 60 initial boundary layer thicknesses downstream from the leading edge of the roughness patch. At this location a profile for the same flow conditions is also shown in Figure 5-7, which was measured with no roughness patch. In this view at least the presence of the roughness appears to have a relatively small effect of the flow behavior.

Figure 5-7 shows velocity profiles measured downstream of different lengths of 40 grit roughness for a nozzle exit speed of 30 m/s and a nozzle height of 12.7 mm, cases 24-27 in Table 4-3. The general behavior of the wall jet is maintained over the roughness patch. Also shown in Figure 5-7 is a smooth wall profile measured at the same location as the most downstream rough wall measurement. Comparing these two profiles shows that the roughness does not reduce U_e at this location relative to its clean plate value.

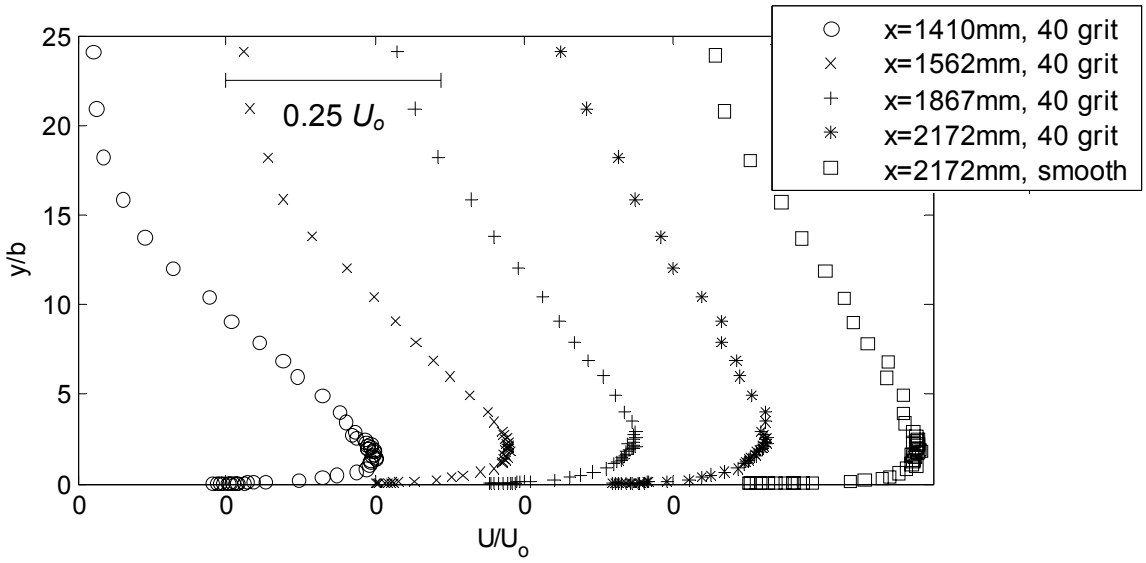

Figure 5-7 Mean velocity profiles measured after different lengths of 40 grit sandpaper. The sandpaper fetch begins at x = 1245 mm for all cases. The curve marked by squares was measured under the same conditions as the curve marked by * but with no roughness on the plate.

Figure 5-8 shows the profiles presented in Figure 5-7 normalized on their local velocity and length scales. The curve in blue corresponds to the case with no roughness present shown in Figure 5-7. In this format, we can see several affects that will be important for determining the appropriate scales to use when modeling the radiated roughness noise. The first result is that the roughness does not noticeably affect the outer region of the flow. Figure 5-8 (a) shows that above a height of $0.5y_{1/2}$ the smooth and rough wall cases all collapse to the same curve. However, in the near wall region, below δ of 1, the roughness has a significant effect. The rough wall cases all show a velocity deficit relative to the smooth wall case. The inner region profile is less full in the near wall region creating a larger boundary layer thickness but not affecting the value of U_e at each location. This shift in profile shape increases the other length scales as well, such as the displacement, and momentum thicknesses, which were fixed ratios of δ or $y_{1/2}$ for the smooth wall case. A final thing to notice is that all the rough wall cases, except case 32 measured at the most upstream location, collapse to the same profile. This suggests that they reach a new equilibrium growth rate at the first measurement location which is 165 mm downstream from the beginning of the roughness patch. The results in Figure 5-8 show that U_e can be modeled for the flow over roughness patches using the same equations as the smooth wall case; however, the length scales associated with the flow cannot be modeled with the smooth wall equations. Figure 5-9 illustrates how well the smooth wall model predicts the maximum velocity variations even in the presence of roughness. The measured maximum velocity for the cases in Table 4-3 are plotted against the values predicted by Equation 5.1, which is the smooth plate model for the same flow and measurement locations as the cases in Table 4-3. The figure shows the model works well, to within a few percent of the measured values.

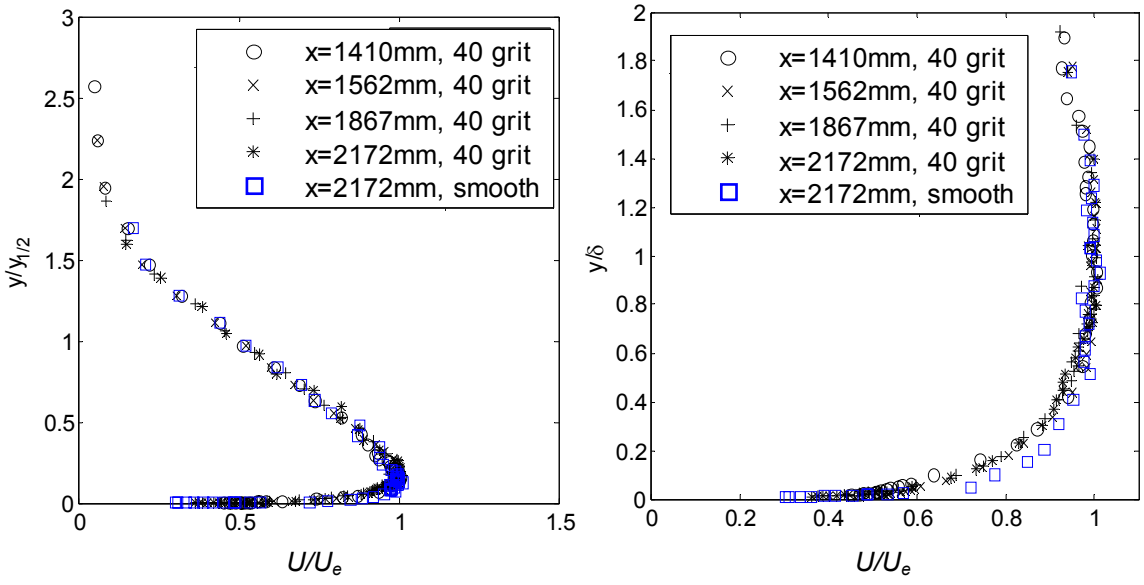

Figure 5-8 Mean velocity profiles measured after different lengths of 40 grit roughness. (a) Shows these profiles normalized on $y_{1/2}$ and edge velocity. (b) Shows the same measurements in the inner region. The blue curve was measured at the same location as the downstream most roughness case but with no roughness present.

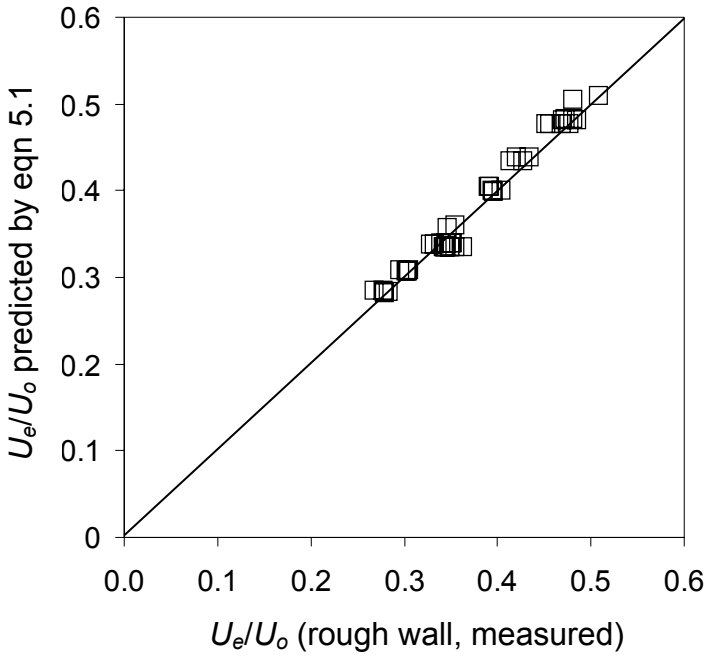

Figure 5-9 Maximum velocity values predicted by Equation 5.1 for conditions of Table 4-3 plotted against the measured maximum velocity values.

Similar results are seen in the turbulence profiles measured for cases 20-24 from Table 4-3. Streamwise turbulence intensity profiles measured with a single hotwire probe are shown in Figure 5-10(a) in absolute terms, and normalized in Figure 5-10 (b) and (c). In Figure 5-10 one can see the turbulence intensity profile shape has three points, which may be of interest as scaling parameters. The maximum turbulence intensity, u'_{max}, values are found in the shear layer away from the wall. The height of the turbulence intensity maximum, given by the symbol $y_{u'max}$, is near $y_{1/2}$ and is almost unaffected by the presence of the roughness. This effect can be seen in Figure 5-11, which shows the influence of different roughness grit sizes on several length scales that could be used for acoustic scaling. There is also a local maximum near the wall region that is defined by u'_{maxbl} and $y_{u'maxbl}$. Just above this local maximum is a local minimum, or in some cases an inflection point, when the local maximum and minimum cannot be separated, in the vertical profile. This location is defined by u'_{min} and $y_{u'min}$. The effectiveness of each of these length and velocity scales in normalizing the far field acoustics are discussed in Chapter 5. Again, the overall behavior of the flow is maintained as flow passes over the roughness patch. The normalized profiles show that the presence of the roughness increases the turbulence intensities near the wall, below δ = 0.5; however, the maximum increase seen is on the order of 10% of the clean plate turbulence intensity.

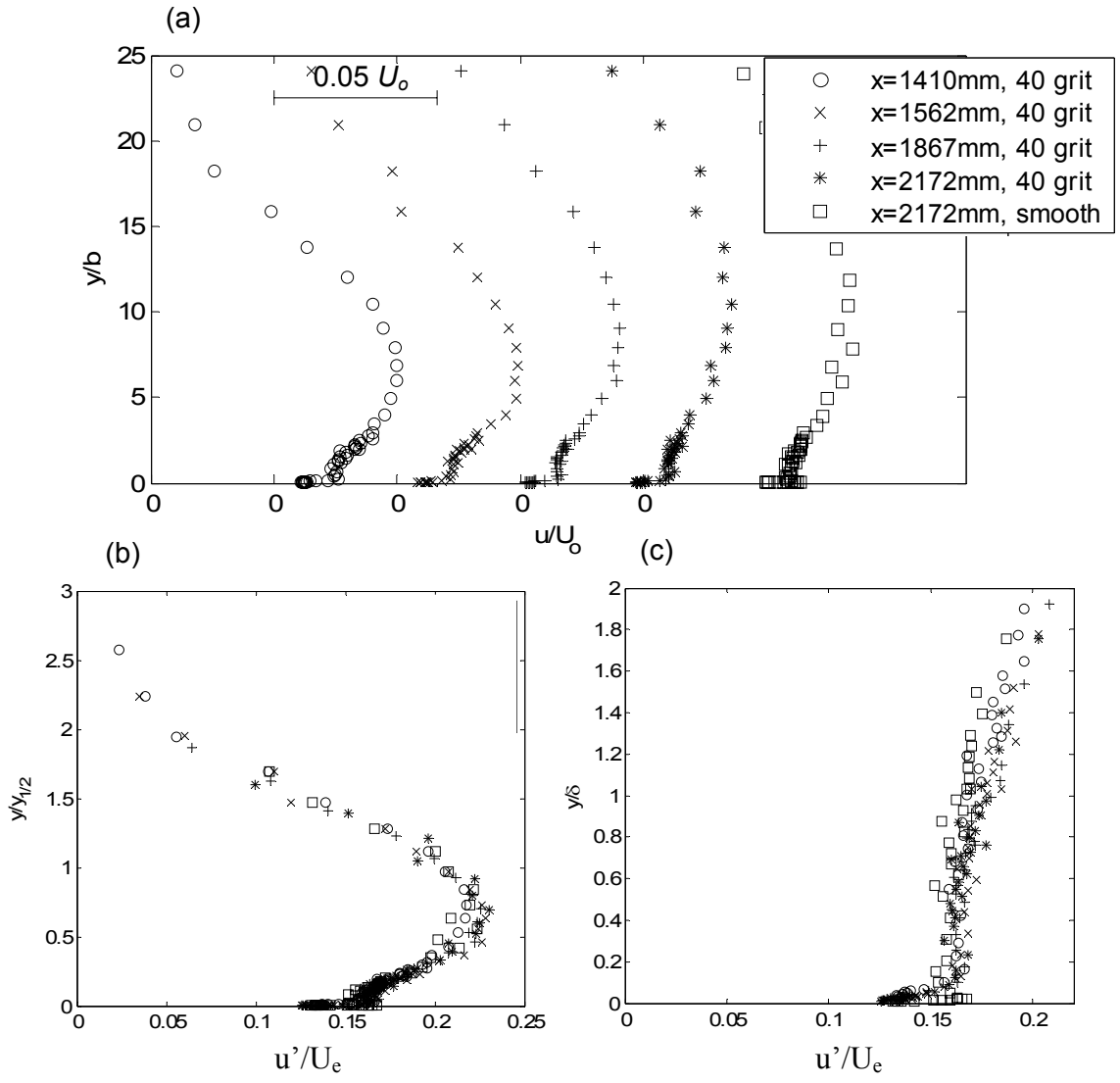

Figure 5-10 Turbulence intensity profiles measured downstream of patches of different lengths of 40-grit sandpaper roughness (cases 32 to 35 from Table 4-3) compared with a profile measured above the smooth wall (case 10 from Table 4-2). The nozzle height is 12.7mm and jet exit velocity 30 m/s for all cases. (a) Normalized on the fixed scales U_o and b, (b) normalized on mixing layer mean flow scales U_e and $y_{1/2}$, (c) Normalized on boundary layer scales U_e and δ.

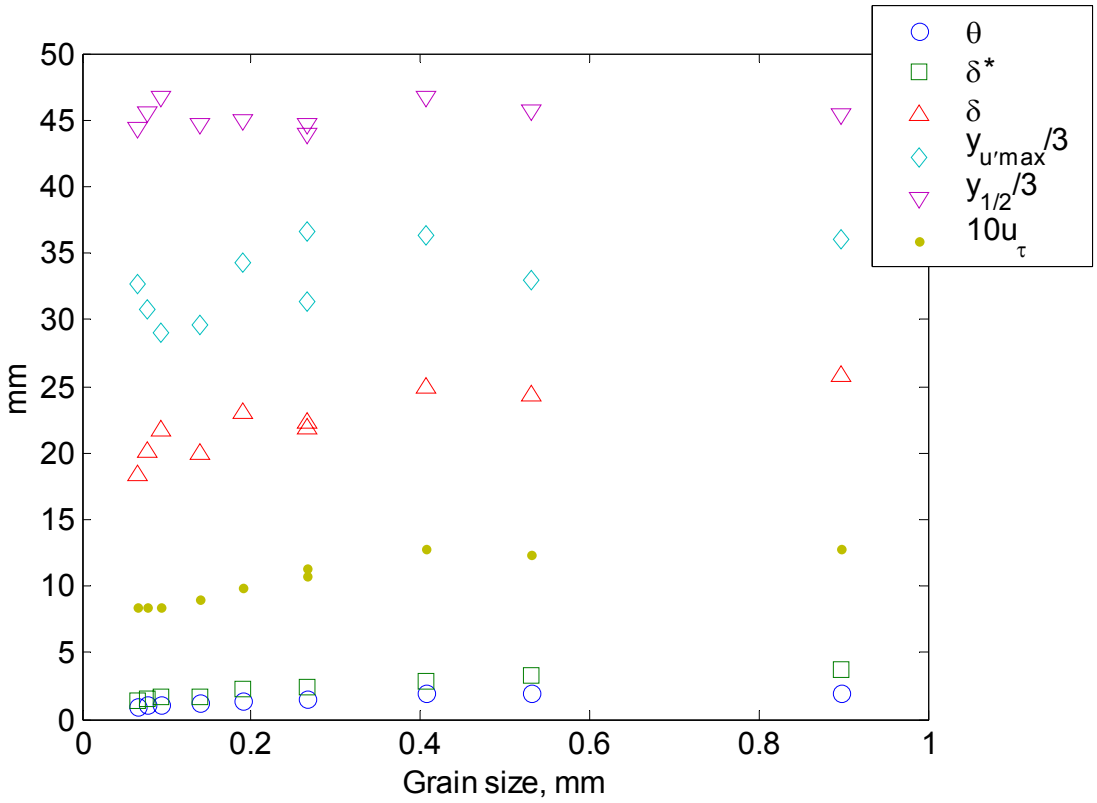

Figure 5-11 Length scales measured downstream of a 305 mm long roughness patches of different sandpaper roughness sizes. Measurements are taken from cases 37-45, group J, of Table 4-3 with a nozzle height of 12.7 mm and a jet exit velocity of 60 m/s.

Figure 5-12 shows the effects of different roughness heights on the streamwise turbulence profile. The profiles shown in this figure were measured under the same flow conditions at the trailing edge of roughness patches made from different grits, Group J in Table 4-3. The flow was generated by a nozzle height of 12.7 mm with a U_0 =30 m/s. The roughness patch began 1245 mm from the nozzle exit, and had a streamwise length of 305 mm, and a spanwise length of 610 mm, keeping it within the two-dimensional portion of the wall jet flow. The mean roughness height ranges from 0.068 mm to 0.95 mm. The profiles show that as the roughness height is increased the velocity deficit seen in Figure 5-8 increases. Smith (2007) shows for all the roughness cases the maximum velocity achieved still matches that predicted for a smooth plate under the same conditions, but the location is pushed progressively farther from the wall. The turbulence intensity profiles display a similar behavior with the near wall maximum being pushed away from the wall and the turbulence levels increasing with the roughness size. Because these profiles were measured 2 mm downstream of the end of the roughness patch, the thickness of the sandpaper backing does affect the near wall profile. The variations in the near wall profiles are unlikely to affect the integrated parameters that are used for scaling the acoustic spectra.

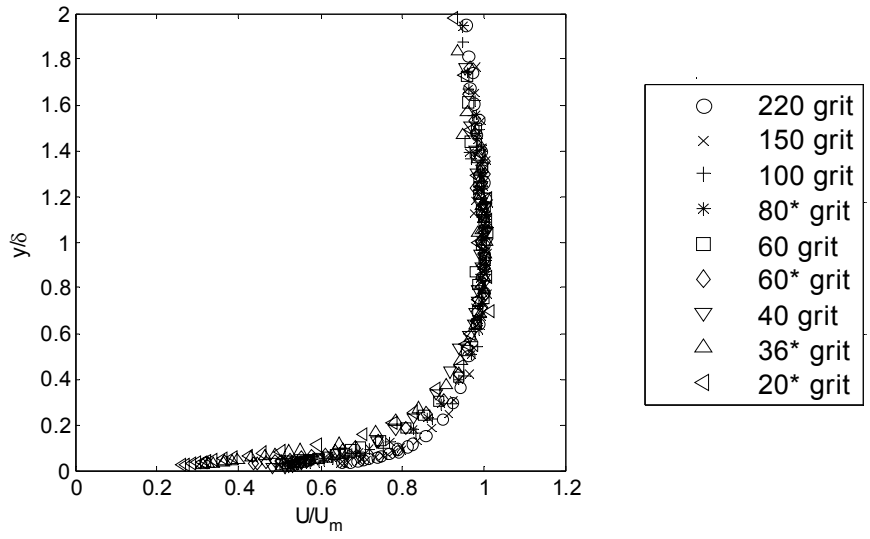

Figure 5-12 Mean velocity profiles measured downstream of a 310 mm long roughness fetch of different roughness heights. The roughness patch began at x = 1245 mm with a wall jet flow from a nozzle height of 12.7 mm and U_0 = 30 m/s

Chapter 6 Acoustic Measurements from Stochastic Roughness

This chapter presents measurements of the acoustic field generated by flow over stochastic surface roughness. Different grits of sandpaper roughness, discussed in Chapter 4, were tested under a number of different flow conditions. The acoustic measurements presented in this chapter are listed as groups G1-G14 in Table 4-4. Aerodynamic data is drawn from Table 4-2 and Table 4-3. The results are presented in four main sections. The first section looks at measurements from groups G4 and G5, which investigated the effects of different flow velocities on the far field sound. The second section looks at the effects of different roughness heights on the far field sound, groups G1-G3. The next section presents the results from group G21 of Table 4-4 that looked at the directivity from a patch of 40 grit sandpaper in a plane normal to the plate surface. The final section looks at the effects of fetch length. In each section acoustic measurements are presented and discussed, along with comparisons with different scaling models discussed in Chapter 1.

6.1 Effects of Velocity

6.1.1 Acoustic Measurements

To investigate the effects of different velocity scales on the far field roughness noise, a series of measurements were taken over a range of flow velocities. The conditions are defined in groups G4 and G5 of Table 4-4. A patch of 40 grit Aluminum oxide sand paper, with a mean grain size of 0.425 mm, was attached to the surface of the plate beginning 1257 mm downstream from the nozzle exit. The patch was 610 mm wide and 305 mm long. The mean two-dimensional region of the wall jet in this region is 800 mm wide, so the roughness patch is fully within the two-dimensional region of the wall jet flow. Acoustic spectra were measured with three B&K microphones facing downstream parallel to the plate located on a 50mm equilateral triangle centered at x = 1000 mm, y = 510 mm, and z = 0 mm. Acoustic spectra were measured at nozzle exit velocities ranging nominally from 20 m/s to 60 m/s in 5 m/s steps. For all cases the nozzle height remained fixed at 12.7 mm. Three of the ten flow conditions were measured aerodynamically, cases 25, 33, and 43 from Table 4-3, to determine the effects of the roughness patch on the wall jet flow. Figure 5-9 shows that the roughness patch had almost no effect on the local maximum velocity as compared to the predicted values for the smooth wall flow. Throughout this section this fact will be used to determine the appropriate velocity scaling of the acoustic spectra.

Figure 6-1 shows the raw 1 Hz-bandwidth spectra measured for both the smooth and rough surfaces for each of the velocities measured, referenced to 20×10^{-6}Pa. The spectra are presented in pairs; the solid curves are measured with no roughness on the plate and the dotted lines with the 40 grit roughness patch installed. The nozzle exit speed for each roughness pair is shown in the legend. The spectra show the roughness

begins to increase sound levels around 1000 Hz, and remains higher than the smooth surface levels until the frequency limit of the measurement at 20 kHz. The acoustic spectra from the rough surface flow are more than 20 dB louder than the smooth wall at frequencies above 18 kHz for the three highest velocities.

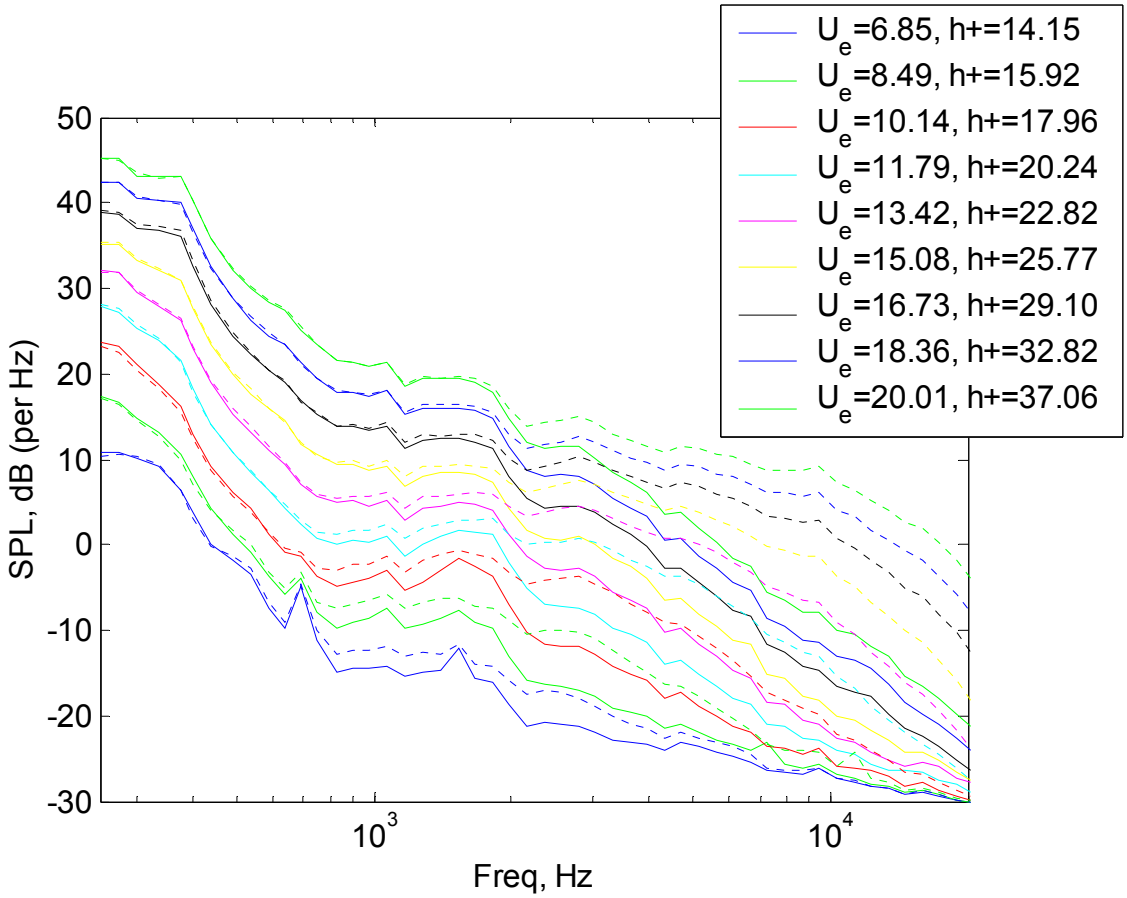

Figure 6-1 Raw acoustic spectra measured by a single microphone at different speeds in m/s over a clean surface (solid) and a 305x610 mm patch of 40 grit sandpaper (dotted).

Figure 6-2 shows the acoustic spectra due only to the addition of the roughness. The clean plate spectra have been linearly subtracted to leave only the additional sound generated when the roughness is added to the plate. The spectra are also shown as spectral density levels averaged in ⅛ octave bands and have been averaged and corrected for chamber effects using the method presented in Chapter 4. This figure clearly shows two important behaviors that result from changes in velocity on the far field acoustic spectra. The first result is that the sound level significantly rises with increases in velocity. The figure shows nearly a 30 dB increase in sound level for average edge velocities which range from 6 to 20 m/s. In addition to the rise in spectral levels, the peak also shifts to higher frequencies as the velocity increases. Both of these effects are consistent with the models presented in Chapter 1 to model roughness noise. The next section will look at how well these models perform with this data.

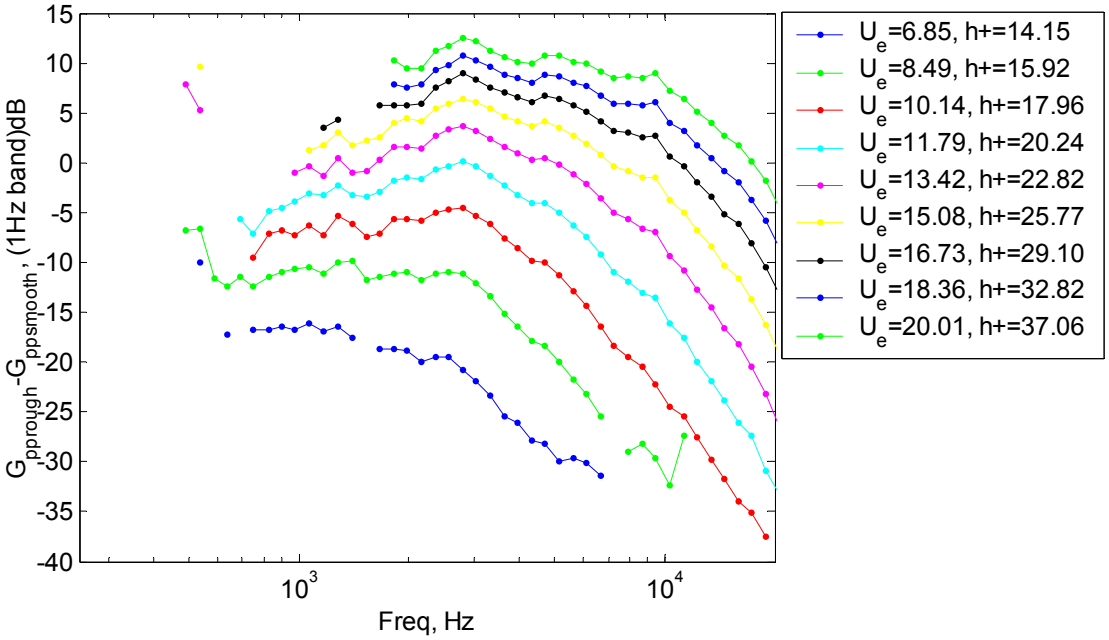

Figure 6-2 Linear difference in rough wall and smooth wall spectra plot on a decibel scale referenced to 20×10^{-6}Pa. The legend lists the mean edge velocity over the patch, averaged between the leading and trailing edge measured values, and h^+, based on the mean skin friction velocity.

6.1.2 Spectral Scaling

This section presents the acoustic spectra scaled on many of the scaling models defined in Chapter 1. This is somewhat complicated by the fact that the aerodynamic scales in the models of Chapter 1 are varying along the length of the roughness patch. The scaling parameters section explains how the aerodynamic scaling parameters are determined for the acoustic cases presented in the previous section. The next section, scaling models, discusses how the various models from Chapter 1 describe the measured spectra.

6.1.2.1 Scaling Parameters

For the data presented in the previous section the patch length is 305 mm, beginning 1245 mm downstream of the nozzle exit. To compare the effectiveness of the scaling models presented in Chapter 1, a single value of the scaling velocity and length scale must be selected for each condition. However for any type of flow these parameters will change over the roughness patch as the flow develops. For the spectra presented in this section the characteristic value for the scaling parameters is taken to been the mean value between the values measured at the front and back of the roughness patch. For the conditions of the run, the local maximum velocity decreases 12% along the length of the roughness patch. If the sound level scaled with the 5th power of edge velocity this would result in the trailing edge producing 2.5 dB less sound than the leading edge of the roughness patch. This effect will not however affect the ability of the model to scale the measured spectra, because this effect will be present in all cases equally. The boundary

layer also continues to grow along the length of the patch, the displacement thickness, δ^*, increases by as much as 220% along the patch. If the frequency scaling varies with δ^*, as suggested by Farabee and Geib (1991), this would have a significant broadening effect in the measured spectra. However, the expected scaling on δ^* is based on the assumption that δ^* is an accurate scale of the wall pressure spectrum. This may not be true in a wall jet, especially at low frequencies. If the low frequency portion of the spectrum varies with the boundary layer thickness, δ, which increases by 10% along the patch for these cases, the broadening effects would be much less. In either case the broadening effects will be similar in all spectra and plotting the normalized spectra will reveal the effectiveness of each model. The value of u_τ is computed for the entire roughness patch as described in Chapter 4. The values at the front of the patch are estimated using the smooth plate model discussed in Chapter 4. Aerodynamic measurements were made for three of the nine cases considered. The measured cases and scaling values measured are listed in Table 4-3, cases 25, 33, and 43. These measurements and the clean plate wall jet model allow for interpolation or extrapolation of aerodynamic quantities for the other cases. The maximum velocity as discussed in Chapter 4 can be determined with the smooth plate wall jet model, even in the presence of roughness. Similarly, the displacement thickness at the end of the roughness patch is shown to be nearly a constant multiple of the clean plate boundary layer thickness based on the three cases measured aerodynamically. Based on cases 43, 33, and 25 $\delta^*_{meas}/\delta_{smooth}$ is 0.185 within 10% of the measured values

6.1.2.2 Scaling Models

Figure 6-3 shows the acoustic spectra normalized for the dipole and quadrupole scaling behaviors proposed by Cole shown in Equations 6.1 and 6.2 respectively.

$$\frac{\Phi_D(\omega)}{(\rho/c_\infty)^2 U^5 \delta^*} \sim f\left(\frac{\omega\delta^*}{U}\right) \tag{6.1}$$

$$\frac{\Phi_Q(\omega)}{(\rho/c_\infty^2)^2 U^7 \delta^*} \sim f\left(\frac{\omega\delta^*}{U}\right) \tag{6.2}$$

This scalings are based on outer flow properties U_e and δ^*. (Cole, 1980) The first result to note in Figure 6-3 is the frequency scaling of the spectra. The frequency normalization brings the measured spectral peaks together. The effectiveness of the amplitude scaling differs between the two scaling methods. Figure 6-3 (a) shows the acoustic spectra scaled using the dipole scaling law. Below a non-dimensional frequency of 5 the acoustic spectra, except for those measured at the two lowest speeds, collapse in a narrow band. The extent of the collapse is difficult to determine due to the scatter in the spectral levels at these frequencies. For most cases these frequencies correspond to dimensional frequencies where the chamber effects were most noticeable. Even with the acoustic correction applied there still seems to be some residual scatter. Outside of these effects the acoustic spectra seem to collapse within a 1 to 5 dB band below $\omega\delta^*/U_e$=5 until the roughness noise cannot be detected. However, above a non-dimensional frequency of 5 the dipole scaling does not align the high frequency roll off of the measured spectra. The high frequency roll off region shows a 5 to 10 dB spread from a non-dimensional frequency of 5 to 10. The spectra then cross near a non-dimensional frequency of 20.

This is at the edge of the measurable frequency range, so whether this collapse continues at higher frequency cannot be judged.

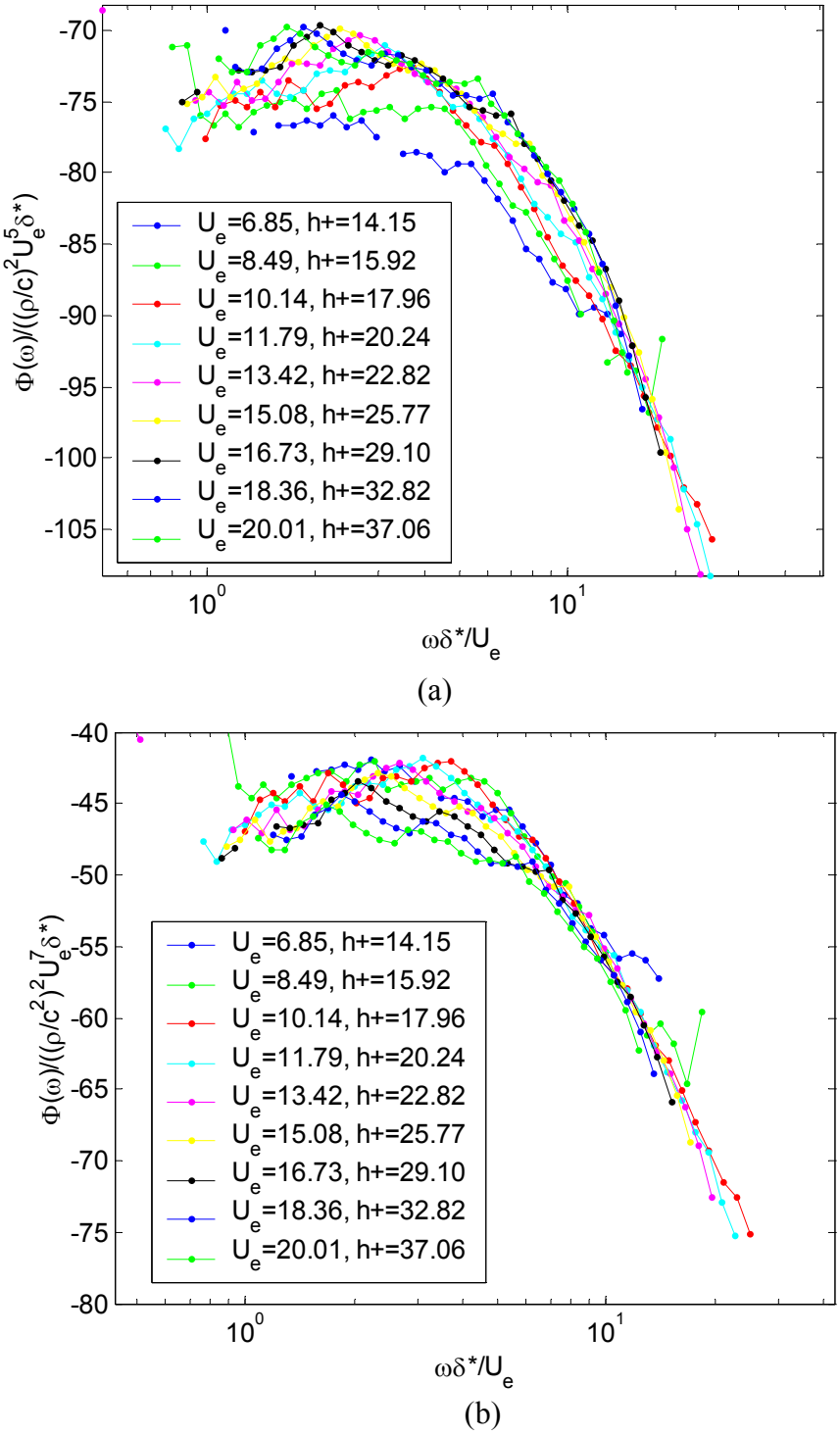

Figure 6-3 Acoustic spectra measured from a wall jet flow over a patch of 40 grit sandpaper at different speeds normalized based on the dipole velocity scaling proposed by Cole (1980), (a), and the quadrupole velocity scaling of Cole, (b).

Figure 6-3 (b) shows the acoustic spectra normalized with the Cole (1980) quadrupole velocity scaling. The effectiveness of this scaling is opposite of that seen in the dipole scaling. At high frequencies, $\omega\delta^*/U_e > 5$, the spectral levels collapse very well. All the spectral levels fall within a 1 dB band over the measured high frequency range. At low frequencies the data collapse is worse than with the dipole scaling law, the data spread being 7 to 10 dB. The collapse of the acoustic spectra on a quadrupole scale based on the edge velocity is paradoxical. It can be taken as an indication that the sound is generated by free turbulence with stress levels characteristic of the maximum flow velocity. However, the aerodynamic measurements show that the roughness affects the edge velocity by only a few percent, far less than would be responsible for the 10 to 15 dB increase in sound level above the smooth wall levels. So the collapse seen in Figure 6-3 (b) has no physical relation to the presence of the roughness. It is likely that the collapse seen in this figure is the result of variations in the wall pressure spectrum due to Reynolds number effects. This is discussed in more detail in Chapter 8.

The results of Figure 6-3 show that the spectrum scales well on U. However, the spectral level may scale on other characteristic velocities of the flow. Three candidates for other scaling velocities are the maximum turbulent fluctuation in the mixing layer, the maximum turbulence level in the near wall layer, and the minimum turbulent fluctuation velocities found between these two positions (see Figure 5-10 to visualize these). Figure 6-4 shows the acoustic spectra based on the maximum value of u' measured in the turbulence profiles. The general behavior is similar to the results shown in Figure 6-3 when the spectra are scaled on U_e. The dipole scaling behavior in Figure 6-4 (a) is slightly better than in Figure 6-3, especially for the low speed cases. In Figure 6-4 (a) the 8.45 m/s flow is collapsed into the main band of curves, while in Figure 6-3 (a) it was clearly outside this band. The lowest speed curve is also brought closer to the group, although it still is not fully collapsed. The quadrupole scaling is made slightly worse. For non-dimensional frequencies above 5 the collapse is not as tight as it was with the spectral levels scaled on U_e, and at low frequencies, there is no improvement in the fit. This scaling suffers from the same non-physical arguments of the quadrupole scaling based on the maximum velocity, because the maximum turbulence levels typically occur above the maximum velocity location. The other two turbulence velocities do a poor job of scaling the acoustic spectra. This may seem somewhat surprising since the location of the maximum turbulence velocity is well into the mixing layer, while the other two levels occur much closer to the wall. One would expect the two closer velocity scalings to better represent the turbulent pressure fluctuations near the wall. However, the scaling behavior of the turbulent velocity spectra show that the outer flow variables, $y_{½}$, u'_{max}, and U_e, scaled the spectra well into the inner flow region. So these outer flow variables are likely to be representative of the large-scale turbulent fluctuations throughout the wall jet flow.

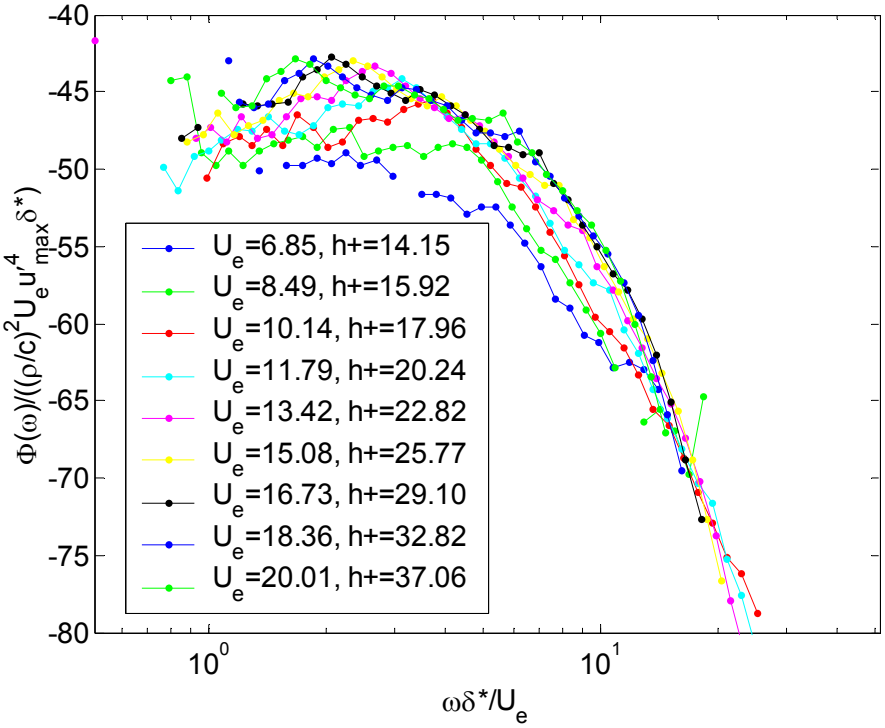

(a)

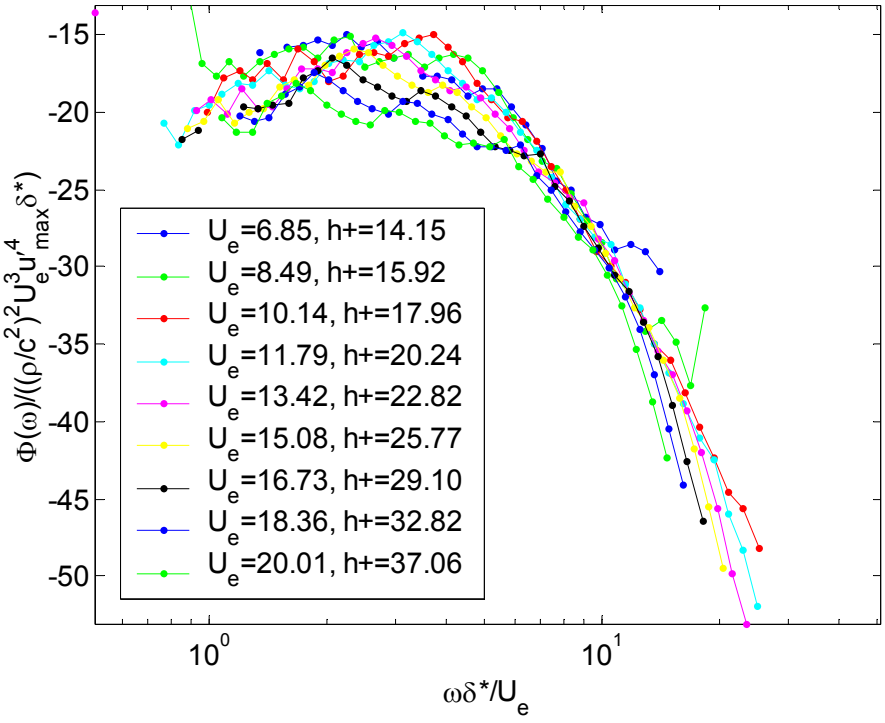

(b)

Figure 6-4 Acoustic spectra measured from a wall jet flow over a patch of 40 grit sandpaper at different speeds with amplitude normalized on the maximum turbulent velocity fluctuations and frequency normalized on the maximum mean velocity. The scaling in figure (a) uses $U_e u'^4$ for amplitude scaling; in figure (b) $U_e u'^4$ is used.

The model presented by Howe (1988) suggests a scaling of the acoustic field on the inner flow variables u_τ and h, as shown in Equation 6.3.

$$\frac{\Phi(\omega)}{(\rho/c_\infty)^2 u_\tau^5 h} \sim f\left(\frac{\omega h}{u_\tau}\right) \tag{6.3}$$

This scale should be representative of the viscous phenomena occurring in the near wall region, close to the roughness elements. Figure 6-5 shows the results of scaling the spectra on inner variables u_τ and h. The figure only shows the effects of u_τ because h is the same for all the spectra in this data set. Figure 6-5 shows that the dipole scaling does a good job of collapsing the low frequency portion of the spectra for all cases except the 6.85 m/s data. This spectrum is below the collapsed band, as is the case for all the dipole scalings presented. The quadrupole scaling, not suggested by Howe (1988) but based on the same scaling parameters, is not as effective as the quadrupole scaling based on the edge velocity, but does bring the 6.85 m/s case into the band. The low frequency region does not collapse well, with over a 10 dB spread in this region.

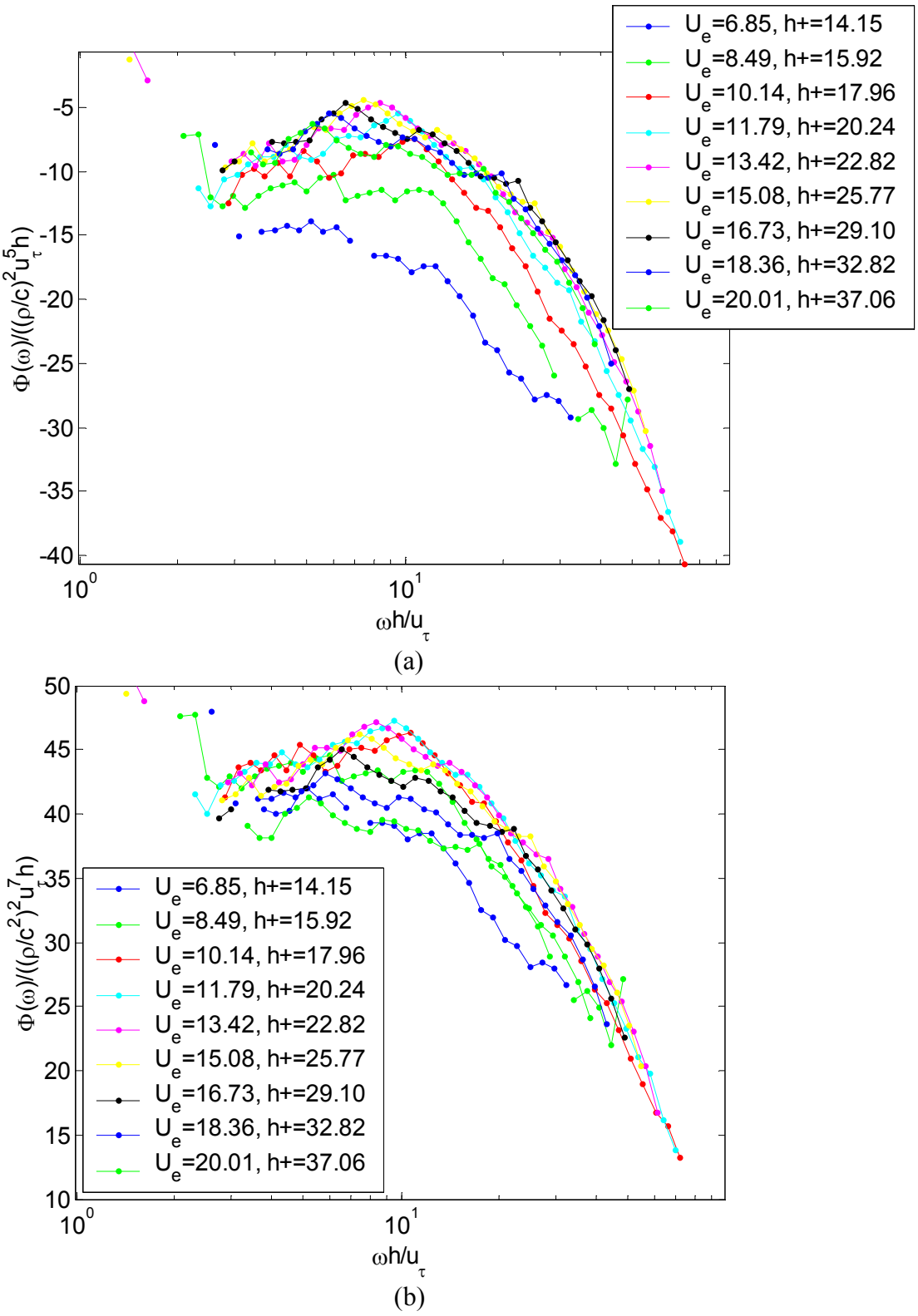

Figure 6-5 Acoustic spectra measured from a wall jet flow over a patch of 40 grit sandpaper at different speeds with amplitude and frequency normalized on the skin friction velocity and roughness height. The scaling in (a) uses u_τ^5 as suggested by Howe (1988) for amplitude scaling, (b) is u_τ^7.

Two other scaling models have been previously proposed. These dipole models are shown in Figure 6-6, and depend on a mixture of inner and outer variables. The plot labeled (a) shows the dipole scaling proposed by Glegg (2007) and shown in Equation 6.4.

$$\frac{\Phi(\omega)}{(\rho/c_\infty)^2 u_\tau^4 U(h^2/l_e)} \sim f\left(\frac{\omega l_e}{U}\right) \tag{6.4}$$

This scaling is based on a scattering model similar to Howe's model, so it has many common features. The amplitude scaling is the same in the case of the grit roughness because the length scale and height of the roughness are proportional. The primary difference is the scale of the frequency on the convection velocity, which is assumed to be proportional to the edge velocity in a wall jet, instead of the skin friction velocity. The plot in Figure 6-6 (b) shows the scaling model proposed by Farabee and Geib (1991) defined by Equation 6.5.

$$\frac{\Phi(\omega)}{(\rho/c_\infty)^2 u_\tau^4 U\delta^*} \sim f\left(\frac{\omega\delta^*}{U}\right) \tag{6.5}$$

This model uses a mixed velocity scaling and the displacement thickness, δ^*, for a length scaling. Both of these models show a similar level of collapse as the models shown earlier in this section. They are able to collapse many of the high velocity measurements, but the low speed measurements fall below this band of collapse. (Farabee and Geib, 1991)

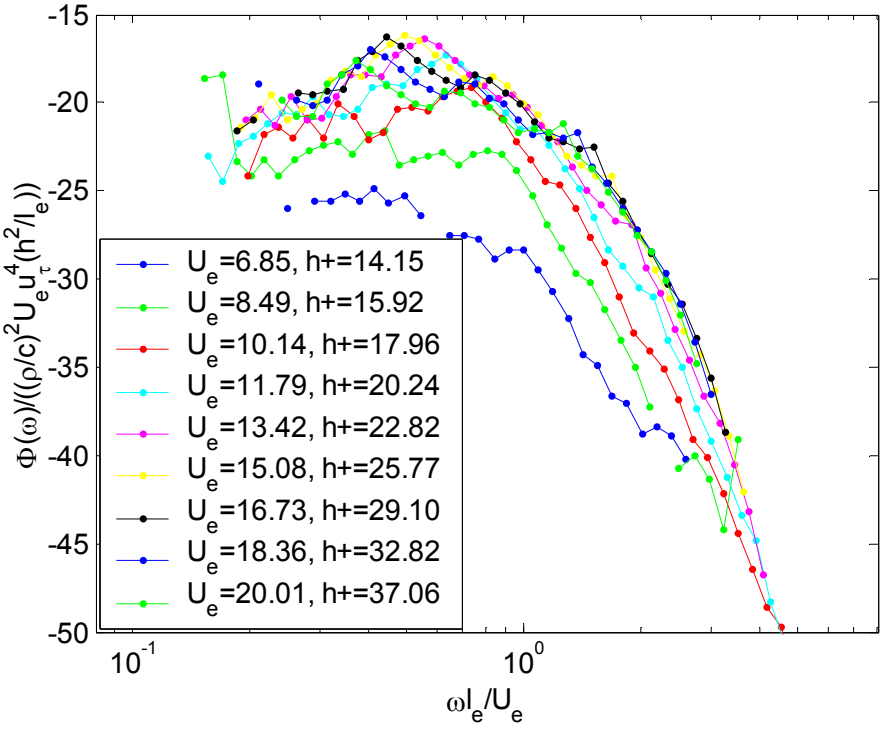

(a)

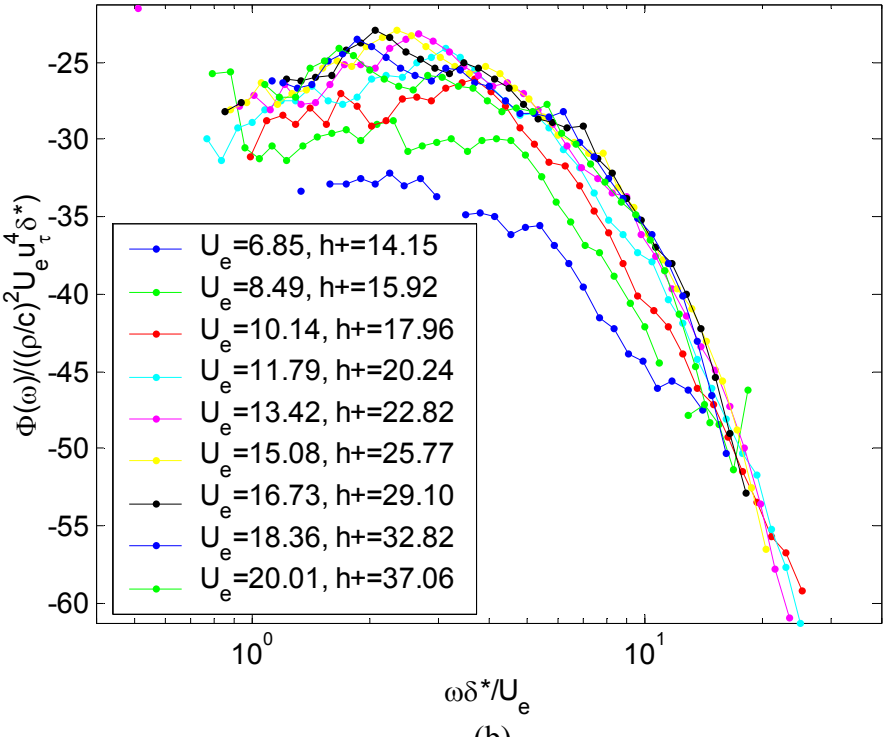

(b)

Figure 6-6 Acoustic spectra measured from a wall jet flow over a patch of 40 grit sandpaper at different speeds normalized on two mixed dipole scales. (a) is the scaling presented by Glegg (2007), (b) is the scaling presented by Farabee and Geib (1991).

In summary, all of the dipole scaling models work moderately well at collapsing the acoustic spectra that result from variations in flow velocity. They all have problems collapsing the lowest speed measurements into the curve in which the higher speed cases collapsed. A number of different velocity scales have been used, but no significant distinction can be seen between them. The collapse seen when using quadrupole models did not reflect the physical processes behind the models. The inner variable quadrupole model, which should more accurately reflect the presence of the roughness, does a worse job of collapsing the measured spectra then the outer variable model. This may indicated that the collapse seen in the outer model is either fortuitous or indicative of an additional Reynolds number affect on the acoustic source.

6.2 Effects of Roughness Size Variation

6.2.1 Acoustic Measurements

To investigate the proper scaling length a test series was conducted which held the velocity scales nearly constant while varying the different length scales associated with the flow. Ten different roughness patches each 305 mm long and 610 mm wide were attached to the plate 1260 mm downstream from the nozzle exit. The roughness patches were made of various grits of sandpaper securely taped to the plate surface. The mean roughness size ranges from 0.068 mm to 0.95 mm, with a nearly random roughness distribution based on the surface image correlation length calculations as shown in Table 4-1. The radiated acoustic spectra were measured from each roughness patch using the same microphone configuration described earlier for measuring the 40 grit patch at different speeds. For this test the nozzle exit velocity was nominally 60 m/s, which results in a maximum flow speed at the leading edge of the roughness patch of 20 m/s. Details of the patch location, microphone location, and flow conditions can be seen in Table 4-4 group G1-4 of Chapter 3. Velocity measurements were taken at the trailing edge of each roughness patch to determine how the different roughness patches affected the wall jet flow. Table 4-3 section G summarizes the flow conditions for each roughness patch upstream and downstream of the patch. The upstream conditions are estimated based on the smooth wall behavior of the wall jet.

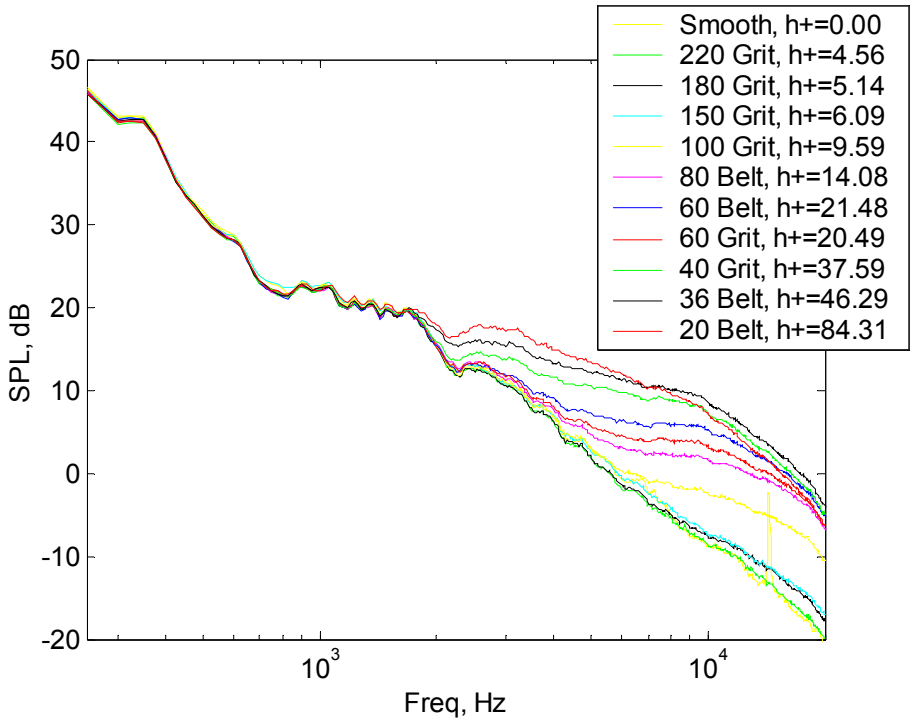

(a)

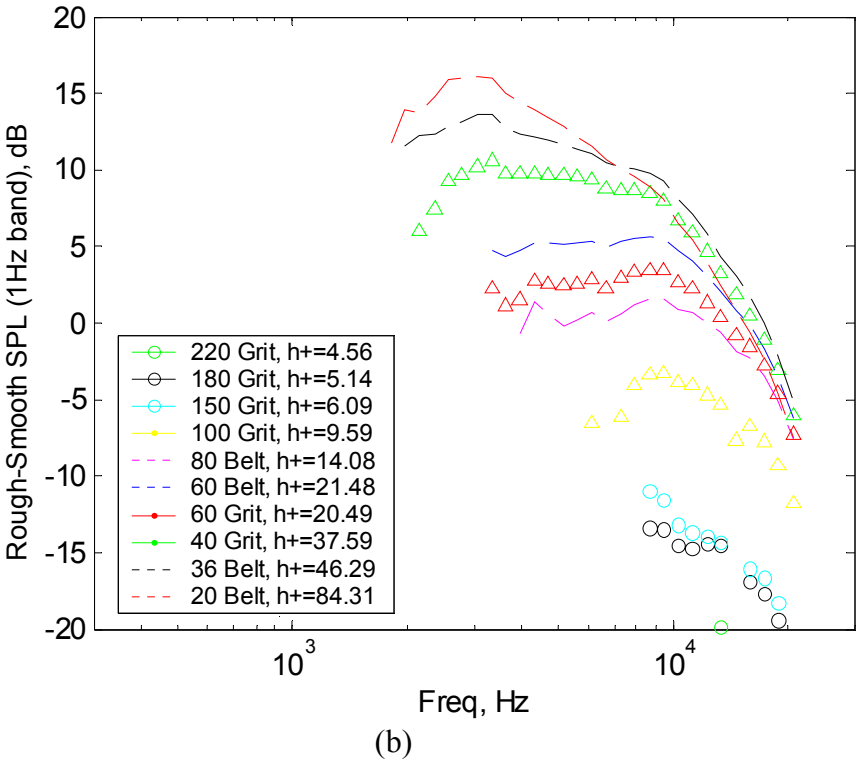

(b)

Figure 6-7 Acoustic spectra radiated by different roughness patches under a wall jet flow with U_o = 60 m/s, b = 12.7 mm. Raw spectra are shown on plot (a). Spectral levels on the right, (b) are the levels above those of the smooth wall flow.

Figure 6-7 shows the acoustic levels measured for each of the different roughness cases. Figure 6-7 (a) shows the absolute sound levels measured by the microphones for each of the roughness cases. Sound levels increase as the mean roughness height is increased except below 1100 Hz where the background noise dominates. Figure 6-7 (b) shows acoustic levels with the smooth wall background removed. The subtraction is done linearly with the pressure spectra levels and the resulting pressure spectra is then normalized on 20×10^{-6} Pa and plotted on a dB scale. Cases 102 through 104 with grit sizes of 0.068 to 0.092 mm, from Table 4-4, had h^+ values between 4 and 5 measured at the trailing edge and h^+ values between 5 and 7 at the leading edge. This suggests that these cases are hydrodynamically smooth or nearly so for the entire length of the roughness patch. These cases are marked with circular markers in Figure 6-7 (b). The levels from Case 102 are barely distinguishable from the smooth wall spectra, so these will not be shown in the remainder of this section. The 180 grit and 150 grit roughness did show acoustic levels significantly above the background levels at frequencies above 8 kHz. The fact that noise is produced by these hydrodynamically smooth surfaces (which presumably generate no additional turbulence) would appear to conclusively indicate the existence of a scattering mechanism.

Case 111 from Table 4-4 also appears noticeably different in Figure 6-7 (b) from many of the other curves. The roughness in this case was a 20 grit sanding belt with nominal roughness size of 0.95 mm. This belt appears to be manufactured using a different technique than the other belts, and uses a different adhesive layer to secure the elements. Without detailed measurements of the belt surface it is unclear how much these differences affect the nominal surface properties listed in Table 4-1 for this case, but this may in part be responsible for the differences in spectral shape seen between case 111 and the others in Figure 6-7 (b). The sand belt surfaces have been marked by dashed curves throughout this section to distinguish them from the other sandpaper roughness marked by continuous lines with dotes. Two general trends that are clear in Figure 6-7 (b) is that as the roughness size increases the radiated sound levels also increase. The peak sound level increases by almost 30 dB from the smoothest case to the roughest case. The second trend is that the peak spectral level occurs at lower frequencies as the roughness size increases. This can be roughly seen by the decrease in the frequency where the spectral peak occurs. The spectral peak is hard to define for some cases due to low signal to noise ratio for the very small grits and scalloping effects for some of the other cases. However, the spectral peak appears to vary from about 10000 Hz for the cases with roughness smaller than 100 grit, down to 3000 Hz for the 20 grit roughness. The fact that as roughness height increases the lowest detectable frequency associated with the roughness noise decreases, also suggests that the frequency peak of the roughness noise spectra is decreasing with roughness size.

6.2.2 Spectral Scaling

6.2.2.1 Scaling Parameters

Aerodynamic measurements were collected at the trailing edge of all the roughness cases presented in Section 6.2.1. The only exception is the 180 grit sand paper, run 103 from Table 4-4. Aerodynamic quantities for this run were estimated using

data from the measurements collected over the 220 and 150 grit patches, cases 37 and 38 of Table 4-3. Mean values over the length of the roughness patch are approximated by averaging the measured values at the leading and trailing edges of the patch. Leading edge values are determined from the smooth plate model with the nozzle conditions for each case, which are nominally a nozzle height, b, of 12.7 mm, and a nozzle exit velocity, U_0, of 60 m/s. The mean flow edge velocity decreases by 10 to 12% along the length of the patch for all roughness cases. As discussed in section 6.1.2.1, the velocity decay will result an acoustic strength variation of 2.5dB from the front to back of the roughness patch if the spectral levels are assumed to scale with the edge velocity. The boundary layer thickness measured at the downstream end of the roughness patch varies from 18.4mm for the 220 grit case to 25.8mm for the 20 grit case, with variations in δ^* from 1.0mm to 2.04mm for the same cases respectively. At the leading edge of all cases the boundary layer displacement thickness was 1.06mm and the boundary layer thickness 13.25mm. If the wall pressure spectrum scales with either of these parameters then the measured spectra will have progressively broader peaks due to variation in the wall pressure spectrum. The raw spectra, shown in Figure 6-7, appear to show this type of broadening. This variation in spectral shape will prevent plots of the normalized spectra from collapsing to a single band, but will still reveal the relative effectiveness of the different models discussed in Chapter 1.

6.2.2.2 Scaling Models

The outer variable scaling of Cole (1980) based on U_e and δ^* is shown in Figure 6-8. The Cole (1980) model spreads the peak acoustic levels over 3 decades, a slight increase relative to the raw levels. The normalized spectral peaks are spread over half a decade on the frequency axis. The scaling appears to have centered the measured portion of the roughness spectrum on the frequency axis. This scaling is less effective at modeling the effects that result from different surface conditions than it was at modeling the affects of changes in edge velocity. This is is because the model is only weakly affected by the presence of the surface roughness. In the wall jet flow the value of U_e is not affected by the presence of the roughness, and since this is the primary scaling factor for the spectral amplitude, U_e^5, the poor collapse is not unexpected.

The weak coupling of the Cole scaling to the roughness height is also not surprising given Cole's research objectives. Cole (1980) was investigating smooth wall boundary layer noise and only wished to use roughness to enhance the turbulence levels, and Reynolds numbers of his flow. An implicit assumption in his work was that the presence of the surface roughness did not create an additional acoustic source mechanism.

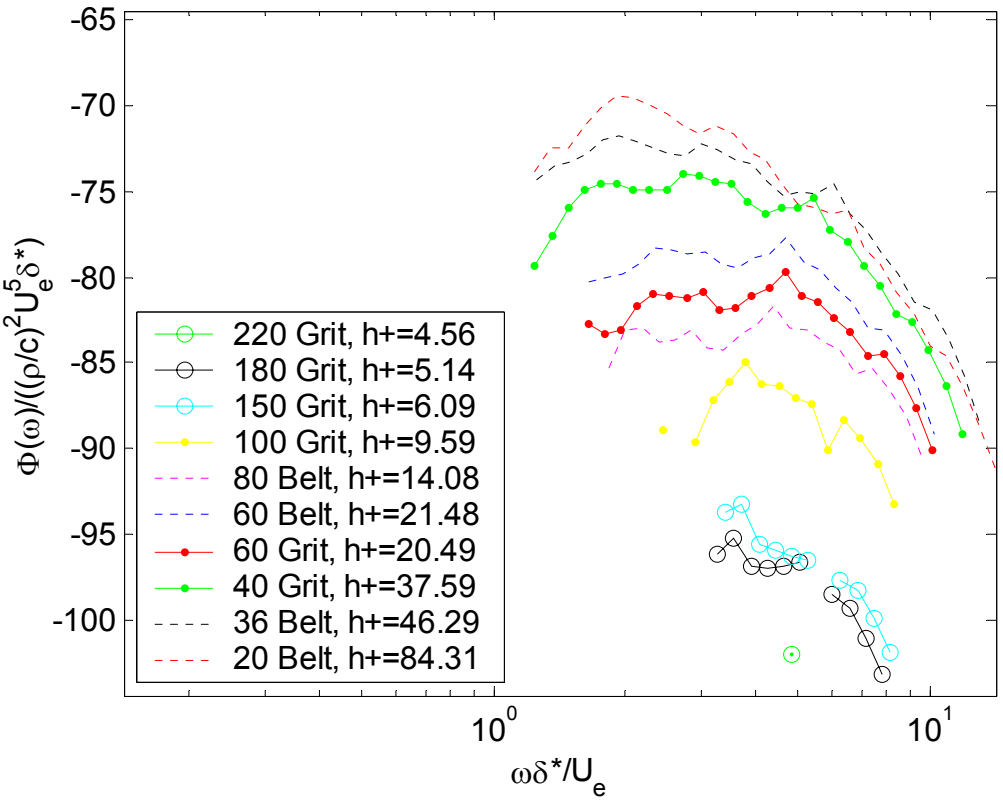

Figure 6-8 Acoustic spectra measured for flow past patches of different surface roughnesse normalized on the outer flow scaling of Cole (1980).

Figure 6-9 shows the scaling proposed by Howe (1988) based on inner flow variables u_τ and h. The first feature to notice in this figure is the separation of the hydrodynamically smooth spectra from the hydrodynamically rough ones. The hydrodynamically smooth cases are normalized to a lower frequency, and lower spectral level than the other measurements. Figure 6-9 shows the normalized spectral levels for all hydrodynamically rough cases collapse within a 7 dB band. The amplitude level of the hydrodynamically smooth group is 5 dB below these curves. While the Cole (1980) scaling aligned the spectral peaks on the frequency axis, this scaling appears to align the lower frequency portions of the measured spectra. The high frequency roll off is not collapsed by the Howe model, but shifts to higher frequencies with increases in roughness height.

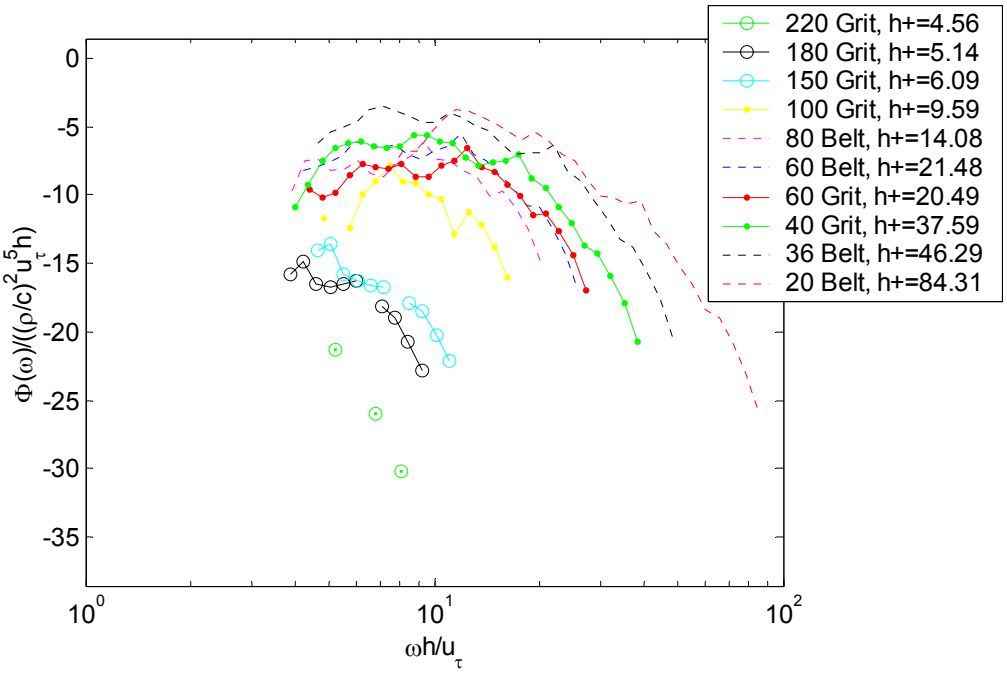

Figure 6-9 Acoustic spectra measured for flow past different surface roughnesses normalized on the inner flow scaling of Howe (1988).

The acoustic spectra scaled using the model presented by Farabee and Geib (1991) are shown in Figure 6-10. Similar to the Howe (1988) scaling, the three hydrodynamically smooth cases are not collapsed with the spectra from larger roughness sizes. This scaling has the same frequency scaling as the Cole (1980) model, and shows similar behavior in the frequency normalization. The spectral peak and high frequency roll off for all hydrodynamically rough cases appear to be aligned on the frequency axis. The spectral peak levels are spread over 25 dB when including the hydrodynamically smooth cases or 12 dB if these cases are not included. Below a non-dimensional frequency of 5 the spectral levels begin to diverge. This may be due to variations in the wall pressure spectrum associated with changes in δ along the length of the roughness patch. These variations would tend to broaden the spectral shape near the spectral peak and increase levels in the low frequency region.

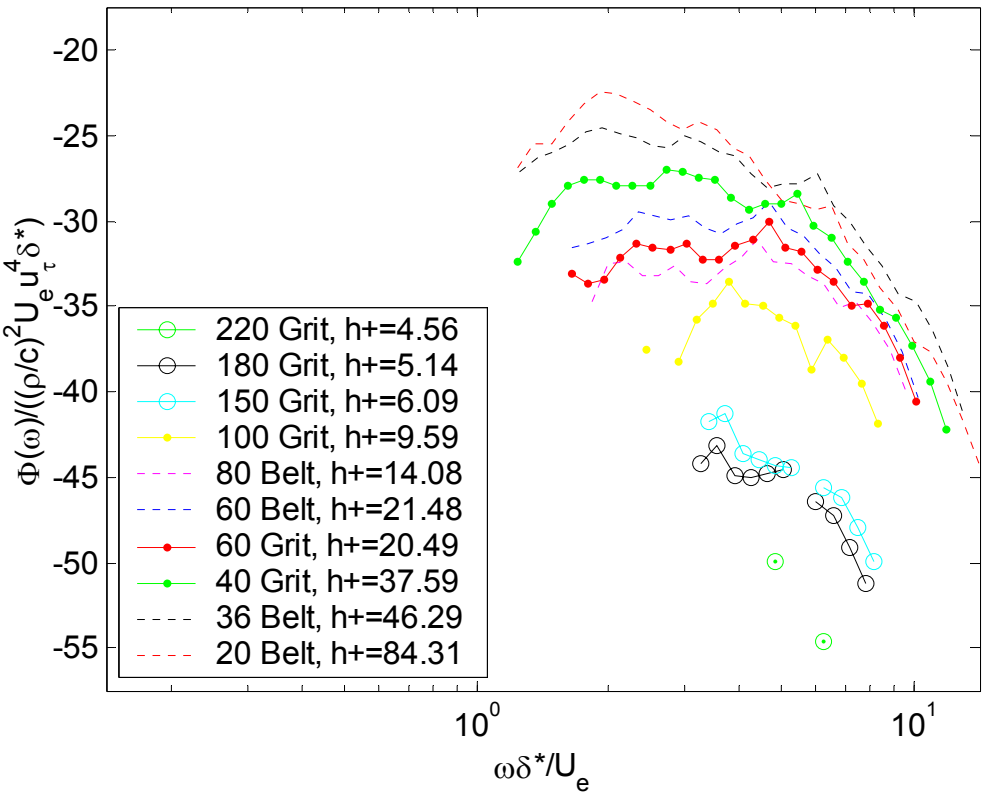

Figure 6-10 Acoustic spectra measured for flow past patches of different surface roughness normalized on the mixed flow scaling of Farabee and Geib (1991).

Scaling with the model of Glegg (2007) is shown in Figure 6-11. This model uses both inner and outer variables to normalize the spectral amplitude. The scaling is based on the skin friction velocity, u_τ, and convection velocity, U_c, as well as two roughness parameters; the roughness height, h, and the correlation lengthscale, l_e. The frequency scaling is normalized on the roughness length scale, l_e, and the convection velocity, U_c. Based on the analysis of images of the sand grit roughness used in these tests, the correlation length scale of the roughness was proportional to the roughness height. The Glegg model shows a 7 dB spread in spectral peak levels, when the hydrodynamically smooth cases are ignored. The hydrodynamically smooth cases are not collapsed with the rest of the spectra measured, similar to the results seen in Figure 6-9 using the Howe (1988) scaling. They appear 5 dB below the group containing the other spectra, and at lower frequencies. The frequency behavior is similar to the Howe model which shows the high frequency roll off occurring had higher non-dimensional frequencies as the roughness size increases.

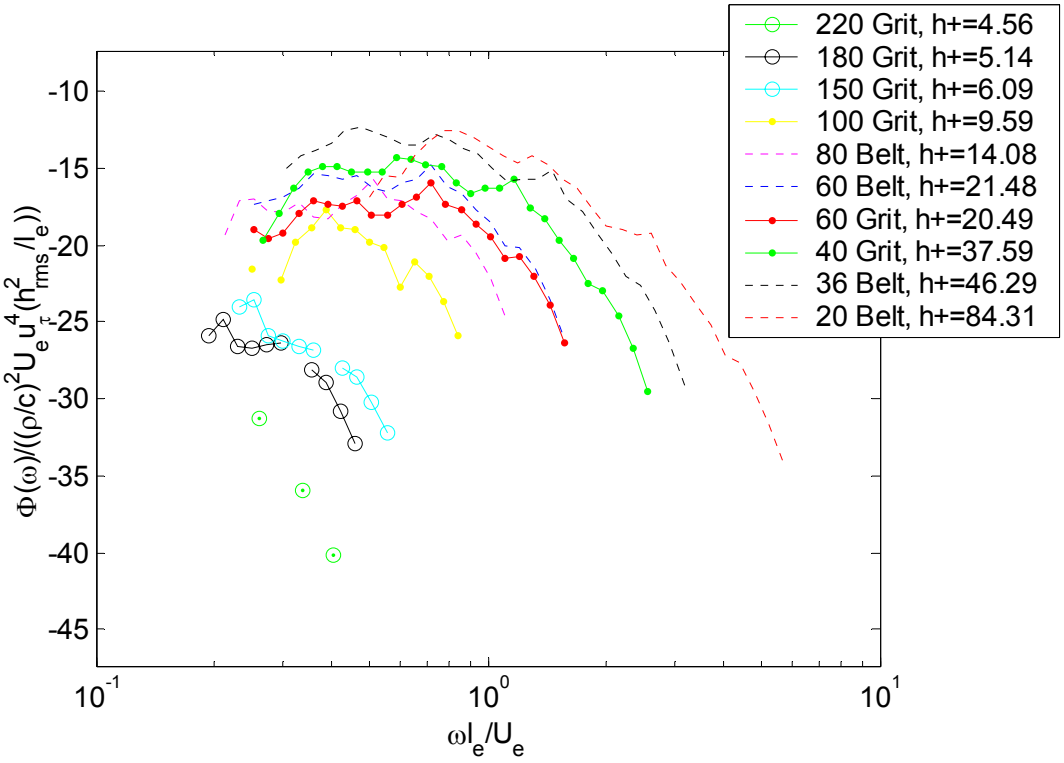

Figure 6-11 Acoustic spectra measured for flow past patches of different surface roughness normalized on the mixed flow scaling of Glegg (2007).

The Cole (1980) quadrupole scaling of this data is shown in Figure 6-12 (a). The amplitude collapse of this model is similar to the collapse seen in the Cole dipole model. A significant contributor to this problem is that the Cole models do not include any inner variables that account for the presence of the roughness. Figure 6-12 (b) shows a quadrupole scaling based on inner variables. The normalized spectra show many of the behaviors seen in scattering models of Glegg (2007) and Howe (1988). The spectral levels are well collapsed with the exception of the hydrodynamically smooth cases, and the low frequency portions of the spectra are aligned. The high frequency roll off occurs are increase frequencies with increases in roughness size. Based on these results and those of various other possible quadrupole scalings it does not appear that there is a quadrupole scaling that can provide a realistic collapse of the spectra which also has physical significance.

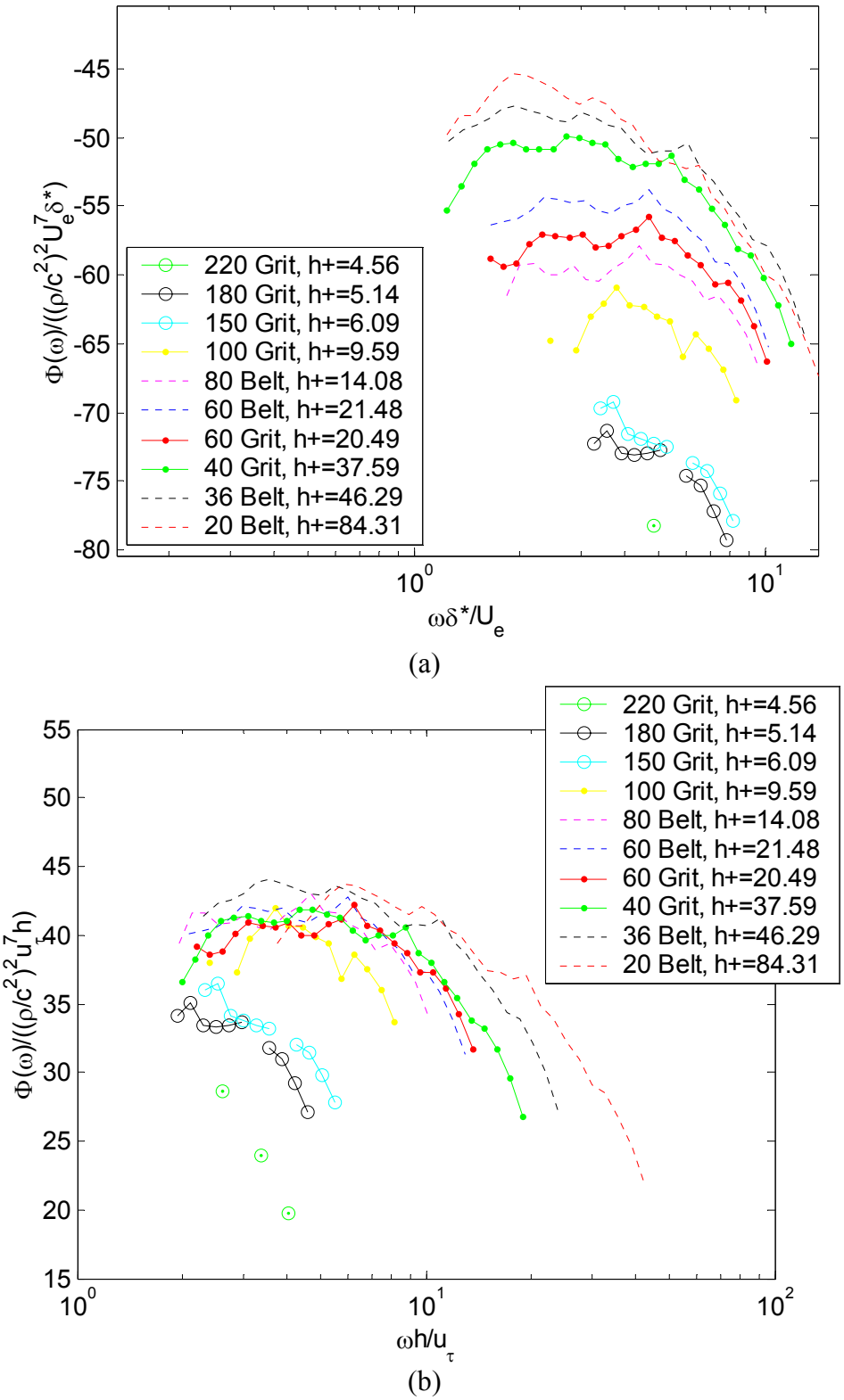

Figure 6-12 Acoustic spectra measured for flow past patches of different surface roughness normalized on the quadrupole scaling model of Cole (1980) (a), and an inner variable scaling model (b).

Beyond the named dipole scalings a number of other possible scaling models were considered. Figure 6-13, Figure 6-14, and Figure 6-15 show three scalings, A, E, and C from Table 1-1 and repeated here as Equations 6.6, 6.7, and 6.8, which are typical of those tested.

$$\frac{\Phi(\omega)}{(\rho/c_\infty)^2 u'^4_{\max} U h} \sim f\left(\frac{\omega h}{U}\right) \tag{6.6}$$

$$\frac{\Phi(\omega)}{(\rho/c_\infty)^2 u_\tau^5 h} \sim f\left(\frac{\omega \delta^*}{u_\tau}\right) \tag{6.7}$$

$$\frac{\Phi(\omega)}{(\rho/c_\infty)^2 U^5 h} \sim f\left(\frac{\omega \delta^*}{U}\right) \tag{6.8}$$

The scaling shown in Figure 6-13 looks at the effects of using the maximum turbulent velocity fluctuation to model the hydrodynamic stress term. This scale generally does a poor job normalizing the spectral levels. This results from the fact that the maximum turbulence level is primarily controlled by the mixing layer, and not by the wall conditions. The second, Figure 6-14, scaling is one similar to the Howe (1988) scaling based on inner variables, but with the time scale and correlation area adjusted to allow the frequency scaling to be $\omega\delta^*/u_\tau$. This scaling seems to collapse the data well in the high frequency roll off. The low frequency roll off occurs at decreasing frequencies with increasing roughness height. This may be due to the variations in wall pressure spectrum along the length of the roughness patch. As noted earlier, the shapes of each spectrum measured are different so no scaling will be able to collapse the spectra over the full frequency range. The final scaling shown in Figure 6-15 incorporates an inner length scale into what is otherwise the outer variable scaling of Cole (1980). This does not significantly change the collapse of this model, since the primary amplitude scaling variable is the velocity scale.

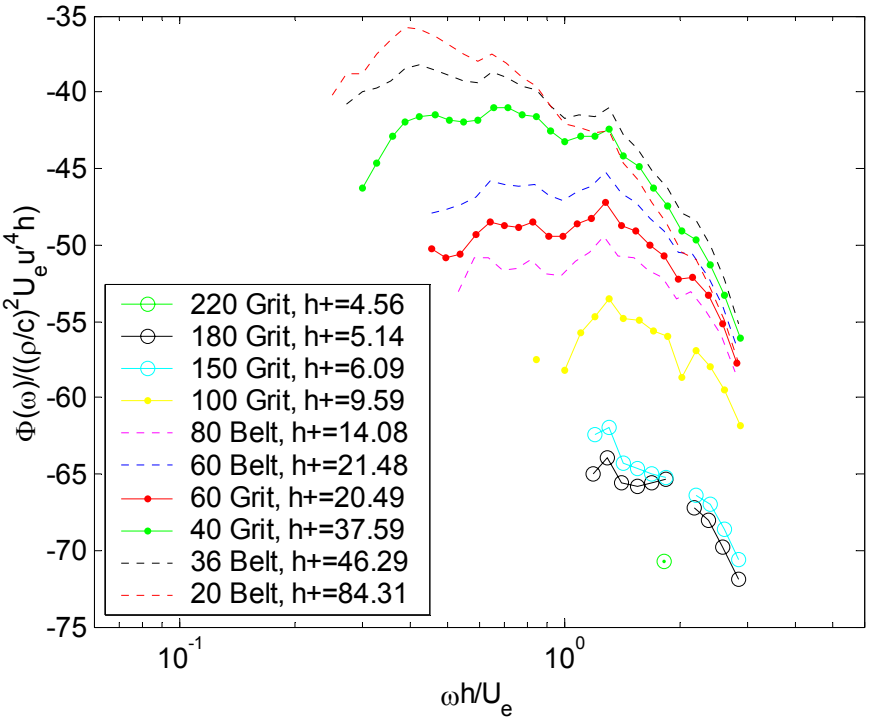

Figure 6-13 Acoustic spectra measured for the same flow conditions over patches of different surface roughness. Spectra are normalized using the maximum turbulence level to scale the hydrodynamic shear, and the roughness height and edge velocity for time and area scales.

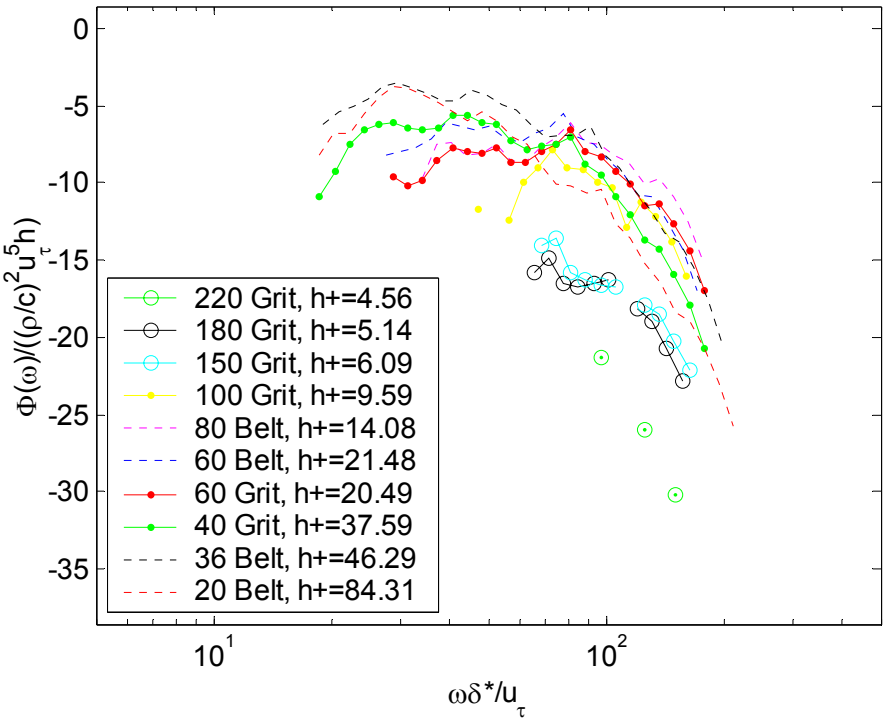

Figure 6-14 Acoustic spectra measured for the same flow conditions over patches of different surface roughness. Spectra are normalized using the skin friction to scale the hydrodynamic shear, and the displacement thickness and skin friction velocity for time and area scales.

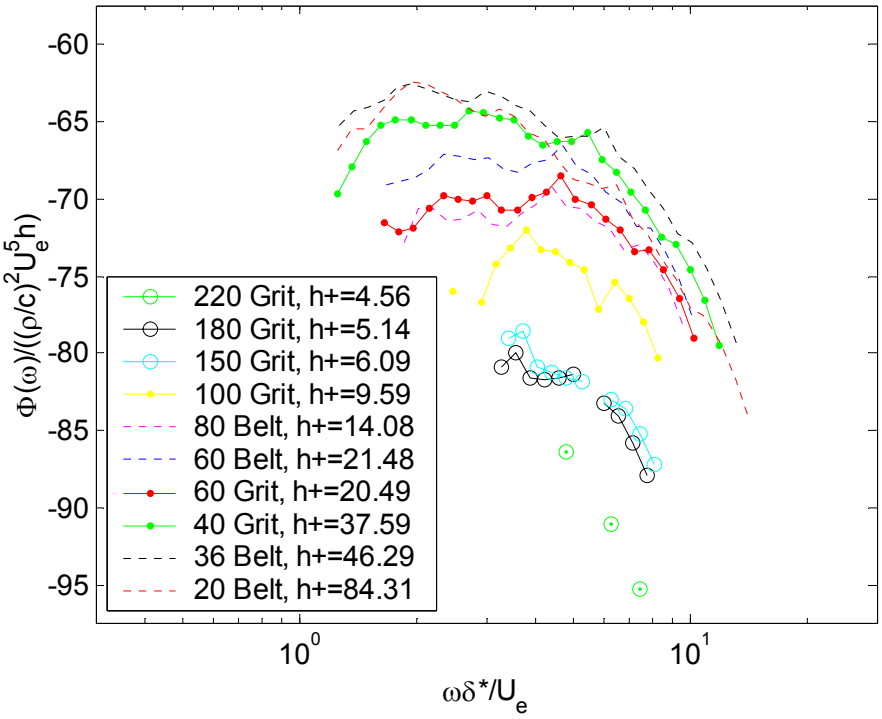

Figure 6-15 Acoustic spectra measured for the same flow conditions over patches of different surface roughness. The scaling shown modifies the Cole (1980) scaling to include the effects of *h* in the spectral level normalization.

Based on the measured spectra and the results seen of the scaling attempts, it does not appear that a single variable scaling set will successfully scale the far field spectra. This result will be further discussed in Chapter 8. Furthermore, the collapse seen in some of the spectra suggest their may be transitional or Reynolds number effects which are causing the characteristic hydrodynamic stress to vary at higher rates than would normally be expected.

6.3 Vertical Directivity

An attempt was made to measure the vertical directivity of the far field sound radiated from a patch of 40 grit roughness. A short roughness patch, only 165 mm, in length was attached to the plate beginning 1346 mm downstream of the nozzle exit. Microphone measurements were collected along an arc with radius 775 mm centered on the center of the roughness patch. Measurements were collected at a single speed and nozzle condition as shown in Table 4-4. The directivity could only be measured over a narrow range of angles due to interference caused by scalloping effects and the jet noise in some regions of the acoustic enclosure. As the microphone position is moved into the downstream half of the arc, the microphone begins to detect the jet noise from the nozzle region of the wall jet. This noise can become dominate when viewed at grazing angles compared to the noise generated from the roughness patch viewed from nearly overhead. For this reason, the directivity is measured from angles of 45° to 85° above the plate based on the center of the roughness patch. Figure 6-16 shows the integrated sound levels due to roughness measured at these conditions. The scalloping effects have not

been removed from the data in Figure 6-16. This is because the correction technique, described in Section 4.7, uses spatial averaging to reduce the scalloping effects. However, the spatial averaging required by this technique would smear out the directivity effects that are being investigated. The directivity is hard to determine from this limited range of measurements. The measured sound level does decrease as the microphone position is moved closer to an overhead position. The highest position measures the sound level to be 8 dB quieter than at the forward-most position. These results do suggest the source radiates more effectively in the flow direction than in the wall normal direction, but the limited range prevents any further conclusions.

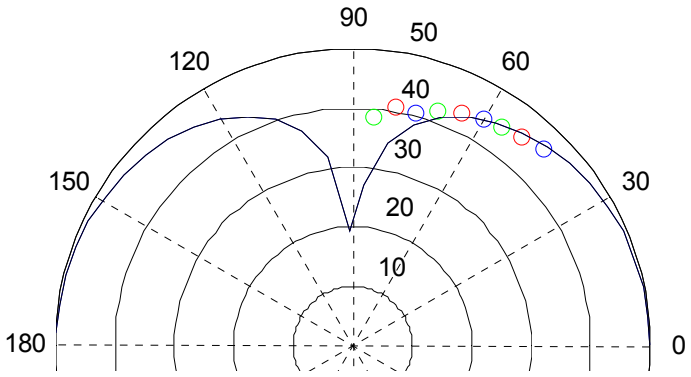

Figure 6-16 Directivity measured in a vertical arc over a patch of 40 grit sand paper. Flow is from right to left, with the roughness patch centered at the origin. The black curve shows the directivity of a flow aligned dipole centered on the roughness patch, the level has been set for comparison with the measurement.

6.4 Buildup Test

To investigate the effects of different roughness patch lengths on the radiated acoustic field, a series of tests were performed with 40 grit sand paper under the same flow conditions. For this test set only the roughness patch length was varied and aerodynamic and acoustic measurements were made to quantify the effects of this change. Patch lengths of 305, 610, and 915 mm were all tested under 4 different flow conditions. To build up to the longer patches, strips of 305 mm long roughness were added on the downstream edge of the previously installed roughness. The results will be discussed for one of these flow conditions. Results from the other conditions support this discussion and will be shown at the end of this section.

One must remember that to change the roughness patch length in the wall jet flow is not a trivial change. Since the various velocity scales and length scales that influence the radiated sound level are a function of the streamwise location of the roughness, when the roughness patch length is extended the new portion of the patch is in a region with different flow conditions than the upstream sections. The flow conditions, which will be discussed in detail, are for a nozzle height of 25.4 mm, and a nozzle exit velocity of 30 m/s. The roughness patch is started at a location 1245 mm downstream of the nozzle exit. Under these conditions the flow at the beginning of the roughness patch has a maximum local velocity of $0.54U_0$, 16.2 m/s, and a boundary layer displacement thickness of 1.13 mm

The flow development along the patch affects the far field acoustics in two ways. First the downstream portions of the patch are subjected to lower velocity flow as the patch length is increased. For a 915 mm long patch the flow speed at the patch exit is 72% the speed it was at the beginning of the patch, while for a 305 mm long patch the velocity at the patch exit is 86% of its initial value. Since the far field sound levels vary as the seventh and fifth power of flow velocity in different frequency regions this variation in flow velocity with length can make the downstream end of the roughness patch much quieter than the upstream side. The second effect is the increase in boundary layer length scales. As discussed in Chapter 5, the acoustic spectrum varies linearly with flow length scales. When compared to the fifth power scaling of flow velocities, these effects are less important. However, flow length scales are affected significantly more than the velocity scales when roughness is added. The displacement thickness, for example, is 50% larger than the clean plate value at the end of a 610 mm long patch of roughness and more than double in size at the end of a 915 mm roughness patch. Since the sound level scales directly with these length scales this will tend to increase the sound from the downstream side of the roughness patch relative to the leading edge.

Beyond the aerodynamic changes that result from different roughness patch lengths, there are also changes associated with the directivity and decay of the acoustic source that complicates the acoustic levels measured. First, if the acoustic source is assumed to act like a simple distributed source, then the points farthest from the observer location will be the least significant due to spherical spreading and decay of the acoustic field. For the geometric conditions of this test, the microphone was located 500 mm above the plate, and 1000 mm downstream from the nozzle exit. All roughness patches were started 1245 mm downstream of the nozzle exit, so the distance from microphone to the patch leading edge was 560 mm, while the distance from the microphone to the end of the roughness patch varied for the three patches from 750 mm, 1000 mm, to 1275 mm. If the acoustic source is assumed to have a streamwise aligned dipole directivity, the relative angle of the microphone to the patch will also affect the measured sound level. This effect will make the most downstream end of the longest roughness patch twice as effective at radiating toward the microphone as the leading edge of the roughness patch.

When the effects of velocity, boundary layer thickness, angle, and distance variations are all accounted for, one can assess the effectiveness of different portions of the roughness patch at radiating sound to the microphones. The source strength relative to the leading edge of the roughness patch is shown in Figure 6-17 as a function of streamwise distance.

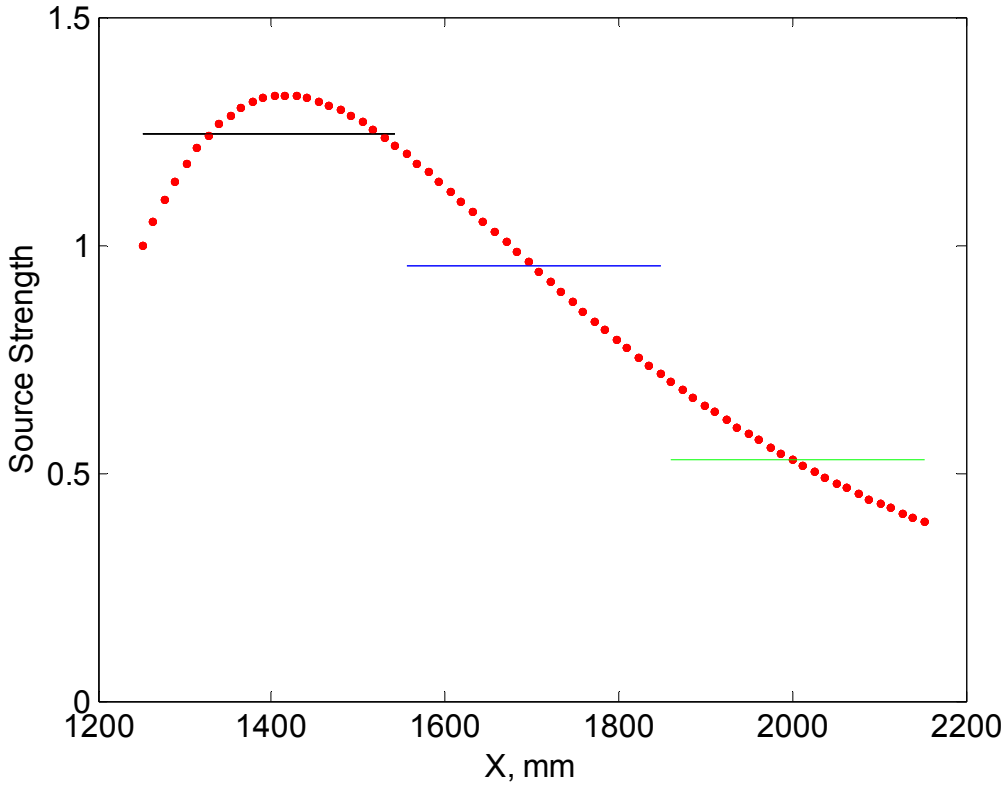

Figure 6-17 Acoustic effectiveness as a function of streamwise distance from the nozzle.

Figure 6-17 shows how the four factors interact as the roughness patch length extends farther downstream for the Cole (1980) dipole scaling model. The horizontal position of the three lines in Figure 6-17 corresponds to the position of each portion of the patch added during the test. The vertical levels of those lines show the averaged effectiveness of acoustic sources in that region. The primary factor controlling the streamwise behavior of the source is the spherical acoustic spreading. This causes the decay seen for sources located more than 1500 mm downstream from the nozzle exit. In the region near the leading edge of the roughness patch, the increase in sound levels is primarily due to the decrease in observer angle from the surface location to the microphones. At the leading edge of the patch the viewing angle is 65°, while at a location near the downstream edge of the first patch the observer angle is decreased to 45°. Since the directivity follows as the square of the cosine of the viewing angle, it results in a 300% increase in efficiency of acoustic transmission to the observer location. The viewing angle from the microphone to the end of the longest patch is 25° which is 450% as effective a radiator as the leading edge of the patch, in terms of directivity effects.

When these effects are integrated over the length of the three patches the increase in sound level for increasing patch length is relatively small. The total sound level increase from the 305 mm patch to the 610 mm patch is only expected to be 170%, or 2.4dB. The 915 mm patch is only expected to be 3.4 dB louder than the smallest patch. Figure 6-18 shows the far field spectra measured for cases 163 to 165 from Table 4-4.

The smooth wall sound level has been removed, leaving only the rough wall spectra for the three patch lengths.

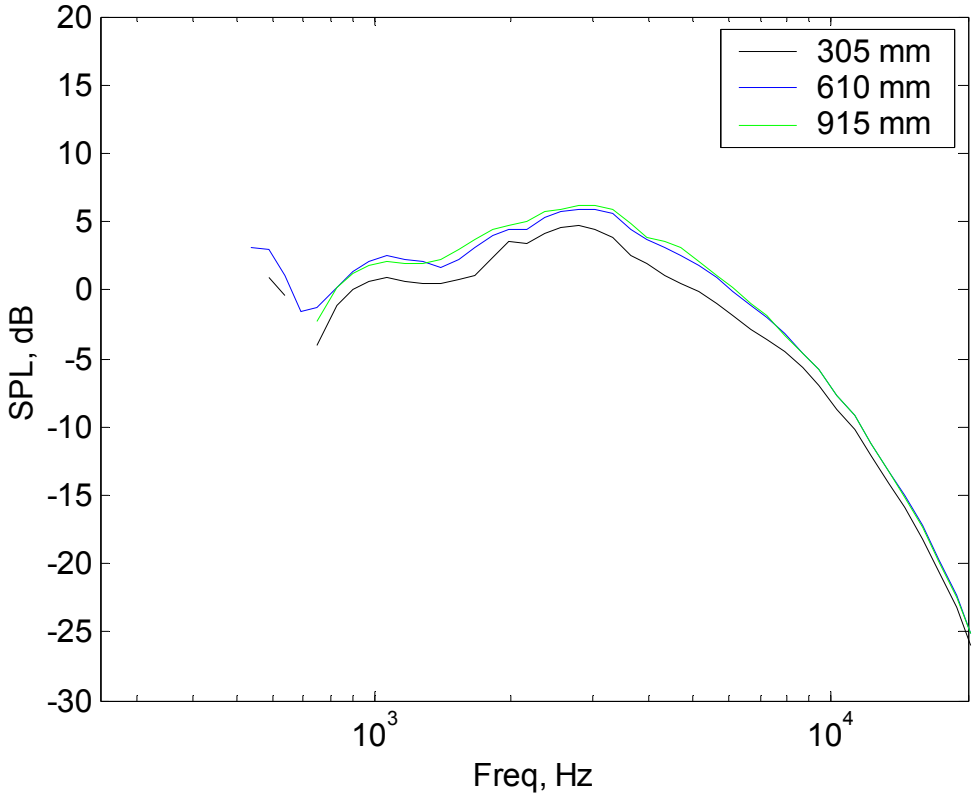

Figure 6-18 Sound levels measured at a fixed observer location for three different roughness patch lengths under the same flow conditions.

The agreement of Figure 6-18 with the expected levels of increase is hard to judge, but in all cases seem low. From the smallest patch to the middle patch an increase of 1.5 to 2 dB occurs over much of the frequency range. This is close to the nominal 2.4 dB increase that was expected. However, the longest patch does not produce a distinguishable change in the sound levels relative to the second patch length. A 1 dB increase in levels was expected, but is not seen in these results. This increase is the order of the spectral uncertainty, making it hard to detect. However given that the sound levels are close to the expected levels it seems unlikely that there are any additional affects that result from larger roughness patches. This suggests that prediction methods which work on short roughness patches may be useful for patches of much larger size, if the variations in flow and acoustic behavior are taken into account. However the present results do not completely rule out the suggestion that the initial portion of the roughness patch contributes disproportionately to the radiated sound.

To further verify these results the same test was repeated for three additional flow conditions. The first change was to decrease the nozzle exit velocity from 30 to 20 m/s, cases 160 to 162 of Table 4-4. This does not affect the decay rate of any of the flow properties, just the absolute flow speeds under which the tests were conducted. Figure 6-19 shows the far field sound levels measured under these conditions. The same basic

behavior is seen in this test set, but all acoustic levels are lower because of the decreased flow speed everywhere over the roughness patches. The increase in sound level from the 305 mm patch to the other is slightly lower than in the results shown in Figure 6-18, but the two longer patches are again indistinguishable in spectral levels.

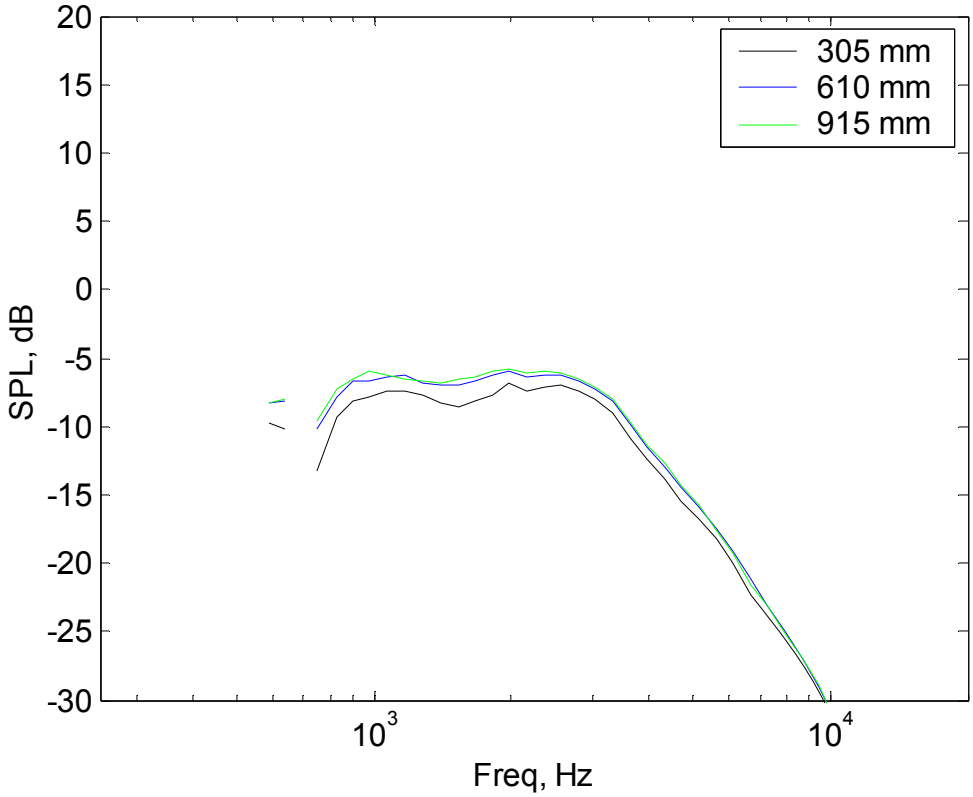

Figure 6-19 Sound levels measured at a fixed observer location for three different roughness patch lengths under the flow generated for a 25.4 mm nozzle exit with a nozzle exit velocity of 20 m/s.

Figure 6-20 and Figure 6-21 show measurements taken for a nozzle height of 12.7 mm with a nozzle exit speed of 30 m/s and 40 m/s respectively. This again effectively lowers the flow velocity over the entire roughness patch, but has little effect on the rate of decay along the patch. These figures show the same behavior seen in the other runs, with a 1 to 2 dB increase in sound levels observed when the roughness patch length increased from 305 mm to 610mm, and no measurable change in sound level for the largest roughness patch.

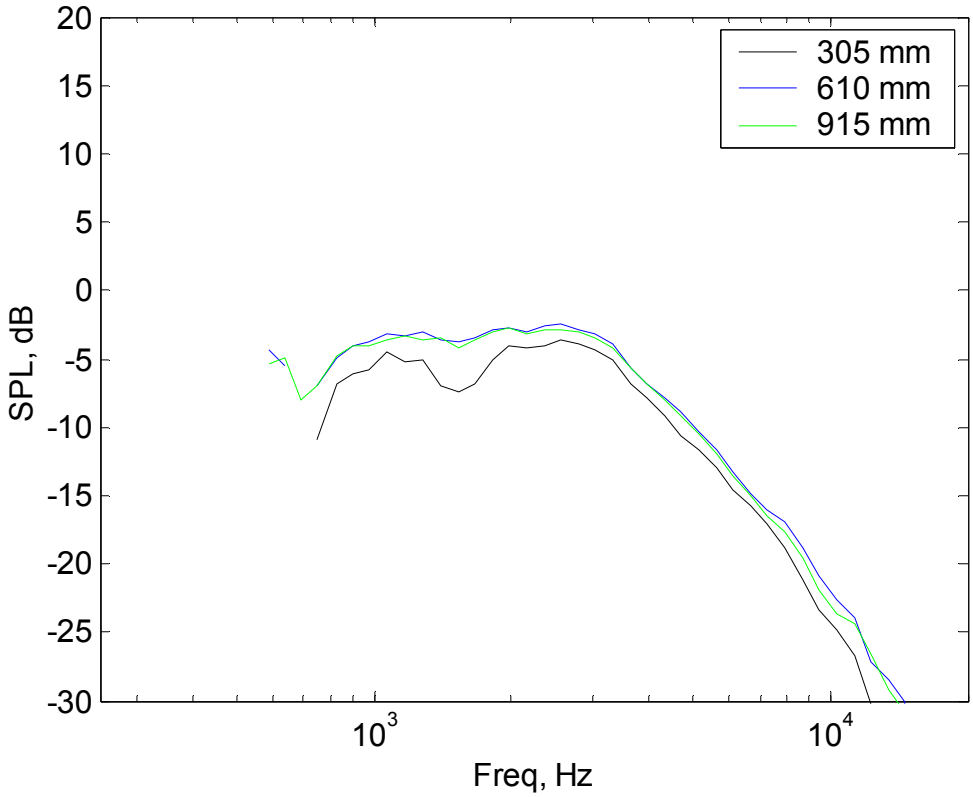

Figure 6-20 Sound levels measured at a fixed observer location for three different roughness patch lengths under the flow generated for a 12.7 mm nozzle exit with a nozzle exit velocity of 30 m/s.

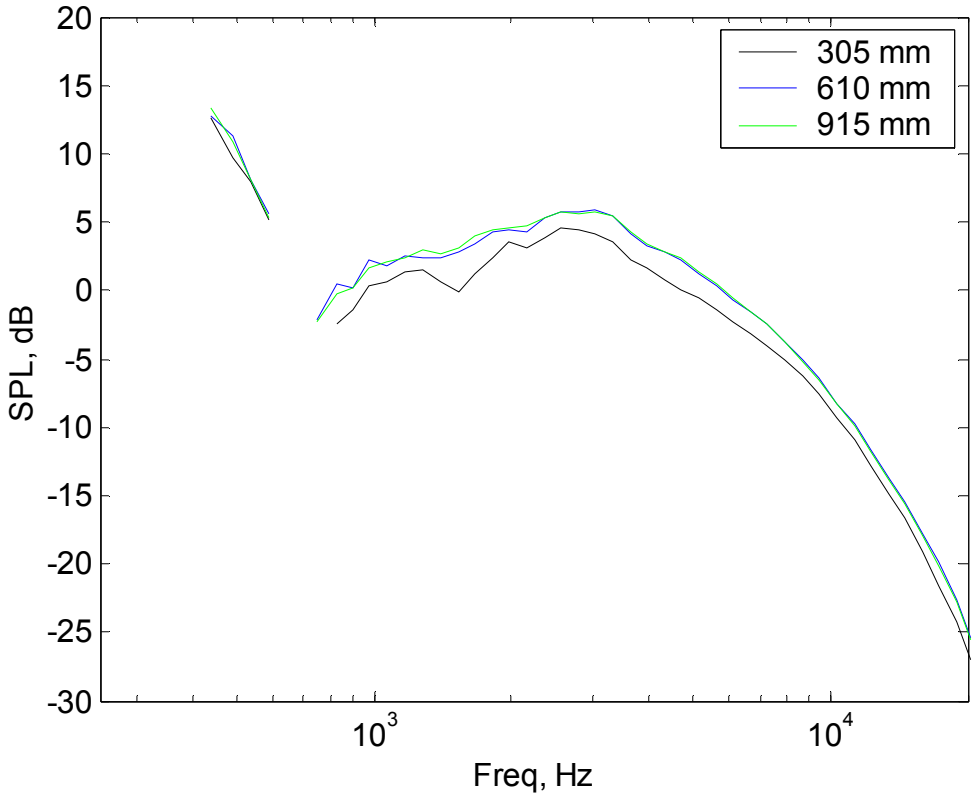

Figure 6-21 Sound levels measured at a fixed observer location for three different roughness patch lengths under the flow generated for a 12.7 mm nozzle exit with a nozzle exit velocity of 40 m/s.

6.5 Summary

The measured acoustic spectra show several important results about the behavior and physics of roughness noise. Measurements over a fixed roughness patch at various speeds show that increasing the flow speed tends to increase the spectral level and frequency of the acoustic spectral peak. Dipole and quadrupole normalization models were used to analyze these results. All dipole models regardless of scaling properties showed a similar collapse. The quadrupole models with the most realistic physical model showed the worst collapse, while those based on outer flow variables, inconsistent with any physical processes, showed the best collapse of the data. Spectra measured for variations in surface roughness size for fixed flow conditions show a strong relation between roughness size and sound level. The acoustic spectral levels increased, and the frequency of the spectral peak decreased as roughness size increased. Measurements over hydrodynamically smooth surfaces generated small but significant sound levels confirming acoustic scattering to be a least one physical mechanism responsible for roughness noise. Scaling of the data showed fundamental differences in the spectral shape, which make it impossible for a simple scaling model to completely collapse all data. Quadrupole models were unable to significantly improve the data scatter, while the

dipole models could provide reasonable collapse of all but the hydrodynamically smooth surfaces.

Measurements of the vertical directivity of noise generated by a patch of 40 grit roughness are consistent with the trends expected for a flow aligned dipole source. However, the limited range and scalloping effects do not allow this conclusion to be made definitively. Tests conducted with roughness patches of different lengths show increasing sound levels with patch size.

Chapter 7 Two-Dimensional Roughness

To investigate surface roughness noise in a significantly different way a two-dimensional rough surface was used. The use of a two-dimensional surface allows several unique capabilities beyond what were tested with the sand grit roughness. The two-dimensional roughness is deterministic and periodic with a preferred direction, unlike the sand grit that had a nearly isotropic correlation function. Based on acoustic scattering theories this would suggest that the radiated sound would be affected by the orientation of the roughness patch. The patch will also interact differently with the boundary layer flow in which it is submerged. This may result in a different scaling behavior based on the nature of this interaction. In this chapter information will be presented on the testing of the two-dimensional surface. The influence of flow speed over the two-dimensional surface will then be discussed and compared with the sand grit roughness tests. Measurements of the vertical directivity will also be examined and compared with the sand grit measurements. Finally, the affects of changing the roughness orientation will be examined.

7.1 Surface Characteristics and Edge Effects

The two-dimensional roughness used for these tests is a patch of lenticular lens material. This material, used for creating the appearance of moving or three-dimensional images, has tight tolerances on surface shape and finish. The lens is produced by Micro Lens Technology Inc. and is designated as Flip LPI 20. The surface used for these tests was at 560 mm by 710 mm patch with a ridge spacing of 1.27 mm. The ridge height was 0.118 mm with a backing thickness of 2.168 mm, giving a total sheet thickness of 2.286 mm.

Because the backing thickness for this material was significantly larger than the sand grit patches, on the order of one tenth of the typical boundary layer thickness, than the sand grit patches, tests of the edge noise needed to be performed. To determine the noise due to the step the same process was used, as used earlier. Figure 7-1 shows sound measurements taken for three different surface conditions subject to the same flow conditions. The flow is the result of wall jet with a nozzle height of 25.4 mm and a nozzle exit speed of 45 m/s. This results in a flow with a maximum velocity of 23 m/s at the roughness leading edge and a boundary layer thickness of 16 mm. The three surface conditions tested are with a smooth surface, with a 560 mm by 710 mm patch of two-dimensional roughness, and the same roughness patch covered with a sheet of Mylar. In the two cases where the roughness patch is used, the patch is attached to the plate surface beginning 1220 mm downstream of the nozzle exit. The patch is centered on the smooth plate, and contained fully within the two-dimensional flow region of the wall jet at this location. The roughness with the Mylar covering is used to produce the same step shape as with the roughness present, but covers the roughness on the surface of the lens.

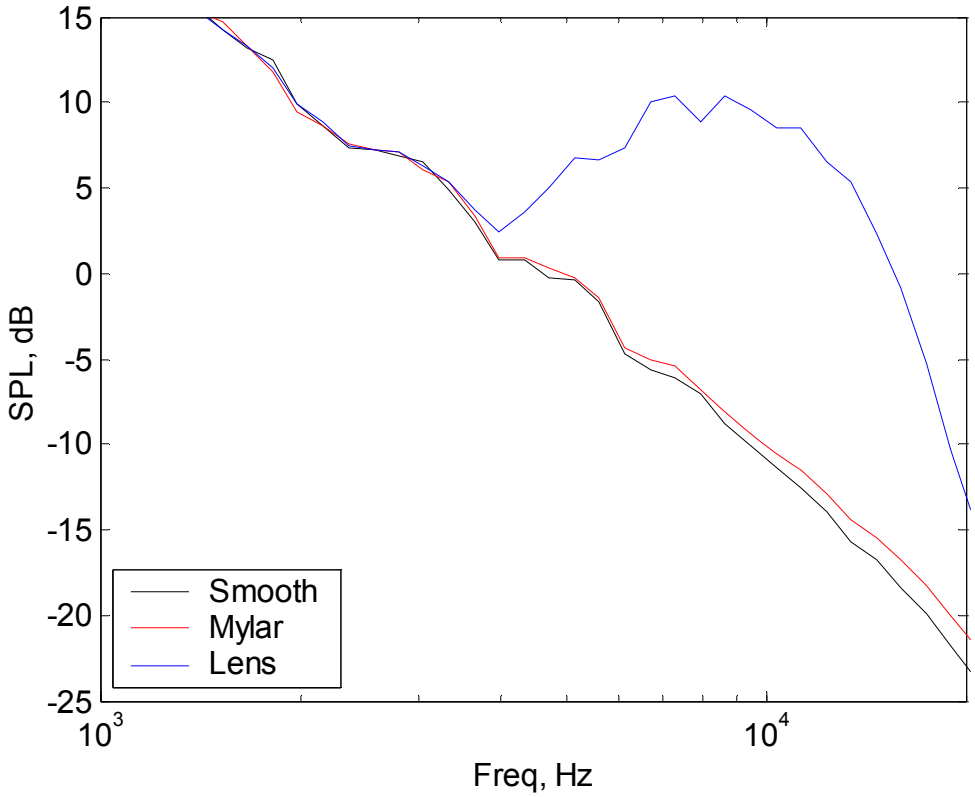

Figure 7-1 Acoustic spectra measured for the wall jet flow generated by a 25.4 mm nozzle with 45 m/s exit speed over a smooth plate, 2d roughness patch, and the 2d roughness patch covered with mylar.

The spectra shown in Figure 7-1 are measured using a single microphone located at x = 905 mm, y = 466 mm, and z = 0 mm with the microphone facing the direction θ = -37°. At this location the microphone was 775 mm away from the patch center, at a location 37° above the plate. The spectra show the roughness patch significantly increases the sound level at frequencies above 4000 Hz, with a peak frequency near 9000 Hz. When the roughness patch is covered with the Mylar sheet, leaving only the step at the edge of the roughness patch, the sound level falls back nearly to that of the clean plate. The sound spectra are less than 1 dB louder at all frequencies with the step present when compared with the clean plate sound levels. Since the surface roughness produces a 10-15 dB larger increase in sound level than this the effects of this step will be ignored in the remaining discussion.

7.2 Influence of Flow Velocity

This section describes the results of a test series, which investigated the influence of flow velocity on sound generated from a patch of two-dimensional roughness. A 560 by 711 mm patch of the two-dimensional roughness described in Section 7.1 was mounted to a fixed location on the plate with the ridges perpendicular to the flow. Changing the nozzle exit speed from 20 to 45 m/s varied the flow speed from 10 to 22

m/s over the roughness patch. The nozzle height remained fixed at 25.4 mm for all cases. The details of this test set are given in group G16 of Table 4-4. Figure 7-2 shows the acoustic spectra measured by a fixed microphone, microphone 1 from Table 4-4, for 7 different flow speeds. The spectra shown have the clean plate sound levels removed. The spectral levels increase with flow speed. The spectral peak also shifts up in frequency as the flow velocity increases. Both of these trends were seen in sand grit roughness measurements. The legend shows the average edge velocity over the roughness patch, computed from the linear average of the front and back maximum velocity. It also shows the roughness Reynolds number, which is in the hydrodynamically smooth range, $h^+<5$, for all cases except the two measured at 23.2 and 25.4 m/s, which are slightly above this range. In these measurements the frequency of the spectral peak increases from 4500 Hz to 8500 Hz from the lowest to highest speed cases.

The aerodynamic parameters used for scaling the acoustic spectra in this section have been estimated from a set of aerodynamic measurements on a subset of these roughness cases. The local maximum velocity is estimated from the clean plate wall jet model; this provides an excellent estimate of the local maximum velocity, as shown in Chapter 5. All other values are estimated from three measurements made at different speeds at the trailing edge of a 305 x 610 mm patch of the same roughness. The patches were centered at the same location on the plate. To account for the differences in patch length between the aerodynamic and acoustic measurement cases, trends from the measurements presented in Chapter 6.4 on the effects of patch length were used. This showed that skin friction varied with the -0.54 power of the patch length, when all other parameters were held fixed. The aerodynamic measurements are also effected by the larger step size associated with the backing thickness of the lens sheet. For these measurements the aerodynamic parameters were calculated using only values measured 1 mm above the plate, which is nearly half the backing thickness. This was done to try and account for the region of separated flow likely to exist downstream of the step. This method is not as accurate as direct measurements, and increases the uncertainty in the trailing edge scaling parameters to 10% of their nominal values.

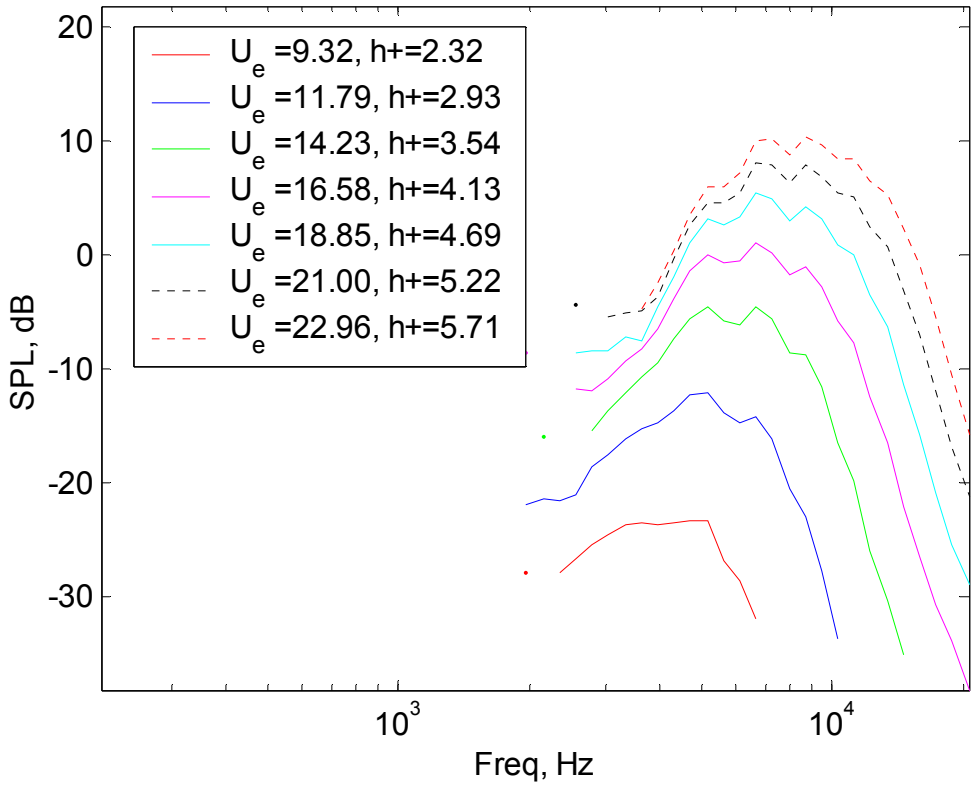

Figure 7-2 Acoustic spectra measured at different flow speeds for flow over a patch of two-dimensional roughness.

Figure 7-3 and Figure 7-4 show two possible velocity scalings based on the mean velocity over the rough patch. Figure 7-3 shows the acoustic spectra scaled on the dipole scaling proposed by Cole (1980), based on outer variables. The frequency scale has been non-dimenionalized using the maximum velocity, U_e, and the boundary layer momentum thickness, δ^*. The amplitude has been normalized on the same parameters, with the velocity raised to the fifth power as is expected of a dipole acoustic source. This figure shows a good collapse in the high frequency region above the spectral peak. Above a non-dimensional frequency of 5 the spectral collapse of the data is within a 1 dB spread. At lower frequencies, from 1 to 5, the collapse is poor, with a 15 dB spread in the peak spectral levels measured at different speeds. The frequency collapse shown in Figure 7-3 is reasonable, but does not align the spectral peaks from the various speeds. It pushes the low-speed spectra to higher frequencies than the high-speed spectra.

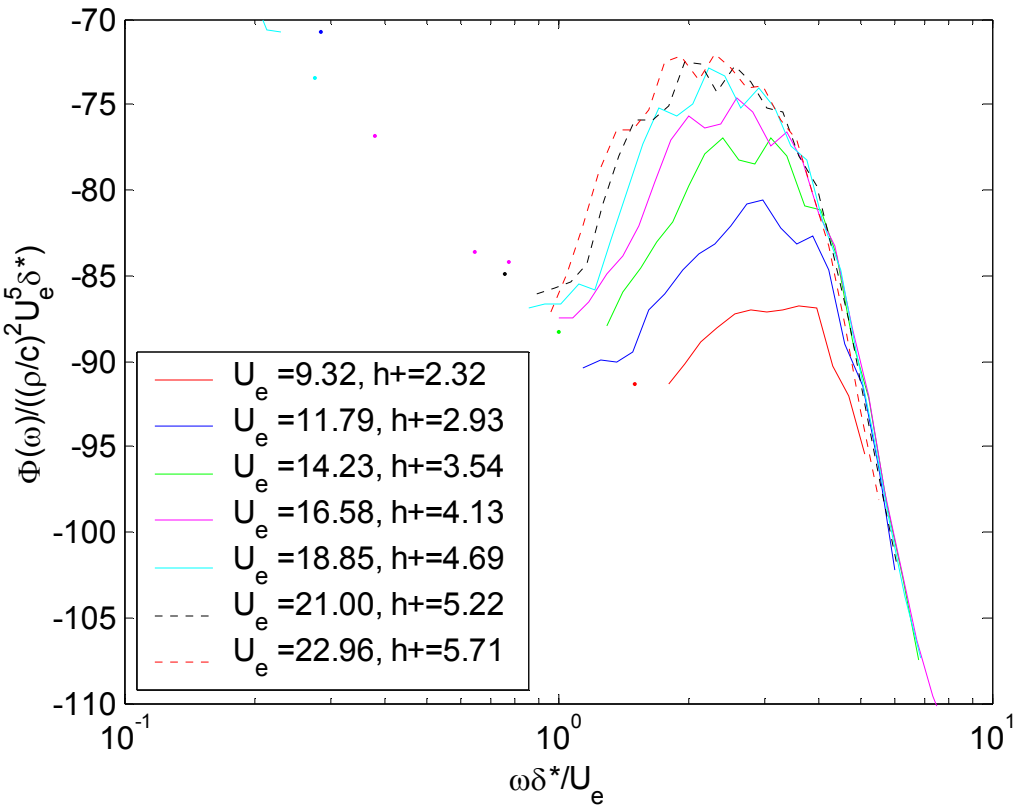

Figure 7-3 Far field acoustic pressure spectra from a two-dimensional roughness patch normalized on a dipole scaling using the local edge velocity, U_e, and displacement thickness, δ*.

Figure 7-4 shows the result of scaling the spectra using the quadrupole velocity scaling law with the same parameters. (Cole, 1980) This does not affect the frequency scaling, but shows significant improvement in the scaling of the power spectral level. The scatter in the peak spectral levels is reduced from 15 to 7dB. The collapse however is made worse in the high frequency region. This scaling still works best at high frequencies. The low frequency region around and below the spectral peak shows a significant spread in spectral level.

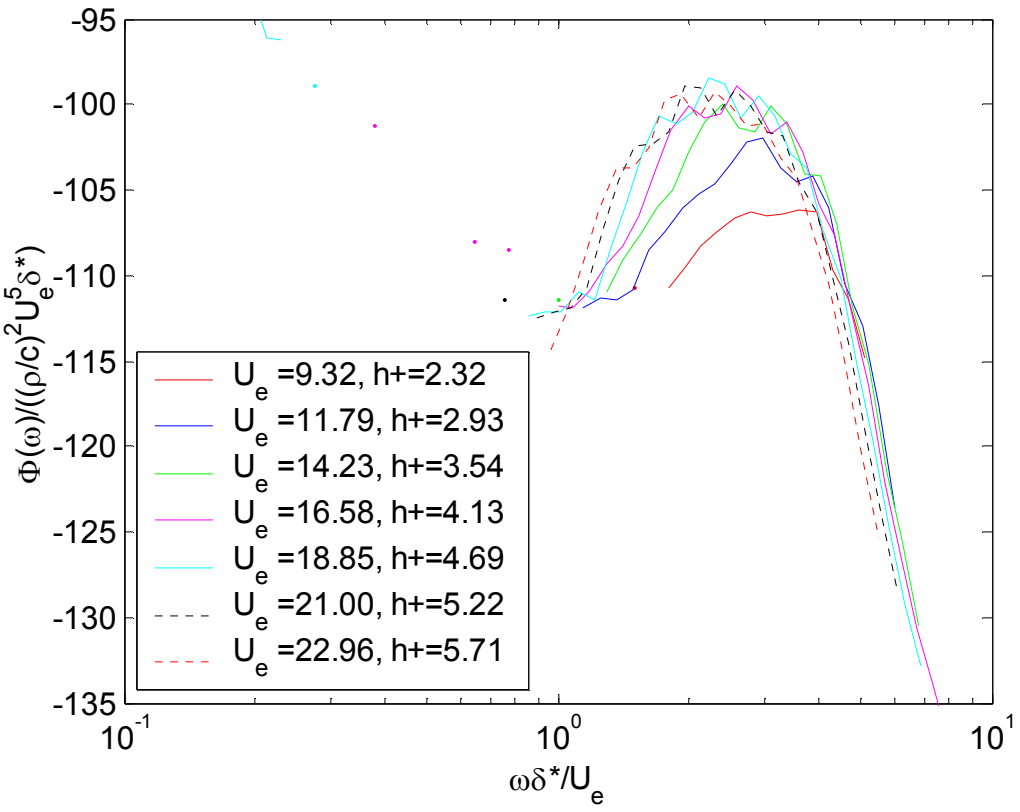

Figure 7-4 Far field acoustic pressure spectra from a two-dimensional roughness patch normalized on a quadrupole scaling using the local edge velocity, U_e, and displacement thickness, δ*.

Figure 7-5 shows the spectra normalized according to the model proposed by Glegg (2007). This model is the only one that explicitly accounts for a roughness streamwise length scale that is different from the roughness height. This model also does a better job collapsing the high frequency spectral roll off than it does collapsing the spectral peaks. The peak levels are spread over 15 dB. The frequency scaling also aligns the spectral peaks within one fifth of a decade. The models of Farabee and Geib (1991) and Howe (1988), Figure 7-6, also show a tight collapse in the high frequency roll off of the measured spectra, but do not collapse the spectral peaks.

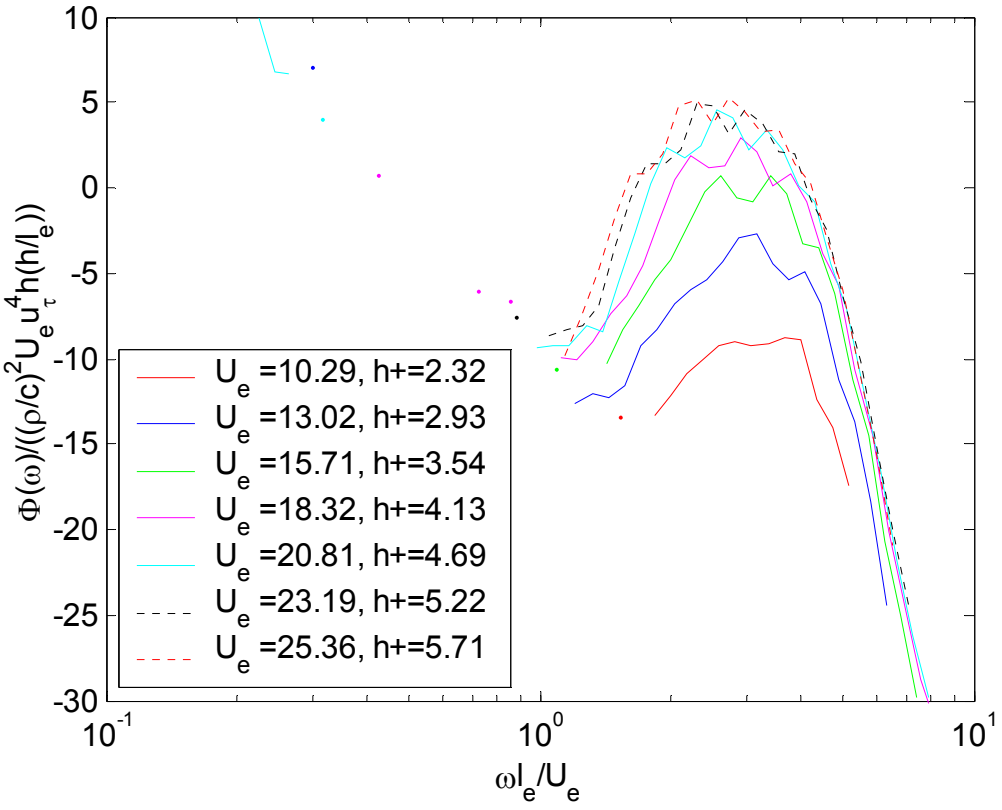

Figure 7-5 Far field acoustic pressure spectra from a two-dimensional roughness patch normalized on the dipole scaling model proposed by Glegg (2007).

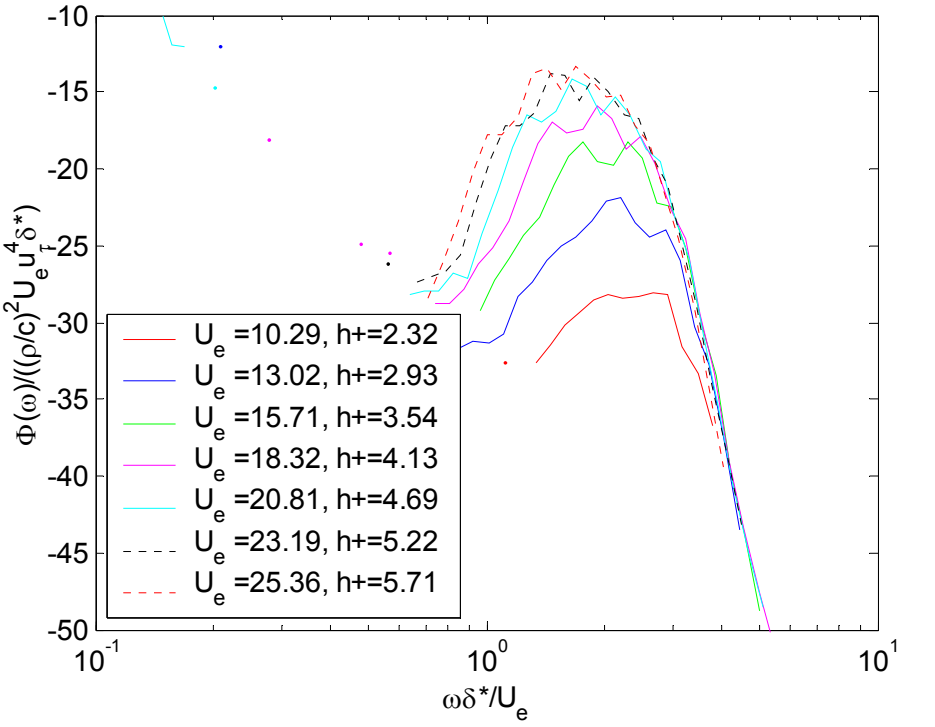

(a)

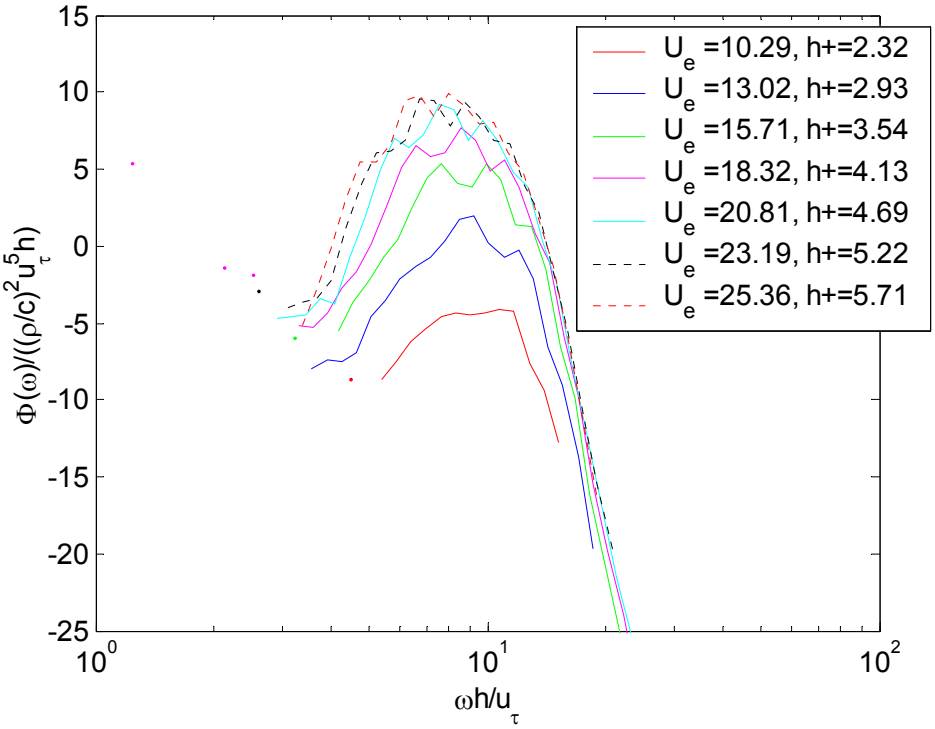

(b)

Figure 7-6 Far field acoustic pressure spectra from a two-dimensional roughness patch normalized on: (a) the model of Farabee and Geib (1991), and (b) the model of Howe (1988).

When the two-dimensional spectra are compared with the sand grit spectra it becomes obvious that the surface shape plays a significant roll in determining the level and form of the far field acoustic spectrum. Figure 7-7 shows the acoustic spectra measured for the two-dimensional velocity tests and the 40 grit velocity tests. The spectra measured over the two-dimensional surface are much narrower and more peaked than the sand grit roughness. This shows that there can be no single scaling law that will normalize roughness noise for all surfaces, because the spectra shapes are fundamentally different from these two surfaces.

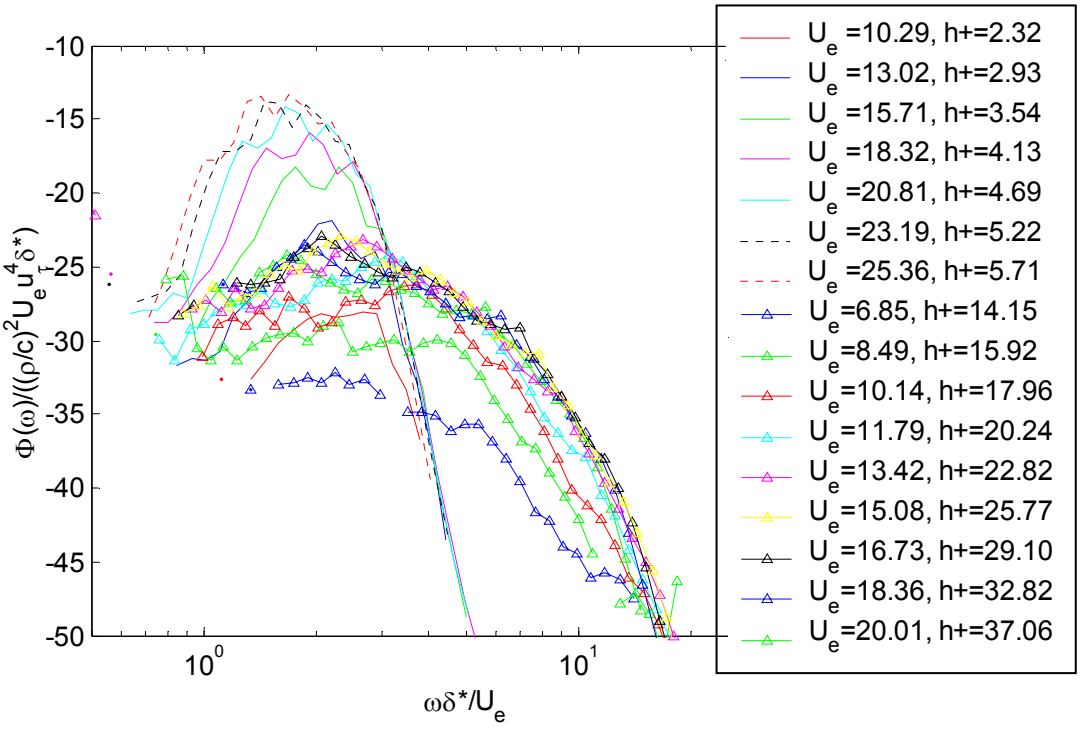

Figure 7-7 Far field acoustic pressure spectra for two-dimensional roughness, shown as solid and dashed lines, and sand grit roughness, shown as lines with triangles, shown for variations in flow speed.

7.3 Vertical Directivity

To investigate the vertical directivity of the acoustic field a similar test was conducted using 4 microphones. The microphones were placed on a circular arc in the *y-z* plane with a 775 mm radius centered on the middle of the roughness patch. The microphones were placed at angles of θ = 37°, 47°, 64°, and 92° measured from the upstream side of the plate, as shown in Figure 7-8. The two-dimensional roughness patch was tested with the ridges aligned normal to the flow, to generate the most noise in the mid-plane of the wall jet flow. Measurements are presented for a nozzle speed of 45 m/s and a 25.4 mm nozzle height.

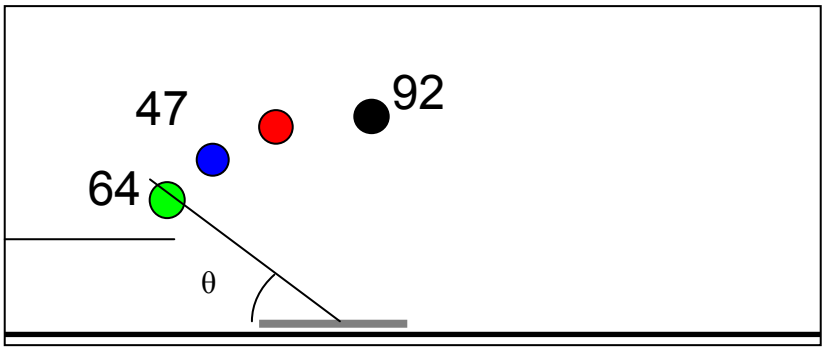

Figure 7-8 Schematic of the microphone arrangement used for the vertical directivity test.

Figure 7-9 shows the spectra measured for these conditions. The first feature of this plot is that the spectral shape of each spectrum appears the same, with only the spectral level shifted up or down. This suggests the microphones are all measuring the same acoustic source, and information about its directivity can be assessed. The sound levels vary directly with the microphone angle. The highest levels are detected by the microphone at 37°, the most upstream position measured. The remaining microphones measured spectral levels, which were 1, 4.5, and 10 dB below these levels at angles of 47°, 64°, and 92° respectively. If the source were modeled with a set of distributed dipoles modeled like that of Section 6.4, a similar directivity pattern would be expected. Relative to the 37° curve the other curves would be expected to be 0.9, 3.2, and 12.5 dB quieter, in order of increasing measurement angle. These predicted and measured variations are in close agreement, further suggesting a dipole source.

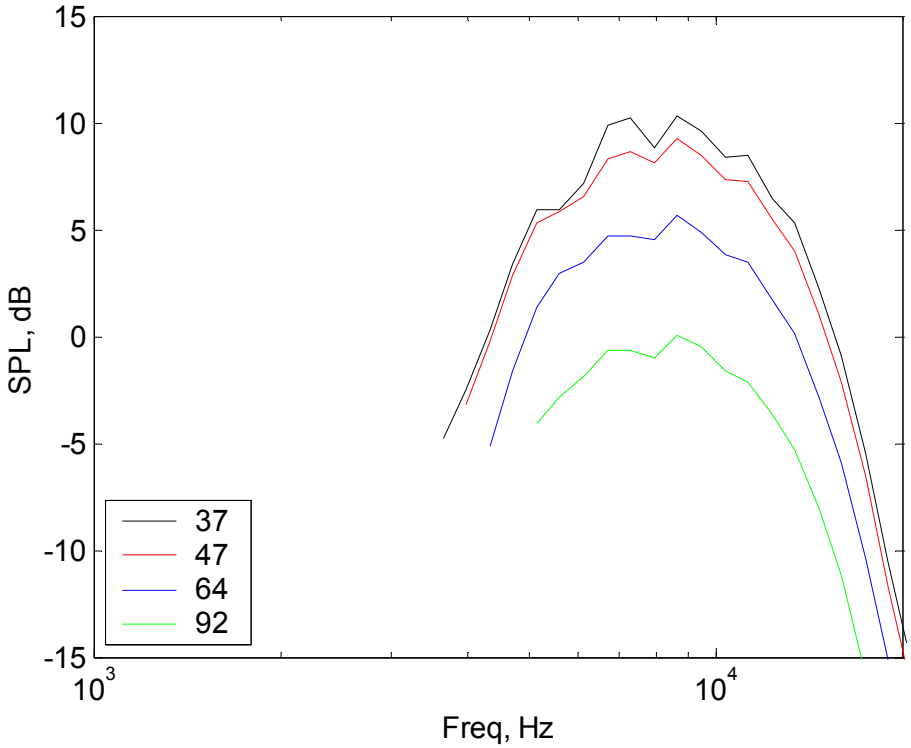

Figure 7-9 Acoustic spectra measured in a vertical arc centered over the two-dimensional roughness patch. The legend values are the vertical angles, θ, between the microphone position and the center of the roughness patch.

The same measurements were also made at different flow speeds, to confirm this measurement was independent of flow speed. Figure 7-10 shows the results of this test. The acoustic spectra were measured at the same locations discussed above and with the nozzle flow speed varied from 15 m/s up to 45 m/s, corresponding to the same speeds shown in the velocity test cases. Figure 7-10 shows the spectral levels at each speed normalized on the spectra measured at 37° for that speed. The 37° microphone line is shown at 0 dB for reference. The figure exhibits that for all the speeds, the results are almost identical to the results presented at 45 m/s. The frequency range and absolute levels of the spectra changed at each speed, but the effects of different angles appeared to be independent of velocity variations.

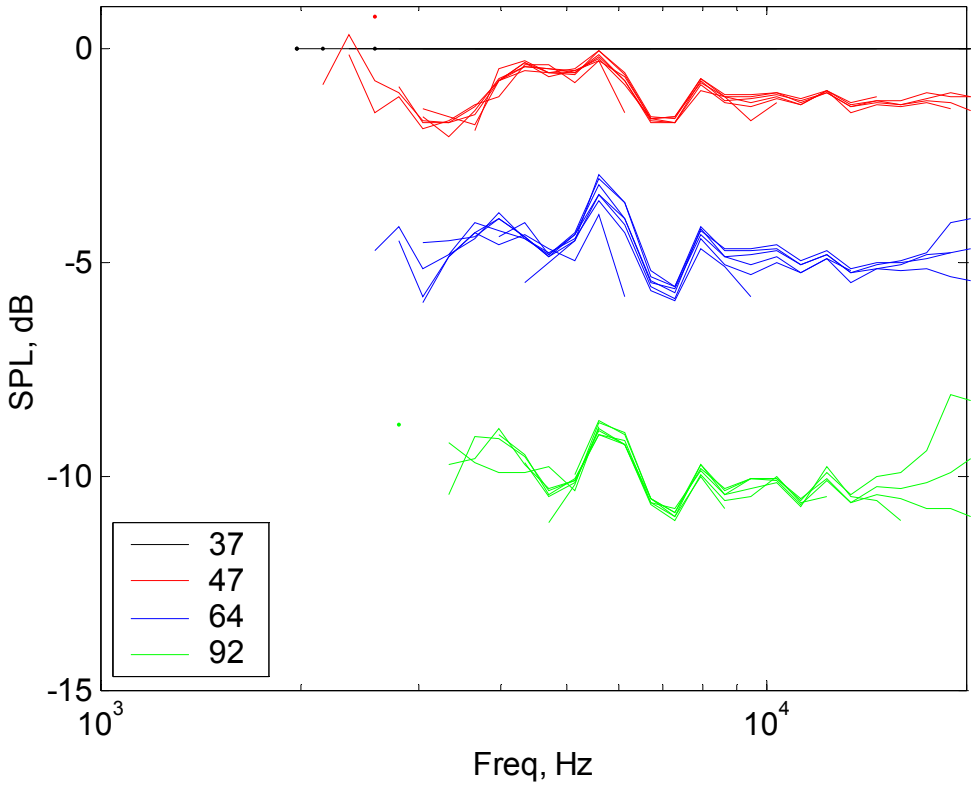

Figure 7-10 Ratio in acoustic spectra levels relative to spectra measured at 37° above the plate for flow over a two-dimensional roughness patch at different speeds. The legend values are the vertical angles, θ, between the microphone position and the center of the roughness patch.

7.4 Effects of Roughness Orientation

Since the lens roughness has an anisotropic roughness pattern it can be used to investigate the effects of roughness orientation on the radiated sound. For this test a 560 mm by 710 mm patch of lens sheet was placed on the plate at different orientations to the flow and far field measurements were made at a fixed location. In all cases the patch was centered at the same location on the plate, x = 1530 mm and y = 0mm. The microphone

was located in the same location described above, 775 mm from the center of the roughness patch, 37° above the plate surface. The microphone locations and surface conditions are shown in Table 4-4 groups G18-20. The patch was tested in 4 orientations with the lens ridges: normal to the flow, 30° to the flow, 60° to the flow, and aligned with the flow. These are shown on the right of Figure 7-11. Because a rectangular patch was rotated about a fixed point the corners of the roughness patch are moved farther up and down stream as the patch is rotated, exposing them to different portions of the wall jet flow. The expected differences in spectral levels due to flow speeds variations resulting from the patch rotation are less than 1 dB. These effects can be neglected in comparison to the larger effects seen as a result of the changes in roughness orientation. All measurements were made under the same tunnel flow conditions with a tunnel exit velocity of 45 m/s and a nozzle exit height of 25.4 mm.

7.4.1 Orientation Effects at a Fixed Observer Position

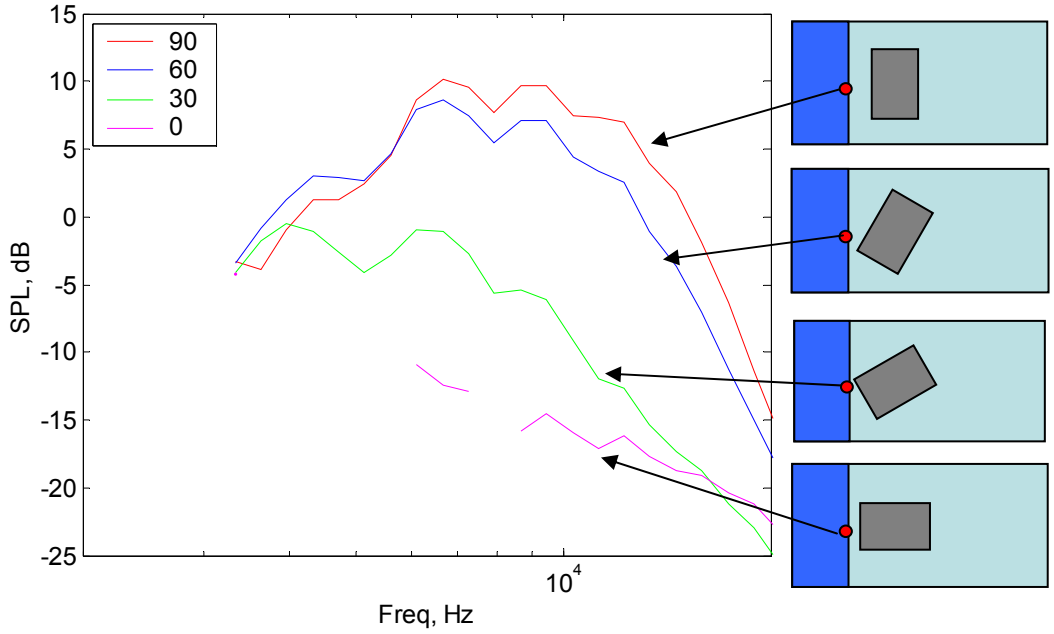

Figure 7-11 Acoustic spectra measured for flow over a lens patch at different orientations to the flow. Legend titles give the angle between the flow and the roughness ridges in degrees.

The spectra in Figure 7-11 show that there is a significant effect from the variation of roughness orientation on the resulting flow field. There is another effect that is clear in Figure 7-11, which is not a result of the roughness noise itself. The scalloping, or bumpiness, of the acoustic spectra seen in this figure is the result of the acoustic enclosure around the plate and is not the result of the nature of the roughness noise. These effects have been eliminated from many of the other spectra presented in this paper but were not removed from these results. In these tests only one microphone was used at each position, which prevented the removal of the scalloping. The red curve, with the roughness ridges at 90° to the flow, is the loudest, with a peak level near 10 dB. The next lowest curve, the blue curve, show the spectra measured after the roughness patch had been rotated to that the angle between the flow and the roughness ridges was 60°. The

overall shape of the spectrum is very similar to the 90° curve. The levels are 2 to 3 dB lower at most frequencies, except low frequencies where the blue curve is louder than the red curve. This is the result of a slight frequency shift that occurs when the roughness patch is rotated which decreases the frequency at which the acoustic spectra peak. The green curve shows the effects of rotating the roughness patch another 30° into the flow. For this case the ridges form a 30° angle with the flow, and show a significant decrease in the measured acoustic level. The spectrum levels at the 30° angle are 8 to 10 dB quieter than the case with the roughness normal to the flow. The peak frequency is also significantly lower. In the flow normal case, the acoustic spectrum peaked near 8000 Hz, while for this case, the spectrum appear to peak near 4000 Hz. Determining the frequency of the spectral peak is difficult given the amplitude of the scalloping, but the peaks seem to be within 1000 Hz of these values. The final curve in Figure 7-11 shows the results of having the roughness ridges aligned with the flow. In this case there was very little measurable increase in noise level. Only at high frequencies, above 9000 Hz was there a consistent increase in sound levels above the smooth plate levels measured for the same flow conditions.

7.4.2 Orientation Effects on Horizontal Directivity

Another aspect of the far field noise that was investigated with the two-dimensional roughness patches was the horizontal directivity. To look at this, four microphones were placed in an arc around the roughness patch. The arc was circular with a radius of 775 mm and centered on the center of the roughness patch, in a plane 470 mm above the plate surface. The microphones were placed at four locations in a single quadrant of the circle at angles, ϕ, of -2°, 26°, 43°, and 53° relative to the negative x-axis from the center of the roughness patch. The microphones are oriented to face the center of the roughness patch. This configuration is shown in Figure 7-12. The microphones could not be placed farther downstream due to interactions with the flow field, which masked the acoustic signal at these locations. Microphone measurements were taken at these locations for the same conditions described above, with the roughness patch in 4 orientations, and the flow speed fixed at a nozzle exit speed of 45 m/s with a 25.4 mm nozzle opening.

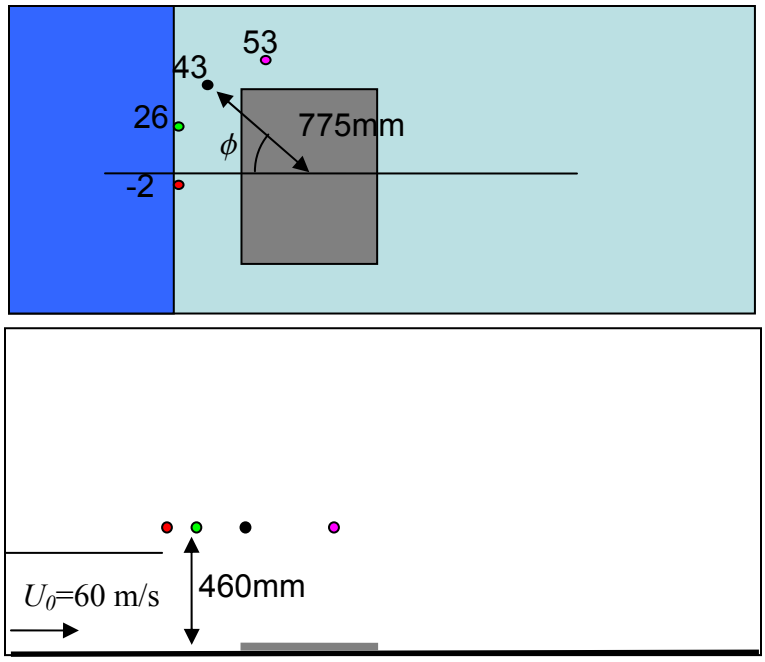

Figure 7-12 Microphone locations shown for the horizontal directivity test over the two-dimensional surface roughness patch.

Figure 7-13 shows the measurements made from the 4 microphones with the roughness ridges oriented perpendicular to the flow. The legend values indicate which microphone is associated with each spectral curve. The figure shows that as the microphones are moved towards the side of the roughness patch the detected sound level decreases. The first two microphones, at -2° and 26°, show levels that are essentially the same over the frequency range measured. The measurement made at 43° shows an almost uniform 3.4 dB decrease relative to the previous two curves, while the measurement at 53° shows a further 6 dB decrease, being nearly 9.5 dB below the two curves measured most directly ahead of the roughness patch. This shows clearly that the sound field is not radiating evenly, but radiates most efficiently forward, and with progressively less strength to the sides. Another thing to notice is the shape of this curve does not change with each microphone location. This suggests that each microphone is measuring the same acoustic source, and the effects are solely the result of the source directivity. The spectral peak does not move with the different microphone positions further confirming this result. Based on the measurements seen earlier, if the microphones were detecting sound from different parts of the roughness patch, or from other sources, the spectral peaks would shift as a result of the variations in flow speed along the wall jet. If the sound source was assumed to be a simple dipole at the center of the roughness patch the expected sound variations would be similar. The first two curves are expected to be within 1.1 dB of one another, with the 26° curve being slightly quieter. The uncertainty in the spectral levels is on the order of 1 dB so this type of variation is hard to determine from the results. The 43° location should show levels 4.7 dB below the -2° curve. The difference in levels seen here is 3.4 dB, with the uncertainty in spectral levels this is close to that expected from the simple dipole model. The spectrum at 53°

would be expected to be 8.8 dB below the -2° curve, again matching closely with the results seen here. This suggests that the sound source would be well modeled with a dipole directivity pattern.

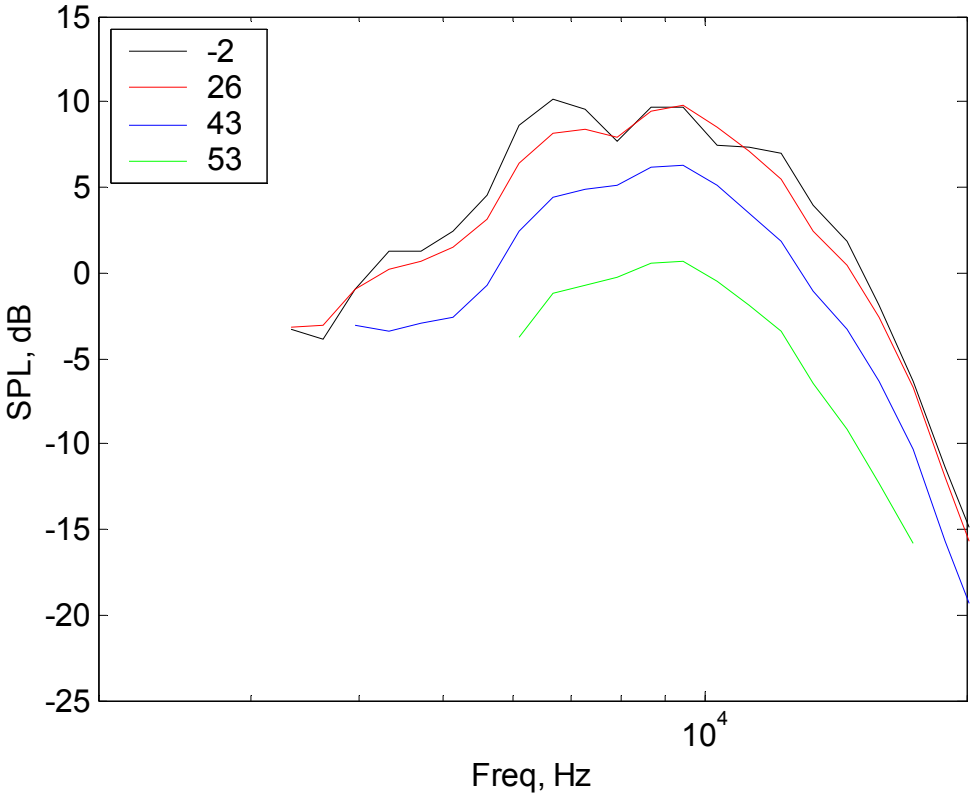

Figure 7-13 Spectra measured by four microphones at different angles along a horizontal arc around a patch of two-dimensional roughness. The roughness ridges were aligned perpendicular with the flow. The legend values are the horizontal angles, ϕ, between the microphone position and the center of the roughness patch.

Figure 7-14 shows the sound field measured by microphones in the same positions, but with the roughness patch rotated 30°, so that the roughness ridges form a 60° angle with the flow direction. This also means the line perpendicular to the direction of the ridges now points 4° away from the 26° microphone. Again we see that the spectral shapes are consistent at each microphone, and we see that there is a significant change in sound level measured at the different microphone locations. However, the variation in levels is different in this case than the previous case. The two forward most microphones are still indistinguishable from each other, but the blue curve, measured at 43° from the flow axis is now much closer to the group as well. The 53° microphone is still the quietest, but is now only 6 dB below the highest spectral peak, not 9.5 dB as seen earlier. If the source is assumed to be dipole in nature with the dipole axis following the line perpendicular to the roughness ridges, the prediction of acoustic levels is reasonable. It would predict the 26° microphone to detect the loudest spectrum, with the 43° microphone detecting levels 0.2 dB below this, and the -2° location 2 dB below the loudest levels. These predictions are not well matched in the results, which show the 43°

microphone picking up levels which are lower than the -2° and 26° microphones, but all three microphone levels are close. The 53° microphone is predicted to be 0.8dB below the loudest level, but this is clearly an underestimation, as the actual levels are nearly 6dB below the loudest spectrum measured. If the dipole axis were at 15° to the flow the agreement becomes much better, but a model that would incorporate this half angle seems unlikely to have much physical meaning.

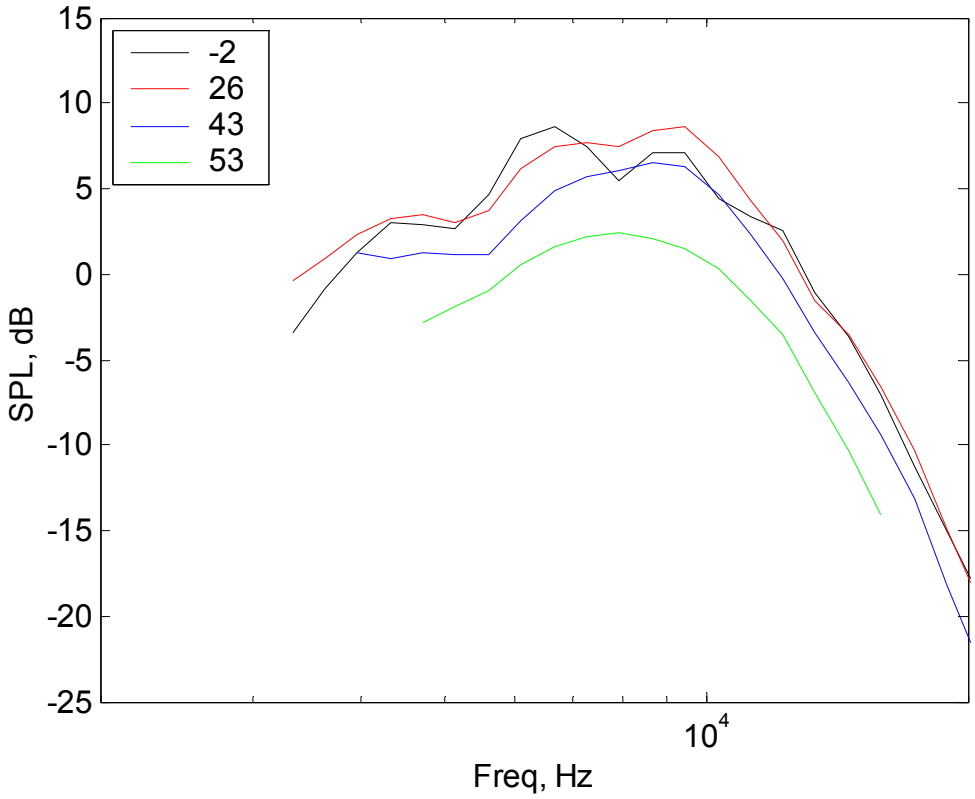

Figure 7-14 Spectra measured by four microphones at different angles along a horizontal arc around a patch of two-dimensional roughness. The roughness ridges form a 60° angle with the flow direction. The legend values are the horizontal angles, ϕ, between the microphone position and the center of the roughness patch.

Figure 7-15 shows spectra measured in the same manner after the roughness patch has been rotated an additional 30°, so that the roughness ridges are now at 30° angles to the flow. These levels show a significant difference compared with the ones seen at the two previous angles. First it is more difficult to determine the shape of the acoustic spectra measured for this condition. The -2° measurement seems to show the familiar scalloped parabola shape, along with the 53° curve, but the remaining two curves are less clear. However, another significant difference is the order of the spectral levels that are seen with the roughness in this orientation. Here, the two highest curves were measured at 26° and 43°. The spectral levels measured at these two locations are very similar, while the spectra measured at -2° and 53° vary from matching the levels of the other two curves to being as much as 4 dB below them. The key difference is that the direction of peak radiation seems to have moved away from the forward facing direction and to a

direction between the 26° and 43° measurement locations. If the dipole source is assumed to follow the roughness direction the highest levels would be expected at 53°, with levels decreases as the angle is reduced. If the dipole is assumed to be at 30° the predicted levels agree fairly well with the measured results. The two middle levels are predicted to be within 0.2 dB of each other, the 53° location 0.8 dB below this, and the -2° location -2 dB below the loudest one. This gives further support to the idea that the dipole is facing the angle midway between the roughness direction and the flow direction.

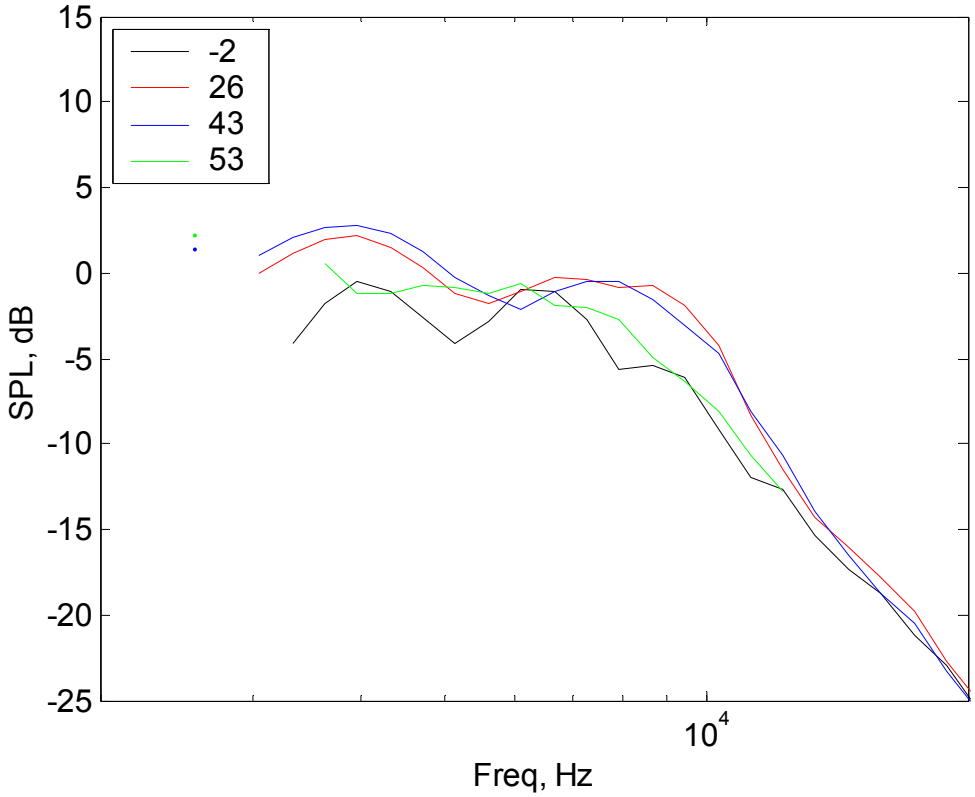

Figure 7-15 Spectra measured by four microphones at different angles along a horizontal arc around a patch of two-dimensional roughness. The roughness ridges form a 30° angle with the flow direction. The legend values are the horizontal angles, ϕ, between the microphone position and the center of the roughness patch.

The final measurement in this series was conducted with the roughness ridges aligned with the flow. Almost no measurable increase in sound levels relative to those of the clean plate was detected. A slight increase was detected at high frequencies at the two forward most microphones, but this increase could not be distinguished from the noise due to the step associated with the edge of the roughness patch, and therefore will not be discussed.

Chapter 8 Discussion

The far field sound measurements presented in the last two chapters represent by far the largest and lowest uncertainty dataset of roughness noise measurements found in literature. There are several behaviors and results that can be drawn from this set that warrant further discussion. In this chapter these topics will be presented and further analyzed. First, the possible influence of Reynolds number effects on the pressure spectra will be discussed and how this would affect the far field pressure spectrum. Secondly, the scattering model proposed by Glegg (2007) will be compared with the measured spectra and the model of Howe (1991).

8.1 Reynolds Number Effects

As discussed in Chapters 6 and 7 all of the previously proposed scaling laws have difficulty relating acoustic spectra measured at different conditions. First, consider the influence of flow velocity presented in Chapter 6.1. In that section, all of the dipole models suffered from a similar problem, the two spectra measured at the lowest edge velocities could not be brought to collapse with the remaining curves, see Figure 6-5. Examination of the normalized spectra show that the scatter in the spectral collapse is not random, but that the curves collapse more and more tightly as the velocity is increased. Spectra measured above a mean edge velocity of 10 m/s appear to collapse into a fairly tight band with many of the scaling models. The momentum Reynolds number ($R_{em} = \theta U_e/\nu$) for the two lowest speed cases are 665 and 790 respectively. Traditional turbulent boundary layers are not considered fully turbulent until reaching a Reynolds number of at least 600 or greater. This suggests that these two cases may not be fully turbulent or are only just beginning to become fully turbulent at the end of the roughness patch. This could explain why the scaling models could not collapse all of the measured data into a tighter band. The scattering models assume a form of the wall pressure spectrum, which is then scattered, creating the modeled far field pressure spectrum. Glegg (2007) uses the Corcos (1963) model, while Howe (1991) uses the Chase (1987) model, although both wall pressure models are very similar in the region around the convective ridge where most of the energy is contained. These models assume the wall pressure spectrum is fully turbulent, and does not account for any Reynolds number dependent changes in the nature of the wall pressure spectrum. This may account for the higher than expected growth in the sound levels for the two lowest speed cases, because it is likely that the wall pressure spectrum levels are growing faster than ρu_τ^2 as predicted in these two models.

A similar situation is shown in the variation in acoustic spectra resulting from variations in roughness size. The two scattering models again show a systematic variation in the collapse of the spectra. In this case, the spectra are shifting to higher frequencies with h^+. This effect can again be attributed to the wall pressure spectrum models on which the scattering model depends. The models were developed for smooth wall turbulent boundary layers, not rough wall boundary layers. If the surface pressure spectrum is affected by the presence of the surface roughness, which it likely is, then the

scattering models will not be able to predict the far field sound levels. The systematic error in the scaling seems to suggest it is dependent on the roughness Reynolds number, h^+. This effect would also likely be most prominent in transitionally rough case, which is the region covered by this study. The wall pressure spectrum would be expected to vary more slowly with h^+ once the flows were fully rough.

8.2 Simple Scaling Models

A number of simple scaling models have been analyzed to collapse the far field acoustic spectra measured. The results show that there are two frequency regions that are unable to be scaled together using a single scaled model. This can be seen because the spectral shape differs in measurements taken over different surfaces. The most obvious example of this is when the measurements taken over sand grit roughness are compared with those taken over the two dimensional roughness. Figure 8-1 shows a comparison of the sound spectra measured over the 40 grit roughness for different speeds, group G5, and measurements made over the two-dimensional roughness at similar speeds, group G16 of Table 4-4. The shape of the acoustic spectra from the two-dimensional roughness has a much narrower peak, with a faster rate of fall before and after the peak. Since simple scaling models can only shift the spectral curves on a log plot there is no way for a simple scaling model to collapse these tests of curves together.

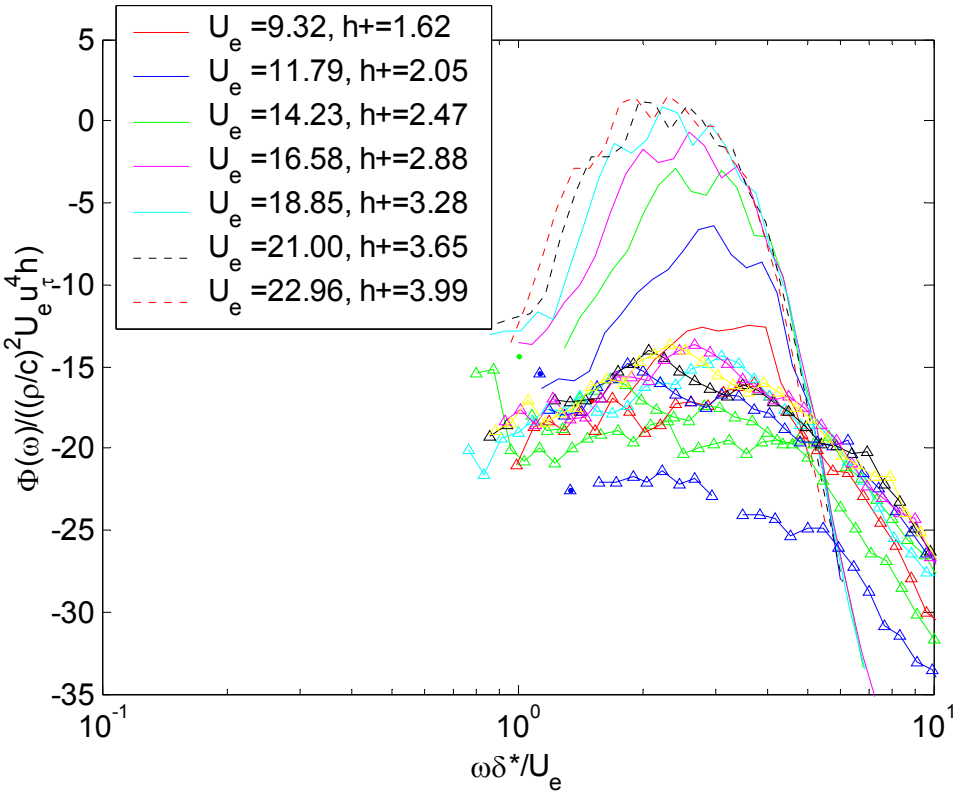

Figure 8-1 Measurements taken over 40 grit sandpaper roughness marked by triangles, compared with measurements over the two dimensional roughness shown with lines.

Beyond the effects of roughness form, the measurements also show changes in spectral shape with variation in flow speed and roughness size. Figure 8-2 shows the acoustic spectra, which show the effects of velocity variation, measured in group G5 from Table 4-4. All spectra are measured over a 40 grit surface subject to different flow velocities. The spectra have been scaled on the frequency axis using outer flow variables, which do the best job of aligning similar parts of the spectrum. The spectral levels are shown in ⅛ octave band levels, so that changes in the amplitude scaling are independent of changes in the frequency scale. Close inspection of the shape of the spectral curves shows that they are not the same. A more defined method for assessing the effectiveness of a scaling variable is to plot the log of the spectral level against the log of the variable. This can be done for each frequency as well. If a variable will directly scale the spectra, the slope of the result curve will be constant, and will be the same at all frequencies. Figure 8-2 (b) shows the result of this process for three different frequencies taken from the spectra in Figure 8-2 (a). The plot shows that at a non-dimensional frequency of 5 the edge velocity should do a very good job of scaling the measured spectra. At this frequency the slope the spectra would be scaled well on the 5.7 power of the edge velocity, nearly matching the 6^{th} power expected from a dipole model. At a non-dimensional frequency of 2.5 the scaling is very similar. The red curve measured for $\omega\delta^*/U_e = 2.5$ has an average slope of 5.8 with slightly more variations in slope than were seen at a non-dimensional frequency of 5. The curve for $\omega\delta^*/U_e = 15$ has a slope of 4.5, showing that the scaling behavior changes at high frequency.

Figure 8-3 shows the results of the same analysis on the measurement sets where the roughness height was varied, but the flow conditions held constant, groups G1 from Table 4-4. The frequency has again been normalized on the outer flow variables. In this figure it is easier to see that a simple scaling cannot collapse the spectra. The spectra from different roughness cases appear to be scaled versions of the same curve; however, on a log scale this means they cannot overlay one another. Some of the broadening of the spectra may be due to variations in the wall pressure spectrum along the roughness patch. As discussed in Section 6.2 the flow length scales varied significantly along the length of the roughness patch. If the wall pressure spectrum varies accordingly the resulting acoustic spectra would be broadened as the roughness size increases. The plot on the right (b) shows the spectral level plotted against roughness height for three frequencies. The curves in Figure 8-3 (b) are not straight indicating a simple power scaling on the roughness height will not collapse the spectra.

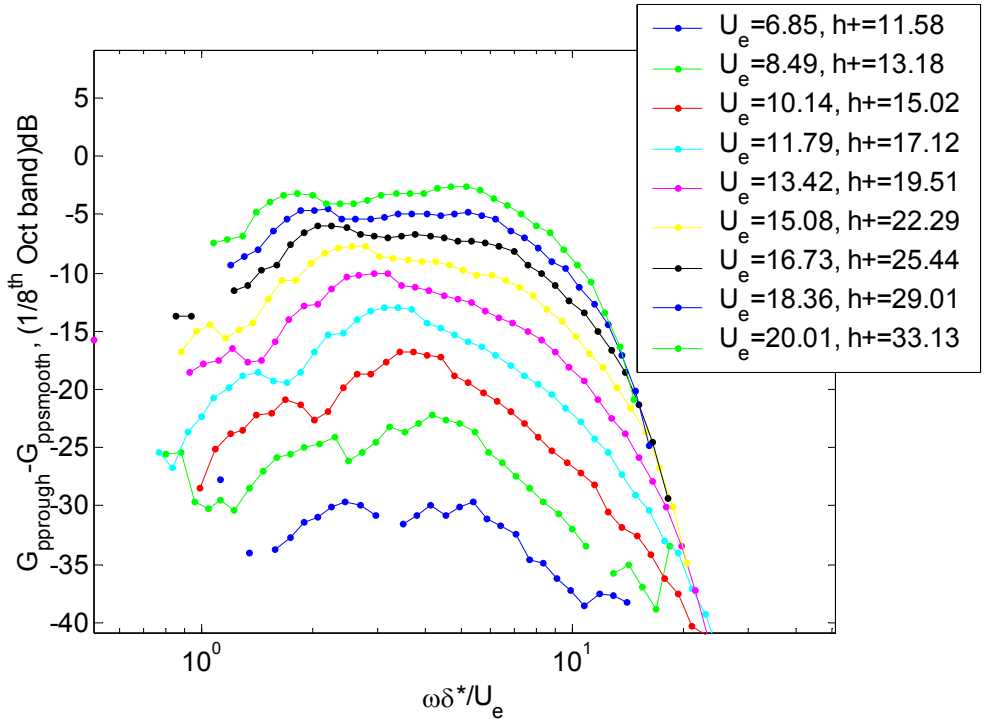

(a)

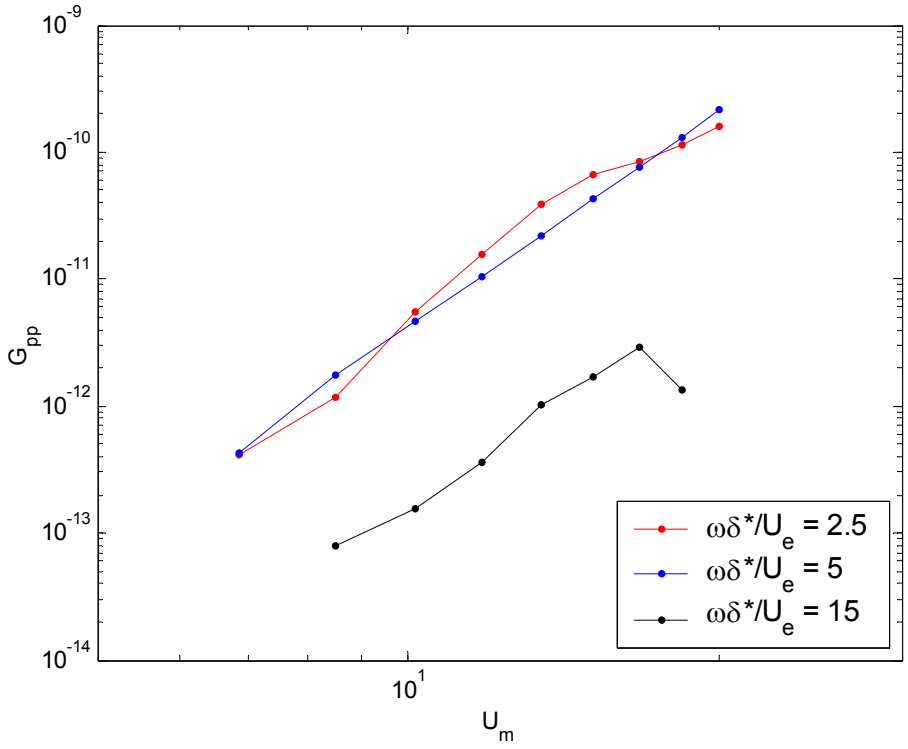

(b)

Figure 8-2 Acoustic spectra measured for flow past 40 grit sand paper at different speeds. The frequency has been non-dimensionalized using outer flow variables, and the amplitudes are shown as 1/8th octave band levels. On the right, the spectral level is plotted against the edge velocity for three non-dimensional frequencies.

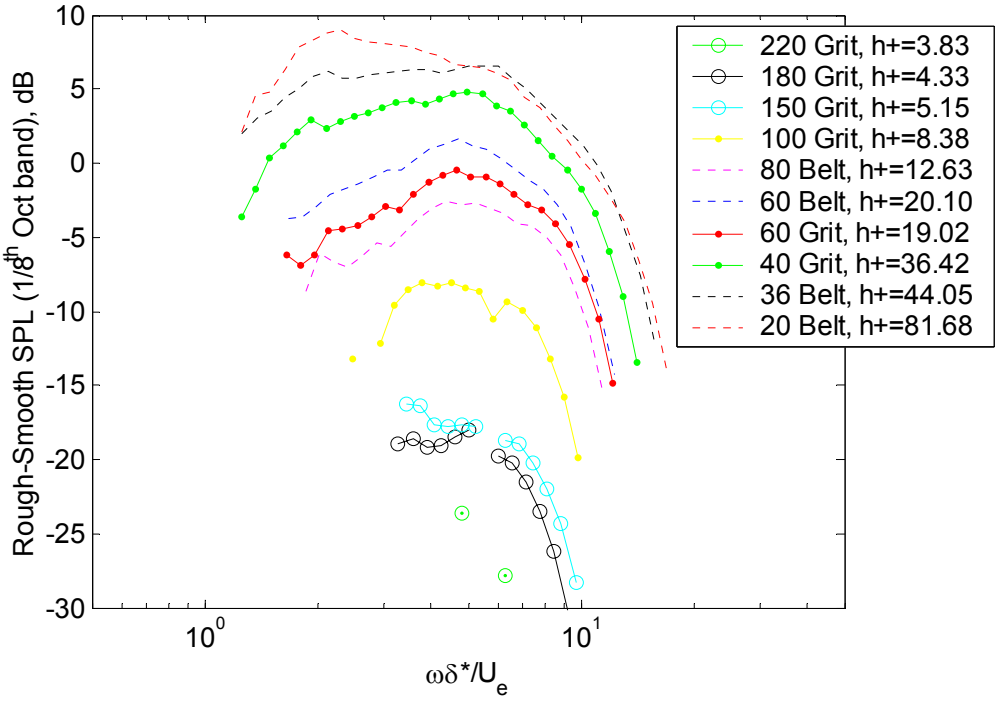

(a)

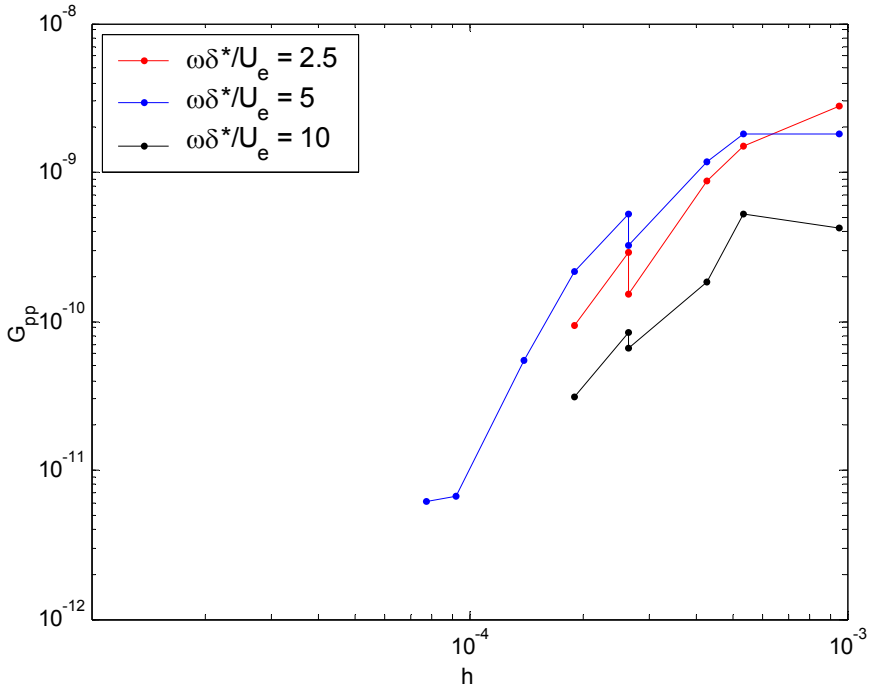

(b)

Figure 8-3 Acoustic spectra measured for flow past different sand grits under the same flow conditions (a). The frequency has been non-dimensionalized using outer flow variables, and the amplitudes are shown as 1/8th octave band levels. In (b), the spectral level is plotted against the roughness height for three non-dimensional frequencies.

Chapter 9 Conclusions

A review of current literature reveals a number of studies on the generation of sound by turbulent flow over rough surfaces. Early experimental studies were conducted using various novel flow configurations that attempted to isolate roughness noise from other aeroacoustic sources. The reported measurements do not agree on a scaling method that universally collapses the measured spectra, which makes physical understanding of this phenomenon difficult. Few theoretical models have been proposed which attempt to explain the physical processes and model roughness generated noise. Due to the limited available experimental data set, it is hard to determine the accuracy of these models.

A new facility has been developed and constructed to allow measurement of sound generated by a rough wall boundary layer flow. The facility is based on a well defined two-dimensional wall jet flow and is quiet enough to directly measure the sound generated by small patches of surface roughness. This facility has been used to create the first set of aerodynamic and acoustic measurements large enough to be used to validate and develop models for rough wall boundary layer noise. These measurements have been compared with the scaling models presented in literature and new models which have not previously been proposed. This section will present conclusions first on the wall jet flow facility and then on the measured acoustic spectra.

Wall Jet Flow Facility

1) Wall jet flows can be made significantly quieter than the equivalent boundary layer flow because the aerodynamic source region is much smaller. The natural decay of the flow allows plat edges to be placed far from the high velocity flow region which reduces edge noise.
2) Turbulent wall jet flow over a clean plate radiates sound which scales with the jet velocity to the eight power, U_0^8, suggesting a quadrupole source resulting from the free turbulence in the jet being reflected by the plate.
3) The maximum mean velocity a wall jet can produce is controlled by the upper shear layer flow, so the addition of roughness on the surface does little to affect this property. The surface characteristics do affect the near wall region and significantly affect the boundary layer thickness, momentum thickness, and skin friction underneath the shear layer.

Roughness noise

1) The shape of the rough surface has a significant impact on the shape of the far field acoustic spectrum. Stochastic sand grit roughness produces a broad spectral peak, while periodic nearly sinusoidal roughness produces much narrower spectral peaks.
2) Hydrodynamically smooth roughness patches produce a small, but significant, level of noise in the far field which is not generated by a smooth plate. This confirms that acoustic scattering is at least one of the mechanisms responsible for roughness noise.
3) The orientation of anisotropic surface roughness affects the directionality, amplitude, and frequency of measured far field acoustic spectra. The directivity

in the plane parallel to the surface is significantly affected when the wavenumber vector of the surface roughness is rotated.

4) As the flow speed over a rough surface is increased, the acoustic spectral levels increase with at least the 5^{th} power of velocity. The frequency of the spectral peak also increases nearly linearly with the velocity.
5) For a fixed set of inflow conditions, as the grit size of a stochastic roughness patch is increased the far field acoustic spectra increase in magnitude, and the spectral peak moves to lower frequencies.

References

Anechoic Flow Facility, 2004, “Facility Data Sheet, Anechoic Flow Facility (1971)” NAVSEA: Carderock Division website, www.dt.navy.mil/hyd/fac/ane-flo-fac/fac-dat-she/index.html.

Arguillat, B., Ricot, D., Robert, G., and Bailly, C., 2005, ”Measurements of the wavenumber-frequency spectrum of wall pressure fluctuations under turbulent flows”, 11th AIAA/CEAS Aeroacoustics Conference (26th AIAA Aeroacoustics Conference) 23-25 May 2005, Monterey, CA, USA, AIAA-2005-2855.

Blake W K, 1986, *Mechanics of Flow Induced Sound and Vibration*, Academic Press, New York.

Bendat, J.S., and Piersol, A.G., *Random Data, Analysis and Measurement Procedures*, John Wiley and Sons, New York.

Carmargo, H.E., Smith, B.S., Devenport, W.J., Burdisso, R.A., 2005, “Evaluation and Calibration of a Prototype Acoustic Test Section for the Virginia Tech Stability Wind Tunnel,” Report VPI-AOE-294.

Chanaud R. C., 1969, “Experimental study of aerodynamic sound from a rotating disk”, *Journal of the Acoustical Society of America*”, vol. 45, pg. 392-397.

Chase, D.M., 1980, “Modeling the wavevector-frequency spectrum of turbulent boundary layer wall pressure,” *Journal of Sound and Vibration*, vol. 70, pg 29-67.

Chase, D. M., 1987, “The character of the turbulent wall pressure spectrum at subconvective wavenumbers and a comprehensive model”, *Journal of Sound and Vibration*, vol. 112, pg. 125-147.

Cole L. D., 1980, “Measurements of Sound Generated by Boundary Layer Turbulence over Smooth and Rough Surfaces”, DTNSRDC Report SAD-288E-1942, July.

Corcos, G. M., 1963, “Resolution of pressure in turbulence”, *Journal of the Acoustical Society of America*, vol. 35, pg. 192-199.

Curle, N., 1955, "The influence of Solid Boundaries Upon Aerodynamic Sound" *Proceedings of the Royal Society of London*, vol. A231 pg 505.

DeGraaff, D.B., and Eaton, J.K., 2000, “Reynolds-number scaling of the flat-plate turbulent boundary layer”, *Journal of Fluid Mechanics*, vol. 422, pg. 319-346.

Duell E, Yen J, Walter J and Arnette S, 2004, "Boundary Layer Noise in Aeroacoustic Wind Tunnels", 42nd AIAA Aerospace Sciences Meeting and Exhibit, 5-8 January, Reno NV, AIAA 2004-1028.

Efimtsov, B. M., 1982, "Characteristics of the field of turbulent wall pressure fluctuations at large Reynolds numbers", *Soviet Physics-Acoustics*, vol. 28(4), pg 289-292.

Fang, Fuh-Min, Chen, J. C., Hong, Y. T., 2001, "Experimental and analytical evaluation of flow in a square-to-square wind tunnel contraction", *Journal of Wind Engineering and Industrial Aerodynamics,* vol. 89, pg. 247-262.

Farabee, T. M., and Geib, F. E., 1991, "Measurements of boundary layer pressure fluctuations at low wavenumbers on smooth and rough walls", *Flow Noise Modeling Measurements and Control.* ASME NCA-vol. 11, pg. 55-68.

Ffowcs Williams, J. E., 1982, "Boundary-layer pressures and the Corcos model: a development to incorporate low wavenumber constraints," *Journal of Fluid Mechanics*, vol. 125, pg. 9-25.

George J and Simpson R L, 2000, "Some effects of sparsely distributed roughness elements on two-dimensional turbulent boundary layers", 38th Aerospace Sciences Meeting and Exhibit, 10-13 January, Reno NV, AIAA-2000-0915.

Glegg, S., Devenport, W. J., Grissom, D. L., 2007, "A theoretical description of the noise from rough wall boundary layers", 13th AIAA/CEAS Aeroacoustics Conference (28th AIAA Aeroacoustics Conference)21-23 May 2007, Rome, Italy.

Goody, Michael, 2004, "Empirical Spectral Model of Surface Pressure Fluctuations", *American Institute of Aeronautics and Astronautics Journal*, vol. 42, n 9, Sept., pg 1788-1794.

Graham, W.R., 1997, "A Comparison of Models for the Wavenumber-Frequency Spectrum of Turbulent Boundary Layer Pressures", *Journal of Sound and Vibration*, vol. 206(4), pg 541-565.

Grissom, D.L., Smith, B., Devenport, W.J., and Glegg, S.A.L., 2007, "Rough-Wall Boundary Layer Noise an Experimental Investigation," 13th AIAA/CEAS Aeroacoustics Conference (28th AIAA Aeroacoustics Conference), 21-23 May 2007, Rome, Italy.

Hersh A S, 1983, "Surface Roughness generated flow noise", AIAA 8th Aeroacoustics Conference, Atlanta GA, April 11-13, AIAA-83-0786.

Howe M., 1984, "On the generation of sound by turbulent boundary layer flow over a rough wall", *Proceedings of the Royal Society*. A, vol. 395, pg. 247-263.

Howe M., 1986, “The influence of viscous surface stress on the production of sound by turbulent boundary layer flow over a rough wall”, *Journal of Sound and Vibration*, vol. 104, pg. 29-39.

Howe M., 1988, “The Turbulent Boundary Layer Rough Wall Pressure Spectrum at Acoustic and Subconvective Wavenumbers”, *Proceedings of the Royal Society*. A, vol. 415, pg. 141-161.

Howe M., 1991, “Surface pressures and sound by turbulent flow over smooth and rough walls”, *Journal of the Acoustical Society of America*, vol. 90, pg. 1041-1047.

Hwang, Y.F., and Geib, F.E., 1984, “Estimation of the wavevector-frequency spectrum of turbulent boundary layer wall pressure by multiple linear regression,” *Transactions of the American Society of Mechanical Engineers, Journal of Vibration, Acoustics, Stress and Reliability in Design*, vol. 106, pg. 334-342.

Inoue, O., and Hatakeyama, N., 2002, “Sound generation by a two-dimensional circular cylinder in a uniform flow”, *Journal of Fluid Mechanics*, vol. 471, pg 285-314.

Landahl, M., 1975, “Wave Mechanics of Boundary-Layer Turbulence and Noise”, *Journal of the Acoustical Society of America*, vol. 57(4), pg. 824-831

Launder, B.E., and Rodi, W., 1981, “The turbulent wall jets,” *Progress in Aerospace Science*, vol. 19, pg 81.

Lighthill, M. J., 1952, “On sound generated aerodynamically. I. General theory”, *Proceedings of the Royal Society London*, A211, pg. 564-587.

Lighthill, M. J., 1954, "On Sound Generated Aerodynamically, II: Turbulence as a sound source", *Proceedings of the Royal Society of London*, vol. A222 pg 1.

Lui, Y. Dowling, A. P., and Shin, H., 2006, “Effects of surface roughness on airframe noise”, 12th AIAA/CEAS Aeroacoustics Conference (27th AIAA Aeroacoustics Conference)8 - 10 May 2006, Cambridge, Massachusetts, AIAA 2006-2510.

Moody, L.F., 1944, “Friction factors for pipe flow”, *Transactions of the American Society of Mechanical Engineers*, vol. 66, pg.671-684.

Narasimha, R., Yegna Narayan, K. & Parthasarathy, S., 1973, “Parametric analysis of turbulent wall jets in still air”, *Aeronautical Journal*, vol.77, pg. 355-359.

Olssen C-O and Sunden B, 1998, “Experimental study of flow and heat transfer in rib-roughened rectangular channels”, *Experimental Thermal and Fluid Science*, vol. 16, pg. 349-365.

Patel, V.C., 1965, "Calibration of the Preston tube and limitations on its use in pressure gradients", *Journal of Fluid Mechanics*, pg. 185-208.

Sadr, r. and Klewicki, J.C., 2000, "Surface shear stress measurements system for boundary, layer flow over a salt playa", *Measurement Science & Technology*, vol. 11, pg.1403 – 1413.

Skudrzyk E. J., and Haddle G. P., 1960, "Noise production in a turbulent boundary layer by smooth and rough surfaces", *Journal of the Acoustical Society of America*, vol. 32, pg. 19-34.

Smith, B, 2007, to be published Ph.D. dissertation, Aerospace and Ocean Engineering Department, Virginia Tech.

Smith, B., Carmargo, H., Burdisso, R., and Devenport, W., 2005, "Development and Testing of a Novel Acoustic Wind Tunnel Concept," 11th AIAA/CEAS Aeroacoustics Conference, Monterey, CA, May 23-25.

Smol'yakov A V, 2001, "Noise of turbulent boundary layer flow over smooth and rough plates at low Mach numbers", *Acoustical Physics*, vol. 47, pg. 218-225.

Smol'yakov, A. V., and Tkachenko, V. M., 1991, "Model of a field of pseudosonic turbulent wall pressures and experimental data", *Soviet Physics-Acoustics*, vol. 37(6), pg 627-631.

Tailland, A. and Mathieu, J., 1965, "Jet parietal", A*cademie des Sciences -- Comptes Rendus*, vol. 261, n 12, pg. 2282-2285.

Wygnanski, I., Katz, Y. & Horev, E. 1992, "On the applicability of various scaling laws to the turbulent wall jet", *Journal of Fluid Mechanics*, vol. 234, pg 669-690.